Design and Noise Study of a Low-Drag Wind Turbine for Airborne Power Applications

A Numerical & Experimental Assessment

B. Van Den Kieboom

Technische Universiteit Delft

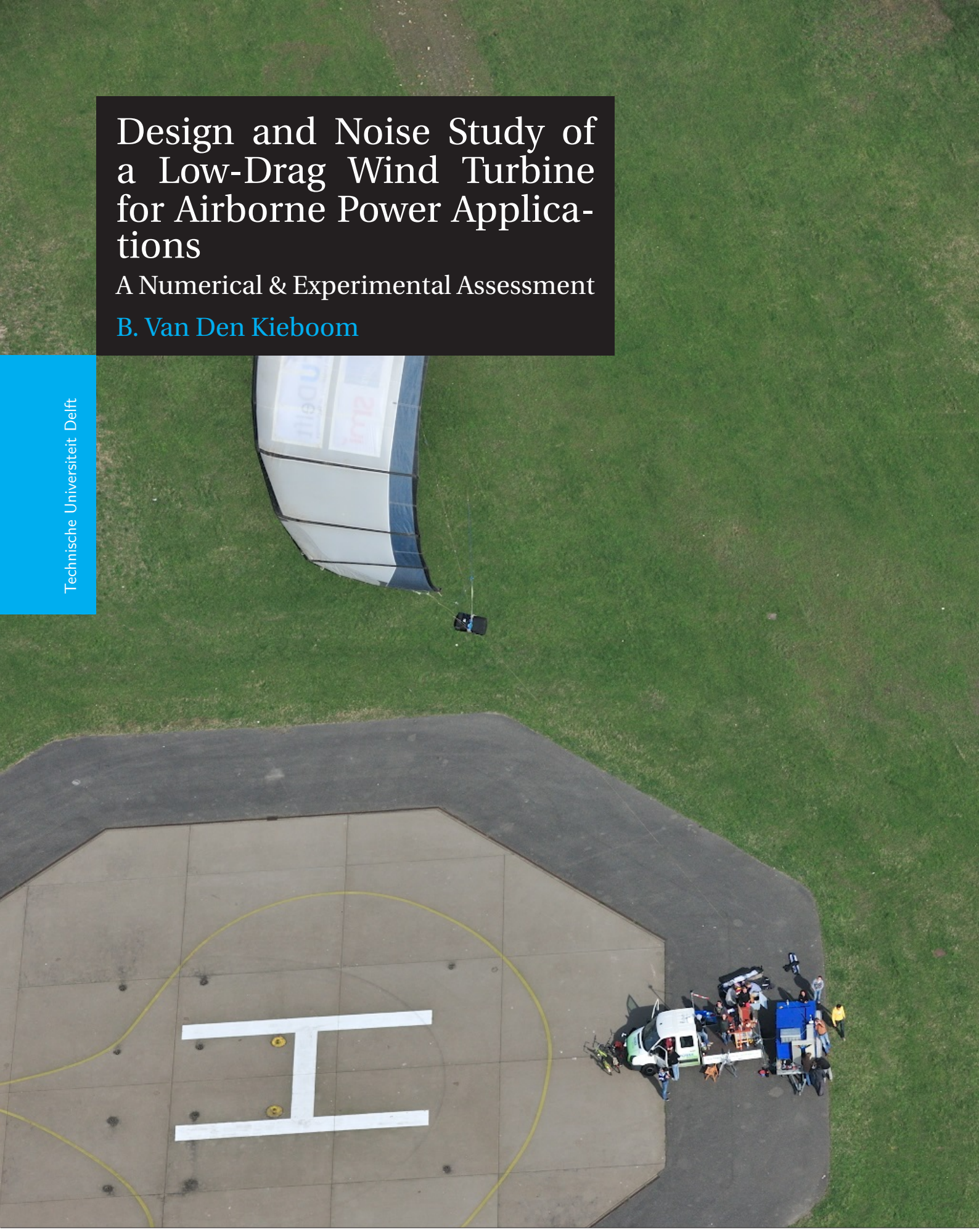

TU Delft Delft University of Technology

Challenge the future

Design and Noise Study of a Low-Drag Wind Turbine for Airborne Power Applications

A Numerical & Experimental Assessment

by

B. Van Den Kieboom

For obtaining the degree of

Master of Science
in Aerospace Engineering

at the Wind Energy Research Group, Faculty of Aerospace Engineering, Delft University of Technology,
to be defended publicly on Wednesday May 10, 2017 at 09:30 AM.

Supervisor:	Ir. W. A. Timmer	TU Delft
	Dr. -ing. R. Schmehl	TU Delft
Thesis committee:	dr. ir. B. W. van Oudheusden,	TU Delft
	MSc. J. Peschel,	Kitepower BV

This thesis is confidential and cannot be made public until May 10, 2017.

An electronic version of this thesis is available at `http://repository.tudelft.nl/`.

TU Delft Delft University of Technology

airborne wind energy KITEPOWER

Acknowledgments

I can still remember the day I walked into the office of Dr.-ing.R.Schmehl to ask for possible thesis options. I told him that I was interested in kitepower and rotor aerodynamics, and from this, he came up with one of the most interesting thesis topic (at least in my opinion). I would like to thank him for giving me this amazing opportunity and to be my supervisor in the initial phase of my thesis. Besides Mr. Schmehl I would like to thank Ir. Nando Timmer, for being the expert on wind turbine design during this thesis project, and for taking over the supervision when necessary.

Besides my two supervisors, this project would not have been possible without the help of Kitepower. A special gratitude goes out to Kitepower for giving this thesis project more meaning. Special thanks to: Johannes, Joep, Bert, Roger, Bruno, Antonello, David, Anna, Roland, and Balázs to make this project more interesting and creating an encouraging working environment. Thank you, Pietro, to calculate the power curves for different kite options. I hope my work will help accomplish to build the first commercial AWE unit.

Next, I would like to thank a person that I only met over Skype, but gave my research so much more content and pointed me to the fact that I need a low drag wind turbine. Thank you, Rob, for your interesting and valuable opinion on my work and steering me in a better direction.

My gratitude goes out to the people of room 6.08 for making the time working on my thesis so much more enjoyable, I could not wish for a better group to work with. Thank you for always listening to my questions and helping me with understanding things better or finding a solution. Special thanks to: Pranav, Delphine, Reynard, Mustafa, Matteo, Ben, Jo, Marcos, Clara, Julia, Ivan, Roberto, Robin, Irene, Viktor, and Luca.

The next group of people I need to thank are all the Belgians, Toine, Mikel, Lucas and Anna to make my student time so much more than studying. Special thanks to Maarten, Fie, and Michiel for proofreading my thesis and for creating awesome memories during this 6,5 years in Delft. "To Industry..."

And , last but by no means least, I would like to thank the people that are dearest to me. I would like to thank my family, especially my parents, for always supporting me and helping me out where they could. Finally, I would like to thank my girlfriend Deborah, for always being there during this thesis and supporting me.

Thank you,

Bas Van Den Kieboom
Delft, May 2017

Summary

Kitepower BV is one of the pioneering companies that wants to succeed in the airborne wind energy industry. Kitepower's concept makes use of LEI kites which move in a pumping cycle, producing energy when reeled out, and consuming a fraction of the energy when reeled in. To steer the kite, they make use of a kite control unit (KCU) that is currently powered by batteries. These batteries limit flying time to 2 hours and it is the goal of this project to come up with a solution to this problem.
The solution chosen by Kitepower BV is to mount a small horizontal axis wind turbine on top of the KCU which will produce 44 Watt of electrical power. During this project, two design methods are chosen to design this wind turbine. The first is a standard blade element momentum theory (BEMT) which is a simple tool to determine the performance of a wind turbine. Besides the blade element momentum theory, a second method will be used which is the free wake lifting line (LL). The lifting line can be used to simulate different inflow conditions such as yaw angles. It is necessary to create a wind turbine with a minimal amount of drag such that total power produced by the kitepower concept is maximised, this is set as the second requirement. The low drag wind turbine is designed with the use of a low order optimiser which tests all possible designs to see which rotor performs best. There is chosen to make two dummy designs which can be tested in the wind tunnel to validate the software so that Kitepower BV in the future can design their own wind turbines. At the end of the work, a final design is created that complies with the requirements from Kitepower BV.
The small wind turbine operates at high wind speeds. Because of these high wind speeds, the wind turbine will achieve high rotational velocities. This rotational speed results in tonal noises, for this reason, noise is investigated. With a semi-empirical model developed by Brooks et al. the sound pressure level of the wind turbine can be calculated. It uses the output conditions from the BEMT or LL codes to calculate the noise in a 1/3 octave band frequency. The accuracy of the model is validated using wind tunnel experimental data. Besides predicting the sound pressure level close to the wind turbine, a model is developed based on the work of DELTA to quantify what the noise levels are at noise sensitive locations. The wind turbine should comply with Dutch noise regulations.
A verification was performed before the wind tunnel test. From this verification, it was found that BEMT showed good agreement, while LL does not work for low Reynold number flows. This is because of the Kutta-Jouwkowsky condition which relates the circulation at the c/4 line to lift. Due to the low Reynolds number flow, the blade will separate earlier which is a violation of the Kutta condition.
During the experiment, it was seen that the BEMT results agree with the experimental data. However, it was observed that the optimum tip speed ratio (TSR) for the BEMT is lower than measured. This has two possible reasons, the first is the method used to measure the power. The second reason can be the difference in airfoil polar. The drag agrees for higher wind speed with the experimental data. While for lower wind speeds there is a larger deviation. This is possible due to the resolution of the measurement equipment with a combination of the airfoil data. When looking at the noise data it was found that there are only tonal peaks at the rotational frequency. When looking at the shrouded case there are no tonal peaks observed. Finally, it was found that the validation between BPM model and experimental result is difficult due to the large difference between data sets. This is due to the lack of measurement quality. The noise measurement is not performed in an appropriate tunnel resulting in high background noise. However, similar trends were observed between the two data sets indicating that BPM works but requires more validation.
The final design consist of a 12.75 cm diameter rotor with 4 blades, which produce the required power. The noise was investigated at 30 m/s at optimum TSR and it was concluded that the noise will never be a problem for residential areas. With the work performed, Kitepower BV will be able to design their own wind turbine based on the operating conditions.

Contents

List of Figures

Nomenclature

Acronyms

Symbol	Description	Units
AoA	Angle of Attack	
AWE	Airborne Wind Energy	
BEMT	Blade Element Momentum Theory	
BL	Boundary Layer	
BPM	Brooks, Pope & Marcolini model	
Exp	Experimental data	
HAWT	Horizontal Axis Wind Turbine	
KCU	Kite Control Unit	
L/D	Lift over Drag	
LBL-VS	Laminar Boundary Layer - Vortex Shedding noise	
LE	Leading Edge	
LL	Lifting Line Theory	
MTTL	Mean Time To Land	
MTTRB	Mean Time To Replace Battery	
R	Receiver	
S	Source	
S-S	Separation-Stall noise	
SPL	Sound Pressure Level	[dB]
TBL-TE	Turbulent Boundary Layer - Trailing Edge noise	
TE	Trailing Edge	
TEB	Trailing Edge Bluntness noise	
TSR	Tip Speed Ratio	
TV	Tip Vortex formation noise	

Constants

Symbol	Description	Units
β	Kite elevation angle	20°

ν	Kinematic viscosity	$1.568\,10^{-5}[Pas]$
σ	Representative flow resistivity grass	$80\ \left[kNsm^{-4}\right]$
c	Speed of sound	$340\ \left[\frac{m}{s}\right]$
h	TE height of airfoil	$0.7\ [mm]$
l_t	Tether reel-out length	$400\ [m]$
p_{ref}	Reference sound pressure in air	$[20\mu Pa]$
z_0	Surface roughness grass	$0.03\ [m]$

Greek Symbols

Symbol	Description	Units
α	Angle of Attack	[°]
χ	Course Angle in *Chapter 7*	[°]
δ	Boundary layer thickness	$[m]$
δ^*	Boundary layer displacement thickness	$[m]$
Γ	Circulation	$\left[\frac{m}{s^2}\right]$
Λ	Turbulence length scale	$[m]$
λ	Tangential velocity factor in *Chapter 7*	$[-]$
λ	Tip speed ratio	$[-]$
Ω	Rotational Speed	$\left[\frac{rad}{s}\right]$
ϕ	Azimuth Angle in *Chapter 7*	[°]
ϕ	Inflow Angle	[°]
Ψ	Airfoil TE slope angle	[°]
ρ	Air Density	$1.225\ \left[\frac{kg}{m^3}\right]$
θ	Boundary layer momentum thickness	$[m]$
θ	Polar Angle in *Chapter 7*	[°]
θ	Twist Angle	[°]
ξ	Airfoil camber	[%]
ζ	Tilt Angle	[°]

Roman Symbols

Symbol	Description	Units
$\dot{m}$	Mass Flow Rate	$\left[\frac{kg}{s}\right]$
$\overrightarrow{u}$	Velocity vector	$[m/s]$
A	Swept area	$\left[m^2\right]$
a	Induction Factor	$[-]$
a'	Tangential Induction Factor	$[-]$

A_{abs}	Atmospheric absorption loss	$[dB]$
A_r	Refraction loss	$[dB]$
B	Number of Blades	$[-]$
c	Chord Length	$[m]$
c_0	speed of sound	$[m/s]$
C_d	Drag Coefficient of 2D aerofoil	$[-]$
C_l	Lift Coefficient of 2D aerofoil	$[-]$
C_P	Power Coefficient	$[-]$
C_T	Thrust Coefficient	$[-]$
D	drag of a blade element	$[N]$
$D_\square$	Directivity for l (low frequency) or h (high frequency)	$[-]$
F	Prandtl-glauert tip loss	$[-]$
f	Reel-out factor	$[-]$
f_b	Blade passing frequency	$[Hz]$
F_n	Force of a blade in normal direction	$[N]$
F_t	Force of a blade in tangential direction	$[N]$
h	Height of the TE	$[m]$
I	Sound intensity	$\left[\frac{W}{m^2}\right]$
J	Mass moment of inertia	$\left[kg \cdot m^2\right]$
k	wave number of a certain frequency	$[-]$
L	Lift of a blade element	$[N]$
l	Viscous core span wise extent	$[m]$
L_w	Sound power level	$[dB]$
M	Mach number	$[-]$
N	Critical amplification factor in Xfoil or Rfoil	$[-]$
ns	Number of Radial Sections	$[-]$
$OSPL$	Overall sound pressure level	$[dB]$
P	Power	$[W]$
p_{rms}	Root mean square sound pressure	$[Pa]$
r	Radial Position of Blade Element	$[m]$
R_c	Chord Reynolds number in BPM model	$[-]$
r_e	Receiver location in BPM model	$[m]$
R_{hub}	Hub radius	$[m]$
SPL_α	SPL of separation stall noise	$[dB]$

SPL_{LBL-VS}	SPL of laminar boundary layer vortex shedding noise	$[dB]$
SPL_{TBL-TE}	SPL turbulent boundary layer	$[dB]$
SPL_{TEB}	SPL of TE bluntness noise	$[dB]$
SPL_{TIN}	SPL of Turbulent inflow noise	$[dB]$
$SPL_{TIN}^{f_{high}}$	SPL of Turbulent inflow noise at high frequency	$[dB]$
SPL_{TV}	SPL of Tip Vortex noise	$[dB]$
T	Drag of a wind turbine	$[N]$
T	Thrust of the rotor	$[N]$
T	Torque	$[Nm]$
TI	Turbulence intensity	$[-]$
u_Γ	Induced velocity due to the circulation	$[m/s]$
V	Velocity	$\left[\frac{m}{s}\right]$
V_{app}	Apparent Velocity from KCU	$\left[\frac{m}{s}\right]$
V_W	Wind Velocity at kite/KCU height	$\left[\frac{m}{s}\right]$
x_p	Evaluation point lifting line	$[m]$

Subscripts

Symbol	Description	Units
$\square_\infty$	Far-Up Stream	
$\square_a$	Blade Element Momentum Theory	
$\square_{max}$	Maximum value of a parameter eg C_P	
$\square_p$	Parameter from pressure side of airfoil	
$\square_s$	Parameter from suction side of airfoil	
$\square_w$	Parameters in the Wake of Far-Down Stream	

Chapter 1

Introduction

Energy is one of the most important demands for any modern, prosperous and thriving society. Energy can be generated with different methods. One can think of oil, gas, nuclear, solar, wind, etc. However, the first three methods are more polluting compared to the others. The pollution of the earth together with the increase in population and energy consumption is one of the most dangerous threats we face today. One of the possible solutions is to reduce or stop the use of these polluting energy generation methods and invest in renewable energy. One of the promising methods of generating energy is by using wind turbines, which can convert a large amount of kinetic wind energy to electricity. Wind turbines have been increasing in size rapidly in the last 40 years to capture the more stable winds at higher altitudes. However, these large machines are running at their structural limits. To solve this problem wind turbine blades can be made more efficient, or new concepts to harvest wind energy can be thought of. Loyd [15] realised that a huge force can be generated by a kite, and thought to convert it to energy. Thus, Airborne Wind Energy(AWE) was born.

AWE systems have as an advantage that they can reach higher altitudes where the kinetic energy available in the wind is higher due to the higher velocities. There are different AWE system concepts. Some have the power generation on board while others have the power generation on the ground. AWE systems have as the advantage, compared to conventional wind turbines, that they can reach these high altitudes with a fraction of the material and cost. Resulting is a cheaper wind energy system with the same energy rating. The disadvantage of AWE systems is that the control of the wing/kite is complicated. The first available AWE systems will be ideal for disaster areas, replacement of diesel generators or energy production for rural areas that are not connected to the grid.

Kitepower BV is a commercial spin-off of the kite power research group at Delft University of Technology, with the goal of creating a commercial airborne wind energy system. They will do this with the use of soft leading edge inflatable (LEI) kites that they fly in a yo-yo motion such that there is positive net energy generated. During the yo-yo motion, three movement blocks can be observed. First, the kite will fly a figure of eight patterns to produce power. Next, when maximum tether length is reached the kite will park itself so it can start the last phase which is reel-in. During reel in the kite is positioned in such a way that it costs a fraction of the produced energy to reel the kite back in and restart the cycle. These complicated movements are performed by attaching a small robot 20 meters under the kite that is providing all the controls. This small control-bot is called the Kite Control Unit (KCU). Another task of the KCU is to communicate with the ground station. To perform all its tasks a stable energy supply is required. Currently, this energy supply is provided by a battery but this needs to be replaced by a constant and reliable power source.

Kitepower BV chose to combine conventional wind energy with a novel concept by using a small wind turbine that will be mounted on top of the KCU. This small wind turbine will be a horizontal axis wind turbine with a protection shroud, so that it will not cut the bridle system. The wind turbine should be able to produce at least 44 Watt of electrical power at a wind speed of 30 m/s. This 30 m/s is calculated by Kitepower BV based on the kite size and the lift over drag of the kite which is 5. During this thesis, the design of this wind turbine is discussed. The design considerations are that the wind turbine will only be designed for aligned flow, so yawed cases are not considered for this thesis. The design will be done by conventional techniques such as blade element momentum theory. It is investigated if a more novel method like a free wake lifting

line is accurate enough during design procedure. Besides the performance software, a simple optimiser is developed to generate a low drag design wind turbine. This low drag wind turbine is required to maintain an efficient kitepower system.

Additionally to the performance assessment, an aeroacoustics wind turbine prediction code is created. This assessment will only take the aerodynamically generated noises into account. Therefore, mechanical noises generated by vibrations introduced by shroud or generator are not considered. The noise sources of interest are airfoil self-noise, which can be calculated with the model of Brooks et all [10] and turbulent inflow noise which was studied by Lowson [16]. For the kitepower system, an atmospheric attenuation model is developed to investigate the occurring noise levels at certain locations of interest. This model is based on spherical spreading, atmospheric absorption, reflection with the ground and wind influence [11, 12]. At the end of the project, a check is performed to see if the final designed wind turbine meets all the certification criteria.

When all the models are verified, an experimental campaign is performed in the W-tunnel at the High-Speed Lab (HSL) in Delft to be able to validate the software. Here the performance of the two wind turbines designed by the optimiser and BEMT is tested. The test includes drag, power and RPM measurements. Finally, a microphone was placed and noise measurements is performed. From the experimental result, the aerodynamic noise prediction code and performance codes are validated. When the software is fully validated and shortcomings are known a final redesign is created which suits the requirements of Kitepower BV.

The report is structured in four main parts which are divided into chapters:

- **Part I**: Background
  - *Chapter 2*: State of the art literature study where the appropriate methods are chosen to solve the problems.
  - *Chapter 3*: Description of the problem and the research question of the thesis.
- **Part II**: Methodology
  - *Chapter 4*: Theory of the performance codes is explained. Here a Verification of Xfoil and Rfoil is performed and the BEMT and lifting line code are discussed and verified.
  - *Chapter 5*: Discussion of the main aeroacoustic noise sources for wind turbines and how they can be modelled. At the end, a verification is performed.
  - *Chapter 6*: Explanation of the atmospheric attenuation model. The location of interest and frequencies of interest are discussed.
- **Part III**: Result and Discussion
  - *Chapter 7*: Explanation of the working principle of the optimiser and first generated designs for wind tunnel testing.
  - *Chapter 8*: Discussion of measurement methods and quantification of results. A comparison is made with shrouded wind turbines. Next, the models are validated and when full insight is obtained on how the codes work a final design is created for Kitepower BV.
  - *Chapter 9*: The effect of the wind turbine is evaluated and its effect on the power gain of the system.
  - *Chapter 10*: This chapter contains a general conclusion to the thesis as well as answers to the research questions and recommendation for further research.
- **Part IV**: Appendices

I

BACKGROUND

Chapter 2

Comparison of Performance & Aeroacoustics Models for Wind Turbines

Before the research questions can be defined a study is performed on what the available methods are to study the performance and noise of a wind turbine. In the research three topics can be distinguished, wind turbine performance, wind turbine noise and the experimental set-up. The performance of the wind turbine contains everything that is related to the produced power and generated drag. Only the aeroacoustic noise generated due to the interaction between blade and wind is considered. For this thesis, the focus lays on the noise generated at the optimum Tip Speed Ratio (TSR). Last, the wind tunnel experiments are used to validate all the designs, here the appropriate measurement equipment needs to be selected.

2.1 Airborne Wind Energy

The conventional wind turbines are almost at their limit of power production because of structural and material limitations. It is also known that the last 25% of the blade generates most energy since it will generate the highest torque at optimum conditions. It could be possible to replace this last 25% of the blade with a tethered flying wing making the system cheaper to manufacture, since no tower construction is needed. The wing could fly to higher altitudes. At these higher altitudes, the wind is more stable and faster. The wind is more stable because of less interaction with obstacles. To reach these high altitudes the wing is connected to a single line to the ground station, which reduce the drag, this line is called the tether. Kitepower BV chose to use a LEI kite instead of a rigid wing. The kite is steered in a pattern which is planned and controlled by the KCU. The KCU controls the kite by using small winches, which are connected to the steering and depower lines. The current problem with the KCU is that it still operates on batteries limiting the flight time. A solution to this problem is to power the KCU by either a conductive wire in the tether or mounting a small wind turbine on the KCU. The mass added to the whole system when choosing a conductive wire would easily be 14 kg assuming 400 meters of 2 phase conducting wiring with a cross section of 2 mm^2. Because of this, the wire was omitted and a wind turbine is chosen. The Lift over Drag (L/D) of the AWE system determines to a large extend the amount of power produced by the AWE system, for this reason, it needs to be maximised by decreasing the drag or weight of the wind turbine. For this thesis, the drag is prioritised since this force will increase quadratically with the velocity. Though the wind turbine will be designed for an AWE system, the physics behind these systems are of minor importance for the project. More information on this topic can be found in the Airborne Wind Energy handbook [17] and the paper of Cherubini [18].

It is important to know what the final set-up would look like. The wind turbine will be mounted on top of the KCU which can be seen in Figure 2.1, which is a generic figure. According to the calculations of Kitepower BV, the apparent wind speed at the KCU is 30 m/s for a kite with L/D of 5, and a ground wind speed of 7 m/s. This can change for the new design of the AWE system so, for this reason, it was decided that a software would be developed to design the blades, which only depend on the power requirements and the velocity. For protecting the bridle system, a shroud is added changes the performance of the wind turbine. The shroud can be seen in Figure 2.1, the shroud dimensions used in this project are 3-5 mm gap size and a shroud depth of 5 cm. The 5 cm is required to ensure that the bridles will not get entangled in the wind turbine. At the end, the

effect of the wind turbine on the AWE system is investigated. There is looked at the power curves and annual energy production. A hypothetical comparison is made between mounting a wind turbine and replacing the batteries every two hours. Note that replacing the batteries every time is not feasible.

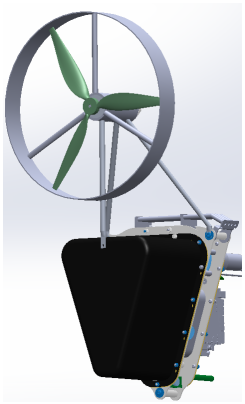

Figure 2.1: KCU with mounted wind turbine and shroud of 30 cm diameter

2.2 Wind Turbine Performance

There are several different methods to simulate the aerodynamics of a wind turbine. Some are more suitable for designing in an initial stage while others are better for detailed design but are more computationally expensive. For the project, it is important that the chosen method is capable of simulating high RPM flows with a low Reynolds number (Re). Factors of interest are the amount of power and drag the rotor will generate for certain inflow conditions. The project is focused on the design of wind turbine rotors, meaning a suitable design procedure should be developed to generate initial blade lay-outs and configurations for a certain power requirement. Besides the performance of the wind turbine, correct airfoil polar data is of utmost importance. Two methods can be used to determine airfoil polar diagrams, first, there can be chosen for measurement data. Secondly, the airfoil polar can be determined with panel codes such as Xfoil or Rfoil.

The discussed methods will be able to calculate the power and drag produced. To assess the different rotors the non-dimensional parameters are of interest. These parameters are the power coefficient C_P and the thrust coefficient C_T. These parameters are used to investigate the performance of the rotor for different inflow conditions. For Kitepower BV the power curves are of interest and these can be calculated with Equation 2.1

$$P = \frac{1}{2}\rho V^3 A C_P \tag{2.1}$$

where, P is the power, ρ is the air density, V is the wind speed and A is the swept area of the rotor.

2.2.1 Blade Element Momentum Theory

Blade Element Momentum Theory (BEMT) was introduced by Glauert [4, 19], the method is a combination between the one-dimensional momentum theory and blade elements. With this method it is possible to determine locally the loads of the wind turbine blade and power production [4–6]. The theory is widely used for analysing and designing rotors. BEMT is the industry standard for quickly designing and assessing the performance of a wind turbine, due to its computational efficiency [4]. The main limitation that BEMT has is that it relies on the quality of the airfoil polar which depends on the angle of attack (AoA) and Reynolds (Re) number.

The method divides the blade into 10-20 equal or cosine spaced sections, as well as assuming that there is no interaction between the section. This assumption simplifies the method significantly and introduces some physical limitations. Each section will have a different apparent wind speed due to the rotational speed component. The 1D momentum theory assumes that behind the rotor, the far upstream flow is decelerated due to a force applied to the flow from the actuator disk. The kinetic energy extracted from the flow is converted to mechanical power. The ratio of flow slowed down can be expressed as an induction factor (a)

(Equation 4.1). From this, the apparent wind speed can be determined for each wind turbine blade section and an equilibrium can be obtained. The BEMT uses as input blade lay-out and inflow conditions:

1. Diameter
2. Hub diameter
3. Chord, Twist and airfoil distribution
4. Velocity
5. TSR

The BEMT will calculate the power and thrust of a rotor for a Tip Speed Ratio (TSR) $\left(\lambda = \frac{\Omega R}{V}\right)$. It is of importance to know the non-dimensional factors C_P and C_T to do a full analysis and comparison of different rotors. If the coefficients are known the rotor performance can be evaluated and it can be seen how it behaves for different wind speeds and rotational speeds.

The original BEMT simplifies the wind turbine to a large extent due to the made assumptions. These assumptions will result in large errors when comparing it with experimental data. To solve the problem introduced by the simplifications, engineering corrections are introduced [6], which are mostly based on empirical models. There is a correction for tip losses of the blade, which is based on Prandtl's tip loss correction [5]. As soon as the flow is slowed down by half of the initial wind speed the rotor will go into turbulent wake state, if no correction is applied the thrust coefficient will decrease while looking at real rotors it will stay equal to the maxim C_T or even increase. There are multiple different corrections for this and a good summary is presented by Clifton-Smith [20], which tested multiple corrections, and concluded that for small wind turbines the correction proposed by de Vries [21] is the most representable. Last, the rotor is turning at a high speed. Due to this the airfoil performance will increase. Because of radial velocity component introduced, the stall angle will be increased causing the flow to stay longer attached. The most common model used to take this phenomenon into from Du and Selig [4, 22]. This model corrects the 2D airfoil polar for the 3D effects.

2.2.2 Lifting Line Theory (Free Wake)

Lifting line theory is getting more attention lately since it can model unsteady inflow condition more precise compared to BEMT. Lifting line theory divides the blade into sections with each a bound vortex at the quarter chord line. The lifting line is based on the Kutta-Joukowski equation [7, 8]. The Kutta condition can relate the lift to the circulation (Equation 4.17) by assuming that the flow leaves the TE with the same speed and same pressure. The main advantage compared to BEMT is that each section has an influence on the neighbouring sections and total flow field. The total flow field velocity is a superimposition of the far stream velocity and induced velocity due to the circulations of the blade sections. The induced velocity can be calculated using Biot-Savart law [7, 8].

There are two main methods of the lifting line. The first, is the prescribed wake and second, the free wake. For this project, the free wake is used, since it would be able to predict the unsteady effect on the blade when the inflow angle is changed. The free wake is a time solving process where for each time instance the blade will shed a vortex in the wake. According to Kelvins theorem the change in circulation must be constant $\left(\frac{D\Gamma}{Dt} = 0\right)$ [8].

The lifting line can be a powerful tool in case good airfoil data is used, which is corrected for stall delay, and if the angle of attacks are low. It is known that the code performs poor and gives numerical errors for angles close to stall angles and higher. For this reason, the lifting line would only be used to determine the C_P at the optimum tip speed ratio.

2.2.3 Vortices Lattice Method

Vortices Lattice Method (VLM) uses the same principles as lifting line, by neglecting thickness and viscosity. However, the major difference is that in the chord wise direction more vortices are introduced. Because of this, the VLM method will be more computational expensive compared to BEMT or lifting line. When there is chosen for a VLM with a free wake, similar behavior will be observed compared to the lifting line. However,

instead of shedding only one vortex now a whole lattice of vortices is shed. The VLM cannot model thickness of an airfoil but it can model the camber. For the cores of the vortices, an extra viscous term should be considered preventing and unstable model. The problem with VLM is that the literature is limited for VLM method applied to wind turbines, for this reason, a closer look is taken at helicopter VLM which is comparable to wind turbines VLM. The only model currently available is of Da Silva et al. [23, 24], their model is verified with a BEMT model, their conclusion is that it takes much more computational time in the order of N_c^2 compared to LL, were N_c is the number of elements in chord wise position. From this, it can be concluded that VLM is too complicated and takes too much time for the designing stage of a wind turbine.

2.2.4 Panel Method

The panel method is a method that creates a shell of vortex structures over the wind turbine blade. The advantage is that it considers the thickness of a blade, making the solution more physical representable. The panel method distributes singularities and dipoles over the geometry, which can be represented by vortex sheets. The number of panels can be variable it will increase accuracy at a cost of computational time. The Kutta condition is used as a boundary which states that the pressure at the trailing edge (TE) at pressure side and suction side should be the same. This is also one of the boundary conditions for Xfoil or Rfoil.

A viscous-inviscid coupling was developed by Ramos-García et al. and they found good results comparing their simulations with the result from the MEXICO program [26]. They used a free wake and found out that a viscous coupling is needed especially when the blades are operating at a high angle of attack. An accurate solution for a panel code requires the use of a high number panels, increasing the computational time [25]. This method is only suitable for detailed design.

2.2.5 Computational Fluid Dynamics

Computational fluid dynamics (CFD) is a very powerful tool for flow analysis. CFD is well known for its accuracy and its high computational time. CFD solves the Navier-Stokes equations, which can be compressible or incompressible. There are several computational methods the first is, direct numerical analysis (DNS). DNS has known that it is the most computational expensive form of CFD, and it is not feasible to use this method for complicated flow problems [4]. Second, there are the Reynolds Average Navier-Stokes equations (RANS). These are time-averaged Navier-Stokes equations. These models showed good result but lack high enough accuracy for stall controlled wind turbine [4]. To model stalled flow one could look at Detached Eddy Simulation (DES), however this method need a fine mesh to model the turbulent flow resulting in a higher computational time than RANS [4].

Another important part of Navier-Stokes solvers is the meshes that must be generated. There are several different mesh styles like cartesian, hexahedral cells or tetrahedral cells. For generating meshes for complicated problems experience is required [4, 19]. Second, since the wind turbine is turning periodically most of the time only 1 blade is simulated to decrease computational time [4, 27]. The rotor is rotating, resulting in an imposed radial velocity component, or a mesh that needs to be updated everythime to rotor moves. Updating a mesh results in a high computational time just for one flow case. During the design of wind turbines, different designs are generated and tested. Because of the high computational time, CFD would be impossible for this project. It is mostly used to understand the flow better or to simulate complicated flow conditions like yaw etc. [4]. CFD will not be used since experience is needed in meshing and the computational time is too high.

2.2.6 Performance Model Selection

The chosen model depends on the capability to simulate the performance of the given rotor. The second requirement is a low computational time to test quickly the performance of different designs. In Figure 2.2 the complexity and calculation time can be seen from different methods. Based on this CFD panel method and VLM is discarded.

The BEMT will be ideal to investigate the overall performance quickly and accurate if reliable airfoil data is used. The next model that is chosen is LL free wake model. The LL can only be used when the AoA is not

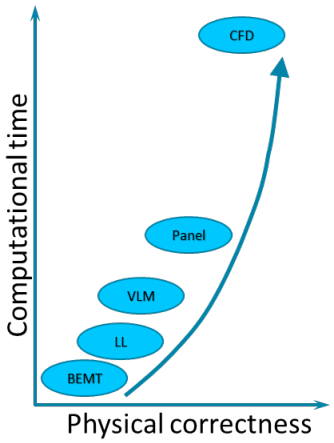

Figure 2.2: Computational time for different aerodynamic performance models

close to stall angle. This is the case for an optimum wind turbine blade which operates close to the optimum TSR. For this reason, the LL will be used to simulate more complex flows at optimum TSR such as yawed inflow. A verification is doen before the models will be used. The model used to verify is Bladed from DNV GL. It is assumed that BEMT should be close to the calculations of Bladed and LL should be similar, during verification steady inflow condition will be assumed.

2.2.7 Low Reynolds Number Airfoils

The Reynolds number of mini wind turbines are in the order of 10^4->$5 \cdot 10^5$, special airfoils will be needed that are designed for low Reynolds number (Re) flows. An efficient and good wind turbine can be developed if the used airfoil has good perfromance. For wind turbine airfoils a good performance is a high lift to drag ratio (L/D) and have a high $C_{l_{max}}$. For this research, a full degree of freedom for designing is required. This means that no restrictions are desired for the requirement of using measured data, for this reason, the BEMT and lifting line code will be coupled with Xfoil or Rfoil. Xfoil is a viscous/inviscid airfoil solver which can calculate lift and drag polar for different Re numbers. This is needed since at each blade station the Re number will vary significantly which resulted in using Xfoil or Rfoil for each section. Besides the lift and drag polar the displacement and momentum thickness are required for the noise models which is also no problem for Xfoil or Rfoil. Xfoil has a correction for compressibility flow if the Mach number is lower than 0.6. The correction applied is the Karman-Tsien rule which corrects the pressure distribution for the Mach number, this is more explained more by Anderson [9].

The airfoil used are mainly found from literature which is described as low Re number airfoils. The biggest set of airfoils is from Selig, who did a test campaign for low-speed airfoils. For this reason, the airfoils described in these reports will be used since it gives a database of measured data [28–31]. The measured data will be used to verify the result generated by Xfoil and Rfoil. Based on this, a decision will be made on which solver is going to be used. It is commonly known that Xfoil or Rfoil over predicts the lift coefficient and under predicts the drag, so what will need to be done is develop factors to correct the Xfoil results. This can be done by comparing Selig measurements and the prediction of airfoil for similar airfoils being used.

2.3 Fundamentals of Aeroacoustics for Wind Turbine

When looking at the noise of a wind turbine there are two big noise sources [32, 33]. First, there is the mechanical noise from all the moving components. And second, there is aerodynamic noise. For this project, the focus will be to analyse the aerodynamic noise since this is the major noise source of wind turbines [1]. First, the theory of aeroacoustics and noise sources of a wind turbine are discussed. Second, there is discussed how the sound level of the sources can be predicted using semi-empirical methods. Third, there will be discussed what the underlying principle is of computational aeroacoustics (CAA). Last, the sound propagation is discussed, this model is needed to investigate what the noise levels are at different locations far away from the

noise source. This model must comply with regulations and it must be investigated what the sound will be at noise-sensitive locations such as residential areas.

2.3.1 Basic Acoustics

Sound is an oscillation of pressure waves that travels through air or another medium [34]. For certain frequency ranges humans and animals can hear this. The audible range for humans is between 20 Hz and 20kHz. The sound travels through air at a speed of 340 m/s (for standard conditions). If the sound is unwanted by a person it is called noise. If one can call sound noise depends on different quantities; "loudness", the frequency and the person. This is because it is highly personal if one perceives sound as noise. A low frequency can be considered as more annoying than a certain high frequency. For example, people find the faucet dripping highly annoying.

Sound Source Quantities

The sound is not perceived linear [34]. When the pressure oscillation is doubled, it is not perceive as twice as high. The reason for this is that sound works on a logarithmic scale. One way of measuring the sound level is by the sound pressure level (SPL). The sound pressure level is a measure of an effective pressure compared to a reference pressure. The equation for the SPL can be found in Equation 2.2 [1, 34].

$$SPL = 20 \cdot \log_{10}\left(\frac{p_{rms}}{p_{ref}}\right) \tag{2.2}$$

where, SPL is the sound pressure level, p_{rms} is the root mean square sound pressure (Equation 2.3), and p_{ref} is the reference pressure which is $2 \cdot 10^{-5}$ Pa, which is the thresholds for human hearing at 1000 Hz [34].

$$p_{rms} = \lim_{T\to\infty}\left(\frac{1}{T}\int_0^T p^2(t)dt\right) \tag{2.3}$$

Besides sound pressure, there is a second quantity that can define a sound source, which is the sound intensity. Sound intensity is the amount of energy a sound source carries per unit area. The sound intensity can be calculated by Equation 2.4 [1, 34].

$$I = \frac{p_{rms}^2}{\rho_0 c_0} \tag{2.4}$$

Where, $\rho_0 c_0$ is the sound impedance, which for standard conditions is 416 Pa·s/m [34]. If the sound intensity is known Equation 2.2 can be rewritten as function of sound intensity I.

$$SPL = 10 \cdot \log_{10}\left(\frac{I}{I_{ref}}\right) \tag{2.5}$$

where, I_{ref} equals to 10^{-12} W/m^2. The sound pressure perceived can vary if the receiver is at different locations. The further away from the source the lower these values will be.

Another quantity that describes a noise source is sound power level. The main difference between SPL and sound power level is that SPL is a quantity that describes the noise at a receiver location, and can be measured by a microphone. While sound power level is a property that describes the amount of power a source has. The sound power is an important parameter for the attenuation model since it can be recalculated to SPL at different calculations if the directivity pattern is known.

Frequency Bands

Besides quantities that characterise the sound there is one other important factor that gives a better understanding about everyday sound. That other factor is frequency, a sound source can consist of multiple signals with each a different frequency. This is called broadband noise. If all the power of a signal is present in one

frequency it is called tonal noise [34].

For analysing noise, different frequency bands can be used. The most commonly used are 1/3 octave band and the 1/1 octave band. Besides octave bands, a narrow band with a fixed Δf is commonly used to quantify the tonal noise. The 1/1 octave band is a frequency band where the higher frequency is twice the amount of the lower frequency. While the 1/3 octave band can be defined as $f_{n-1} = f_n/2^{1/3}$.

Octave bands are useful if the SPL over large frequency ranges is analysed. While the Δf band is useful for analysis the tonal component of a wind turbine. The major tonal components are: Rotational frequency and blade passing frequency with each their harmonics. In this thesis, the constant band frequency is used to analyse tones while for the total noise characteristics a 1/3-octave band is used. The 1/3-octave band frequencies can be calculated with Equation 2.6.

$$\begin{aligned} f_u &= 2^{1/3} f_l \\ f_u &= 2^{1/6} f_c \\ f_c &= 2^{1/6} f_l \end{aligned} \tag{2.6}$$

Humans are more sensitive to certain frequencies. The threshold is 0 dB for frequencies between 3000-4000 Hz while the threshold of hearing for a lower frequency is much higher [1]. The goal of the research is to investigate the noise which is more sensitive for humans. This means that a certain weighting must be performed on the noise to make it more representable for humans. For this frequency weighting, will be applied when investigating total noise in the 1/3-octave band. There are different weighting filters the most common ones are A, B and C which can be seen in Figure 2.3 [35]. They have as main function to de-emphasize the lower frequencies.

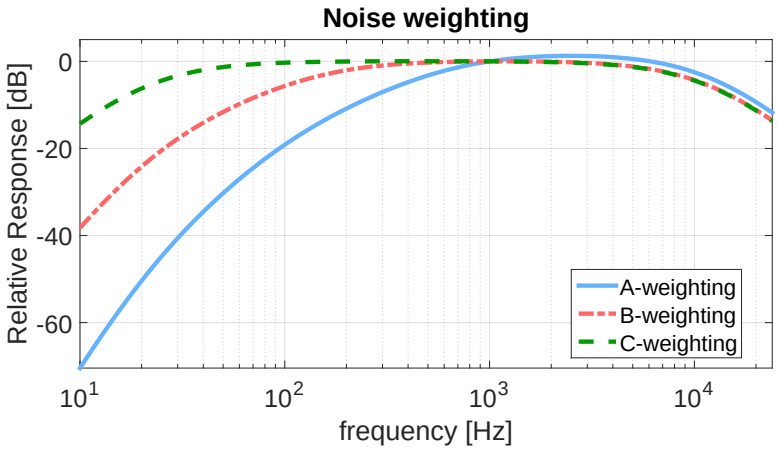

Figure 2.3: A-, B-, C-weighting [1]

The weighting used in this thesis will be the A-weighting since the two others are only used when there are strong low-frequency sound levels. Small wind turbines are fast rotating meaning that most of their noise will be in the high-frequency range so this is the reason why an A-weighting filter is used.

Directivity Patterns.

There are different patterns in which a sound source distributes its sound. There are omnidirectional patterns which are called monopoles this can be seen in Figure 2.4. The sound can radiate in different direction the most known directivity patterns are the dipole and quadrupole. A dipole source will radiate it sounds in two directions. The best example of a dipole source is a normal loudspeaker. A quadrupole is a sum of two opposing dipoles and will emit its sound in four directions.

In theory, the wind turbine should show a dipole directivity pattern where the largest magnitude faces the flow direction [36]. For the attenuation model, a monopole will be assumed which simplifies the model. The

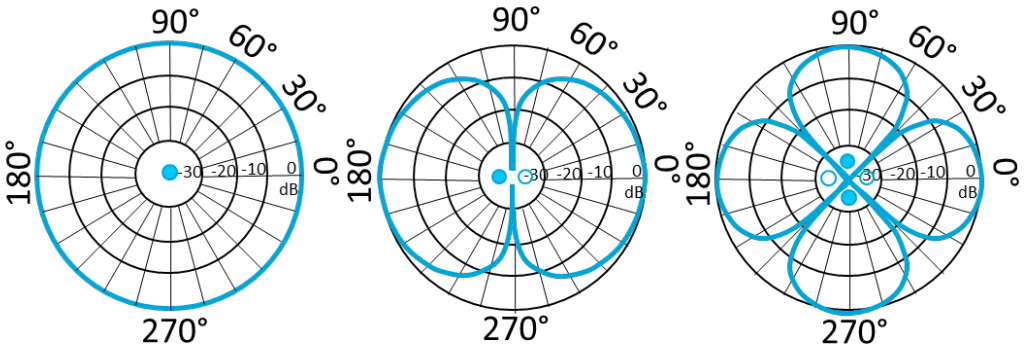

Figure 2.4: Directivity patterns for acoustic sources: (left) monopole, (middle) dipole and (right) quadrupole [2]

monopole is valid since the wind turbine is so small and the kite can face any direction depending on the wind direction.

2.3.2 Theory of Aeroacoustics

The study of noise generated by a turbulent fluid motion or a fluid interacting with a solid surface is called aeroacoustics. The study of aeroacoustics is difficult and the first attempt to create a general theory is from M.J. Lighthill [37, 38]. He rearranged the Navier-Stokes equations into a wave equation, combining the fluid dynamics and acoustics [38]. In this equation Lighthill introduced the Lighthill stress tensor which can be seen in Equation 2.7 [33, 38].

$$T_{ij} = \underbrace{\rho v_i v_j}_{1} - \underbrace{\sigma_{ij}}_{2} + \underbrace{\left(p - c_0^2 \rho\right)\delta_{ij}}_{3} \tag{2.7}$$

where, the first term is the contribution of convection, second term the shear stress and lasts a non-linear term for the acoustic generation process. T_{ij} represents the Lighthill stress tensor which represents the radiation source terms per unit volume [38]. The Lighthill equation is difficult to solve numerically (comparable to Navier-Stokes equations) making it difficult to use for estimating the noise produced in most flow cases.

The first simplification of the Lighthill equation was done by Kirchhoff and Helmots. They assumed the radiation of sound from a source can be encapsulated [32]. Kirchhoff defined a volume where the turbulence fluctuations occur. This method is more known as the Kirchhoff integrals. Kirchhoff integrals only considers the far field solution because of the complexity introduced. Meaning that the Lighthill equations are only solvable for far field noise radiation and will be only useful for jet noise.

Lighthill theory of aerodynamic sound firsts extension was proposed by N.Curle [33, 39]. This extension introduces a solid boundary. In his paper, he discussed two main topics. First, he discusses the reflection and diffraction of sound waves at the solid boundaries, and second, a distribution of dipoles at the solid boundaries are introduced. The conclusion of this paper where that noise is more dominant when a solid boundary interacts with a turbulent flow.

The next theory is from J.E. Ffowcs-Williams, L.H. Hall, and D.L. Hawkings, they did research to the noise propagation of an arbitrary moving body in a fluid [40]. The theory follows from the Lighthill's analogy. From the theory, it was found that a moving body can be represented as a distribution of monopoles and dipoles (Figure 2.4), whose strength equals to the local acceleration of the body and the net force applied to the fluid. This model is more commonly known as the FW-H model. Based on this model, most empirical models for wind turbines are based [40].

R.K. Amiet [33, 41] developed a method that can be used for turbulent inflow noise. Normally the noise radiation is at the trailing edge, but with the model of Amiet, it is located at the leading edge. The model was

developed for a linearized flat plate wing. Currently, this model is used to develop turbulence inflow models for a wing with different airfoil properties. Lowson based his model on Amiet's work to develop his turbulent inflow model for wind turbines [16].

2.3.3 Wind Turbine Aeroacoustics

The sound generated by wind turbine will come from several regions. As already mentioned mechanical noise is not considered and this thesis focusses on aeroacoustic noise. The sources of the sound can be split up into several different acoustic sources most of them located at the trailing edge. There are three types of noise: turbulent inflow noise, airfoil-self noise and tonal noise [10, 32, 33, 42]. Turbulent inflow noise is noise generated by the interaction between a turbulent flow and a blade which is discussed in subsection 2.3.2. Tonal noise is a noise source at a discrete frequency which is clearly higher in SPL than the other frequencies. Most of the time this is generated due to a change in flow when a blade passes an object like the tower, $(f_{tonal} = B * \Omega)$. And then there is airfoil self-noise which can be split into 5 different noise sources according to Brooks et al. [10, 32, 33, 42]:

- Turbulent Boundary Layer trailing edge noise
- Separation-stall noise
- Tip vortex formation noise
- Trailing edge bluntness vortex shedding noise
- Laminar boundary layer vortex shedding noise

The airfoil self-noises can be seen in Figure 2.5 [3]. T.F. Brooks et al. studied and tested airfoils for different airfoil self-noise sources [10]. They tested an NACA0012 airfoil in wind tunnels and derived several empirical models for predicting airfoil self-noise. This model is called BPM model, named after the developers of this model. The BPM model calculates Sound pressure levels for each of the individual components of airfoil self-noise by the use of scaling laws based on Strouhal numbers and this method is discussed further in subsection 2.3.4.

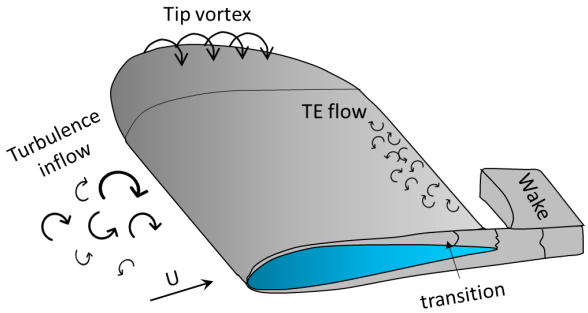

Figure 2.5: Different aeroacoustics noise sources of a wind turbine blade, adapted from Oerlemans [3]

Turbulent Boundary Layer Trailing Edge Noise

TBL-TE noise is the result of the interaction between trailing edge and turbulent boundary layer. Extra turbulence is created in the boundary layer that interacts with the trailing edge and, generating a sound source [10, 32, 33, 42]. The TBL-TE noise has a broadband noise spectrum and has its peaks in the hearing range of humans. This means that TBL-TE noise is an important noise source and should be minimised.

Separation Stall Noise

At low angles of attack, the flow will separate at the trailing edge, however when the angle of attacks increase the flow will start to separate [10]. This noise is important for a wind turbine, since the root of a blade is sensitive to stall due to low rotational speed, and this noise source is especially important for stall controlled wind turbines. The blades operate in low Re number flows, this can lead to earlier laminar separation. Meaning that for lower Re number flows this noise must be considered.

Tip Vortex Formation

At the tip of the blade, tip vortices will be generated. The vortex is created due to the pressure difference between the suction and pressure side. These vortices interact with the trailing edge in the same way that the TBL-TE noise does. This noise depends on the vortex strength which depends on the blade load or geometry [10, 32, 33, 42]. To decrease this noise source different tips can be considered [3]. The BPM model takes only flat or round tips into account. They found that round tips will reduce the noise.

Trailing Edge Bluntness Vortex Shedding Noise

TEB-VS noise is noise due to vortex shedding of a blunt trailing edge. There is an interaction of the shed vortices at specific rates and the boundary layer passing through the trailing edge. If the trailing edge bluntness is higher than the boundary layer thickness this noise source can become a major problem. However, most of the time in rotor and wing the trailing edge thickness is smaller than the boundary layer thickness [10, 32, 33, 42]. During this thesis, there is looked at small wind turbines with a diameter lower than 20 cm. Meaning that the TE thickness mainly depends on the manufacturing methods used. Meaning that the bluntness noise can become dominant.

Laminar Boundary Layer Vortex Shedding Noise

LBL-VS noise is generated because of the interaction between the vortex being shed, and the instability waves in the laminar boundary layer. For a certain Reynolds number range, there will be instabilities in the laminar boundary layer that generates pressure fluctuations which result in sound [10, 32, 33, 42]. Laminar vortex shedding noise has the characteristic that it is a tonal noise. Tonal noise can be perceived as annoying and so it should be minimised or be avoided. For large wind turbines this noise is of lesser importance, but for small wind turbines, it can create a problem since they are more sensitive to laminar flow [1].

2.3.4 Semi-empirical Methods

One of the two methods of predicting noise from wind turbines is semi-empirical models. These models are based on a combination of theory and measured data. The models use the general flow conditions of the blades (e.g. AoA, inflow angle, wind speed, etc.) calculated by models like BEMT theory or a lifting line model.

The empirical models are developed using measured aeroacoustics properties of certain airfoils in the wind tunnels. One of the largest series of experiments on airfoil acoustics were performed by Brooks [10]. The purpose of these test was to measure the trailing edge noise of an NACA0012 airfoil. Brooks et al. defined different sources of noise as discussed in subsection 2.3.3. The BPM model is based on the work of Ffowcs-Williams et al. [40]. From this, and the experimental data available they developed a set of scaling laws for the different airfoil sounds.

The test performed by Brooks et al. consist of the NACA0012 profile and was tested under different conditions [10]. The conditions were: different Mach number, different Re number, different inflow angles, different Strouhal number [10, 32, 42]. Due to the many different test set-ups, there is a lot of data available to scale the model. The model that was developed based on the test of Brooks is called the BPM model. The model can calculate the sound pressure level for different frequencies, for this case the 1/3-octave band will be used. Boudnary layer parameters are determined with Xfoil or Rfoil, since they are important for the TE noise. The BPM use a set of scaling laws based on different parameters to determine the SPL of the sound generated.

Lowson [16] used R.K. Amiet result and theory to update the BPM model for turbulent inflow noise. Lowson also defined 3 classes for noise prediction models that depend on different parameter inputs. A class I

model depend on basic wind turbine parameters like RPM, wind speed, and power. Class II is already a bit more elaborate and takes into account different noise mechanism, Class III is the most complicated and depends on different inputs as can be seen in Table 2.1 [16].

Table 2.1: Class III input parameters [16]

Group	**INPUT PARAMETER**
Rotor	Number of blades Diameter Hub Diameter Chord distribution Twist distribution Airfoils 3D flow around blade Trailing edge bluntness angle Blade tip shape Blade tip angle
Acoustic	Position receiver
Operational conditions	Mean wind speed Rotational speed Yaw, pitch and tilt angle
Atmosphere	Speed of sound Air density and viscosity surface roughness length TL and TI

The goal of this thesis would be to combine the lifting line model or BEMT with the BPM model. Similar projects were already done such as XNOISE. Different commercial and open source aeroacoustics software's can be found in Table 2.2. NAFNoise will be used to verify the BPM model developed.

Table 2.2: Aeroacoustic programs for wind turbines or airfoils

Name	**Company**
XNOISE	Institute of Aerodynamics and Gas Dynamics
NAFnoise	NREL
SILANT	ECN

The disadvantage of BPM model is that it is like the BEMT theory. These models are empirical models, which can provide reliable result if similar inputs are used as the inputs on what the model is based on. Meaning, that the results obtained by such program are depending on how similar the shape is of the airfoil compared to the NACA0012. Because of this, some discrepancies will be found between experimental and predicted results. However still reasonable result were obtained by S. Vanhaeverbeke who applied the BPM model on small wind turbines [42]. Vanhaeverbeke tested the model for different inputs and compared the results with experimental data. She also pointed out that an attenuation model must be created to predict the noise at a certain receiver location (residential area, human, etc.).

2.3.5 Computational Aeroacoustics

Computational aeroacoustics or CAA is solving aeroacoustics problems using numerical methods, this is comparable to CFD, since the solution for CFD needs to be used to calculate the SPL. CAA tries to calculate the sound radiation by solving the pressure fluctuations, it does not use theoretical acoustic models since these do not have an exact solution due to the high non-linearity. However, using DNS or LES techniques to capture the high spread and spatial resolution of the pressure fluctuations the noise can be determined. CAA as already mentioned is like CFD but there are some differences which make CAA much more computationally demanding than CFD. The difference between the two is that CAA solves for wave behavior and CFD does

not (depending on the method used).

A well-known problem with CFD is that the denser the mesh the higher the computational time meaning there is a trade-off between computational time and accuracy, the same goes for CAA. However, when using DNS or LES to solve a problem high mesh density is always needed, which increases the computational time. From this, it can be concluded that DNS CAA is not the best method for designing silent rotors. More research was done by C.Tam [44] about CAA and said that "CAA is still in its infancy"(p. 1795), meaning that currently, computers are not powerful enough to solve the equation for CAA for complex flows.

2.3.6 Noise Propagation

The wind turbine will be mounted on top of the KCU, and the noise generated by the wind turbine will not be the same as the sound received at a location on the ground. For simulating the sound received a good sound propagation model is required.

The wind turbine is modeled as a monopole source at the location of the KCU. For this thesis, the sound will be calculated for a tether length of 400 m and elevation angle of 20°. The sound pressure level will decrease when traveling to the receiver. The reason why the SPL decreases is because of: spherical spreading, source directivity, air absorption, temperature and wind gradient and the reflection of the terrain. The SPL received at the receiver can be calculated with Equation 2.8 [11, 12, 42, 45].

$$SPL_{receiver} = SPL_{S+D} + SPL_A + SPL_D + SPL_{T\&W} + SPL_T \tag{2.8}$$

The calculation of the sound propagation will be done according to Nord 2000 manual [11, 12], which comply with the regulations according to the ISO 9613-2 standards [42, 45]. A good explanation of all noise losses can be found in the book: *Handbook of Acoustics chapter 4* [34]. For this model only spherical spreading, wind, reflection and atmospheric absorption are taken into account.

Atmospheric Absorption SPL_A

When sound waves are traveling some of the energy is transformed into heat. This is because of the shear viscosity, thermal conductivity and heat dissipation of air. The absorption process depends on the distance between receiver and source, and the air absorption coefficient, which is different for different frequency of the 1/3 octave band [11, 42].

Reflection SPL_T

When sound travels, it will be reflected on the ground or obstacles. Most of the time the sound is reflected by the ground. The strength of the reflection depends on the shape of the terrain and material. If the terrain is curved it must be divided into straight line segments [11]. Another variable that influences the propagation is the material of the ground or coverage (building, tree etc.). If the reflected ray arrives at the source it will have a time delay compared to the direct ray. Depending on the frequency and time delay the reflected signal will increase or decrease the SPL at the receiver.

Effect of Wind and Temperature $SPL_{T\&W}$

The straight rays assumed earlier, will curve if wind or temperature is considered. This will increase traveling time and the noise received at a location might change compared to the straight-line analogy. The sound propagation depends on the temperature gradient and wind speed gradient. The temperature has an influence on the speed of sound ($c_0 = \sqrt{\gamma RT}$). During the night or day, the atmosphere is more stable, meaning that the traveling sound will vary compared to during the day [12].

If the sound is traveling in wind direction the speed of sound will increase and reach the receiver with a lower time delay, while traveling upstream, the speed of sound will decrease. The sound propagation depends on day/night time and the wind speed. Considering that the wind has a larger effect on the sound propagation than the temperature, it is decided to neglect the influence of the temperature. A model is developed to take the wind into account which is based on the work of DELTA [11, 12].

2.3.7 Dutch Regulations

For each country, there are different regulations regarding wind turbine noise [46]. Kitepower is in the Netherlands and for this reason, there is looked at the Dutch regulations. The regulations define a quantity SPL_{den} which is the sound pressure level on a yearly average. This is corrected for the evening and night since the sound is perceived louder when the background noise is lower. Also during the night, the people sleep which result in an extra 10 dB during the averaging. According to the regulations the SPL_{den} cannot be higher than 47 dB [46]. The goal of this thesis is to investigate the sound of the wind turbine in a residential area. The project will be successful if the noise is lower than 47 dB.

2.4 Wind Tunnel Experiments

During the thesis, a wind tunnel measurement campaign will be performed in the W-tunnel of TU Delft. The wind tunnel has a cross section of 40 cm x 40 cm. And a maximum wind speed of 35 m/s. The generator was provided by Maxon motors. The alternator used is a motor which is operated as a generator [47]. It is during this test campaign that the influence of the shroud will be tested. It will be tested what the effect is of the shroud on the power and drag of the blades. Besides the performance, a tonal noise investigation is performed.
The parameters of interest to validate the designs and how to measure them are:

1. Mechanical power: measure rotational frequency in time signal
2. Drag: 6 component balance
3. Noise/ Tonal noise: M51 linearX microphone
4. Electrical power: Voltage and current brick tinkerforge
5. Rotational frequency: Oscilloscope, M51 LinearX and optical tachometer

Chapter 3

Problem Statement

3.1 Objective

As stated earlier kitepower will be the future energy supplier in rural and disaster areas due to its mobility. Kitepower BV is one of the pioneering companies that is developing one of these AWE systems. Their system is based on the pumping cycle with a kite. To do this the kite reels out while flying in a figure of eight patterns. When the maximum height is reached, the kite will park and be reeled in as energy efficient as possible. The problem with the current system is that the kite must land after 2 hours of flight because the batteries of the KCU are empty. If this problem is solved a major milestone for Kitepower BV is reached, because from this moment they should be able to fly 24 hours and longer. From this, it can be concluded that the main objective will be to provide enough energy to the KCU to keep the controls and communication working.

Multiple preliminary designs were performed by placing a wind turbine on the KCU to transferring the power necessary trough a conductive cable through the main tether. From Kitepower side a reliable solution is needed. A conductive wire was soon eliminated because of the amount of money it would cost to braid a wire in the tether, the loads the wire would carry (fatigue loads), the creep, and it would make it more difficult to include a light emitting tether for regulations. Due to the reason mentioned and the increase in mass when choosing a wire it was chosen to design a single horizontal axis wind turbine that can be mounted on top of the KCU. The design requirements are that it at least produces 44 Watt of electrical energy at an apparent wind speed of 30 m/s. The wind turbine will need a protective shroud to prevent that the bridles wold be cut. The whole project is done in collaboration with Maxon motors which will provide a motor which will be used as an alternator. For the safety of the bridle, a shroud is added as protection of which the dimensions are determined by Maxon motors. In theory, the shroud could be optimised such that the efficiency would be increased but this is out of the scope of this thesis.

It is the goal of Kitepower BV to maximise the production of energy from their system. This is directly related to the L/D of the complete AWE system. For this reason, the wind turbine should have a low drag and weight. The drag is more important since it will increase quadratic with the apparent wind speed. Because of this requirement, a small part of the thesis is added to create a simple optimiser to design a low drag wind turbine without looking at the mass.

Besides the design of the wind turbine, a study will be done about the noise levels and with a close attention to what will happen with the tonal noises. The reason for this is that the final design will have a high RPM (in the range of 9000-15000 RPM). This will generate a tonal noise in the frequency range where the human ear is quite sensitive too. Besides tonal noise, investigation research will be done what the effect will be on the tonal noise when adding a shroud. Since the wind turbine will be around hundred meters in the air the noise levels at the ground station or right beneath the kite are interesting. To simulate the noise levels calculated by the BPM model an atmospheric attenuation model is developed. This model considers the spherical spreading, reflection and wind speed and atmospheric absorption.

A wind tunnel experiment is performed to validate the software developed. During the tests, mechanical power, drag, and noise will be measured. During the measurement, it is also investigated what the effect will

be when a shroud is mounted. From all previous points, two main research objective can be created:

"Investigate how a low drag wind turbine can be developed by the use of numerical and experimental methods."

"Investigate the noise characteristic of the wind turbine and see what effect of the shroud is on tonal noise by experimental measurements."

From this and the state of the art literature study, three-main research question can be defined with each their sub-questions:

1. **How can a combination of blade element momentum theory and lifting line method be used to develop a low drag wind turbine?**
   (a) Is BEMT or LL method accurate enough to predict the performance of a fast spinning small wind turbine.
   (b) What is the difference in accuracy between the two methods compared to Bladed?
   (c) What is the best method for determining the airfoil polar?
   (d) Is a Brute force optimiser efficient enough?
   (e) What is the effect of the airborne wind turbine on the performance of the AWE system?
2. **What is the effect measured when mounting a shroud on the wind turbine?**
   (a) What happens with the mechanical power?
   (b) What happens with the drag of the blades?
   (c) What happens with the noise?
3. **What is the difference between measured noise and predicted? And do small spinning wind turbine make more than 47 dB(A) noise at sensitive location?**
   (a) Can the tonal peaks be observed in an experimental setup?
   (b) Can BPM be used to determine the general noise levels of small wind turbines?
   (c) What is the effect of the shroud on the sound pressure levels
   (d) What are the main noise losses in the atmosphere and what is the effect?

II

Methodology

Chapter 4

Aerodynamic Performance Calculations Models

In this chapter, an elaborate explanation is given about the Blade Element Momentum theory (BEMT) and the Lifting Line method (LL) for small Horizontal Axis Wind Turbines (HAWT). Both models are used to determine the power and aerodynamic loads of wind turbine blades. The BEMT is a theory that combines a set of equations derived from momentum theory and blade element theory, and solves them iteratively until convergence occurs. The BEMT requires extra engineering add-ons to take other physical phenomena into account due to the simplifications made in the original model. The LL model is a model that predicts the lift distribution over a wind turbine blade based on the geometry and airfoils used. The LL method used is a free wake method which means that the wake is part of the solution, and that it will evolve over the cause of time. The LL model is mainly used for verifying the design of the BEMT model and to gain a better understanding in the physics of the wind turbine. The LL will only be used close to the optimum TSR since this is the area of interest for power production. Both models need reliable airfoil data which will be generated by Xfoil or Rfoil. A small study is performed to investigate what the best software is to predict the airfoil performance. Airfoil performance is defined as the parameters that are related to the airfoil, such as lift, drag and boundary layer parameters. A verification is done at the end comparing LL and BEMT to Bladed. From this verification, a conclusion will be formulated on the accuracy of the two models.

4.1 Blade Momentum Element Theory (BEMT)

The BEMT is a model that can predict the aerodynamic loads of a wind turbine which can be converted to power and a thrust force that is generated by the rotor. This thrust force is the force that the blades apply on the wind to slow it down. The wind pushes in its turn on the blades which can be defined as a drag force. For this reason, C_T is interpreted as a drag coefficient of the wind turbine (thrust is only used on the derivation of the BEMT). The BEMT is a model that combines the actuator disk model and the blade element method. Both are explained in the next sections. Besides the coupling between the actuator disk model and blade element method, correction factors must be applied because of the assumptions made in both models. These corrections are called engineering models which are mostly based on experimental data [5, 6]. The BEMT discussed here contains only the main derivation steps. All the minor steps for a full derivation can be found in any standard wind energy book. E.g. the book of D. Wood [6] or the book of Burton et all. [5].

4.1.1 Actuator Disk Model

The actuator disk model or axial momentum theory assumes the wind turbine as an ideal rotor. The momentum and energy transportation are modelled in one control volume which is the stream tube, outside the control volume the conditions are the same as far upstream of the actuator disk. The rotor generates mechanical power by means of extracting power from the wind (kinetic energy). The rotor will be represented as a permeable disc (actuator disc) and is considered ideal which means that it is frictionless and no rotational velocity component is present in the wake [5, 6]. The rotor will decrease the wind speed V_∞ which results in a pressure difference between the front and back of the rotor which can be seen in Figure 4.1. This pressure

difference can be related to a thrust force that is generated, which is the reason why the speed decreases. This thrust force can be seen in Figure 4.1. The streamlines will diverge because of the decrease in wind speed in the stream tube, this is visible in Figure 4.1.

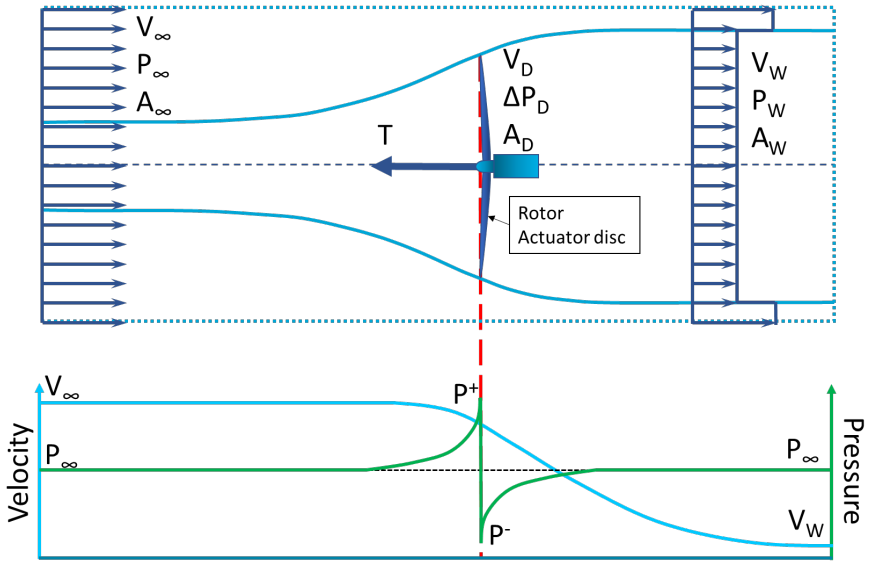

Figure 4.1: Streamlines past a rotor and axial velocity, adapted from Hansen [4]

The velocity drop introduced by the rotor will decrease the wind from V_∞ to V_w. V_w is the wind speed downstream. To relate these two speeds the induction factor a is introduced. The relationship between the two variables can be seen in Equation 4.1. The induction factor is the ratio of the amount of wind speed that is decelerated compared to the far upstream velocity.

$$a = \frac{V_\infty - V_w}{V_\infty} \tag{4.1}$$

To determine the relation between velocity and power, one can use the above found relation for the induction factor together with the Bernoulli equation which assumes: incompressible and steady flow. Using the Bernoulli equation, the pressure before and after the actuator disk can be determined. From this pressure difference, the thrust force can be determined. Then the momentum balance will be used to find a relation for the thrust which is substituted into the Bernoulli equation. The following equations are found:
Power and thrust expression:

$$T = \frac{1}{2}\rho A V_\infty^2 \cdot 4a(1-a) \tag{4.2a}$$

$$P = \frac{1}{2}\rho A V_\infty^3 \cdot 4a(1-a)^2 \tag{4.2b}$$

In wind energy, the power and thrust are described as a function of non-dimensional factors C_P and C_T. Equation 4.2 can be rewritten as function of the non-dimensional parameters C_P and C_T and Equation 4.3 will be found.

Power and thrust coefficient expression:

$$C_T = \frac{T}{\frac{1}{2}\rho A V_\infty^2} = 4a(1-a) \tag{4.3a}$$

$$C_P = \frac{P}{\frac{1}{2}\rho A V_\infty^3} = 4a(1-a)^2 \tag{4.3b}$$

From Equation 4.3b, the theoretical maximum efficiency of the wind turbine rotor can be calculated. The maximum C_P equals 16/27 which is roughly 59.26% and this is achieved when the induction factor a equals $\frac{1}{3}$. This factor is known as the Betz limit named after Albert Betz.

4.1.2 Blade Element Momentum Theory

The BEMT is an adaptation of the actuator disk model. The problem with the actuator disk model is that it does not consider the rotor configuration and blade lay-out. In the BEMT method, the stream tube is divided in annular stream tubes each with a length of dr (which can vary in spanwise direction). It is assumed that the stream tubes have no interaction with each other. The BEMT combines a momentum analysis from the actuator stream tubes and a force analysis of these stream tubes.

The momentum theory assumes that each radial section is independent of each other. The thrust and torque equations derived from the momentum theory now become:

Power and thrust expression:

$$dT = \frac{1}{2}\rho V_\infty^2 4a(1-a)2\pi r dr \tag{4.4a}$$

$$dQ = 4\pi r^3 \rho V_\infty \Omega(1-a)a' dr \tag{4.4b}$$

where, Ω is the rotational speed of the rotor and a' is the tangential induction factor to consider the rotational effect of the wake. The tangential induction factor is the ratio between the angular speed of the wake and the angular speed of the rotor.

The change in momentum that is described in Equation 4.4 must be balanced with the aerodynamic forces generated by the blades. The forces on these blades are derived from a single blade element which can be seen in Figure 4.2. The whole derivation can be found in the book of Wood [6]. In Figure 4.2 the normal and tangential forces can be seen. α, θ and ϕ represent the angle of attack, twist angle and inflow angle ($\phi = \theta + \alpha$). The normal and tangential forces are related to the lift and drag of one section, as well as the inflow angle ϕ. The lift depends on the air density, surface of the blade element, inflow velocity V_{app} and lift coefficient C_l, which in turn depends on the AoA $\left(L = \frac{1}{2}\rho V_{app}^2 A C_l\right)$. The same equation as the lift can be used to determine the drag force but with C_d. The lift coefficient depends not only on the AoA but also on the Reynolds number. Its influence is discussed in section 4.3.

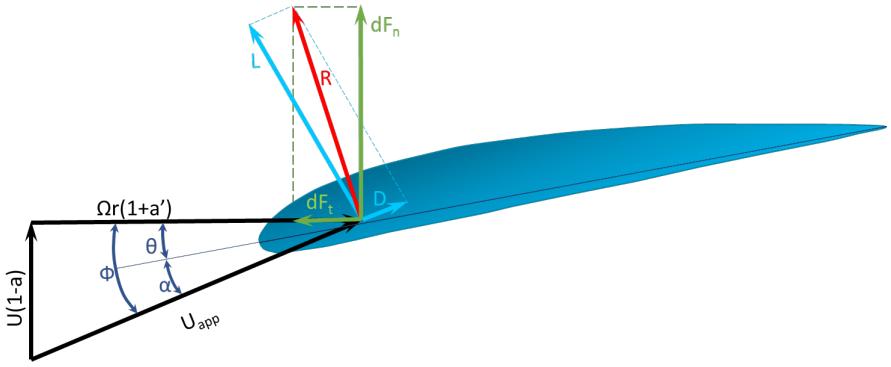

Figure 4.2: Blade element with velocity's, Forces and angles , adapted from Manwell [5]

The inflow angle can be calculated using Equation 4.5 which follows straight from Figure 4.2.

$$\phi = \tan^{-1}\left(\frac{(1-a)V_\infty}{(1+a')\Omega r}\right) \tag{4.5}$$

When the inflow angle is known, the normal and tangential force can be determined with Equation 4.6.

Normal and tangential forces:

$$F_n = L\cos\phi + D\sin\phi \tag{4.6a}$$

$$F_t = L\sin\phi - D\cos\phi \tag{4.6b}$$

where, L=$\frac{1}{2}\cdot\rho\cdot V_{app}^2\cdot C_l\cdot c\cdot dr$. The same goes for the drag D. The normal and tangential force is calculated for each blade element. By integrating the individual forces of each blade section over the total blade span, the total normal and tangential force can be calculated of the rotor. For the torque, the total tangential force must be multiplied with the radial distance of the respective blade element. The mechanical power is defined as the product of the angular speed of the rotor and the total generated torque.

There are now two sets of equations derived, one from the blade element and the other from the actuator disk model. These can be coupled and solve it iteratively to find the power of different rotor configurations and blade lay-outs. However, as mentioned before, due to the simplifications, correction factors must be applied to make it more representable for a real rotor.

4.1.3 The BEMT model and Engineering Corrections

The BEMT as discussed in previous sections can be used for predicting the load distributions, power, and thrust of the rotor. However, there are still limitations when it comes to BEMT, due to the assumptions made in the 1D momentum theory and the blade element section. There is no correction applied to the 2D airfoil data, and there is no tip and hub loss correction. When the induction factor is larger than 0.4 the rotor will enter the heavily loaded state and the BEMT will predict a lower thrust force compared to experimental data. In this section, all the different add-ons will be discussed and the final BEMT model will be developed, which will be used in designing the wind turbines for powering the KCU.

Tip/hub Loss Model

It is assumed that the speed of the rotor is constant in circumferential direction because the actuator model assumes average velocity. This cannot be true since some non-uniformities arise due to the finite number of blades. In other words, the axial velocity at stream tubes can vary compared to the speed at the rotor V_d.

To solve this problem, Prandtl developed a tip loss correction based on the number of blades, inflow angle and the properties of a blade section such as the location on the blade. Glauert adapted the Prandtl tip loss correction so it can be used in the BEMT model. The Prandtl-Glauert tip loss correction factor is given by equation Equation 4.7. The physical meaning of F is defined as the ratio between the average induction factor of the whole rotor and the local induction of the blade element.

$$F = \frac{\pi}{2}\cos^{-1}\left(e^{-f}\right) \tag{4.7}$$

where f is the tip or hub loss factor:

$$f_{tip} = \frac{B(R-r)}{2r\sin\phi} \tag{4.8a}$$

$$f_{hub} = \frac{B(r-R_{hub})}{2r\sin\phi} \tag{4.8b}$$

$$f = f_{tip}\cdot f_{hub} \tag{4.8c}$$

where, B is the number of blades, r is the radial position, R is the rotor radius, R_{hub} is the hub radius and ϕ is the inflow angle. This tip loss model is combined with the heavy loaded rotor correction in next section. It is known that the factor F will be close to 1 in the middle of the blade and be lower at the hub and tip [5]. For this reason, a cosine spacing will be used to create smaller sections at the tip and root and larger in the middle of the blade as can be seen in Figure 4.3.

Heavy Loaded Rotors

From Figure 4.4 another limitation of the BEMT can be seen. It is visible that when the induction factor is higher than 0.5 the experimental and BEMT result deviate largely from each other. When the induction factor

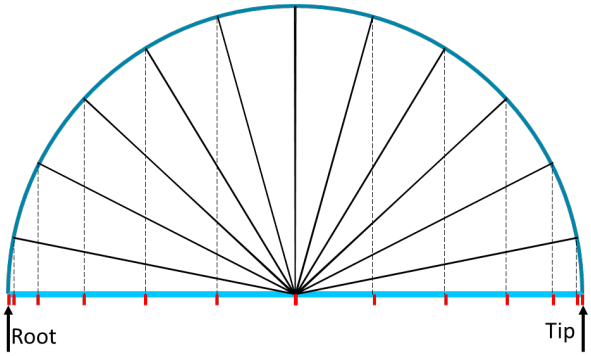

Figure 4.3: Cosine spacing of the blade

is higher than 0.4 the rotor will enter the turbulent wake state or a highly-loaded state. During the turbulent wake state the flow far downstream will start to propagate upstream [6, 33]. This happens because the wake is disintegrating and becoming more turbulent. If this happens the wake will start mixing with flow outside the stream tube, which is a violation of the BEMT. Due to this phenomenon, the BEMT shows numerical errors for induction factors greater than 0.5. It is generally assumed that the initial equation for the thrust coefficient is

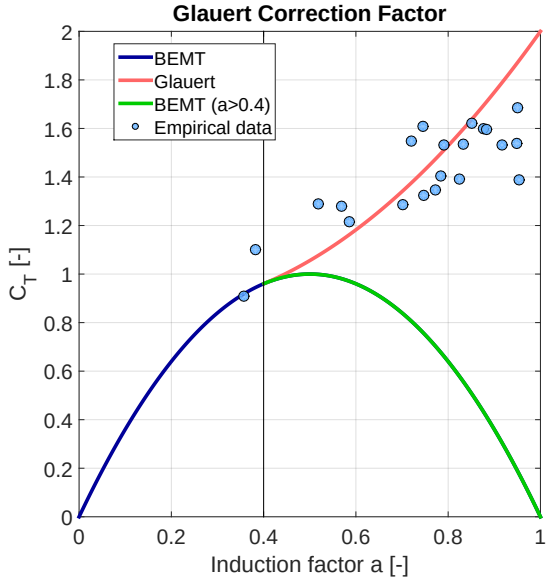

Figure 4.4: C_T values for high induction values [6]

applicable for axial induction values below 0.33 (Betz limit) [6]. Once the axial induction factor is higher that this value, a replacement has to be derived for the thrust coefficient equation of Equation 4.2b. Clifton-Smith tested different tip loss models and found that the corrections proposed by de Vries are most suitable for wind turbine design [20]. The model of de Vries rewrites Equation 4.6 including the tip correction factor F in the following form.

$$\begin{aligned} \frac{a_b F(1-a_b F)}{(1-a_b)^2} &= \frac{\sigma C_n}{4\sin^2\phi} \\ \frac{a'_b F(1-a_b F)}{(1+a'_b)(1-a_b)} &= \frac{\sigma C_t}{4\sin\phi\cos\phi} \end{aligned} \tag{4.9}$$

Then the original Glauert correction for C_T becomes Equation 4.10

$$C_{T_r} = \begin{cases} a_b F(1-a_b F) & a_b \leq \frac{1}{3} \\ a_c^2 F^2 + (1-2a_c F)\, a_b F & a_b > \frac{1}{3} \end{cases} \tag{4.10}$$

where, C_{T_r} is the thrust coefficient for a blade element, a_c is the axial induction factor where maximum power is obtained, which is $\frac{1}{3}$, a_b is the induction factor of a blade element. Shen et al. [48] defined two intermediate

functions, Y_1 and Y_2. The equations for these intermediate functions can be found in Equation 4.11.
Shen et al. intermediate equations:

$$Y_1 = \frac{4F\sin^2\phi}{\sigma C_n} \tag{4.11a}$$

$$Y_2 = \frac{4F\sin\phi\cos\phi}{\sigma C_t} \tag{4.11b}$$

where, the normal force coefficient is $C_n = C_l\cos\phi + C_d\sin\phi$ and the tangential force coefficient equals $C_t = C_l\sin\phi - C_d\cos\phi$. C_n and C_t are used to determine a new guess for the axial and tangential induction factor (Equation 4.12). When the factor Y1 is larger or equal to 2 Equation 4.12a has to be used since the blade is in the low thrust region. If this is not the case the new induction factor guess is based on Equation 4.12b, which is used for high thrust region.
Shen et al. induction factors:

$$a_b = \frac{2 + Y_1 - \sqrt{4Y_1(1-F) + Y_1^2}}{2(1+FY_1)} \tag{4.12a}$$

$$a_b = \frac{2 + Y_1C_t - \sqrt{(Y_1C_t+2)^2 - 4\left(1-\left(\frac{1}{3}\right)^2 FY_1\right)}}{2} \quad \left[C_t = 1 - 2\frac{1}{3}F\right] \tag{4.12b}$$

$$a_b' = \frac{1}{\frac{(1-aF)Y_2}{1-a} - 1} \tag{4.12c}$$

3D Stall-Delay Correction

The airfoil data used in the BEMT model is based on 2D flow. Using this 2D data showed a bad correspondence with the experimental results. This is because BEMT assumes only axial flow while there is a radial velocity component present on the blade sections. For this reason, 3D airfoil data should be used [4, 6]. Obtaining 3D data for every wind turbine flow case is difficult and expensive. Therefore, there are models that take the 2D airfoil data and convert them to 3D airfoil data. There are many different models and P. Dijkstra gave a good summary of the most common ones in his thesis [33].

Therefore, a 3D correction needs to be applied because of the rotational effect. Stall delay will cause the lift coefficients to increase and delay stall to higher angles of attack, which is beneficial for wind turbine performance. In Figure 4.5 a case of stall delay can be seen with the correction from Du & Selig.

There are several models for simulating stall delay. The one that will be used is a stall delay model developed by Du and Selig [4, 49]. Which applies a correction on the 2D lift and drag polar. The set of equation, can be seen in Equation 4.13.

Stall delay model Du & Selig [49]:

$$C_L = C_l + f_{cl}\Delta C_l \tag{4.13a}$$

$$C_D = C_d - f_{cd}\Delta C_d \tag{4.13b}$$

$$\Delta C_l = 2\pi(\alpha - \alpha_{C_l=0}) - C_l \tag{4.13c}$$

$$\Delta C_d = C_d - C_{d_{\alpha=0}} \tag{4.13d}$$

$$f_{cl} = \frac{1}{2\pi}\left[\frac{1.6(c/r)}{0.1267}\frac{a-(c/r)^{\frac{d\cdot R}{\Lambda\cdot r}}}{b+(c/r)^{\frac{d\cdot R}{\Lambda\cdot r}}} - 1\right] \tag{4.13e}$$

$$f_{cd} = \frac{1}{2\pi}\left[\frac{1.6(c/r)}{0.1267}\frac{a-(c/r)^{\frac{d\cdot R}{2\Lambda\cdot r}}}{b+(c/r)^{\frac{d\cdot R}{2\Lambda\cdot r}}} - 1\right] \tag{4.13f}$$

$$\Lambda = \frac{\Omega R}{\sqrt{U_\infty^2 + (\Omega R)^2}} \tag{4.13g}$$

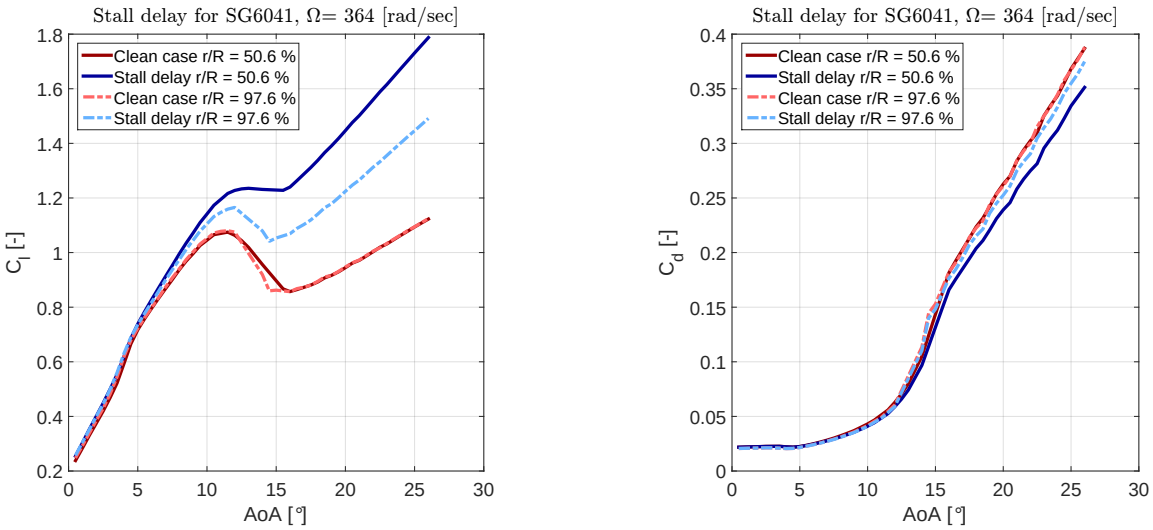

(a) AoA-C_l curve for SG6061 with stall delay applied

(b) AoA-C_d curve for SG6061 with stall delay applied

Figure 4.5: Stall delay applied on an airfoil rotating at an angular speed of 606 rad/s. Based on Du & Selig stall delay mehod

The developed model depends heavily on c/r, r/R which is the spanwise location and Λ, which is the modified tip speed ratio. a, b and d are factors that are assumed to be 1. Figure 4.5 shows the results of two cases; one at 50.6% and the other at the tip of the blade. For the case at 50.6% the lift is increased more compared to the other case, this is because of the stronger radial component, resulting in a larger delay of the stall. Looking at the case closer to the root the drag is decreased more than compared to the tip. Other than using the stall delay model only for BEMT, it is also used for the LL model since this model also depends on accurate airfoil performance data.

Kirke Extrapolation

A wind turbine has many different operational areas. The wind turbine can experience a wide range of AoA for different TSR. For low TSR the AoA will be higher and deep stall could arise for certain airfoil sections. It is difficult to determine c_l and c_d in these region with panel codes such as Xfoil. For this reason, a post stall extrapolation method must be applied. Bianchini et al. [50] researched different extrapolation models such as the Viterna-Corrigan method and Kirke's method and compared this with experimental results and CFD. They founded that Kirke, AERODAS and Montgomerie gave better results compared to the others. For this thesis preference was given to Kirke's model for its simplicity. Kirke started from Beans and Jakubowski expression but he proposed to make it as a function of the camber ξ [50]. Kirke's extrapolation equation can be seen in Equation 4.14-4.15.

$$C_l = (1 + 0.05\xi)\sin(2\alpha) \tag{4.14}$$

$$C_d = (0.9 + 0.025\xi)(1.5\sin^3(\alpha) + 0.5\sin(\alpha) + 0.05\xi) \tag{4.15}$$

A demonstration of Kirke's method can be seen in Figure 4.6. In this figure, the lift and drag curve is calculated by Rfoil for AoA of 0° until and angle of 26°. Next, the data is extrapolated with Kirke's method. The large gap after the stall angle will result in a large error for low TSR or where the blade is operating in the deep stall region. This problem was eventually solved by applying a linear cut-off to make a smooth transition between Rfoil and Kirke's extrapolated lift curves.

Total BEMT Equations

All the engineering corrections discussed will create a more reliable and accurate BEMT code. The final BEMT code will have the following corrections applied to the conventional BEMT theory derived from 1D momentum theory and blade element:

- Tip loss correction

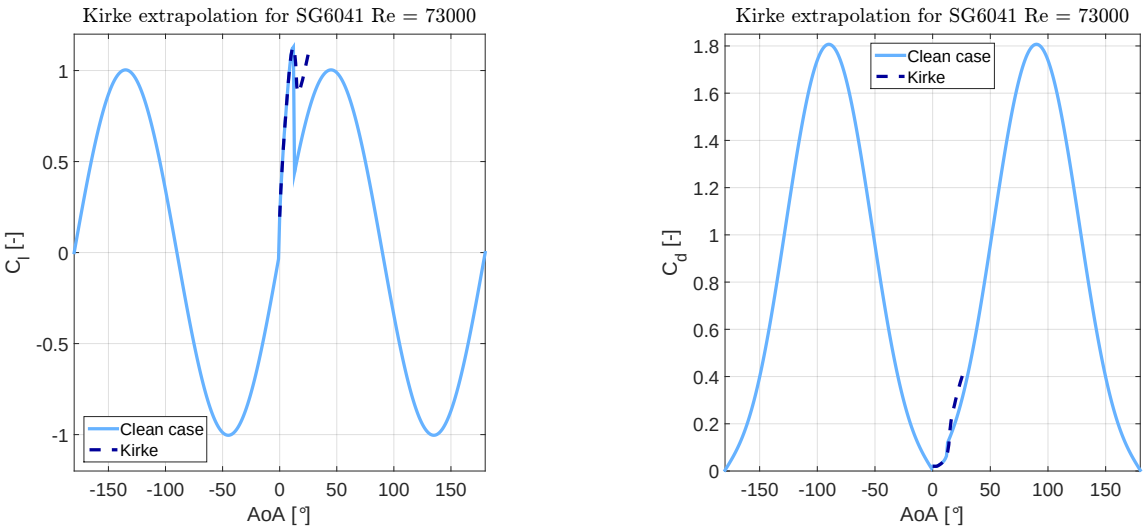

(a) AoA-C_l curve extrapolated

(b) AoA-C_d curve extrapolated

Figure 4.6: Kirke extrapolation

- Stall delay correction
- Heavy loaded rotor correction based on the model of de Vries and the two functions defined by Shen et al. [21]
- Kirke correlation for airfoil extrapolation discussed in section 4.3.

The combined equations can be seen in the code flow chart in Figure A.1. The verification of the BEMT model is discussed in section 4.4. The strength of this code is that it is computationally faster compared to higher fidelity methods. The disadvantage is that reliable airfoil data is needed to obtain a reliable prediction.

4.2 Lifting Line Model (LL)

BEMT has as advantage that it is commonly used in industry and that it gives reliable results if good airfoil data is used. The disadvantage is that there is a need for correcting for physical phenomena. The BEMT model solves this problem by using engineering corrections. The advantage of lifting line is that it does not have this problem and it is more physically correct. The lifting line is based on Prandtl's lifting line in combination with a free wake. The free wake will take unsteady effect into account. This is something that the current BEMT does not consider. The reason why a free wake is chosen is because it can model unstable effects such as yaw angle. The model is based on the model of van Garrel [7, 25] and the code is based on WinDS [51].

4.2.1 Flowfield

The flow around a body (blade) can be described trough a distribution of sources and vortices [51]. This can be seen in Figure 4.7. The vorticity in the flow field around a body (as can be seen in Figure 4.7) can

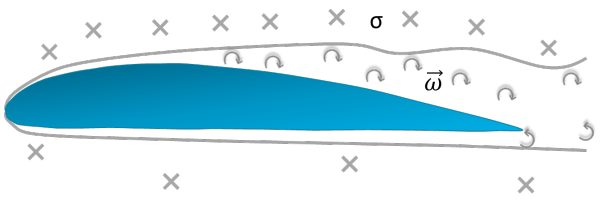

Figure 4.7: Flowfield around an airfoil or wing, adapted from Garrel et al. [7]

be replaced by a circulation on one point (2D case). This 2D case can be translated to a 3D case where the

circulation can be placed on one single line, which is called the lifting line. There are three simplifications for the flow field; first the panel method, second the lifting surface method and last the lifting line method. All three can be seen in Figure 4.8

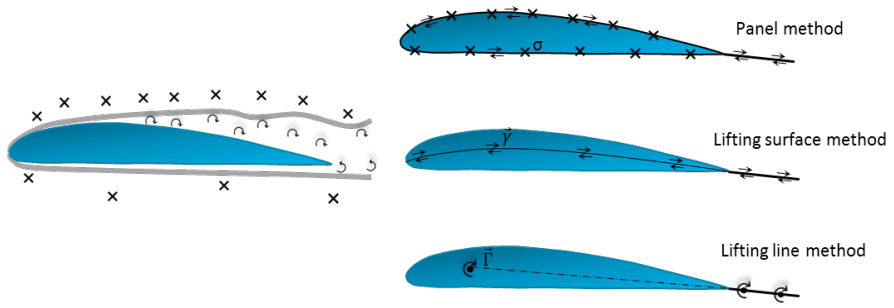

Figure 4.8: Flowfield simplifications: panel methods, VLM and LL method, adapted from Garrel et al. [7]

For the panel method, all vorticity and sources are distributed over the contour of the airfoil. The vortex surface method assumes no thickness and the sources are distributed along the camber line of the airfoil. The lifting line is represented by lumping all vorticity of the surface lifting method to one point. This point is at the quarter chord point of the airfoil.

4.2.2 Vortex Line

The main assumption of the lifting line is that the lift and drag act at the quarter chord line. A second assumption is that the velocities of the flow are much smaller than the speed of sound so that incompressibility can be assumed. Because thickness is not taken into account it will lead that $\sigma = (\vec{\nabla} \cdot \vec{u}) = 0$ and only the vorticity effect has to be modelled. The last assumption comes from Kelvin's theory and states that the vortex tubes must be in a closed ring [7, 8]. The total representation of the lifting line free wake model can be seen in Figure 4.9, in this figure the closed vortex loop can be observed. The total external force exerted on a body

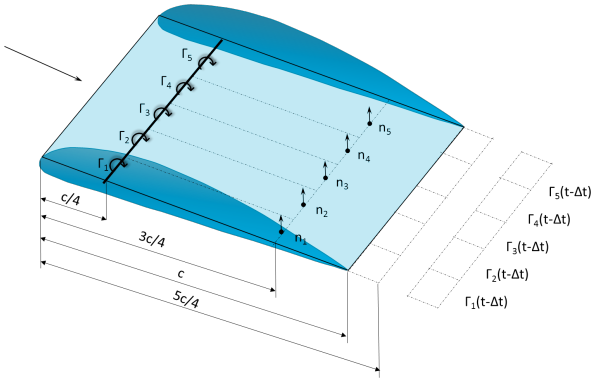

Figure 4.9: Flowfield with circulations at c/4 line, adapted from Katz [8]

by the fluid can be calculated with Equation 4.16.

$$\vec{F} = \int\int\int \rho\left(\vec{u} \times \vec{\omega}\right) dV \tag{4.16}$$

were the fluid vorticity equals $\vec{\omega} = \vec{\nabla} \times \vec{u}$. For a vortex line element of length $d\vec{l}$ this force transform to Equation 4.17, which is the Kutta-Joukowsky theorem [7, 8].

$$d\vec{L} = \rho\left(\vec{u} \times \vec{\Gamma}\right) dl = \rho\Gamma\left(\vec{u} \times d\vec{l}\right) \tag{4.17}$$

The velocity field can be calculated with Equation 4.18, which is the Biot-Savart law.

$$\vec{u_w}(\vec{x}_p) = \frac{1}{4\pi}\int\int\int \frac{\vec{\omega} \times \vec{r}}{r^3} dV \tag{4.18}$$

where, $\vec{x}_p$ is the evaluation point at which the velocity is calculated due to the influence of the vorticity [8]. r is the distance between the vorticity and evaluation point.
Equation 4.18 can be rewritten so that it can determine the induced velocity by a volume of vorticity lumped into the quarter chord line. This equation is the Biot-Savart equation and can be seen in Equation 4.19.

$$\vec{u_\Gamma}(\vec{x}_p) = -\frac{1}{4\pi}\int \Gamma \frac{\vec{r} \times d\vec{l}}{r^3} \tag{4.19}$$

For simplifications, it is assumed that the vortex lines are straight lines with constant circulation Γ. This simplifies the Biot-Savart equation to Equation 4.20.

$$\vec{u_\Gamma}(\vec{x}_p) = \frac{\Gamma}{4\pi}\frac{(r_1+r_2)\left(\vec{r}_1 \times \vec{r}_2\right)}{r_1 r_2\left(r_1 r_2 + \vec{r}_1 \cdot \vec{r}_2\right)} \tag{4.20}$$

The relation between the different position vectors can be seen in Figure 4.10 where a vortex line segment is represented.
When x_p comes close to the vortex line, Equation 4.20 will become singular. If the equation becomes singu-

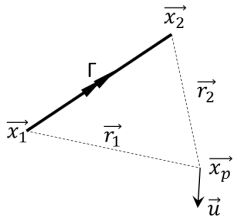

Figure 4.10: Vortex line segment, adapted from Garrel et al. [7]

lar, the code will become numerical unstable and difficult to solve for this reason a cut-off factor is introduced and Equation 4.20 will become Equation 4.21.

$$\vec{u_\Gamma}(\vec{x}_p) = \frac{\Gamma}{4\pi}\frac{(r_1+r_2)\left(\vec{r}_1 \times \vec{r}_2\right)}{r_1 r_2\left(r_1 r_2 + \vec{r}_1 \cdot \vec{r}_2\right) + (\delta l_0)^2} \tag{4.21}$$

In this equation δ is the cut of parameter. The cut-off parameter has influence close to the vortex line while if the point of interest moves further away from the circulation the influence is not noticeable. This can also be seen in Figure 4.11. Equation 4.21 is used to determine the induced velocity due to the blade. It must be noted that this equation needs to be used for each segment, this way the influence from each blade segment onto each other is considered. This was not the case with the BEMT theory.

4.2.3 Vortex Wake

The blades are split up into different sections with each a ring vortex where the bound vortex is placed at the quarter chord line. The free wake model will depend on time, and for each time step a vorticity is shed from the trailing edge and convected downstream. A graphical representation can be seen in Figure 4.9.

The goal of the free wake lifting line model is to calculate the strength of the circulation from these shed vorticities for each time step. After each time step, the new shed vortices will join the old shed vortices and form a lattice of vortices. The position of the shed vortices is determined for each time step. There are several methods for this, the one used is a Euler method and can be seen in Equation 4.22.

$$\Delta\vec{x} = \vec{u}\,\Delta t \tag{4.22}$$

where, $\vec{u}$ is the sum of the rotational speed, the induced velocity, and the free stream velocity. If the kite would be moving, an extra vector must be considered for the kite movement.

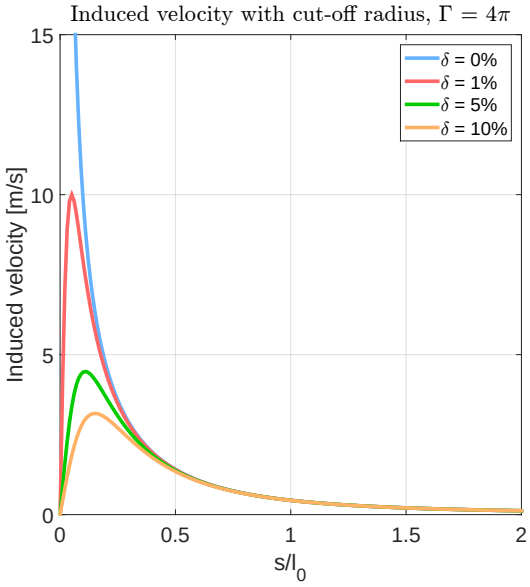

Figure 4.11: Effect of the cut-off factor, adapted from Garrel et al. [7]

4.2.4 Vortex Strength Calculations

Calculating the lifting force from a section can be done by calculating the lift force with the use of Equation 4.17, and match it with Equation 4.23.

$$L = \frac{1}{2}\rho V_{app} C_l(\alpha) dA \tag{4.23}$$

where, α is the angle of attack, V is the apparent wind speed and dA is the blade element area.
First, the lift force can be calculated if the local flow speed and direction is known with Equation 4.23. The lift force for each blade can be converted to circulation using Equation 4.17. Then the total velocity field can be calculated by the Biot-Savart equation (Equation 4.21). Each element (circulation) influences the flow field and eventually the lift.

To solve for the new circulation one has to match the element's circulation from Equation 4.17 with Equation 4.23. This is done by calculating the angle from the induced speed on the collocation point. x_{cp} is the collocation point and is located at the three-quarter chord line. The orientation of a blade element can be seen in Figure 4.12. In this figure $\vec{a}_1$ is the unit vector in chordwise direction and the unit vector in normal direction is $\vec{a}_3$. The equations for these two unit vectors can be found in the report of ECN [7, 25]. The lift

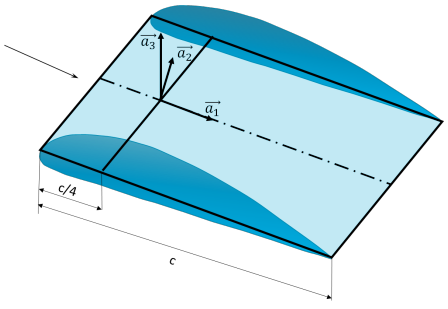

Figure 4.12: Blade element geometry, adapted from Garrel et al. [7]

force can now be calculated using Equation 4.24.

$$dL_\Gamma = \Gamma\rho\sqrt{\left(\left(\vec{u}_{cp} \times d\vec{l}\right)\cdot\vec{a}_1\right)^2 + \left(\left(\vec{u}_{cp} \times d\vec{l}\right)\cdot\vec{a}_3\right)^2} \tag{4.24}$$

$\vec{u}_{cp}$ is the velocity on the collocation point (Equation 4.25).

$$\vec{u}_{cp} = \vec{u}_{wind} + \vec{u}_{rotational} + \vec{u}_{\Gamma} \tag{4.25}$$

The AoA can be calculated with Equation 4.27. From this the lift force can be calculated with Equation 4.26. Where, C_l can be found from the lift polar.

$$dL_{\alpha} = C_l(\alpha_{cp}) \frac{1}{2} \rho \left((\vec{u}_{cp} \cdot \vec{a}_1)^2 + (\vec{u}_{cp} \cdot \vec{a}_3)^2 \right) dA \tag{4.26}$$

Where, α_{cp} on the collocation point is defined by Equation 4.27.

$$\alpha_{cp} = \tan^{-1} \left(\frac{\vec{u}_{cp} \cdot \vec{a}_3}{\vec{u}_{cp} \cdot \vec{a}_1} \right) \tag{4.27}$$

The code flow chart can be seen in Figure A.2 which is based on the LL code of WInDS [51]. The numerical method to determine the new circulation strength for a new time step is.

1. Guess a distribution of circulation
2. Calculate for each blade strip the velocity using equations 4.21 and 4.25 .
3. Determine the AoA on the collocation point for each blade element using Equation 4.27.
4. Compute for each blade strip the lift force with the use of Equation 4.26 and convert this lift to circulation using Equation 4.24.
5. Determine the difference between two circulations. $\Delta\Gamma = \Gamma_{ii} - \Gamma_{ii-1}$
6. When $\Delta\Gamma$ is converged a solution is found for the new circulation for the time step.

4.3 Airfoil Data

A wind turbine blade is divided into sections with each their own airfoil section. These airfoils will generate lift and drag, which will generate power. Different airfoil sections are used for large multi mega Watt wind turbines. This is done for structural strength e.g. at the root large bending stresses arise. For small wind turbines, it is common to only have one airfoil over the whole span of the blade [6]. The airfoil used are airfoils with high lift coefficient and low drag.

The lift and drag of an airfoil depend mostly on the Reynolds number, Mach number, and roughness of the airfoil. For designing the wind turbine, the preference was given towards Xfoil or Rfoil. Measured data is not preferred since it limits the design possibilities to the limited amount of airfoils available. Xfoil and Rfoil have one other big advantage compared to experimental data. They can calculate the displacement thickness and other boundary layer parameters that are of importance for the models. The data of interest for the BEMT, LL and noise models are:

- C_l: Lift coefficient
- C_d: Drag coefficient
- H: Shape factor
- δ^*: Displacement thickness at TE
- θ: Momentum thickness at TE
- δ: Boundary layer thickness TE

The first 5 parameters can all be determined numerically using panel codes such as Xfoil. Before the panel program is chosen, a deeper understanding is necessary of the boundary layer of airfoils. There are three parameters that influence the properties of the boundary layer and forces generated by the airfoil. The first, is the Reynolds number, which is defined as: $Re = \frac{V \cdot c}{\nu}$ [9]. The Re number will have the most influence on the size of the viscous boundary layer. The second parameter that influences the forces is the Mach number. If the Mach number is lower than 0.3 incompressible flow can be assumed, but if the Mach number is higher the flow will behave compressibly. If Mach number is high the lift coefficient will increase and the drag will stay almost constant until the Mach number reaches 0.6, then it increases rapidly [9]. This will be considered by Xfoil or Rfoil by the Karmen-Tsien rule [9]. The Karmen-Tsien rule corrects the pressure coefficient for different Mach numbers. The equations for the Karmen-Tsien rule can be found in Equation 4.28 [9].

$$C_p = \frac{C_{p,0}}{\sqrt{1-M_\infty^2} + \left(\frac{M_\infty^2}{1+\sqrt{1-M_\infty^2}}\right)\frac{C_{p,0}}{2}} \tag{4.28}$$

where, C_p is the pressure coefficient after the compressible correction and $C_{p,0}$ is the incompressible pressure coefficient. From the pressure distribution over the airfoil, the compressible C_l and C_d can be calculated. The last factor influencing the performance of the airfoil is the roughness of the surface. A smooth surface can have a negative effect for airfoils in low Re number flows since laminar separation can start easier, while a rough surface will increase the transition to a turbulent boundary layer, which will increase drag but laminar separation is prevented (same analogy as trip wire). Somewhere, an optimum will be present on the amount of roughness. The roughness is important since the blades will be 3D printed making it an important parameter to consider.

4.3.1 Boundary Layer Theory

The boundary layer was first mentioned by Prandtl in 1904 [9]. Due to Prandtl, the Navier-Stokes equations could be reduced to the boundary layer equations. The boundary layer is the flow close to a surface which will have a lower speed due to friction forces between the surface and flow. The friction forces are largely related to the roughness of the airfoil, which will have a big influence on the boundary layer shape. The flow inside the boundary layer is highly viscous for small wind turbines due to the low Re numbers.

At the surface of the airfoil, the velocity is zero this is called the no-slip condition. Second, the temperature of the flow at the wall equals that of the airfoil surface. In Figure 4.13 it is observed that the velocity increases in y-direction until it equals the free stream speed. The boundary layer thickness is the height where the velocity is close to the free stream velocity. δ is commonly defined as the location where u=0.99$\cdot u_e$ (there are multiple definitions of the δ but for this thesis 0.99$\cdot u_e$ is used). The boundary layer thickness increases when the flow moves closer to the TE. The reason why the boundary layer increases is because of the friction force affecting a bigger region in the flow. When moving more downstream the flow can become retarded. This retarded flow will not stay attached to the surface of the airfoil and will cause separation. The separation will lead to vortex generation, which will increase the drag significantly and reduce the lift. This flow separation can be seen in Figure 4.13.

The boundary layer can be in three states: laminar boundary layer, mixing boundary layer and turbulent boundary layer. In the laminar flow, the flow moves in planes where little mass and momentum mixing happens between the planes. While in a turbulent boundary layer the mixing of momentum and mass is present across the whole boundary layer.

In the average velocity profiles, it can be noted that the laminar profile is slower close to the surface, while for turbulent profiles the speed is faster close to the wall (for a flat plate). This can be observed in Figure 4.14. Most of the time the flow over an airfoil has two clear regions, a laminar and a turbulent one. The flow stays laminar until a transition point. At this point, the viscous forces are not able to suppress the disturbances, and a turbulent state is reached. These disturbances can occur because of turbulence intensity in the free stream, surface roughness or the profile used.

For an airfoil, the flow speed will increase before the highest point on the airfoil and will decrease further downstream. The pressure gradient is lower upstream while downstream it is positive or adverse (this depends on the profile). This will result in separation. Separation will start at the point where $\partial u/\partial y$ equals

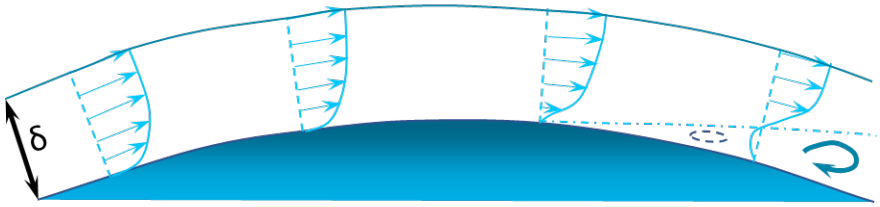

Figure 4.13: Boundary layer evolution over a wing, slope down has an adverse pressure gradient

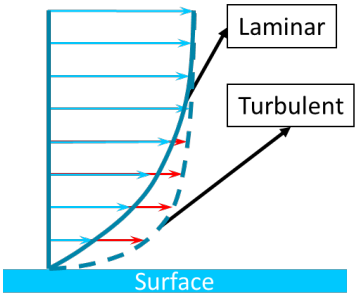

Figure 4.14: Average velocity profiles of a laminar and turbulent boundary layer

zero. For turbulent boundary layers, $\partial u/\partial y$ is higher so will be able to withstand more of these disturbances and this will result that the separation point moves downstream. Except for the boundary layer thickness, there are three other variables that define the boundary thickness: displacement thickness (δ^*), momentum thickness (θ) and H which is the shape factor.

The displacement thickness represents how much a stream line will be deflected up due to the boundary layers' presence [9]. See Figure 4.15 at the left (1) the mass flow rate equals: $\dot{m} = \int_0^{y_1} \rho_e u_e dy$ at station two the mass flow rate equals: $\dot{m} = \int_0^{y_1} \rho_e u_e dy + \rho_e u_e \delta^*$ [9]. The mass flow rate at station 1 and 2 must be equal. By substituting both equation the equation of the displacement thickness can be obtained. This equation can be found in Equation 4.29 [9]. The displacement describes how much the outer stream line of an inviscid flow is displaced due to the obstruction caused by the boundary layer [9].

$$\delta^* = \int_0^{\infty} \left(\rho_e U_e - \rho u\right) dy \tag{4.29}$$

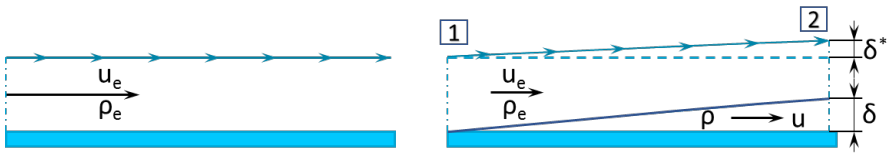

Figure 4.15: Displacement thickness left inviscid case right boundary layer present, adapted from Anderson [9]

The second important boundary layer property is the momentum thickness. The momentum equals to the product of the speed and the mass flow, from this the momentum thickness equation can be determined with the same analogy as the displacement thickness. The momentum can be calculated by Equation 4.30. The momentum thickness describes the amount of momentum missing due to the boundary layer present (same analogy can be applied to displacement thickness).

$$\theta = \int_o^{\infty} \frac{u}{U_e}\left(1 - \frac{u}{U_e}\right) dy \tag{4.30}$$

The shape factor H describes the ratio between the displacement thickness and momentum thickness $\left(\frac{\delta^*}{\theta}\right)$. The value of H determines the state of the boundary layer. The higher H the higher the adverse pressure gradient, this gradient can create a turbulent boundary layer, or if the adverse pressure gradient is high enough separation can occur.

Boundary Layer Thickness

Boundary layer(BL) parameters can be determined with programs such as Xfoil and Rfoil. Xfoil nor Rfoil can directly calculate the boundary layer thickness. Most of the methods to determine a boundary layer thickness are focused on the flat plate theory. There are few methods that could be used to determine the BL thickness, the most common one to use is Green's lag entrainment method [52]. Which defines a new shape factor H_1 which depends on different boundary layer parameters which can be seen in Equation 4.31.

$$H_1 = \frac{\delta - \delta^*}{\theta} \tag{4.31}$$

$$H_1 = 3.15 + \frac{1.72}{H-1} - 0.01(H-1)^2 \tag{4.32}$$

Laminar Separation Bubble

Because of the small chord, there are low Reynolds numbers which result in a possibility of laminar separation bubbles (depending on the airfoil). All laminar separation bubbles occur when the flow has laminar separation, but during the separation, the flow becomes turbulent and attaches further downstream. A bubble will decrease the airfoil performance due to the extra drag introduced [28]. A separation bubble can be observed in Figure 4.16. It is more common to have a bubble on a thin airfoil or close to the leading edge of thick airfoils. Laminar bubbles are easier to arise when the flow is laminar.

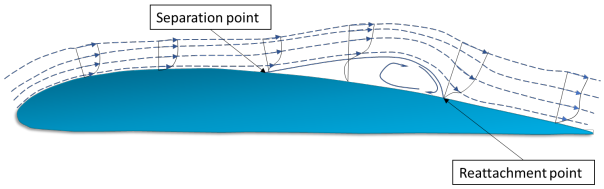

Figure 4.16: Flow over an airfoil with separation bubble

The separation can be prevented by using airfoils designed for low Re numbers or by tripping the flow before separation occurs, making the boundary layer turbulent. This tripping can be done by using a tripping wire, zigzag tape or a vortex generator. The approach chosen during design is to use 3D printing which will have a natural roughness making it easier to create a turbulent boundary layer and, prevent a laminar bubble. For the final design, a redesign of the proposed design will be done to determine the tripping location in case it is chosen to not use 3D printing.

4.3.2 Xfoil/Rfoil

All the codes used to determine the noise or performance of the wind turbine are required to use reliable 2D airfoil data. As mentioned it was chosen for panel codes such that there is no restriction on choosing airfoil from measurment results. Well known panel codes are Xfoil developed by Drela [53] and Rfoil developed at Delft university of Technology and ECN [54]. Both are codes that evaluate the performance of airfoil in subsonic flow. Xfoil is a panel code that is coupled to a viscous- inviscid solver. Xfoil works by panelling the airfoil in N number of panels, and by placing a bound vortex for each panel, a figure can be seen in Figure 4.8 (panel method). Xfoil predicts for a set of angles of attack the lift, drag and momentum coefficient as well as the boundary layer parameters such as δ^*, θ, H and C_f which will be required for the noise model. Rfoil has almost completely the same solver but has according to Timmer et al. a different viscous correction to predict the stall angles better [54].

The critical amplification factor N is investigated before the verification of Xfoil or Rfoil is performed. N is a quantity that describes the amount of TI in a flow. The boundary layer will transition earlier to turbulent when the critical amplification ratio is lower. Both Xfoil and Rfoil use a standard TI of 0.07% which corresponds to a N of 9. When N is high the flow is laminar and will be more sensitive to laminar separation bubbles. The separation bubble can be clearly seen in Figure 4.17b where N equals 11. It is noticed that in the bucket an increase in drag is observed this is due to the presence of the laminar separation bubble. The drag increases compared to the more turbulent flows (lower N). This effect can be seen for Xfoil and Rfoil. The vertical line for low N values does not have a dip (where C_d is almost constant). Meaning that there is no separation bubble present due to the turbulent boundary layer created because of the high TI in the flow.

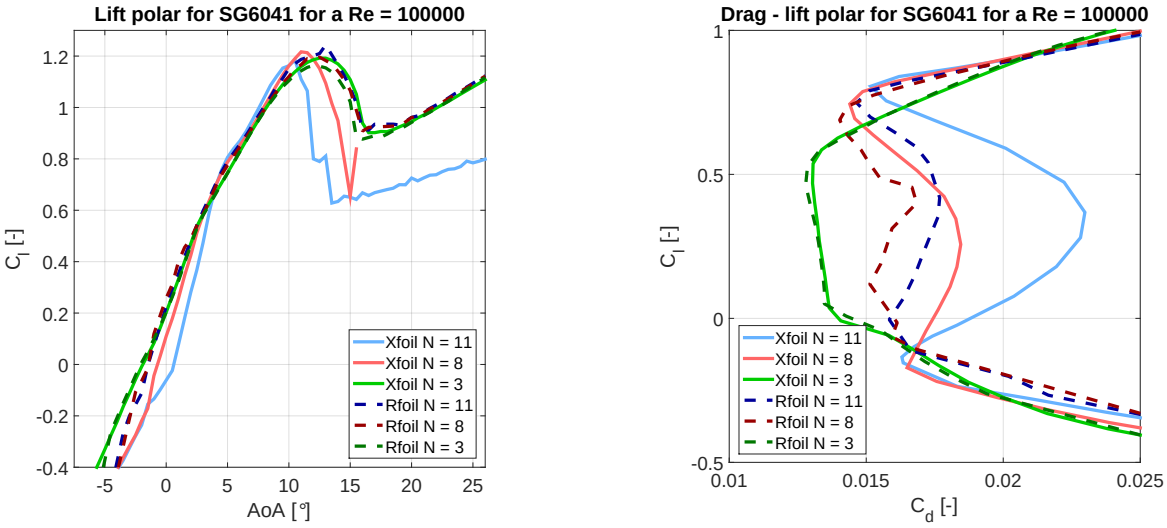

(a) AoA-C_l curve for SG6061

(b) C_d-C_l curve for SG6061

Figure 4.17: Effect of N_ crit on airfoil polar prediction

When designing the wind turbine, it is important to consider in what kind of conditions the wind turbine will be operated or tested in. The W-tunnel has a minimum TI of 0.5% which equals a critical amplification ratio of 3. This factor will be used for designing, while the correction values are determined based on the real laminar flows based on the experimental data of Selig [29–31, 55, 56]. The test of Selig was done in a low TI tunnel resulting that the data from Xfoil and Rfoil will be validated for a N of 8 and 11 to investigate what the difference is.

4.3.3 Verification of Xfoil and Rfoil

The first step in choosing the appropriate program is to test which code performs better compared to the experimental data measured by Selig [29–31, 55, 56]. The Reynolds number range that needs to be investigated is from 50000 - 100000. These Re numbers are low so for this reason, there is looked at low Re number airfoil. The most famous experimental campaign was performed by Selig [29–31, 55, 56]. The measurement campaign focuses on the airfoil performances of low Re number airfoil for different application in a laminar flow. The airfoil is tested in the UIUC low-turbulence wind tunnel which has a TI lower than 0.1 %. Xfoil and Rfoil prediction will be compared to Selig's measurement data. The two airfoil discussed here are SG6041 with an RE number of 100000 and the A18 airfoil has a Re number of 60000. There is chosen for two different amplification ratios of 8 and 11 to see what the effect is. In Figure 4.18a Xfoil predicts the lift more accurate than Rfoil. Rfoil overpredicts the stall angle for both values of N. In Figure 4.18b all cases show large discrepancies. From the data shown here for a Re number of 100000, it can be said that Xfoil predicts better compared to Rfoil. The second case is a thin airfoil at a Re number of 60000.

From Figure 4.18c it is seen that the lift is over predicted for all cases and the stall angle is predicted too early. For the drag prediction of Xfoil with an N factor of 11, there is a big influence of a laminar separation bubble. However, in the experimental data from Selig, the laminar separation bubble is presented but it does

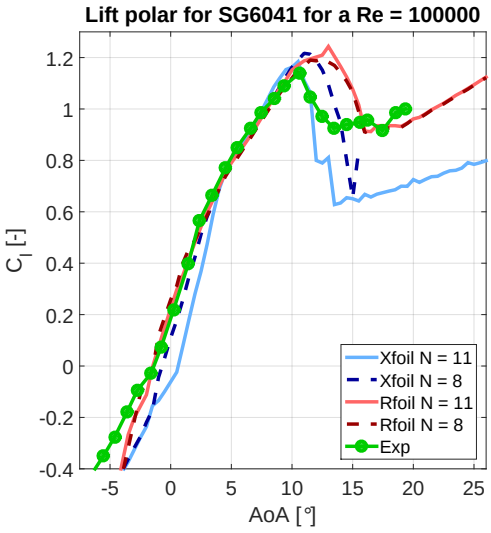

(a) AoA-C_l curve for SG6041 Re= 100000

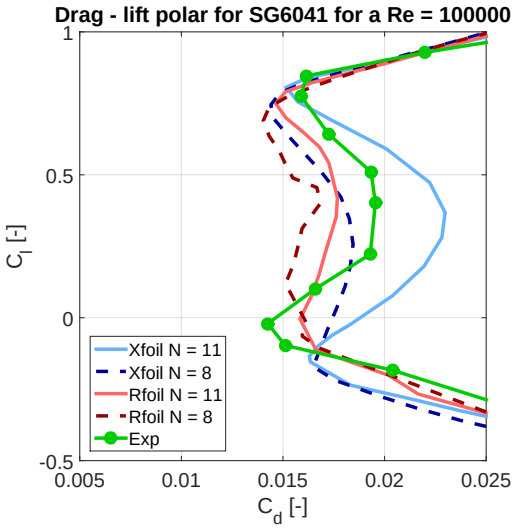

(b) C_d-C_l curve for SG6041 Re= 100000

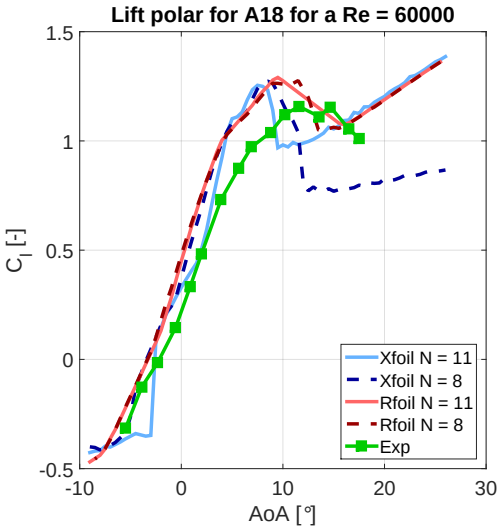

(c) AoA-C_l curve for A18 Re= 60000

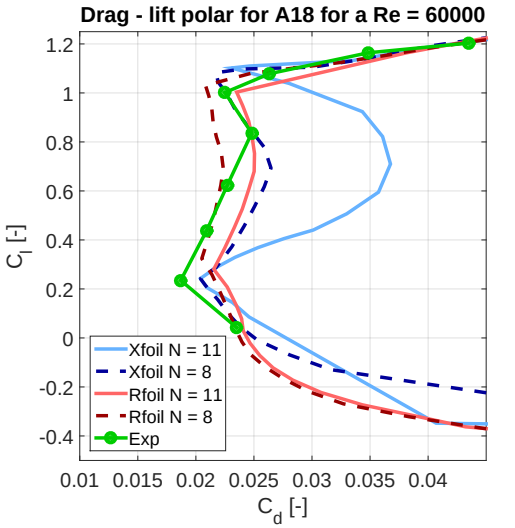

(d) C_d-C_l curve for A18 Re= 60000

Figure 4.18: Comparison of Xfoil and Rfoil with experimental data

not have as much influence as Xfoil predicted. From this, it can be concluded that both programs are off for these low Re numbers.

For verification, there is looked at the shape of the data and two points on the graph. The first point is the angle where the maximum lift will be produced. The second point is the point where the drag is maximal in the vertical part of the drag lift curve. Tabulated values can be seen in Table 4.1. For SG6041 it can be observed that Xfoil predicts the $C_{l_{max}}$ with an error of 4% and Rfoil has an error of 9% for the case where N=11. It can be seen that the lift point is predicted better by Xfoil for thin airfoils. Looking at the angle calculated by Xfoil where max C_l is obtained for the A18 airfoil, it can be concluded that a large discrepancy is present. Rfoil predicts the stall angle better for thin airfoil at low Re numbers. From the first part of the verification, it can be concluded that Rfoil predicts the stall angle better. While Xfoil is better in determining the value of $C_{l_{max}}$. The second part in verification is the investigation of the maximum drag point in the drag lift curve. The vertical part or bucket of this curve is important since this corresponds to the linear part of the lift curve. This part is important since the wind turbine will operate in this region for the optimum TSR. Meaning that it is more important that the drag and lift are determined correctly compared to stall angle. Lift and drag determine the power of the wind turbine, while AoA only determines at what TSR this maximum power is obtained. The

Table 4.1: Tabulated values of verified airfoil in between brackets is the percentage difference

Case	Reference		Xfoil		Rfoil	
SG6041	Angle	Max lift	Angle	Max lift	Angle	Max lift
N = 11	10.6	1.14	10.5 (1%)	1.184 (4%)	13 (18%)	1.243 (9%)
N = 8	10.6	1.14	11 (4%)	1.217 (6.5%)	12.5 (15%)	1.196 (5%)
A18						
N = 11	11.6	1.158	7.5 (54.6%)	1.255 (8%)	9.5 (22%)	1.291 (11.5%)
N = 8	11.6	1.158	8.5 (36.5%)	1.273 (10%)	11.5 (1%)	1.276 (9.2%)
SG6041	Drag (bucket)	Lift	Drag (bucket)	Lift	Drag (bucket)	Lift
N = 11	0.01955	0.4012	0.02298 (17.5%)	0.3682 (9%)	0.01768 (10%)	0.4192 (4.5%)
N = 8	0.01955	0.4012	0.01845 (5.6%)	0.2568 (35.9%)	0.01684 (13.8%)	0.4001 (0.3%)
A18						
N = 11	0.02481	0.8362	0.03676 (14.8%)	0.7099 (15%)	0.02502 (0.1%)	0.6796 (18.7%)
N = 8	0.02481	0.8362	0.02647 (6.2%)	0.6932 (17.1%)	0.02236 (10%)	0.6911 (17.35%)

points of interest are the points with the highest drag in this region (if drag increases significantly it could be that there is a laminar separation bubble present). Looking at the maximum drag it can be observed that both codes predict the drag wrong. However, when looking at both airfoils Rfoil's error is lower compared to Xfoil. The same can be seen for the lift, meaning that Rfoil might not be better in predicting the stall angle but it is better in predicting the drag to lift curve. It is of importance that this curve is predicted as accurate as possible for the wind turbine performance codes.

Last, the shape of the graphs is investigated of the different airfoils. First, the SG6041 lift polar plots have a comparable shape from the moment the lift coefficient is higher than 0 up until the maximum lift. In this graph, it can be seen that for Xfoil where N equals 11 there is a lower lift coefficient for the low AoA region compared to the measured data and it last until the AoA is 5°. When looking at the higher angle the graph shows that Xfoil for N=11 predicts a larger drop in C_l, while Rfoil predicts this dip better but too late. It can be said that Rfoil predicts the general curve better than Xfoil but it predicts the stall angle to high. Looking at the drag-lift curve all methods predict the curve good at lower and higher C_l. The graph shows much more deviation for the vertical bucket part of the graph. Here it is clear that both for Xfoil and Rfoil with a case of N equals to 8 that there is a limited similarity. Looking at the N=11 case for Xfoil the data does not agree with the experimental data. This is something that is not observed in the Rfoil simulation. From this, it is concluded that Rfoil predicts the SG6041 better compared to Xfoil. Looking at the A18 lift curve, the graph shows in the linear part that the simulation programs predict much more lift than it is measured. The stall angle is predicted better with Rfoil than Xfoil, and looking at the post stall lift the same lift decrease can be observed for Rfoil. While for Xfoil the dip is much more, this confirms that Rfoil has a better result for the stall region which is important in the low TSR region of wind turbine design [54]. Looking at the bucket from the A18 curve the drag predicted by Xfoil is wrong with a significant difference compared to experimental results. The drag predicted by Rfoil is much better and for this reason, it is determined that Rfoil predicts better the A18 airfoil performances. Based on the verification it is chosen to use Rfoil. Rfoil predicts general trends better compared to Xfoil. Rfoil performance is less good when the maximum C_l needs to be calculated, but this is compensated by its ability to predict the general curves better.

4.4 Verification of Blade Element Momentum Theory and Lifting Line Method

A verification of the wind turbine performance codes is necessary before they can be used in the design of the small wind turbine. Three rotors will be analysed, first the NREL 5 Mega Watt wind turbine which is a standard reference wind turbine [57]. Second, a small wind turbine with a diameter of 0.9 m [58], and last a mini wind turbine with a diameter of 15 cm and a constant airfoil distribution. All the rotors are three bladed since this is the maximum number of blades Bladed allows. The BEMT and lifting line will be verified with Bladed from DNV-GL. First, the rotor will be verified for the optimum TSR and here the lift and drag

distribution is investigated as well as the induction factors. If there is a similarity for the first verification a second verification will be performed to investigate if the $\lambda - C_P$ curve is similar. The LL code runs at an azimuthal step size of 10° and to let the wake develop at least 10 rotations are performed.

4.4.1 Verification of the NREL 5 MW

The NREL 5 MW is a standard wind turbine developed to do extensive measurement campaigns so that new models and methods can be improved and validated. The NREL 5MW wind turbine is a three-bladed upwind variable speed turbine with variable pitch control. It has a rated power of 5 MW at a rated speed of 11.4 m/s. The rotor diameter is 126 m with a blade length of 61.5 m. The design TSR is 7, so for the first verification of the BEMT and LL wind turbine will be operated at a TSR of 7 with a wind speed of 11.4 m/s. The blade layout can be seen in Table B.1.

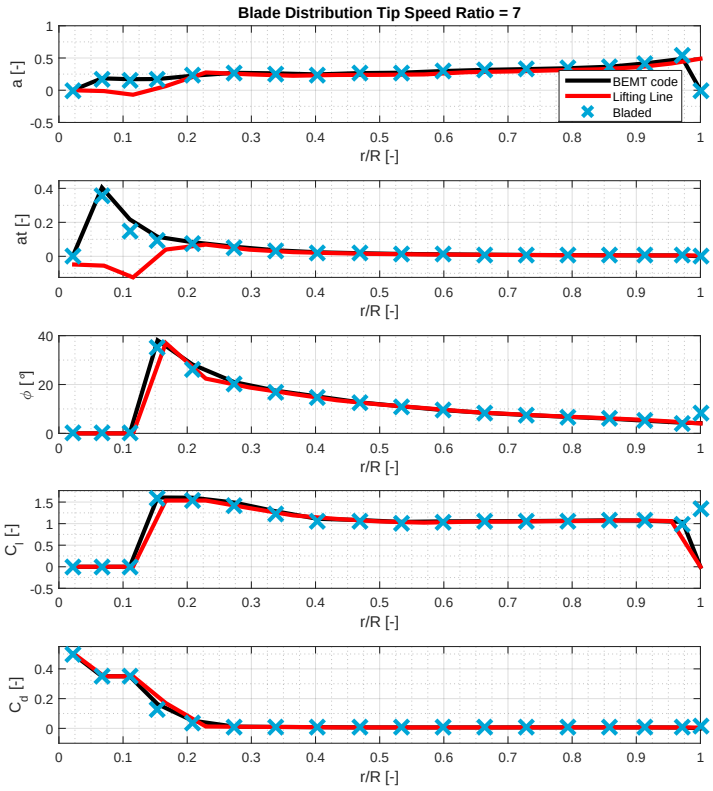

Figure 4.19: Radial results for NREL 5MW, black line BEMT results, red line lifting line result and crosses Bladed results for a wind speed of 11.4 and TSR=7

The result of the calculations can be seen in Figure 4.19. For the BEMT code compared to Bladed it shows good comparison, and no large deviation is observed, meaning that for large wind turbines the BEMT is working and has similar prediction capabilities compared to available commercial softwares. For this case, the BEMT Rfoil runner used a critical amplification ratio of 9 due to the assumption of normal operating conditions.

From the lifting line, most of the result match the BEMT methods. The only deviation can be seen at the root, which is interesting since this is a normal circular cross section. This is highly likely due to a numerical instability. Due to the Kutta conditions, the lifting line has as a limitation that it cannot simulate the performance close to stall angle since separation is present. To be sure that the lifting line would give good results the rotor should turn at least 10 times to be sure that the wake is developed good enough. However, since the

NREL is designed also in a structural way it can be safely assumed that if an optimal aerodynamics design (operate at max L/D) was used the stall angles would be avoided and similar results would be achieved as was obtained for the mid and tip section of the blade. It was observed for BEMT and Bladed that the induction factors increase at the root which is strange since the section used here is circular. Up till now, no real explanation can be given. The only possible reason that could cause this is that the initial assumption is that the induction factor equals 1/3 and that for the second iteration the relaxation factor did not do properly its job.

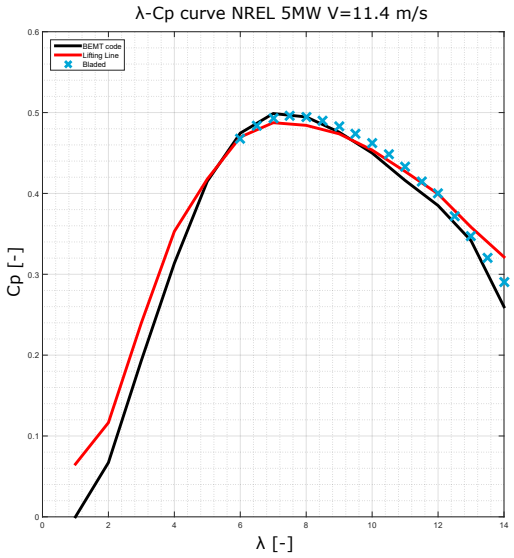

Figure 4.20: NREL $\lambda - C_P$ curve for NREL: 5 MW turbine for a wind speed of 11.4 m/s

For the NREL 5 MW turbine, the results are promising for a TSR of 7, This is the design TSR so the LL and BEMT where used to calculate the C_P for a TSR range of 1.5 to 14. It can be expected that there will be deviations between the LL and BEMT for low TSR region. When a wind turbine operates in low TSR regions the AoA will go up, resulting in larger errors for LL due to the Kutta condition and the separating of the flow over the airfoil for these large AoA. The Kutta-Joukowski condition assumes that the flow leaves at TE and this is not the case when an airfoil is stalled, this is the main reason why the deviation is present for low TSR [8]. In Figure 4.20 the TSR-C_P curve can be seen. Bladed calculated the performance for a TSR of 6 to 14. The LL has a large deviation compared to the BEMT. For the design TSR region, the BEMT and Bladed are similar. The LL compared to BEMT is good for the calculated results though for the BEMT calculation the slope is much steeper for the high TSR, while the LL has a lower slope. It can be concluded that both models perform comparable to Bladed with some minor difference between LL and BEMT. It can be assumed that for this rotor the LL does predict the performance with acceptable accuracy when looking at the optimum TSR.

4.4.2 Verification of the Small Wind Turbine

The next step is to look at a smaller wind turbine, which has a rated C_P of 0.45 and a rotor diameter of 0.9 meters. The case investigated is the TSR design which for this rotor is 6 [58]. The same procedure was performed as was done with the NREL 5MW turbine. The rotor designed here is an optimum rotor so it should be noted that the AoA in the optimum case should be around the highest L/D value at each section. The blade layout can be seen in Table B.2. The blades of the rotors have a constant airfoil distribution. The airfoil used here is S826 which is a typical airfoil for small wind turbines. The Re number is low and varies from 80000 un till 100000 due to the low wind speed of 7 m/s. This will result that the airfoil will be sensitive for laminar separation. In the original report a amplification factor of 3 is used [58], meaning that for the verification the same N is used. The wind turbine is a three-bladed upwind wind turbine.

In Figure 4.21 the results can be seen. The BEMT model and Bladed show similar results. The LL model compared to the two others is completely different. The induction factor across the blade lower as well as the

tangential induction factor. Due to this, the inflow angles will be larger and this will increase the AoA since the twist is constant. If the AoA increases, it will suffer more drag and in this case, it will create more lift. But according to LL the rotor is not operating at optimum conditions and its overshoots its AoA into the stall zone. The Kutta condition relates the circulation to lift. Due to this assumption, the prediction made by LL is

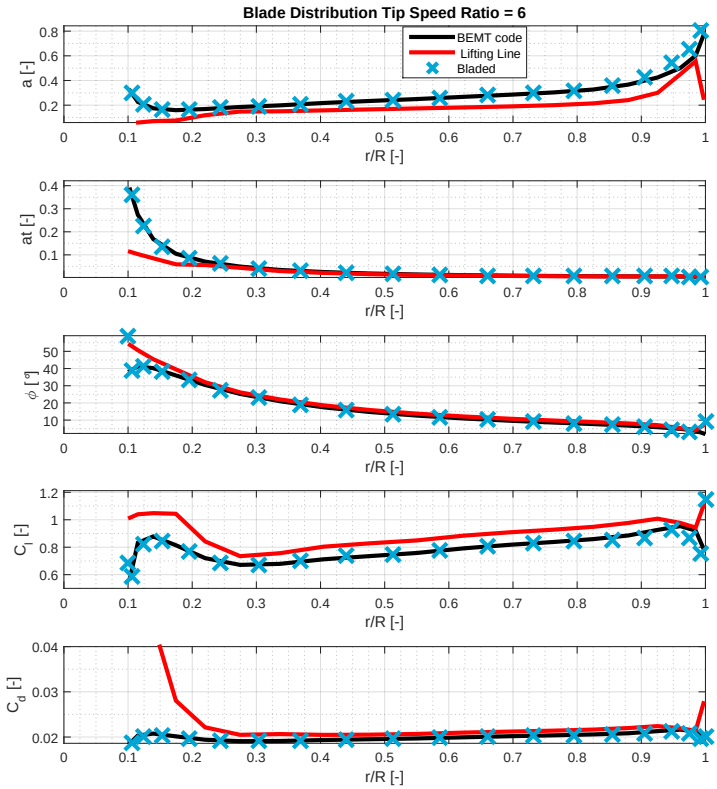

Figure 4.21: Radial results for small wind turbine, black line BEMT results, red line lifting line result and crosses Bladed results

significantly different compared to the two other methods. The lifting line is known to predict wrong for high AoA or angles close to stall. If the angles of attack start to increase separation will occur and lift will be lost, from this moment kutta-jouwkowsky lift theorem is not valid any more [8]. The reason why Kutta condition is not valid is that the Kutta condition assumes that the flow leaves at the TE, while if there is separation the flow leaves before the TE violating the Kutta condition. The Kutta condition will assume that the flows leave at the TE and this will result in an extra lift that can only be obtained at a higher angle of attack. Because the LL model does not agree with the bladed no calculation was performed for the $\lambda - C_P$, since it was shown that the LL will not work for this rotor.

4.4.3 Verification of the Mini Wind Turbine

Last a small wind turbine which will be comparable to the designed wind turbines will be tested. The verified wind turbine is a three-bladed wind turbine with a diameter of 15 cm. The hub size is 5 cm and each blade has a length of 5 cm. In Figure 4.22 the results can be seen for the BEMT, LL, and Bladed. The calculation was performed at a wind speed of 30 m/s and a TSR of 2. It can be seen from a first observation that the lifting line is not comparable to bladed or BEMT. For the case, the BEMT and bladed are similar but only some small numerical instabilities can be seen at the hub and tip. This is due to the different models used. These two have minor influence since a cosine spacing is used resulting in a low contribution. Next, the LL is completely off compared the BEMT result this is again to the Kutta-joukowsky condition. The Inflow angle is predicted higher than BEMT resulting in higher lift and drag. The reason is that the Kutta condition assumes that the flow leaves at the TE, while for low Re flows the flow is separated earlier. This will result in a loss

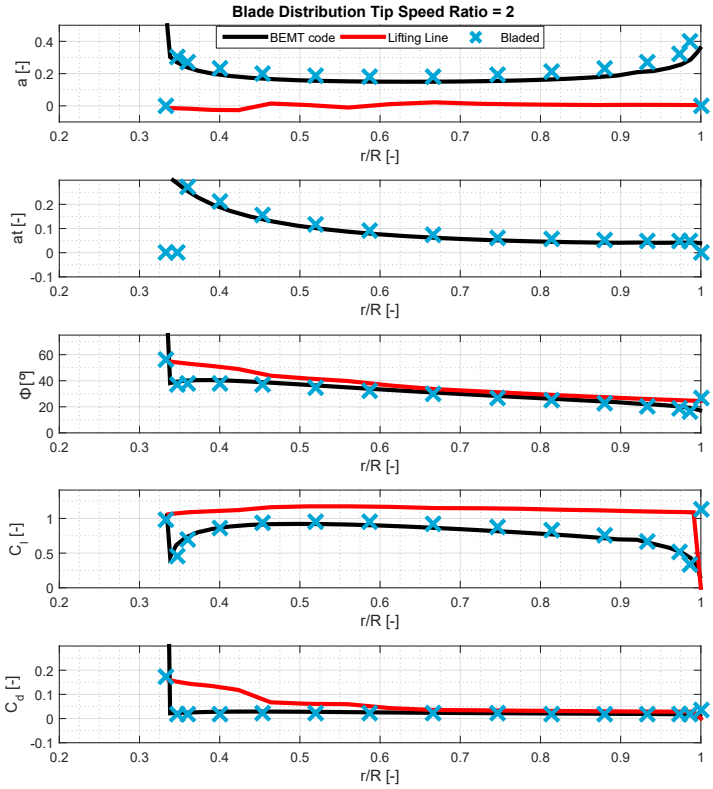

Figure 4.22: Radial results for mini wind turbine, black line BEMT results, red line lifting line result and crosses Bladed results

of lift which is not considered in the Kutta condition but is considered by Rfoil. The second reason why the lifting line has errors is because the Kutta condition is derived for inviscid flows over airfoils while for these low Re numbers there are considerable viscous forces. This viscous region is predicted by Rfoil, but is not by the Kutta condition resulting in another reason for deviations.

4.4.4 Conclusion Verification

It is verified that the BEMT has comparable results to Bladed from DNV GL. Meaning that BEMT will be used for further calculations of wind turbine aerodynamic performance. Lifting line has only given reliable results for large wind turbines, small and mini wind turbines have proven to be impossible for LL. The reason is that the aerodynamics for these small rotors is different compared to large turbines since the viscous forces become more important. This is not considered in Kutta conditions resulting in a wrong lift distribution.

After the verification, the first part of one of the research questions can be solved. It was shown that the lifting line will not be sufficient to predict the performance of a rotor at optimum TSR. The reason is that for small rotors the Re is low and this will result in earlier separation. The flow over the airfoil does not leave at the TE if it is separated which is a violation of the Kutta-Joukowsky theorem on which the lifting line is based.

Chapter 5

Wind Turbine Noise

This chapter discusses the theory behind the noise model that will be used to predict the sound pressure level (SPL). The chapter will progress towards explaining the tonal noise, trailing edge noise as well as turbulent inflow noise which are the main noise sources for wind turbines [1, 10, 16, 32, 33]. Next, the code is explained together with the equitations to recalculate the SPL to the total SPL for a 1/3-octave band at a given wind speed and tip speed ratio. At the end, a verification of the model will be done by verifying it against NAFNoise. It was not possible to verify the tip vortex noise, and turbulent inflow noise, since NAFNoise has different models for this and are not comparable with the BPM model.

5.1 Tonal Noise

Tonal noise is a noise source at which clear peaks are visible in the broadband spectrum. In wind turbines, this is mostly at the rotating frequency and the blade passing frequency [1]. The reason why there is a noise source at the blade passing frequency is because every time the blade passes the tower there is localised flow that is disturbed due to the tower that is present. In Figure 5.1 it can be seen that the streamlines need to move around the tower due to its blocking effect, and this is the reason why there is this instability.

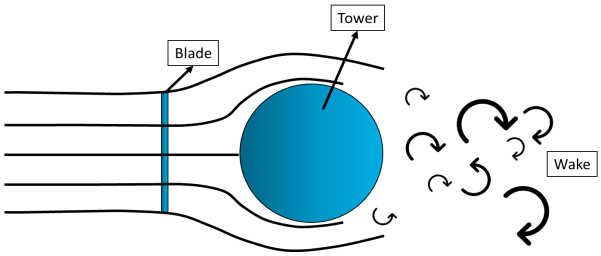

Figure 5.1: Blocked flow around a wind turbine tower, adapted from Wagner [1]

If the blade passes through this flow instability the flow over the airfoil changes which results in unstable loading on the blades. The main instability will be that the angle of attack will change as well as the inflow velocity. This will result in a thumping sound which for large wind turbines can be perceived as annoying.

As said the dominant tonal frequency will be the blade passing frequency which can be determined by Equation 5.1.

$$f_b = \frac{\Omega}{2\pi} \cdot B \tag{5.1}$$

where, f_b is the blade passing frequency, Ω angular speed of the rotor and B number of blades. Tonal frequencies have as a characteristic that they have harmonics. The harmonic can be determined by the following relation: $f_b \cdot n$ where n is a constant. The higher the harmonic frequency the lower the magnitude of the SPL.

Large wind turbines have a low blade passing frequency (in the order of 1-3Hz), which is out of the audible frequency (or just inside). Noise in this low-frequency range it is called low-frequency noise. For small

wind turbines, the rotational speed is much higher, it is in the order of 9000-15000 RPM. This means that the rotational frequency is 150 Hz (assuming 9000 RPM). Second, besides the higher rotational speed for mini wind turbines, it is often seen that there are more blades than 3. Considering the higher rotational speeds and higher number of blades compared to large wind turbines the blade passing frequency tonal noise is an important problem for mini wind turbines.

In general, there are two types of HAWT upwind and downwind. It can be seen in Figure 5.1 that there is a large disturbance after the tower which is the wake of the tower. This will result in a high tonal noise if there is chosen for a downwind turbine. This is because of the increase in disturbed flow, and increase in turbulence which is clearly observed in the wake in Figure 5.1. For this reason, it is chosen to use an upwind turbine.

5.2 Airfoil Self-Noise

Airfoil self-noise is due to the interaction between an airfoil and the instabilities created in the boundary layer [10]. This was broadly investigated by Brooks, Pope and Marcolini [10]. They did extensive wind tunnel experiments with an NACA0012 at NASA. They tested different set-ups and derived a semi-empirical scaling law. They concluded that there are 5 dominant noise sources generated by the airfoil:

- Turbulent boundary layer - trailing edge noise (TBL-TE)
- Separation -stall noise (S-S)
- Laminar boundary layer - vortex shedding noise (LBL-VS)
- Trailing edge bluntness noise (TEB)
- Tip vortex formation noise (TV)

They did the test in a low TI tunnel since the research investigates what the influence of the boundary layer will be on the noise without considering turbulent inflow noise. Doing these test in a low TI tunnel would result in less interaction between the airfoil and the eddies of the wind tunnel also known as turbulent inflow noise. In this section, the 5 noise sources are discussed and how to determine them. It is stated by Brooks et. al that the noise sources are all located at the trailing edge [10].

5.2.1 Turbulent Boundary Layer - Trailing Edge Noise (TBL-TE) & S-S Noise

One of the first airfoil self-noises is TBL-TE which is characterised by the sound produced when a turbulent boundary layer interacts with the TE. The turbulent boundary layer depends on the airfoil, Re number and the roughness of an airfoil. The boundary layer will start laminar at the LE and become turbulent at a certain chordwise position as can be seen on Figure 5.2. Turbulent eddies are not an efficient noise source on their own, but if they interact with for example a TE they are becoming more effective [10]. The TBL-TE can be estimated by using different boundary layer parameters. The TBL-TE is split up in pressure and suction side of the airfoil.

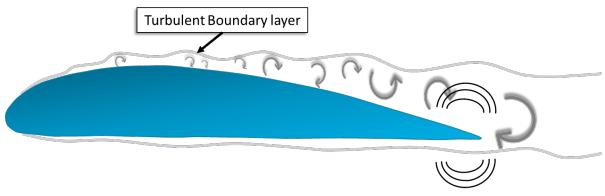

Figure 5.2: TBL-TE noise radiating at the TE, adapted from Brooks [10]

In the BPM model a third turbulent source is recognised which is the separation stall noise. For medium, to high angles of attack, the flow can separate which result in an extra noise source at the TE. If the airfoil has separation eddies will form on the suction side of the airfoil. When the airfoil is completely stalled, it will become a dominant noise source and TBL-TE for suction and pressure side is negligible ($-\infty$ dB). The stall

noise can be avoided by not operating at these high angles of attack. The visual representation of stall noise can be seen in Figure 5.3, it can be seen that large instabilities occur at the suction side of the airfoil.

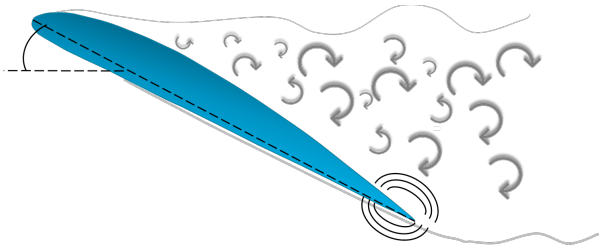

Figure 5.3: Deep stall of an airfoil, adapted from Brooks [10]

In the BPM method, the TBL-TE is split in three sources, the noise source at suction side, pressure side and separation stall noise. The total TBL-TE can be predicted with equation Equation 5.2.

$$SPL_{TOT_{TBL-TE}} = 10\log_{10}\left(10^{\frac{SPL_s}{10}} + 10^{\frac{SPL_p}{10}} + 10^{\frac{SPL_\alpha}{10}}\right) \tag{5.2}$$

To determine the individual SPL of the TBL-TE noise Brooks et al. developed scaling methods based on Strouhal numbers (St) [1]. A Strouhal number is a dimensionless number that gives a relation of the dominant frequencies in an oscillating flow. BPM method uses Equation 5.3-5.5 to determine the SPL of each individual turbulent boundary layer noise mechanism. The SPL depends mostly on the boundary displacement thickness of the airfoil and the Mach number [10].

$$SPL_p = 10\log_{10}\left(\frac{\delta_p^* M^5 L\bar{D}_h}{r_e^2}\right) + A\left(\frac{St_p}{St_1}\right) + (K_1 - 3) + \Delta K_1 \tag{5.3}$$

$$SPL_s = 10\log_{10}\left(\frac{\delta_s^* M^5 L\bar{D}_h}{r_e^2}\right) + A\left(\frac{St_s}{St_1}\right) + (K_1 - 3) \tag{5.4}$$

$$SPL_\alpha = 10\log_{10}\left(\frac{\delta_s^* M^5 L\bar{D}_h}{r_e^2}\right) + B\left(\frac{St_s}{St_2}\right) + K_2 \tag{5.5}$$

where, δ_p^* is the displacement thickness at the TE, L is the length of the blade section being evaluated, r_e is the distance between observer and source, D is directivity for high frequency which is explained in section 5.5, A, K_1, K_2 and B are scaling functions based on Strouhal number and Re number which is explained in section C.2.

If the AoA is higher than the stall angle, then it is assumed that the airfoil is in a deep stall. This will result that the separation stall noise will become the dominant noise source. The TBL-TE for the pressure and suction side can be neglected. At angle higher than the stall angle, Equation 5.6-5.8 have to be used [10].

$$SPL_p = -\infty \tag{5.6}$$

$$SPL_s = -\infty \tag{5.7}$$

$$SPL_\alpha = 10\log_{10}\left(\frac{\delta_s^* M^5 L\bar{D}_l}{r_e^2}\right) + A'\left(\frac{St_s}{St_2}\right) + K_2 \tag{5.8}$$

where, D_l is the directivity for low frequencies.

5.2.2 Laminar Boundary Layer-Vortex Shedding Noise (LBL-VS)

The second noise source for an airfoil is laminar boundary layer vortex shedding noise (LBL-VS). When at least one side of the airfoil has, a laminar boundary layer this noise can occur. In a laminar boundary layer, small instabilities occur in the boundary layer which is called Tollmien-Schlicting waves [1]. These waves are small instabilities that could convert a laminar boundary layer to a turbulent boundary layer. These small instabilities can be seen in Figure 5.4. The instabilities will interact with the TE and create a resonance frequency or a tonal noise. The LBL-VS noise is not important for large wind turbine since they operate at much

Figure 5.4: Vortex shedding of a laminar boundary layer (LBL-VS), adapted from Brooks [10]

higher Reynolds numbers than mini wind turbines. For small wind turbines, this is more important since LBL-VS generate large tonal component noise. If this is a problem for the small wind turbine the boundary layer should be tripped such that it becomes turbulent. The LBL-VS can be calculated with Equation 5.9.

$$SPL_{LBL-VS} = 10\log_{10}\left(\frac{\delta_p M^5 L\bar{D}_h}{r_e^2}\right) + G_1\left(\frac{St}{St'_{peak}}\right) + G_2\left(\frac{R_c}{(R_c)_0}\right) + G_3(\alpha) \tag{5.9}$$

It can be noted that the main scaling factor is not the displacement thickness at the TE but the boundary layer thickness. G_1 is a shape function that is dependent on the Strouhal number. G_2 is a shape function as a function of the Reynolds number and G_3 is a function of the angle of attack contribution. The equation for the shape function G can be found in section C.3. If the boundary layer becomes turbulent TBL-TE noise will be present but also LBL-Vs noise. The reason why LBL-VS cannot be neglected is because the front part of the airfoil might have a laminar flow [10]. Brooks et al. developed their model that there is a transition between LBL-VS and TBL-TE noise which is based mainly on the Re number.

5.2.3 Trailing Edge Bluntness Noise (TEB)

Brook et. al tested the TEB noise by adding attachments at the TE of an airfoil to investigate the effect of the bluntness of an airfoil on the noise [10]. This sound source is induced when there is a vortex shedding due to the bluntness of the TE. When this happens a flow pattern will occur that is asymmetrical this can be seen in Figure 5.5. This oscillatory flow pattern will create a pressure fluctuation which will generate noise.

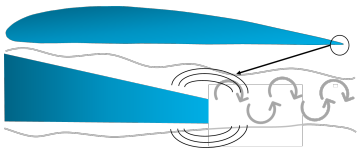

Figure 5.5: Oscillatory flow pattern at TE due to bluntness of TE, adapted from Brooks [10]

This noise source is mostly dependent on h/δ^*. The larger the trailing edge thickness the larger the amplitude of the oscillations and the lower the frequency will be. This noise source will result in a high tonal sound. A solution to decrease the noise is to make the trailing edge sharp such that the oscillatory movement will have a higher frequency which is more difficult to hear for humans. In other words, the problem is shifted towards a frequency spectrum that is outside the audible hearing range. The TEB noise can be determined by Equation 5.10 [10].

$$SPL_{TEB} = 10\log_{10}\left(\frac{hM^{5.5} L\bar{D}_h}{r_e^2}\right) + G_4\left(\frac{h}{\delta^*_{avg}}, \Psi\right) + G_5\left(\frac{h}{\delta^*_{avg}}, \Psi, \frac{St'''}{St'''_{peak}}\right) \tag{5.10}$$

where, the SPL depends on a large scale on the TE thickness and the average boundary displacement thickness. G_4 is a spectral shape function depending on the ratio between height and displacement thickness and

the slope angle of an airfoil. G_5 is the spectral function which determines at which frequency the maximum SPL will be. The spectral shape functions equations can be found in section C.4.

5.2.4 Tip Vortex Noise (TV)

Brooks et al. [10] tested the difference between finite and infinite wings in the wind tunnel. They concluded that the last airfoil self-noise is due to the interaction of the tip circulations on the trailing edge. At the tip, there is a cross-flow due to the pressure differences between the pressure and suction side of the airfoil. This cross-flow will react with the TE generating a noise source. The vortex generated by this pressure difference has a strong turbulent core which reacts in the same way with the TE as TBL-TE [10]. The TV noise is a high-frequency broadband noise which is depended on the shape of the tip. An illustration of the noise source can be seen in Figure 5.6.

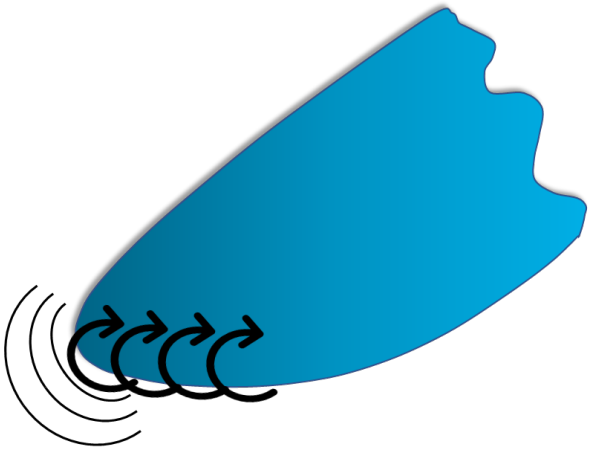

Figure 5.6: TV noise, with a clear distinction of the circulation generated at the tip, adapted from Brooks [10]

The TV noise is only present at the end of the blade. The outer part that is taken in to account for the noise is determine the viscous core size l. Predicting the TV noise can be done with Equation 5.11.

$$SPL_{TV} = 10\log_{10}\left(\frac{M^2 M_{max}^3 l^2 \bar{D}_h}{r_e^2}\right) - 30.5\left(\log_{10}(St'') + 0.3\right)^2 + 126 \tag{5.11}$$

where, M_{max} is the maximum Mach number in or outside in the separated flow. It depends on the angle of attack at the tip which is calculated by BEMT. As mentioned the TV noise depends on the tip shape, The BPM model considered two tips: one a round tip and a flat tip. l can be determined for round tips with Equation C.43 and l for a flat tip can be determined with Equation C.45.

5.3 Turbulence Inflow Noise (TIN)

In outside condition, the wind consists of a large amount of turbulence. When the atmospheric turbulence interacts with an obstacle it will a generate broadband noise. The noise generation due to the interaction between a turbulent flow and an object is called turbulent inflow noise. This noise source is the last aerodynamic noise source for a wind turbine that will be discussed in this thesis. Turbulence is created due to the pressure and temperature differences in the atmosphere together with the surface roughness of the earth. The temperature will result that air parcel rises and decline which generates turbulence [1, 33].

TIN consist of a high and low-frequency noise component. Both are generated by eddies but for each noise source the size of the eddy matters. The size of the turbulence is called turbulence length scale and if the length scale is many times larger as the blade chord a low-frequency noise will be generated. When there is, large eddy interacting with the blade a complete load change will be introduced since the pressure distribution on the airfoil is affected. This can be seen on Figure 5.7. When the size of the eddy is much lower than the chord length the effect will be felt locally on the blade. The eddy interacts on a local level with the pressure

distribution on the airfoil. This will generate a high-frequency noise. TIN noise is difficult to understand but it is believed that it is a major sound source under 1000 Hz [1].

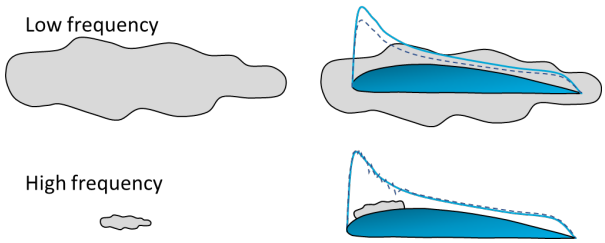

Figure 5.7: Turbulent inflow noise with different turbulence length scale, adapted from Wagner [1]

It was found by Amiet that besides the shape of the eddy (large or small) that the airfoil shape is important, especial the leading edge (LE) shape [41]. The BPM model is a TE interaction noise so the noise source is placed at the trailing edge, while the TIN noise is an LE noise source. The equations to estimate the noise generated due to the turbulent inflow can be found in Equation 5.12. This method was developed by Lowson [16] based on the work of Amiet [41]. The first term on the right-hand side is the SPL due to the high-frequency noise and the second term is a correction term for low frequency.

$$SPL_{TIN} = SPL_{TIN}^{f_{high}} + 10\log_{10}\left(\frac{K_c}{1+K_c}\right) \tag{5.12}$$

The SPL for high frequency can be calculated by using Equation 5.13.

$$SPL_{TIN}^{f_{high}} = 10\log_{10}\left(\frac{\rho^2 c^2 L\bar{D}_l}{2r_e^2}\Lambda(TI)^2 M^3 \frac{k^3}{\left(1+k^2\right)^{7/3}}\right) + 58.4 \tag{5.13}$$

where c is the speed of sound Λ is the turbulence length scale, TI is the turbulence intensity and k is the wave number which is determined with Equation 5.14.

$$k = \frac{\pi \cdot f \cdot c_{chord}}{V_{app}} \tag{5.14}$$

For the low frequency part K_c can be determined by Equation 5.15

$$K_c = 10\left(\frac{2\pi k}{1-M^2} + \frac{1}{1+\frac{2.4k}{1-M^2}}\right)^{-1} \cdot M\frac{k^2}{1-M^2} \tag{5.15}$$

5.4 Total Noise

It is interesting to know what the SPL is from each individual noise source or blade section, but it is of more importance to know what the total SPL is for each frequency at a certain receiver. The BPM model calculates the noise 1 meter behind the rotor centre (this is kept constant for the whole thesis). It needs to calculate for each blade section the SPL and recalculate the SPL using directivity pattern to the receiver location. A graphical view of the distance travelled from each blade element towards the central receiver can be seen in Figure 5.8. It is assumed that there is a dipole present for the airfoil noise at the TE. While the TIN noise it is placed at the LE (this is considered into the model).

The total SPL can be calculated by converting the dB to pressure for all the blade section and noise sources. If the SPL is known in Pa the sum can be taken from all individual sources and can be converted back to dB. The equation to calculate the total noise can be seen in Equation 5.16. To have the total noise the individual noise source of one blade needs to be multiplied with the number of blades.

$$SPL_{total} = 10\log_{10}\left(10^{\frac{SPL_{TOT_{TBL-TE}}}{10}} + 10^{\frac{SPL_{LBL-VS}}{10}} + 10^{\frac{SPL_{TEB}}{10}} + 10^{\frac{SPL_{TV}}{10}} + 10^{\frac{SPL_{TIN}}{10}}\right) \tag{5.16}$$

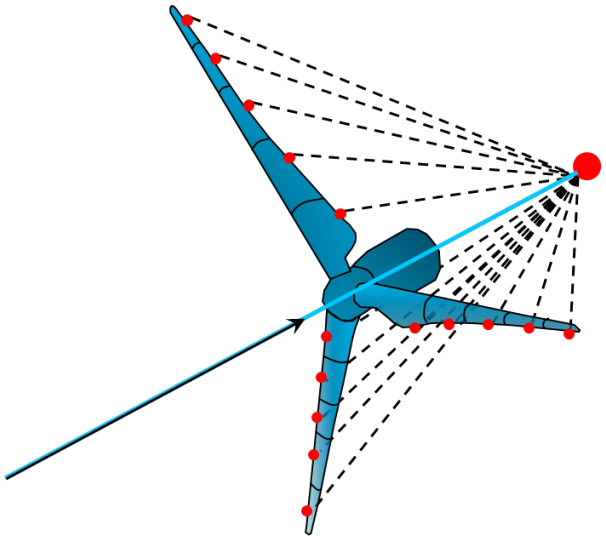

Figure 5.8: Location of the sources (small red circles) and the receiver one meter behind wind turbine (big red circle)

Doubling the pressure for a certain frequency will result in an increase of 3dB. A graphical representation of summing of noise sources can be seen in Figure 5.9. The dashed line is the total noise. The individual sources are the calculations of sum of the individual blade elements, so the sources seen are the ones from the whole rotor.

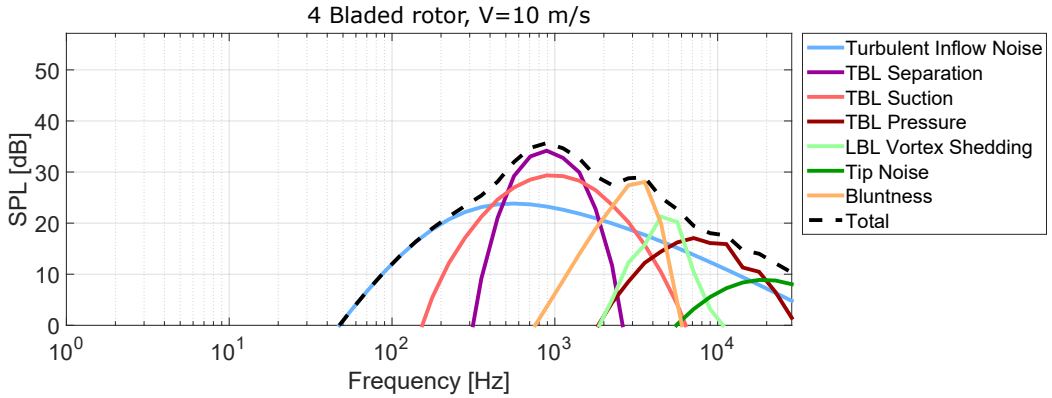

Figure 5.9: Summation of different noise sources

5.5 Directivity

Directivity is noise spreading pattern. The directivity pattern for airfoil noise is a dipole source of which the shape can vary [1]. The directivity shape depends on the wavelength if the wavelength is much shorter than the chord length the directivity shape will be a baffled dipole [10, 33]. When the wavelength has similar lengths as the chord length it will behave as a pure dipole.

The equation of the baffled dipole can be found in Equation 5.17. To determine the angle θ on needs to calculate the angle between the blade flow and the source-receiver line. And Ψ is that angle between the plane of the blade and the receiver. A graphical presentation can be seen in Figure 5.10.

$$\bar{D_h} = \frac{2\sin^2\left(\frac{\theta}{2}\right)\sin^2(\Psi)}{(1+M\cos(\theta))\left[1+(M-M_c\cos(\theta))\right]^2} \tag{5.17}$$

where, M is the Mach number of the free stream velocity and M_c is the convection Mach number which per Brooks et al. [10] it equals to 80% of the free stream Mach number. The convection Mach number is based on the convection velocity of the turbulence present in the boundary layer.

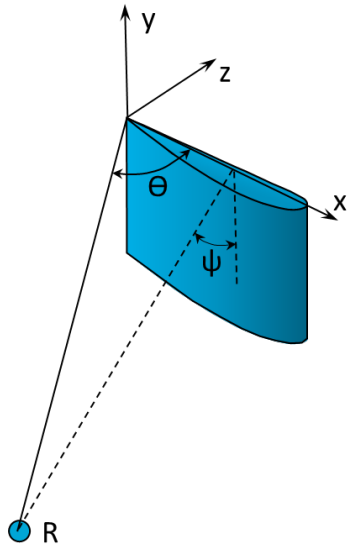

Figure 5.10: Coordinate system for a wind turbine blade, adapted from Brooks [10]

When the airfoil chord are comparable the noise directivity will have a pure dipole shape. This can be determined with Equation 5.18.

$$\bar{D}_l = \frac{\sin^2(\theta)\sin^2(\Psi)}{(1+M\cos(\theta))^4} \tag{5.18}$$

5.6 Verification

The BPM model is verified against NAFNoise [43] which was created by NREL. It has the capability to calculate and the major noise sources of a single airfoil section. It can calculate the TBL-TE with the BPM model or the TNO model. Since it is a verification the BPM will be used. NAFNoise cannot calculate a whole wind turbine but can calculate one blade element. The input of NAFNoise can be seen in Table 5.1. Both programs are

Table 5.1: Input parameters for NAFNoise and BPM model

Parameter	**Case 1**	**Case 2**	**unit**
Airfoil	SG6041	SG6040	-
Chord	2	2	cm
AoA	5	5	deg
V	60	60	m/s
L	4	4	cm
TI	5%	5%	-
Λ	0.06	0.06	m
speed of sound	340	340	m/s
Re	1e5	1e5	m
θ	90	90	deg
ϕ	90	90	deg

based on the same method and use the same equations. The only difference is that is not known under what conditions the Xfoil in NAFNoise operates and which version it is. For the verification, it is assumed that N=9 for Rfoil and that the flow on the airfoil is not tripped. The main differences between the two verification cases are that they use different airfoils.

5.6.1 Verification of TBL-TE Noise

In Figure 5.11 and Figure D.1 the TBL-TE noise can be seen. It can be observed that the results from BPM and NAFNoise are almost similar. As explained the BPM model calculates the noise with advanced scaling laws and Strouhal numbers. The Strouhal numbers determine the shape of the noise profile and the profile is almost identical. However, a small deviation can be observed for the TBL-TE at the suction side. The discrepancy between can probably be related to the small difference in displacement thickness. It was mentioned that it is not known what the input parameters are for Xfoil in NAFNoise, and because of this, a small variation can be observed for the displacement thickness at the TE. The only main difference between the two is the NAFNoise has a cut-off and converts the SPL lower than -100 dB to this value. From this first analysis, it can be concluded that the BPM model for TBL-TE noise performances comparable to NAFNoise.

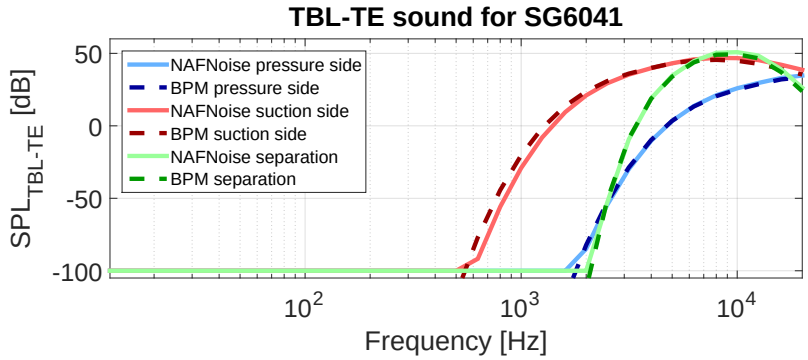

Figure 5.11: TBL-TE noise verification between NAFNoise and Code

5.6.2 Verification of TEB Noise

TEB noise is a tonal noise that is scaled according to h/δ^*_{avg}. Where δ^*_{avg} is the average displacement thickness between the pressure and suction side. h is the thickness of TE and is assumed to be 0.7 mm since this is a limit due to manufacturing. It was mentioned the thinner the TE the more the tonal noise will shift towards the higher frequency ranges. Figure 5.12 and Figure D.2 the tonal component of the TEB can be observed. Again, it is shown that NAFNoise and BPM model are similar. When looking at the peak the noise level of BPM is slightly lower compared to NAFNoise, and this is again due to the difference in Xfoil-Rfoil results.

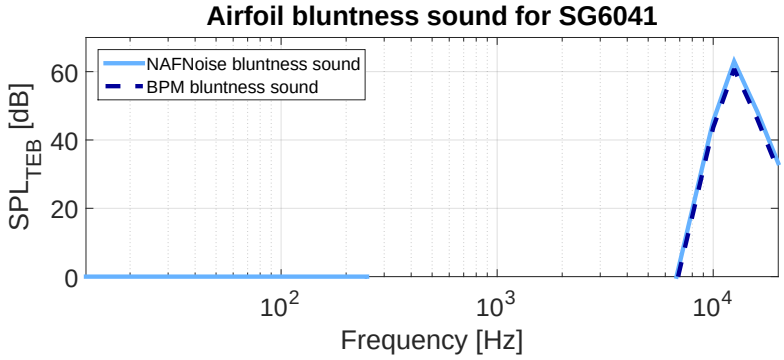

Figure 5.12: TEB noise verification between NAFNoise and Code

5.6.3 Verification LBL-VS Noise

The last noise source that can be verified with NAFNoise is the LBL-VS noise. Results can be seen in Figure 5.13 and Figure D.3. It can be observed that the difference is much larger compared to the other verified noise sources. The main reason for this is that the LBL-VS noise depends on the boundary layer thickness. The problem is that programs such as Rfoil cannot calculate the BL thickness immediately. For this Green's

method is used which is explained in section 4.3.1. From this method is can be seen that the BL thickness is a function of shape factor, displacement thickness and momentum thickness which can be calculated with Xfoil or Rfoil. When there are discrepancies between H, δ^* and θ for NAFNoise and Rfoil, it will result that δ will even have a much larger discrepancy resulting in larger differences for the noise. Because it is not known what the settings are of Xfoil in NAFNoise, discrepancies arises between the developed BPM model and NAFNoise. However, the two lines follow the same trend and it can be concluded that the program does what it supposed to do. But one must be careful with the values calculated trough Xfoil or Rfoil.

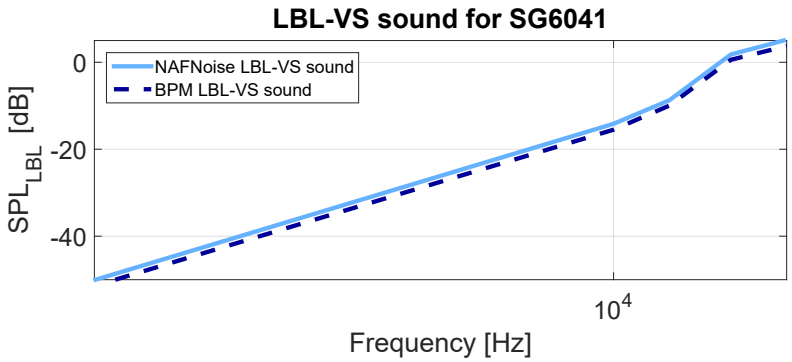

Figure 5.13: LBL-VS noise verification between NAFNoise and Code

Chapter 6

Atmospheric Attenuation Model

The methods for determining aeroacoustics noise from a wind turbine are discussed and this chapter will focus on the attenuation model. This model is created such that it is possible to calculate what the SPL would be at a receiver location in open atmosphere. The model developed is based on the Nord2000 program that is developed by DELTA [11, 12]. The model that is developed here has six main simplifications.

- The KCU and kite are stationary.
- The wind turbine has a omnidirectional noise spreading.
- The ground material is constant trough this work. It is assumed that it is grass.
- There is looked only in 2D case since 3D complicates the noise propagation significant.
- Temperature gradient is not considered wind gradient is.
- It is assumed that the speed of sound varies linearly with height.

The model developed here is based on the general ray theory which assumes that from the source the sound travels in a collection of rays. The first loss discussed is the spherical spreading loss which will be the major loss source for the wind turbine. Second, the atmosphere will convert some of the pressure fluctuations into heat. This is called atmospheric absorption. The last attenuation source is the reflection. reflection is the "bouncing" of the ray on the ground which reflects it to the receiver increasing or decreasing depending on the frequency of the sound. The reflection depends on the location of the source and receiver, the type of the ground and the wind speed at hub height, or this case KCU height. The kite is most of the time above 100 meters height this will have as effect that the wind will have an influence on noise received at a location. The wind will bend the straight rays, which causes that the reflection model must be adapted for this.

The equation to determine the noise at a given location can be seen in Equation 6.1. The losses will be calculated for a 1/3-octave frequency band.

$$SPL_{x,y} = L_w - \underbrace{20\log_{10}(r) - 11}_{1} - \underbrace{A_{abs}}_{2} - \underbrace{A_r}_{3} \tag{6.1}$$

where, the first part on the right-hand side is the loss due to spherical spreading, the second term is the loss because of atmospheric absorption and the last is the attenuation due to refraction which includes the wind. L_w is the sound power level of the noise source at different frequency band. From the BPM the SPL is calculated 1 meter behind the rotor, which can be converted to sound power level.

6.1 Spherical Spreading

The first assumption made to simplify the model is that the source its directivity pattern is omni-directional. This assumption can be made since the rotor can face any direction during flight and the worst-case scenario is of interest. Due to this assumption, we can state that the directivity does not matter. If a source is omnidirectional it will spread spherical and this loss does not depend on frequency. The next assumption is that the

sound intensity level will stay constant over time. The sound will spread spherical and the sound power over the surface of the sphere will decrease if it is moving further away from the source. This will result that the SPL will decrease, since the sound power will be spread over a bigger surface, and this is visualised by Figure 6.1. The first step is to determine the spreading loss and this equal to Equation 6.2.

$$\Delta SPL_{spreading} = 20\log_{10}(r) - 11 \tag{6.2}$$

The 11 in above equation is due to the conversion from sound power level to SPL. A graphical representation of the spreading loss can be seen in Figure 6.1. Here it is clear that the power from the source is distributed over a larger area resulting in lower SPL at the location. This loss is independent of the frequency

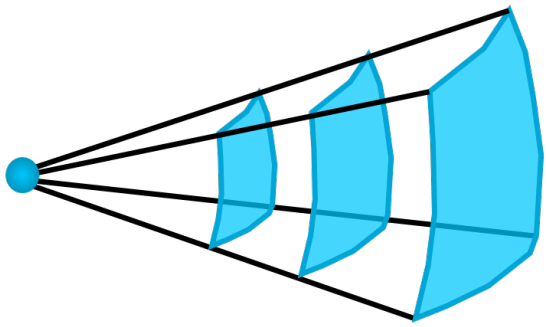

Figure 6.1: Spherical spreading of a monopole noise source

6.2 Atmospheric Absorption

The sound will be dissipated in the air by two mechanisms. The first is due to friction between air parcels resulting in heat transformation, which is a cause for SPL loss [1, 11, 59]. The second loss is a relaxation process. A sound wave will hit an air molecule, which will absorb part of the energy and release it with a small-time delay which might interfere with the signal. The atmospheric absorption can be calculated with the Equation 6.3.

$$A_{Abs} = \alpha_{abs} r/100 \tag{6.3}$$

where, α is the absorption coefficient in dB/100m and r is the travelled distance. The absorption coefficient depends on humidity, frequency, and temperature. A good explanation can be found in ISO 9613 [59]. The atmospheric effect is an effective noise reducer for high frequency since for higher frequencies the energy levels are lower, meaning that it is easier converted into heat.

6.3 Reflection and Wind

The sound is transmitted from the source in all directions, to explain reflection first it is assumed that the wind does not have any effect. Assuming the noise leaving the source travels in ray the general ray theory can be used. From the source, exactly one ray will arrive in a straight direction to the receiver. However, (assuming no obstacles) there is one extra ray that will bounce off the ground and be scattered to the receiver. This is what reflection means, it is the bouncing of the sound against the ground and being scattered to the receiver. The reflected sound will arrive there with a time delay since it will have a longer travelling path. Depending on the frequency the reflected noise will increase the noise received (in the case of harmonic excitation) or have a destructive characteristic if the phase is shifted too much compared to the direct signal [11].

Next assuming there is a wind gradient the reflected sound will behave differently. When the sound ray is travelling with the wind it will travel faster, while when it is travelling against the wind it will take a longer time to reach the receiver. To take the wind into account one cannot assume that the sound travels straight to

the receiver. It will travel by curved rays which can be seen in Figure 6.2. Delta [12] developed a model that is used to take this curved ray model into account. It is assumed that the sound varies linearly with height (this is for simplification reasons) where the speed of sound can be determined with Equation 6.4.

$$c(z) = c(0) + \frac{\Delta c}{\Delta z} z \tag{6.4}$$

where, $\frac{\Delta c}{\Delta z} = \xi$ is the sound speed gradient. There are two cases the first where $\xi > 0$ this will result in downward reflection while when $\xi < 0$ it will result in upward reflection. A clear example of the two cases can be seen in Figure 6.2. The first step is to determine the distance between the source and the refraction location

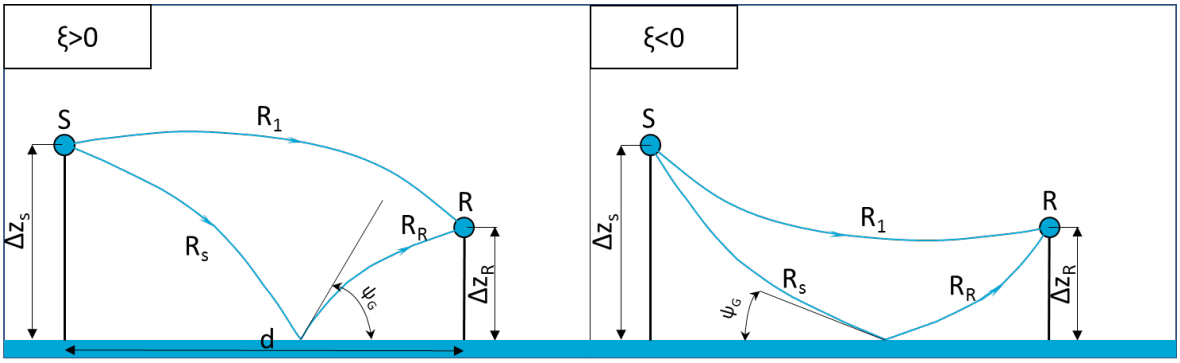

Figure 6.2: Reflection of a noise signal including effect of wind, adapted from DELTA manual [11, 12]

with the ground. A good explanation is given in the Delta Manual [11, 12]. Next the curve of the ray must be determined for three cases. From source to receiver, from receiver to ground and ground to receiver. The total attenuation due to refraction and wind can be calculated with Equation 6.5.

$$A_r = 20\log_{10}\left|1 + \frac{R_1}{R_2} Q(\Psi_G, \tau_2)\, e^{j\omega(\tau_2 - \tau_1)}\right| \tag{6.5}$$

In this equation, R_1 is the distance travelled from source to receiver, τ_1 is the time travelled. While R_2 is the total distance travelled of the reflected ray (Source -> Ground -> Receiver), with τ_2 the total time travelled of this signal. Ψ_G is the grazing angle which defines the angle of incidence of the sound ray and the ground (same as the light that hits a mirror). ω is the angular frequency which is defined as $2\pi f$. Last, there is Q which is the spherical reflection coefficient. Q self is a function of acoustic ground impedance, which is a quantity on how good a sound ray is bounced or absorbed by a certain material. A complete explanation of how to calculate Q and acoustic impedance is given in the first DELTA manual [11].

6.4 Location of Interest

Looking at the Netherlands regulations are strict and it is known that the noise level SPL_{den} cannot be higher than 47 dB [46]. SPL_{den} depends on the noise during the day, and for the evening and night different noise is added because the people are calmer during these periods, and might the perceive the noise more intense. The equation to calculate the SPL_{den} can be found in Equation 6.6 [46]. Here it can be seen that for the evening 5 dB is added and for the night 10 dB extra is considered.

$$SPL_{den} = 10 \cdot \log_{10}\left(\frac{12 \cdot 10^{\frac{OSPL_{day}}{10}} + 4 \cdot 10^{\frac{OSPL_{day}+5}{10}} + 8 \cdot 10^{\frac{OSPL_{day}+10}{10}}}{24}\right) \tag{6.6}$$

where OSLP is the overall SPL and it is assumed that for a day, night and evening the same SPL is used that is calculated trough BPM which is coupled to BEMT to calculate the local conditions of the wind turbine rotor. The rule is that SPL_{den} must be lower than 47 dB at a sound sensitive location such as a residential area. Because of this, the sound will be calculated at three locations:

1. Ground station

2. Right under the kite
3. Residential area

It will be assumed that the kite is stationary and the is tether reeled out for 400 m, and is at an elevation angle of 20°. It is assumed that the residential area is 100 meters away from the projection of the kite on the ground. A visual representation of the locations can be seen in Figure 6.3. The goal is that the SPL_{den} is below 47 dB at the residential area.

It is known that the locations are the ground station and the residential area. Assuming a wind speed of 7 m/s at 10 meters height in the direction of the residential area, with soft grass as uniform ground one can see the losses at the two locations in Figure 6.4. It can be seen in Figure 6.4a that for the ground station bigger spreading losses are present due to the larger distance between the source and the receiver. In Figure 6.4b the atmospheric absorption can be seen, and it is noted that the higher frequency ranges are sensitive to this loss. The reason is that it is easier dissipated and is much more sensitive to the relaxation phenomenon. Last, the reflection and influence of the wind can be seen in Figure 6.4c. For some frequencies, the reflection will increase the SPL at a location while for the other frequencies it will decrease. This is only possible when the time delay between refracted and straight noise is just right such that the refracted frequency will be in phase with the direct ray, thus increasing the received sound.

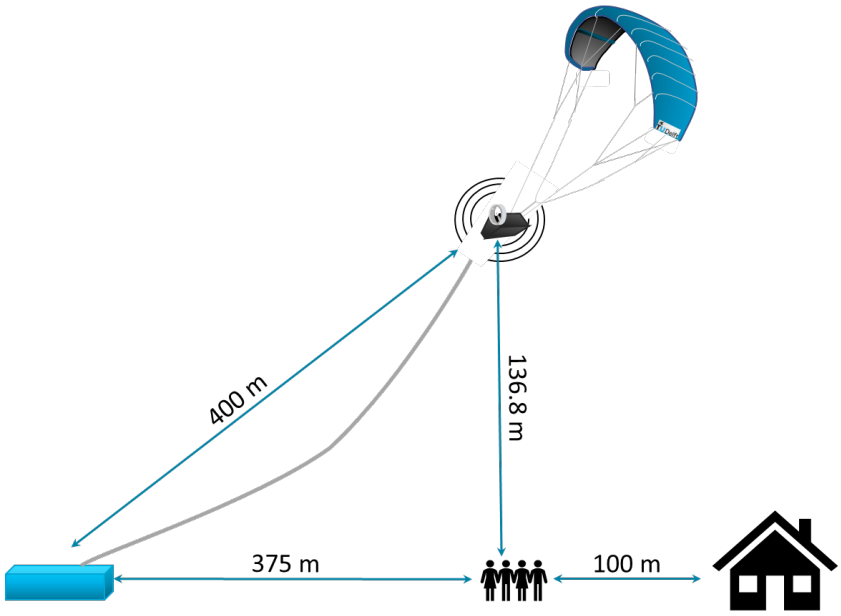

Figure 6.3: Locations of interest

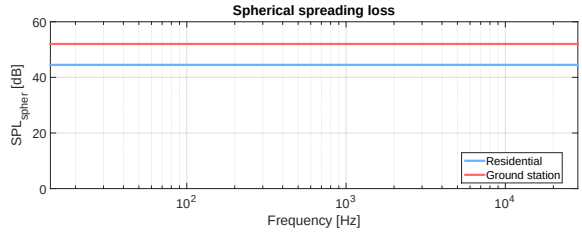

(a) Spherical spreading loss

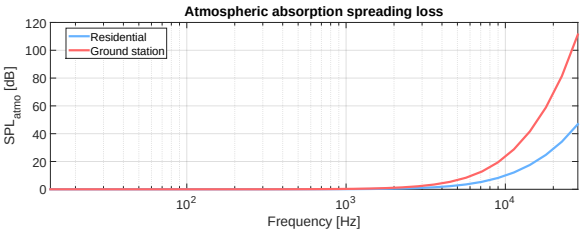

(b) Atmospheric absorption losses

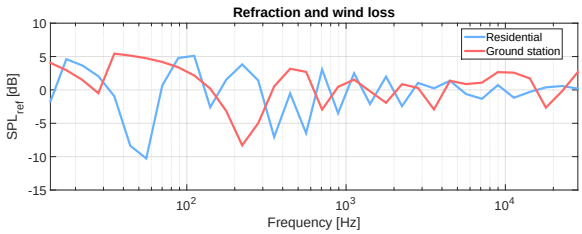

(c) Refraction losses

Figure 6.4: Attenuation losses for two different location: grounds station and residential area

III

Results and Discussion

Chapter 7

Wind Turbine Design

Before the experimental campaign starts two designs are developed. These designs are developed with the help of a brute force optimiser because of its simplicity. From the optimiser, a design will be generated which is verified with BEMT and the noise is calculated at optimum TSR. The two designs generated have different input conditions. The first has as input that the maximum thickness should be 4 mm and the second design considers the shroud. At the end, the most appropriate manufacturing method is chosen and it is explained how the test set-up is built.

7.1 Optimiser

The main requirement for the wind turbine is to have minimum drag and weight. If this is achieved the total power produced by the AWE system will be maximised. The drag will increase quadratic with the wind speed, while the weight of the wind turbine is constant, this means that the drag will be the critical factor that needs to be optimised. A brute force optimisation is chosen because of its ease of implementation. This was done for its ease to be implemented. A brute force optimiser is an optimisation algorithm that is the least efficient of all. It means that all possible options are tested and that the best result is taken as the final design. This means that the optimiser is only as accurate as the number of designs tested, so it can never be concluded that it is really the lowest drag design.

The goal of the optimiser is to minimise the drag of the wind turbine. The drag depends on velocity, swept area, air density and thrust coefficient. From all these variables, only two depend on the rotor layout, these are the swept area A, and thrust coefficient C_T. When $C_T \cdot A$ is minimal the wind turbine corresponding to this value is the final design.

All optimisers work based on a set of boundaries on which designs are approved or rejected. There are three main boundaries. The first one is the power that needs to be produced, this is a key requirement set by Kitepower BV. The minimum electrical power needed is 44 Watt. The two other boundaries are torque and RPM which depend on the specifications of the generator. The alternator chosen is the EC32 80 Watt from Maxon motors [47]. The main difficulty with this alternator is that its initial purpose is to be used as a motor. Due to this only a data sheet is available when the alternator is operated as a motor. This resulted in choosing the two other boundaries based on the motor data sheet. The minimum and maximum RPM and torque can be seen in Table 7.1. The problem with the generator is that the generator efficiency is unknown and for this reason, it is assumed that the efficiency is 60%.

Table 7.1: Boundaries

	minimum	maximum
Electrical power [Watt]	44	50
RPM	0	25000
Torque [Nm]	0	150

The brute force optimiser will optimise parameters that are of importance for a wind turbine. The follow-

ing parameters will change until an optimised design is obtained: airfoils, the diameter of the rotor and RPM. From the RPM and diameter, the TSR can be calculated. To choose the number of blades there is a strong correlation between TSR and the blades. The relation between TSR and blades can be seen in Table 7.2 [5].

Table 7.2: Relation between TSR and number of blades [5]

λ_{min}	λ_{max}	Number of blades
0	1	5
1	4	4
4	8	3
8	20	2

The chosen optimiser is not advised if there are many variables that must be changed. If enough computational power available and the system is not too complicated it is feasible to use this method effectively. The optimiser chosen here will loop over the airfoils, the diameters, and different rotational speeds. If a new airfoil is chosen the lift and drag polar are calculated by assuming the Reynold number to be 6.4e4 and M=0.16. These numbers are based on initial runs from earlier designs created without the optimiser. This was chosen such that the optimiser does not have to run Rfoil for every design. Going one step further in the loop the diameter is chosen. In the next nested loop a design RPM is picked. The RPM can be converted to TSR. From the TSR the corresponding number of blades can be determined with Table 7.2. From the diameter, TSR, number of blades, and lift and drag polar an initial design can be set up. The initial design will be created by assuming optimal axial induction factor of 1/3, the twist is calculated with Equation 7.1 and the chord is calculated with Equation 7.2 [60]. If an induction of 1/3 is assumed for the initial blade design the blade power will exceeds the required power. If the first blade lay-out is known, BEMT can calculate the power and drag produced by the wind turbine. It was noticed that the BEMT has low computational time, while Rfoil requires more time. When the initial design is ready the optimisation can start by only varying the chord. The twist is kept constant and it is assumed that the Re change does not have significant effect on the airfoil performance. If the chord is changed the BEMT recalculates the performance of the new design to see if this performs better and meets all constraints. If it does it is stored as the new optimum blade. The chord is always decreased by a factor of 0.95 compared to the previous design. This is done 50 times unless no improvement is noticed or the power is lower than the required power, in that case a new design RPM is chosen. If the inner loop for the rotational speed is finished, a new diameter is chosen and the inner loop is performed again. This is done until all diameter and airfoils are tested. The working of all the nested loops can be seen in the flowchart in Figure A.4.

$$\theta = \frac{2}{3}\tan^{-1}\left(\frac{R}{r\cdot\lambda}\right) - \alpha_{L/D=max} \tag{7.1}$$

$$c = \frac{16\pi}{B}\frac{r}{C_{l_{LD=max}}}\sin^2\left(\frac{1}{3}\tan^{-1}\left(\frac{R}{r\cdot\lambda}\right)\right) \tag{7.2}$$

7.2 Designs

The objective of this thesis is to design a rotor that will produce sufficient electrical energy. This will be achieved by first designing two rotors and after validation, a final design will be created. However, as mentioned before a design is needed that generates 44 Watt electrical power which equals 73.5 Watt of mechanical power, assuming a generator efficiency of 60%. The second design will take the shroud into account. For the initial design, it is assumed that the power will decrease by 20%, if the wind turbine's shroud is mounted. Considering the shroud, the second design will need to produce at least 88 Watt of mechanical power. The blades will be 3D printed and because of this, an extra boundary is introduced for the first design. For the first design, a minimum root thickness is imposed of 4 mm to ensure structural strength. It is chosen to use one airfoil over the blade span. The airfoils considered for design can be seen in Table 7.3.

For both rotors, a standard hub and interchangeable blades are chosen. To ensure that the structure would not fail the hub diameter is chosen to be 5 cm. More information on the manufacturing methods used can be found in section 7.3.

Table 7.3: Airfoils used in simulation

SG6043	SG6042	sD7003
SD2083	SD2030	E392
E387	S1223	SG6041
FX63137	NACA0012	S826
D2030	SD2083	SD5060
NACA4418	E61	SA7035

7.2.1 First Optimised Design

For the first design, it was assumed that the minimum mechanical power should be 73.5 Watt (44/0.6), and a root thickness of at least 4 mm for structural strength. Using this as inputs for the optimiser the design proposed would be a 4-bladed rotor with a diameter of 15 cm. The airfoil chosen is an NACA4418 across the whole span. The design TSR is 1.846 for a wind speed of 30 m/s. It has a rated power of 73.53 Watt and a drag of 3.94 N at 30 m/s. The drag mentioned here consist of only the blade drag. The blade lay-out can be seen in Figure 7.1. The length of the blades is 5 cm. The root twist angle is 36.5° and the tip twist angle is 16.7°. The airfoil proposed by the optimiser is a thick airfoil. The NACA4418 is proposed due to the root thickness requirement of 4 mm. However, the NACA4418 is an airfoil that is normally not considered for small wind turbines, due to its poor performance for low Re numbers.

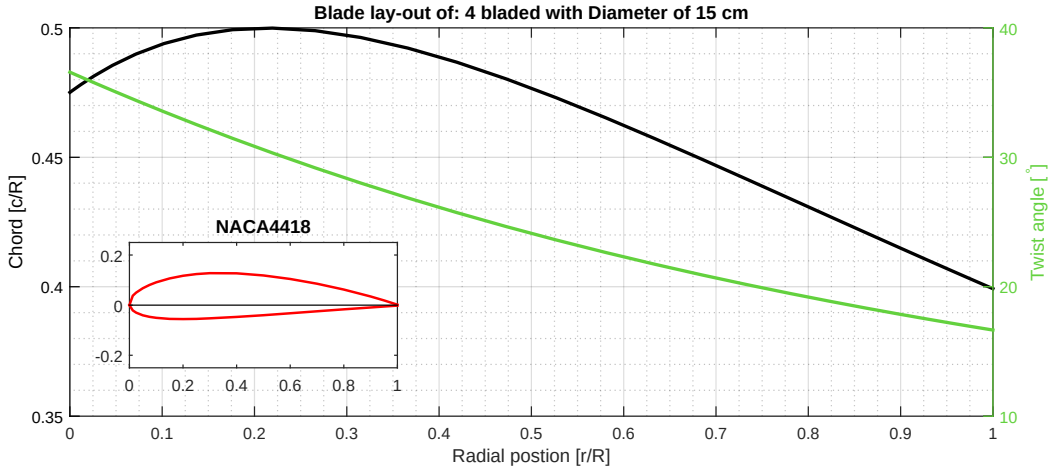

Figure 7.1: NACA4418 rotor from optimiser 4 bladed rotor

The initial design is ready and a verification of the design is performed. The performance of the blade can be calculated with BEMT for different wind speeds and TSR. The main difference between BEMT and optimiser is that BEMT calculates the airfoil performance for each section, thus considering the variation in Re number along with the span. After the performance is determined the difference between the optimiser and BEMT will be quantified. The optimum TSR will differ because of the assumption made by the optimiser to not vary the lift drag polar for different Reynolds numbers, together with the assumption of an ideal blade. The results for the NACA optimised blade can be seen in Figure 7.2. In this figure, the performance can be observed for following wind speeds: 10, 15, 20 and 30 m/s. It is observed that for 30 m/s the optimum TSR is shifted to 2, while the optimiser assumed it to be 1.846. It can be stated that the optimum TSR does not change much. The reason why the optimum TSR is higher according to BEMT is due to the assumptions made by the optimiser. The optimiser assumes that the optimum TSR does not shift after the optimum design is proposed. However, this is not the case as was just showed by the verification of the blade design. The power at the optimum TSR for 30 m/s is 83.00 Watt which is 10 Watts more than the 73.5 Watt predicted. The drag of the blades is 4.26 N at 30 m/s according to BEMT while the optimiser predicted a C_T of 0.4049 which is 3.944 N. This is a difference of 8% which is acceptable for all the simplifications made. The main difference is due to the assumption made that the airfoil performance does not change with Reynolds number, and the assumption that the optimum TSR does not change after the optimum design calculation. It can

be concluded that the optimiser works but caution is advised when interpreting the results (the optimiser is verified in section B.4). It is advised to do a full BEMT simulation after the optimiser determines a blade. It is observed for the BEMT result at 10 m/s a small discrepancy is present for a TSR of 1 and 1.2. It was found that this is a numerical unsteadiness in the code. The reason for this is an error in the airfoil data which is due to the linear cut-off in the Kirke extrapolation. This linear cut-off is to bridge the Rfoil data and Kirke's post stall polar.

The BEMT calculates the performance of the wind turbine for different wind speeds. It can be seen that the $C_{P_{max}}$ varies significantly between the different wind speeds. The C_P drops from 0.2840 at 30 m/s to 0.2157 at 10 m/s. This is a big difference and the reason for this is due to the bad performance of the NACA4418 at low Reynolds numbers. Similar behaviour can be seen for the drag of the wind turbine. The C_T at TSR_{opt} varies from 0.4342 for 30 m/s to 0.3757 for 10 m/s.

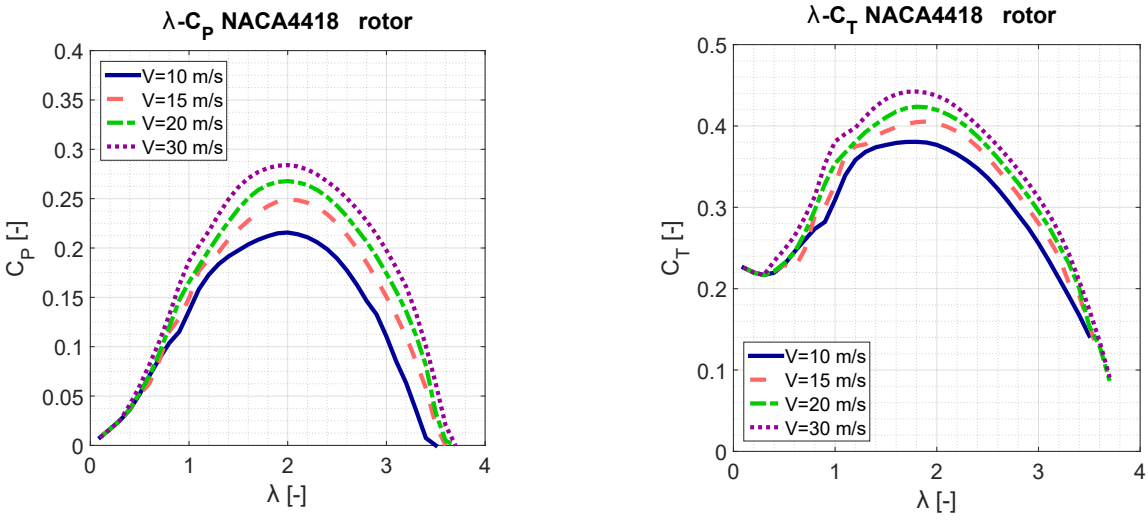

(a) C_P curve for NACA4418

(b) C_T curve for NACA4418

Figure 7.2: Power coefficient and thrust coefficient BEMT calculations for NACA4418

The given blades will also generate broadband noise. It is of interest to know the noise levels at 30 m/s for optimum TSR which is 2 for different octave frequencies. In Figure 7.3 the SPL can be seen with all the individual noise sources. For this simulation, it is assumed that the TE thickness is 0.7 mm due to the limitations of the 3D printer. It can be seen that because of this the TE bluntness noise is dominant together with the TBL separation. The reason why S-S noise is dominant is due to the NACA4418 thick characteristic. These thick airfoils will have a large displacement thickness increasing this noise source significant. All the main noise sources are located in the high-frequency range due to the small chord and the high speeds over the blade. The TIN noise is the dominant noise source for the lower frequencies, this is due to the small chord and the larger eddies.

It was found that the power from the optimiser would be lower than what was predicted with BEMT. Similar behaviour was found with the rotor drag. The optimum TSR from the optimiser is close to the optimum TSR according to the BEMT which support the assumption that the twist needs to be kept constant during optimisation and that the assumed Re and Mach number can be used. The small difference is because of the assumptions made.

7.2.2 Second Optimised Design

The second optimisation was performed to include the shroud this resulted in an increase of 20% extra power with respect to the previous design. This value was established by previous measurements done for Kitepower BV [61]. The minimum mechanical power necessary is 88 Watt. In this design solution, no minimum thickness was imposed. From the optimiser, it followed that a 4-bladed rotor with a diameter of 16.5 cm is pro-

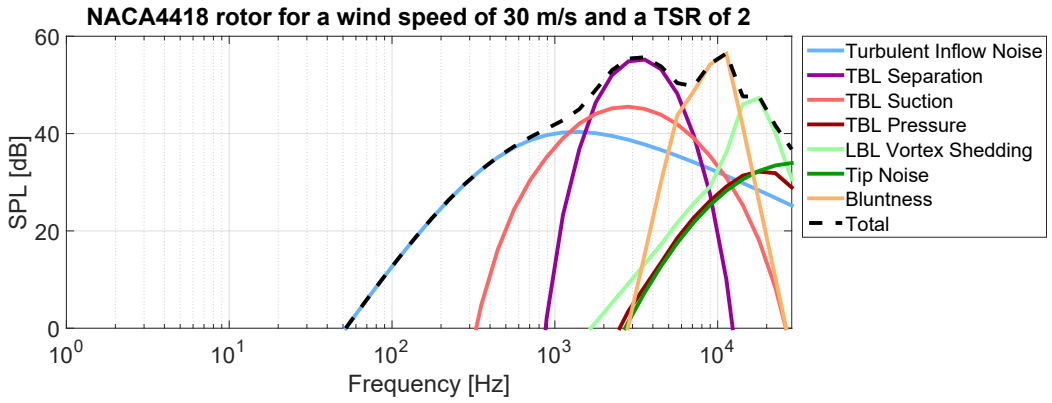

Figure 7.3: NACA4418 rotor airfoil self-noise for a wind speed of 30 m/s at an optimum TSR of 2

posed. Again, a single airfoil was chosen, and the SG6041 is selected by the optimiser, which is designed for small wind turbines. This airfoil has a maximum thickness of 10% at 34.9% of the chord and a max camber of 1.6% at 49.7% of the chord. It is a typical small wind turbine airfoil with high L/D. In Figure 7.4 the blade lay-out can be seen and in Table B.4 the numerical blade lay-out can be seen. The blade has a root twist of 34° and a tip twist of 12.59°. The chord changes from 3.09 cm at the root to 2.135 cm at the tip, meaning that the blade is not slender, which is commonly seen in large wind turbines. It is as expected that the NACA4418 is not chosen anymore due to the poor aerodynamic performance, a more slender profile such as SG6041 is chosen which has better performance for lower Reynolds numbers.

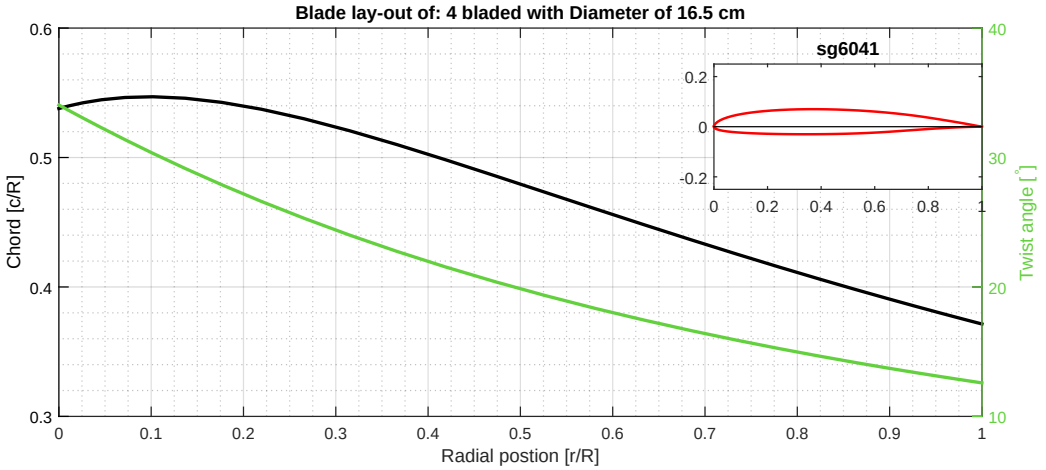

Figure 7.4: Blade layout of the SG6041 4 bladed rotor

The BEMT simulated the performance for different wind speeds and it is noticed that for the 30 m/s results in Figure 7.5a the power coefficient is 0.3553 for a TSR of 2.4. The optimiser predicted that the optimum TSR is around 2.01 with a C_P of 0.27. The TSR max is predicted with a large discrepancy and again the $C_{P_{max}}$ is significantly underpredicted. The reason for this is, the assumption made that the lift and drag polar is not affected by Re number changes. This problem will be solved in the final design and is discussed in section 8.4. The optimiser calculated that the drag would be equal to 5.1474 N for 30 m/s while according to BEMT it would be 6.29 N. This is a difference of 19% which is not acceptable. It was found that the drag is still the lowest compared to other designs from the optimiser, but there is a necessity to calculate the full performance and do a second check with BEMT. In section B.4 it can be seen that it is indeed true that the optimiser gives the lowest drag design of the tested blades.

From Figure 7.2a it is noticed that the C_P decreases significantly for different wind speeds. This is not the case for the SG6041 rotor for which the $C_{P_{max}}$ varies from 0.3553 till 0.3291 for 10 m/s. This confirms that it is better to choose appropriate airfoils that are designed for these low Re numbers. The C_T for the 30 m/s case

is 0.534 and this will result in a drag of 6.29 N. It was found that the C_T does not change much compared to the different wind speeds. The operational range of the wind turbine is between a TSR of 0 and 4.5.

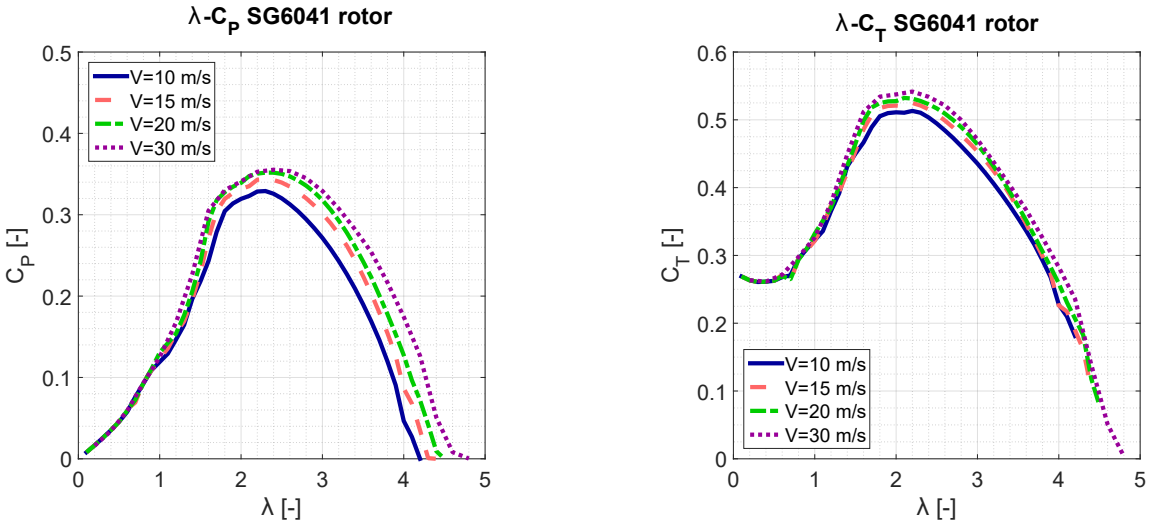

(a) C_P curve

(b) C_T curve

Figure 7.5: power coefficient and thrust coefficient BEMT calculations for SG6041

The same analysis was performed as was done for the NACA rotor for the noise. The BPM simulated the noise levels at an inflow speed of 30 m/s for a TSR of 2.4. Like the NACA the TE bluntness noise is the dominant noise source together with the separation noise. The reason why the bluntness noise is higher than the NACA profile is due to the reason that the ratio between the displacement thickness and TE height is higher than for the NACA case. The laminar vortex shedding noise will create a small peak just outside the audible range. This is because the flow over the thin airfoil, in general, will be more laminar compared to thick airfoils. The TBL on the suction side is higher that on the pressure side which is due to the positive angle of attack which results in the flow being pushed towards the pressure side which makes it more difficult to separate. The other dominant noise source is the S-S noise. The reason why it is such a dominant source is because the BPM is a semi-empirical model that is based on the NACA0012 airfoil. Which behaves differently in low Re flows than a SG6041. Also for low, Re number flows the displacement thickness will be larger than for higher Re number cases.

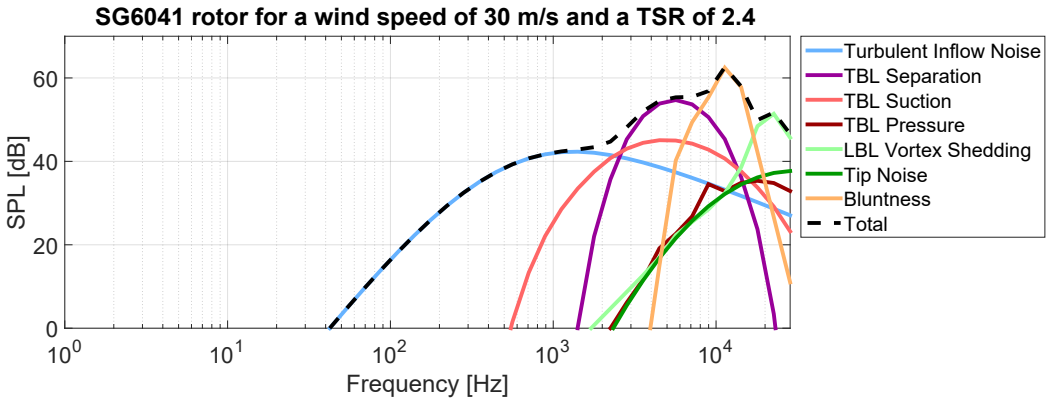

Figure 7.6: SG6041 rotor airfoil self-noise for a wind speed of 30 m/s

7.3 Manufacturing

The two designs discussed have to be manufactured. It was mentioned that a central hub will be used, where different blades can be inserted in. The hub was made from aluminium and was milled with a CNC machine. The hub can be seen in Figure 7.7 and it has a diameter of 5 cm. The reason that it is so big is that the connection type could be big enough to withstand the induced forces. The connection type chosen is a dovetail so that it is easy to attach different blades. The second reason why a dovetail is chosen is for its self-locking capabilities due to the centrifugal forces.
The Blades were created in SolidWorks with their receptive airfoil. Three production methods are considered

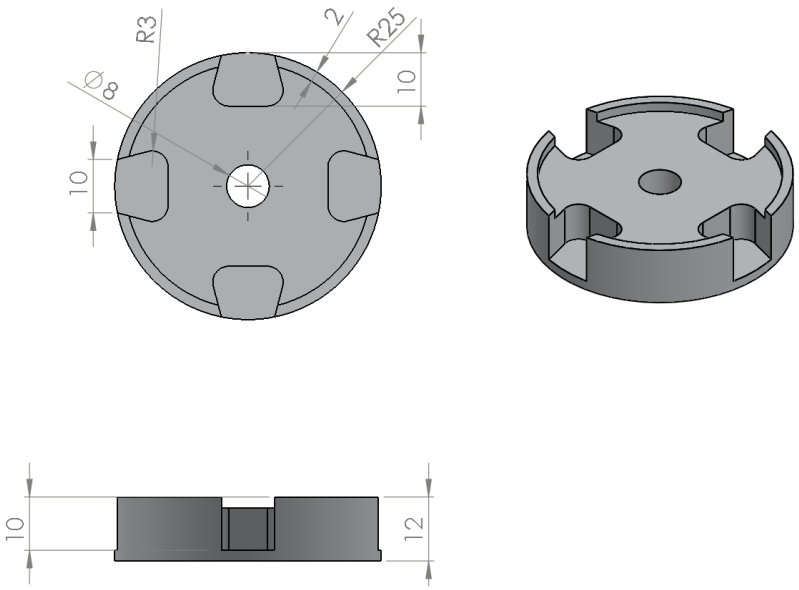

Figure 7.7: Hub for 4 blades

to manufacture the blades:

- CNC machining in aluminium
- Hand lay-up glass fibre/carbon fibre
- 3D printing

Hand lay-up was quickly omitted as a manufacturing method since it would be costly to build and, it would be the most sensitive to manufacturing errors. The reason why it would be expensive is because of the reason that for every design a double-sided mould had to be manufactured and, that the blades are thin compared to the dovetail connection which would create an extra manufacturing challenge. Creating the blades out of aluminium would be possible but expensive for each blade. A small milling cutter would need to be used due to the complicated shape. If a small milling bit is used the feeding rate of the machine would be slow and it would take a considerable time to create 8 blades. Which would raise the man hour cost. From mentioned points, it was decided to not use CNC milling or glass/carbon fibre hand lay-up mainly to suppress the cost of the project.

The advantage of 3D printing is that it is ideal for prototyping since it is cheap and can handle complicated shapes. the manufacturing was outsourced to ShapeWays which is a 3D printing service offering different materials. The material chosen here was strong and flexible which is the company name for PA2200 and has a density of 0.45 g/cm^3. The minimum thickness is 0.7 mm (important for bluntness trailing edge noise). The strong flexible plastic is laser sintered to create the 3D product. The final finished product had the option to be smoothed by ceramic spheres. It was chosen to not do this since a certain roughness was desired to prevent laminar separation. The two different blades can be seen in Figure 7.8a. The full assembled rotor can be seen in Figure 7.8b

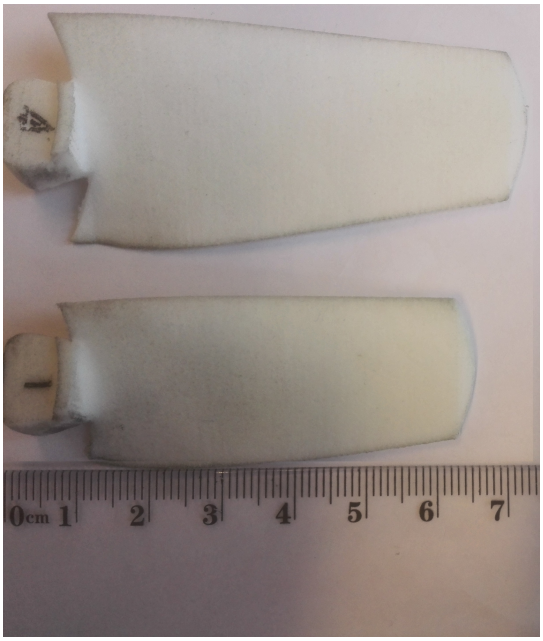

(a) 3D printed blades 1 is NACA4418 and 4 is SG6041

(b) Assembled rotor NACA4418

Figure 7.8: Manufactered rotors

7.3.1 Manufacturing of the Shroud

The wind turbine has a high rotational speed and this poses a threat of possibly cutting the bridle lines. For this reason, a cylindrical shroud made from aluminium was chosen to protect the bridle lines. The shroud was customised by Maxon Motors. Maxon motors chose that the shroud depth should be 5 cm to be sure there is enough protection for the bridle system. The space between blades and the inner side should be no more than 5 mm for safety reasons. The reason why the shroud was not made the same as the rotor diameter was because the vibrations induced in the shroud could hit the rotor blades and jeopardise the power production during testing. The shroud is manufactured by hand by rolling a sheet of aluminium into a cylindrical shape. The shroud is mounted with three connection points to the nacelle. Three connections were chosen to create a test set-up that relates as closely as possible to how to real flying wind turbine will look. In Figure 7.9b the shroud connection can be seen, two are connected to the nacelle and the bottom one is connected to the front connection rod.

7.3.2 Experimental Test Set-up

The last part that was manufactured is the test set-up to place in the wind tunnel. It is chosen to mount everything on a wooden base plate of 35 x 35 cm. The wind turbine is mounted on an acrylic disk which is able to turn 360°. Next, the nacelle is created from a 5 cm PVC pipe and in there the Maxon EC32 80 Watt generator is mounted. The generator has a 5 mm shaft while the hole of the hub is 8 mm. To solve this problem a collet adapter is used, this is a coupling part that is used in drones to converts the smaller generator shaft to the 8 mm shaft. The CAD design and built test set-up can be seen in Figure 7.9.

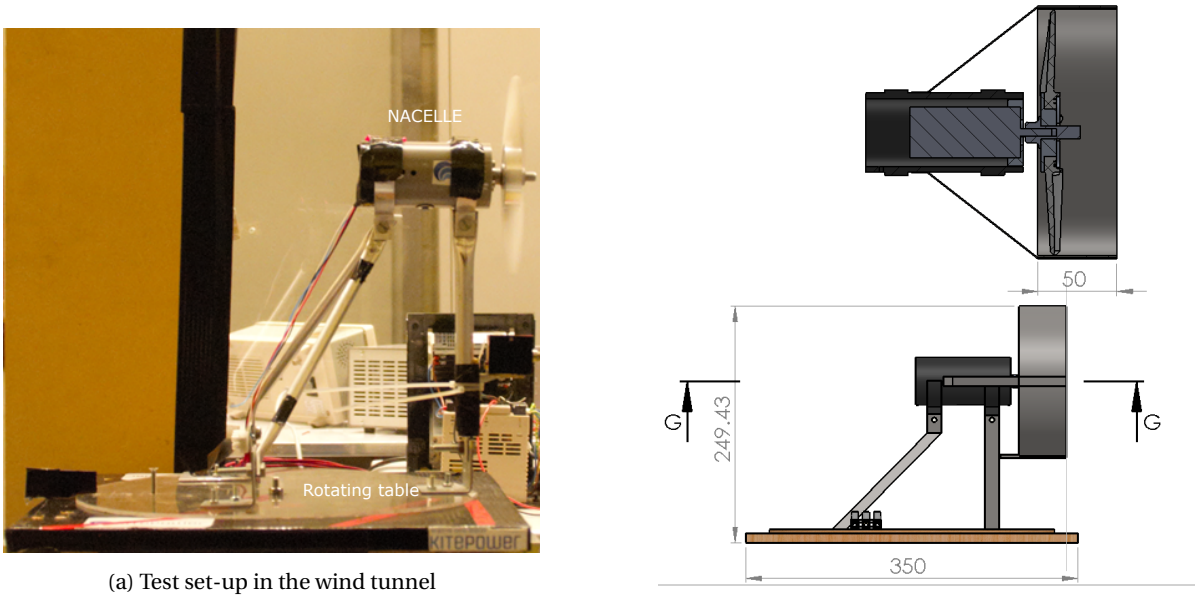

(a) Test set-up in the wind tunnel

(b) CAD version of test rotor plus shroud

Figure 7.9: Test set-up for in the wind tunnel

7.4 Inflow Angles

During the design of the wind turbine, it is assumed that there is a steady and straight inflow. However, during flight, this will not be the case. During the figure of eight and reel-out, the inflow angles will vary and this will affect the power of the wind turbine. First, it is looked what the inflow angles will be. A distinction is made between two angles, the first angle is the tilt angle which is defined as the angle in the vertical plane between the axis of rotation and the projected wind speed which can be seen in Figure 7.10 and is defined as ζ. The second angle is defined as Ψ which is the angle between V_{app} and $V_{app,xz}$. Kite dynamics is used to determine these two angles as well as the apparent wind speed.

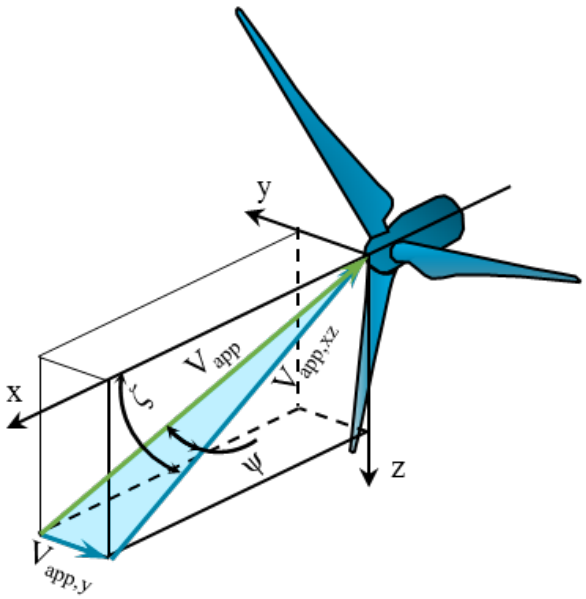

Figure 7.10: Wind turbine with apparent wind velocity

First, some assumptions need to be made, the first one is that the kite has no mass and there is no tether drag or mass considered. The kite is modeled as a point mass model to keep it so that it can be assumed that there is no slip angle. The ground wind speed is 7 m/s. It is assumed that the elevation angle is 20° and the tether length of 400 meters, which results in a wind speed of 10.15 m/s at the resulting height for a surface roughness scale of 0.03 meter which corresponds to grass. Next, it is assumed that the operating conditions are optimal so there is no tether force control. According to U.Fechner [13] it can be assumed that the kite is aligned in with the apparent wind speed. This means that Ψ is equal to zero and that the apparent wind speed is located in the xz-plane which can be seen in Figure 7.11. It is further assumed that there is no misalignment between the KCU and kite, meaning that the same coordinate system can be used for the kite and KCU.

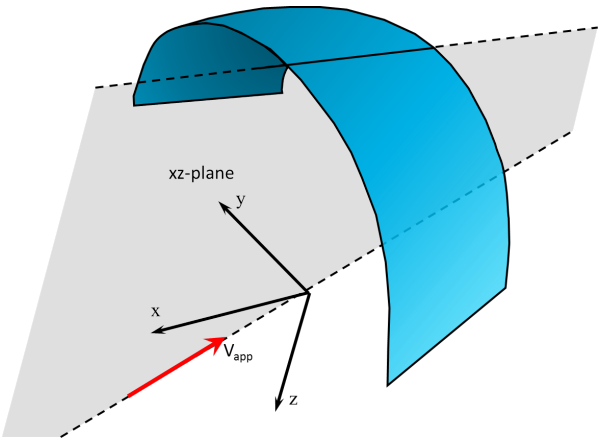

Figure 7.11: Reference frame of a point kite model, adapted from U.Fechner [13]

If the apparent wind speed is aligned in the xz-plane the only angle that is present is the inflow angle. The inflow angle can be determined with the component of $V_{app,xy}$ and $V_{app,r}$ which is the velocity component of the reel out speed and wind. A graphical representation can be seen in Figure 7.12.

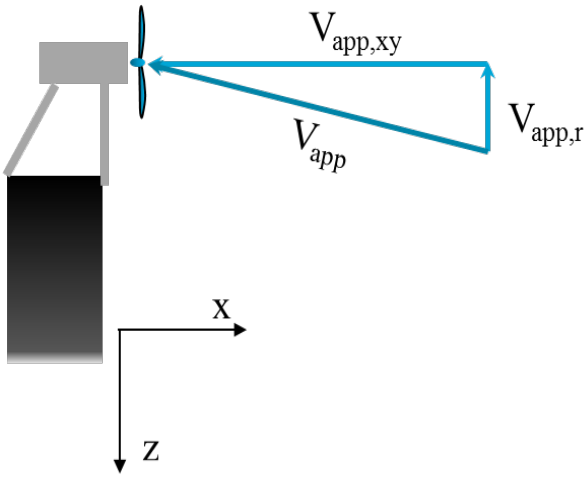

Figure 7.12: Side view from KCU with the individual velocity component visible

The angle is determined with Equation 7.3. The individual velocity component is determined with the equations of the airborne wind energy handbook [17].

$$\zeta = \tan^{-1}\left(\frac{V_{app,r}}{V_{app,xy}}\right) \tag{7.3}$$

The apparent wind velocity can be determined with Equation 7.4.

$$V_{app} = \begin{bmatrix} V_{app,r} \\ V_{app,\theta} \\ V_{app,\phi} \end{bmatrix} = \begin{bmatrix} \sin(\theta)\cos(\phi) - f \\ \cos(\theta)\cos(\phi) - \lambda\cos(\chi) \\ -\sin(\phi) - \lambda\sin(\chi) \end{bmatrix} \cdot V_w \tag{7.4}$$

where, λ is the tangential velocity factor, f is the reel out factor and ϕ, θ and χ are angles related to the position and heading. For maximum power extraction the radial component is 2/3 of the wind or $f = \frac{1}{3}\sin(\theta)\cos(\phi)$. The definition of the angles can be seen in the coordinate system in Figure 7.13.

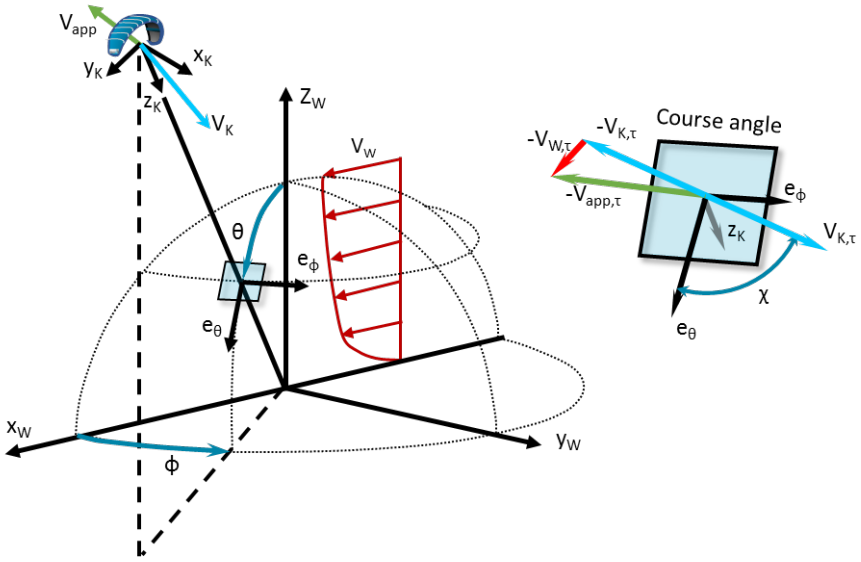

Figure 7.13: Coordinate frame of a point kite model, adapted from U.Fecner [13]

Assuming no mass, it is found that the kite apparent wind speed only depends on the L/D (λ is dependent on L/D) of the kite, location in the spherical reference frame, and wind speed. For this thesis, it is assumed that the kite has an L/D of 5. Because optimum conditions are assumed it can be stated that following requirement is valid.

$$\frac{V_{app,xy}}{V_{app,r}} = \frac{L}{D} = \frac{\sqrt{V_{app,\theta}^2 + V_{app,\phi}^2}}{V_{app,r}} \tag{7.5}$$

From this assuming that the L/D of the kite is 5 the tilt angle ζ will be constant trough flight and will be 11.31°. Now that the angle is known a simple solution could be to tilt the wind turbine with 11.31°, such that the inflow misalignment is minimised. But this depends mostly on the kite used and is only valid when the kite is without mass and a straight tether is assumed. This will not be the case and the apparent velocity will not be in the xz-plane anymore since there is always a small slip angle present, which could lead to larger deviations.

When these inflow angles change the performance of the wind turbine will change. The change in performance will be from inflow misalignment and the unsteady effect from the changing inflow angle. The unsteady effect will mainly be a delay in performance compared to the steady effect, while the inflow angle change will have a larger effect. When the inflow is not aligned one part of the blade will be further upstream. While the other part of the blade is more in downwind position, this can be seen in Figure 7.14a. The blade upwind will have a higher wind speed resulting in a larger load. This higher load will start pulling the blade even further in higher yaw angle. The wake will be skewed with an angle which is defined as χ. Due to the unsteady blade loading, the rotor will produce less power. The amount of power loss depends heavily on the rotor and is out of the scope of this thesis to determine. Energie onderzoeks Centrum Nederland (ECN) did a study for yawed inflow conditions for the MEXICO rotor at 15 m/s and a TSR of 6.7. The result of this can be seen in Figure 7.14b. Here it is observed that the performance can drop with more than 5% for a misalignment above 20°. Assuming that the misalignment due to kite is minimal and stays within 10° the effect will not be dominant. It is advised to investigate this further in further research.

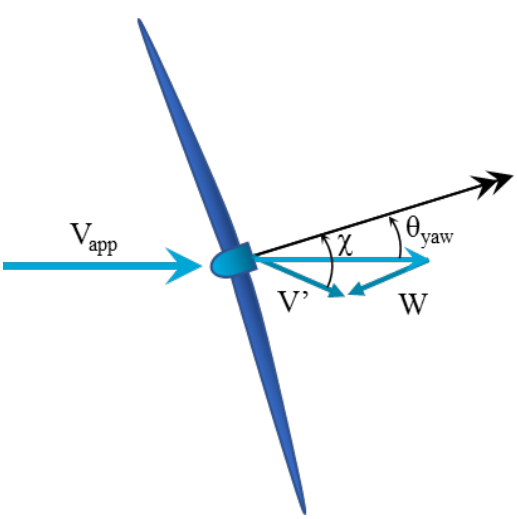

(a) Wind turbine in misaligned inflow

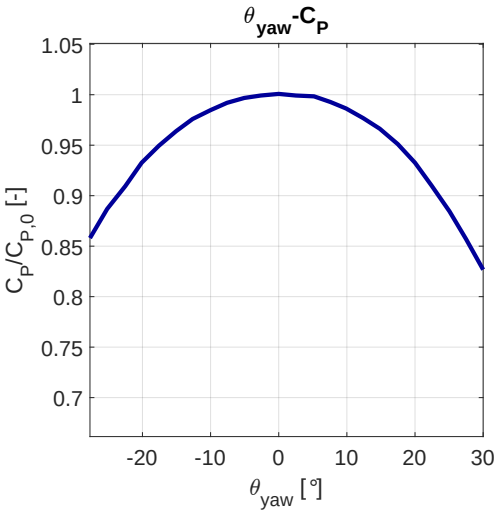

(b) MEXICO simulated result for different yaw angles, adapted from ECN [14]

Figure 7.14: Diagram of a yawed rotor and results according to ECN for MEXICO rotor in yawed conditions [14]

Chapter 8

Results

In this chapter, the results of the experimental campaign will be discussed. First, it is explained how everything is measured. Initially, electrical power was being monitored but due to heating problems of the generator, the Tinkerforge component and generator broke. Next, the results are discussed and the clean and shrouded case are compared. The data considered for comparison is the mechanical power, drag, and noise of the wind turbine. After this, the BEMT and BPM models are compared to the measured data. After performing the validation, a final design is created that complies with the requirements of Kitepower BV. The final design created will have a smaller hub diameter since there are no interchangeable blades anymore.

8.1 Experimental Set-Up

The designed rotors must be validated by an experimental campaign. The test is performed in the W-tunnel at the high-speed wind tunnel lab of Delft University of Technology. The W-tunnel has as specifications that the maximum wind speed is 35 m/s. It has a closed or open test section of 0.4 x 0.4 meter. The minimum turbulence intensity for this wind tunnel is 0.5% [62].

8.1.1 Test Set-Up

The wind turbine is mounted on top of a rotating disk such that it could simulate the flow coming from different directions, this is eventually not included in this thesis due to time constraints in the wind tunnel. The base plate is mounted on a balance which can monitor the forces in x, y and z directions. For this project, the drag in the flow direction (x-direction) is of interest. For measuring the noise a microphone of linearX is used that operates at a sampling frequency of 51200 Hz. The rotational speed can be monitored with three devices:

- RPM sensor: Measures the rotational frequency optical due to a reflection of a reflecting surface on the shaft.
- Oscilloscope: Measures the frequency between two electrical phases, which equals the rotational frequency of the generator.
- Microphone: The microphone will have clear tonal peaks at the rotational frequency and the harmonics of this frequency.

For Kitepower the electrical power is of interest and this is monitored using a Tinkerforge component. The component measures the current and voltage over the variable load and calculates the power by taking the product of the measured voltage and current. A problem arose during testing, the generator overheated, short-circuiting the Tinkerforge, and causing electrical problems across the whole system. The electrical problem is highly likely due to the melting of the isolation cables in the generator. This will result in a small short-circuit between two phases resulting in only one phase is providing the electrical power. This was noticed because of the decrease in power which was roughly one-third of what it used to produce. This resulted that the power was validated with the mechanical power, which is measured in an unconventional method. In Figure 8.1 the different components of the measurement set-up can be seen and, how everything is connected. The RPM sensor, the M51 microphone, and balance are connected to the desktop in the W-tunnel

and the laptop is connected to the TinkerForge component which logs the data of the electrical power. In Table 8.1 a quick summary is given what component is monitoring or logging which data. The RPM sensor is the only RPM sensor that can measure the rotational frequency over the time.

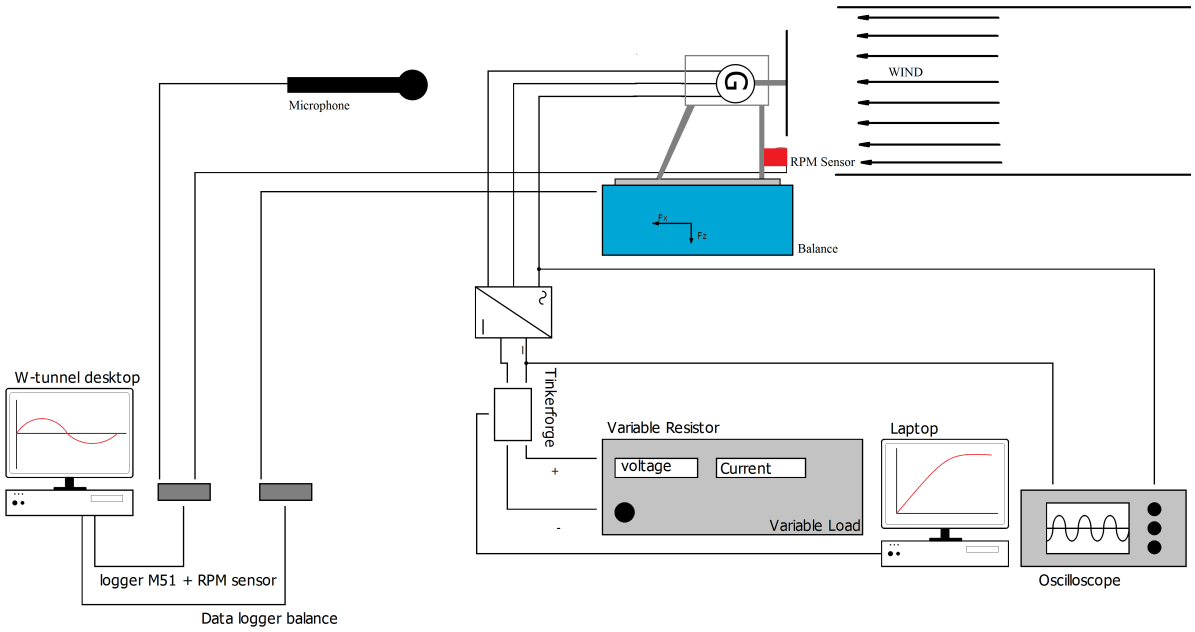

Figure 8.1: Electrical diagram with connections

Table 8.1: Measurement devices

	RPM	P_{elec}	Force	Noise
Tinkerforge		✓		
OJF balance			✓	
Tachosensor	✓			
Osciloscope	✓			
LinearX M51 microphone	✓			✓

Measuring the Mechanical Power

Mechanical power can be defined as the product of rotational speed and the torque. The angular speed can be determined with the microphone, oscilloscope or the RPM sensor. The problem during the experiments is the ability to accurately determine the torque. Torque is measured with a torque transducer, the problem, however, is that the rotors produce low torque, which results in the requirement of having an accurate transducer which is designed to measure in these range of torque values. These specialised sensors are expensive and therefore, an alternative method was used to determine the power. The method used is based on the principle that the torque for a rotating body can be expressed as the product of the mass moment of inertia and angular acceleration as can be seen in Equation 8.1 [63].

$$T = J \cdot \alpha = J \cdot \frac{d\Omega}{dt} \tag{8.1}$$

where, J is the mass moment of inertia, alpha is the angular acceleration which equals the time derivative of the angular speed. To determine the angular acceleration the RPM should be measured during the start-up of the rotor. This is done by preventing the rotor from turning while the wind turbine is settling to the right wind speed. Then the rotor is released such that it can spin up fast to it maximum RPM which is called free spinning speed. This experiment must be performed with no load on the wind turbine so that free spinning

speed can be reached. During the accelerating of the rotor, the angular speed is measured with the RPM sensor and microphone. When the RPM is stabilised, the oscilloscope is used as a validation of the other measurement devices. This procedure was performed for following wind speeds: 10, 15, 20 and 30 m/s, for the configuration without the shroud. For the shroud, the following wind speeds are used: 10, 15 and 20 m/s. This was done to prevent damage to the blades due to the vibration of the shroud. This vibration was induced due to the large blocking effect of the blades which can be considered large in chordwise direction.

The next step to determine the torque is to perform a polynomial fit on the RPM data. It was found by comparing the RMS error of different polynomials that, the best order of polynomial for high wind speeds is 12 and for lower wind speeds it is 10. An example of a polynomial fitted RPM signal can be seen in Figure 8.5. When the polynomial for the rotational frequency is determined, it is converted to angular speed. From the rotational speed, the angular acceleration can be calculated. This is done in Matlab by using the function *polyder()* which derives a polynomial function with respect to the variable, which in this case is time. The two functions that are determined, one for the angular acceleration and the other for angular speed can be multiplied with each other together with the mass moment of inertia to determine a function for the power that depends on time. The mass moment of inertia can be determined using a CAD program such as SolidWorks or Catia. In Figure 8.6 an example can be seen how the angular speed, torque, and power are evolving in time. It is observed that when the angular speed is at its maximum, the torque is at its minimal and the power is low. The signal obtained can be converted to a TSR-C_P curve. This is done by converting the angular speed to TSR ($\lambda = \frac{\Omega R}{V}$). The Power can be made non-dimensional to C_P with Equation 4.3b. The C_P and TSR are known at each time instant and from this, the TSR-C_P curve can be constructed.

Wind Turbine Drag Measurements

One of the main research objectives is to quantify the drag of the wind turbine. This is done by placing the wind turbine on top of a balance, which consists of a set of load cells. The balance is a 6-component balance meaning that it measures the force in three directions. The force in the x-direction is defined as the force in the wind direction and is the one of most importance for this project. The force of the wind turbine is measured for different wind speeds when the wind turbine is aligned with the flow (yawed inflow drag measurements were not possible due to time constraints in the wind tunnel). The procedure for each wind speed is to first test the drag of the wind turbine without the influence of the rotor, and then it is tested considering the blades. The drag is measured for different tip speed ratios. A variable load is seen in Figure 8.1 which will provide control over the rotational speed of the rotor. The variable load changes the current and voltage by changing an internal resistance, the lower the resistance in the load the slower the wind turbine will spin, this is because of the current flowing back to the generator creating a counteracting force increasing the torque necessary to turn the rotor. The drag measurement is performed when the rotational speed of the rotor is stabilised. The drag is measured for different speeds and tip speed ratios. The result can be seen in section 8.2. The drag is not measured for 30 m/s. The reason for this is that for the low TSR a significant amount of torque is required which creates an internal heat in the generator which caused a malfunction. It was found that the RPM could only be controlled till a certain lower boundary. This is because the TSR depends on the resistance of the total system. When the resistance of the load is low the TSR will be low. It was not possible to change the TSR if the load resistance is below a certain point (different for each test condition). A possible reason for this is that the blades might be in stall. However, a more likely reason for the loss of control is because of something else, the resistance of the whole system is not only from the variable load, the total resistance is the sum of the load resistance, the rectifying bridge its resistance, the wiring resistance and the internal generator resistance. From a certain point, the resistance is so small compared to the constant resistance that the influence of the load is minimal resulting in a constant TSR.

Before looking at the drag of the blades, the data from the clean case without blades and shroud is analysed. This is necessary so that the total drag measured can be converted to the drag of the blades. In Figure 8.2 the drag of the set-up can be seen without blades. The drag of the clean case is the highest and reaches 3 Newtons at a wind speed of 20 m/s. The drag of the SG6041 shroud is larger since the diameter is bigger than the diameter of the NACA. Though both drag curves are similar to each other as can be observed in Figure 8.2.

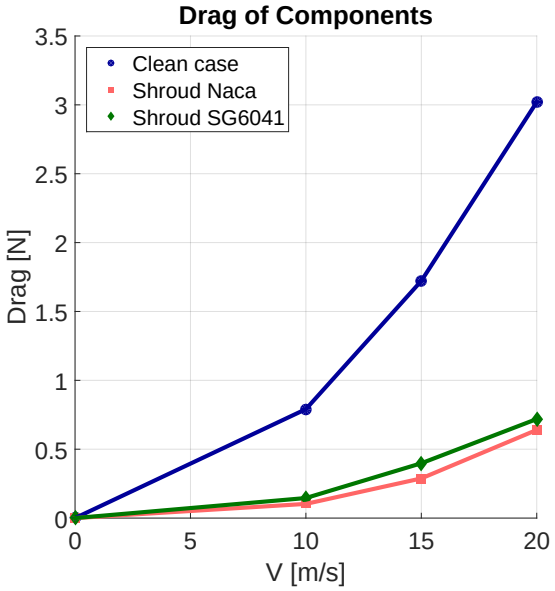

Figure 8.2: Drag of the nacelle, NACA shroud and SG6041 Shroud

Noise Measurements

For the noise measurements, one microphone is used of the type M51 of linearX. The first step to analyse the data is to calibrate the microphone which is done by using a G.R.A.S. Piston phone. The piston phone has a constant sound pressure level of 114 dB at a frequency of 250 Hz. This 114 dB depends on the atmospheric pressure so a small barometer is present, and a correction must be applied to this 114 dB. The microphone signal is a voltage-time depended signal which needs to be converted to dB in the frequency spectrum. To obtain the gains of the microphone the piston phone's signal measured by the microphone is converted to the frequency spectrum with a Fourier transform. It was found that there is a peak present at 250 HZ with a magnitude of 85 mV. This voltage can be converted to a gain because the piston phone has a constant SPL of 114 dB at standard conditions. Before determining the gain the 114 dB needs to be converted to Pa. The gain for the microphone at 250 Hz was found to be 118.84 Pa/V. The next step in the calibration is to determine the gains for different frequencies since the microphone performance is frequency depended. The frequency dependency of the microphone is measured by the manufacturer by using a white noise signal. The frequency dependent gains of the microphone can be seen in Figure 8.3. Here it is observed that a bigger correction needs to be applied for the low and high frequencies.

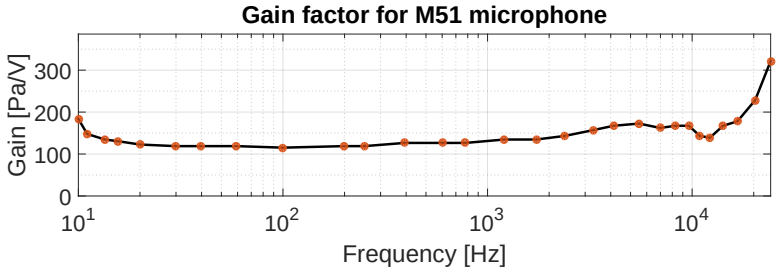

Figure 8.3: Gains of the M51 microphone.

The measured data by the microphone contains the noise of the environment and noise of the wind turbine. To obtain the noise levels of the blades the noise is measured without the blades mounted in the hub. The surrounding noise was measured multiple times to be able to average the signal and gain a more representable data set for the environmental noise. The next step is to subtract the environmental noise from the total measured noise to obtain the wind turbine noise. The three signals can be seen in Figure 8.4. The green signal represents the noise of the wind turbine. The measurement quality is not ideal, which resulted in

difficulties analysing the tonal noises. It can be observed in Figure 8.4c that some of the environmental tonal peaks are not filtered out. This is due to the difficulties with averaging the signals, and the large backscatter from walls and objects in the wind tunnel.

Before the measurement can be performed it must be decided for how long the microphone will measure

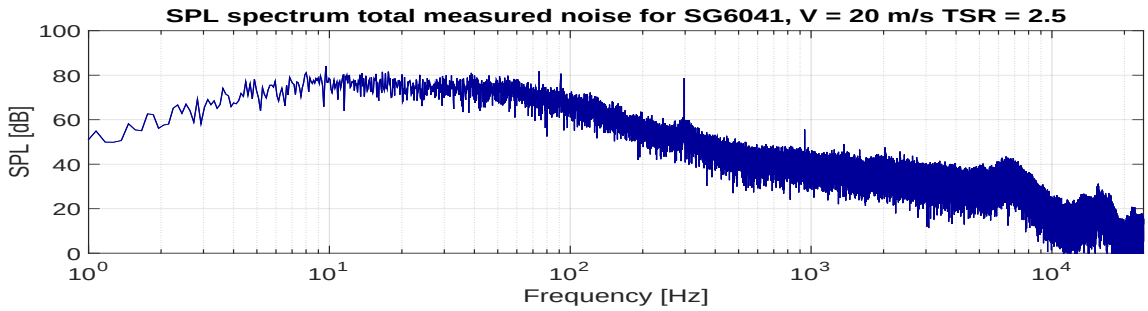

(a) Total measured SPL from microphone

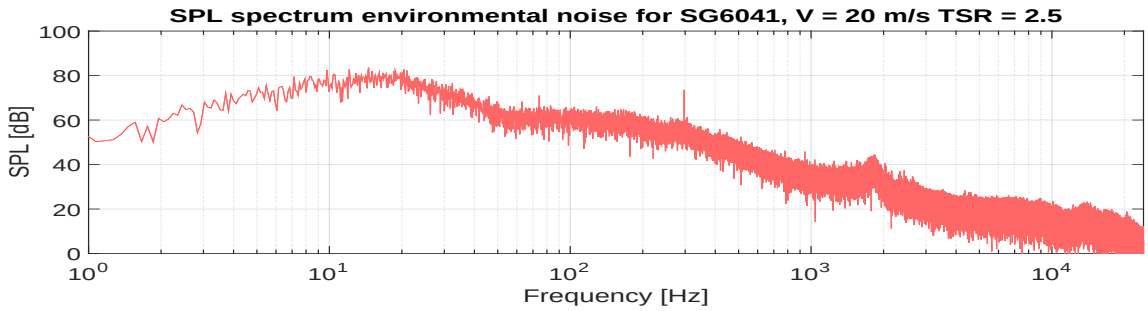

(b) Surrounding noise (without the wind turbine blades)

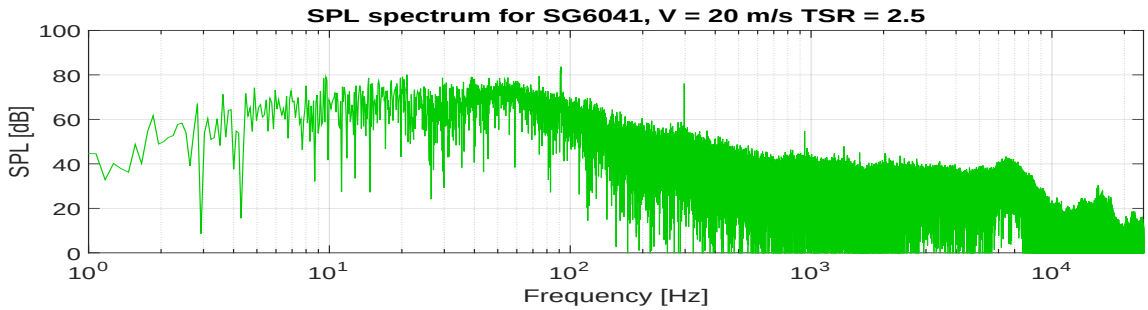

(c) Wind turbine SPL after subtracting the surrounding noise from the total noise

Figure 8.4: SPL signals measured with microphone and how to convert them to wind turbine SPL

the noise of the surrounding and wind turbine. The M51 microphone has a sampling frequency of 51200 Hz which means that the frequency range analysed by the Fourier transform will be from 0 HZ till 25600 Hz which is due to the Nyquist frequency. Since tonal components will be investigated an accuracy of 0.1 Hz is desirable. Then the time needed to measure is $1/\Delta f$ meaning a measurement time of at least 10 seconds should be sufficient.

8.2 Results

Both rotors are tested, with each a different rotor lay-out. The results shown will be discussed further in section 8.3 where the validation is done. In this section, the comparison will be performed between the clean and shrouded case. This is of interest to fully understand what the performance change is due to this shroud.

8.2.1 Mechanical Power

As discussed, the mechanical power was measured using an RPM sensor. The rotor was kept stationary until the wind tunnels wind speed was constant. Then the rotor was released and the rotational frequency was measured until the angular frequency is constant. This procedure was done 4 times for each rotor and for each wind speed. An example of the rotational frequency measurement can be seen in Figure 8.5, where the 4 rotational frequency signals are visible on the zoomed plot. The four lines in the figure are close to each other and it is difficult to distinguish them from each other. To determine the power the average of this signal is calculated and this is represented by the green dotted line.

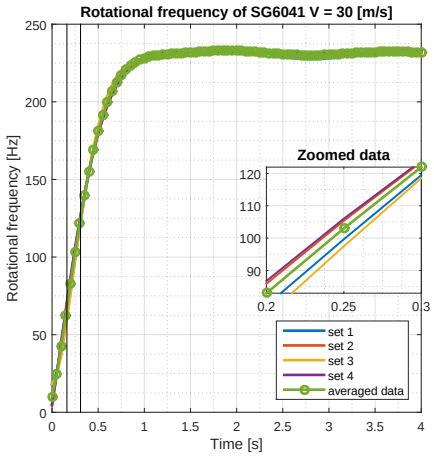

Figure 8.5: Experimental rotational frequency, 4 signals, and their equivalent averaged signal (green). V=30 m/s

From the average signal that can be seen in Figure 8.5 the torque can be calculated by deriving this signal with respect to time and multiplying it with the mass moment of inertia (Equation 8.1). The mass moment

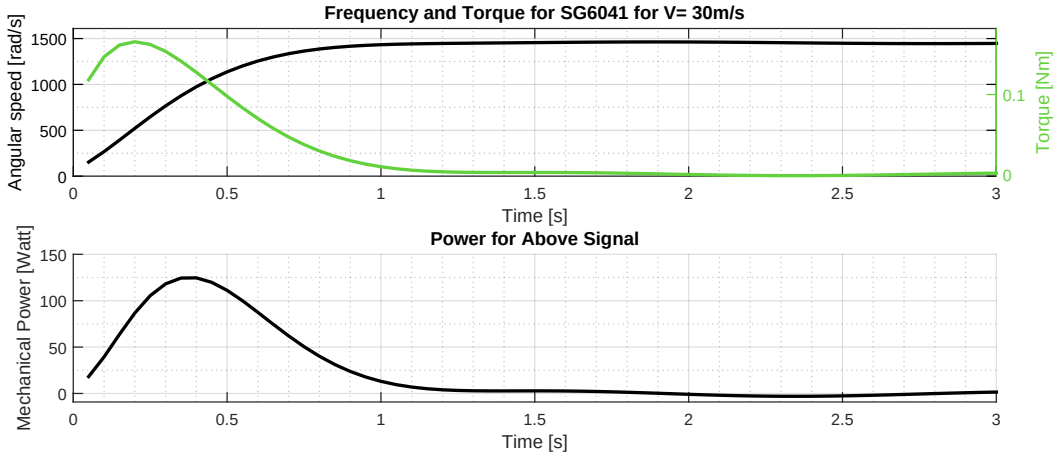

Figure 8.6: Angular velocity, Torque and Power as a function of time for the 4 bladed SG6041 rotor at a wind speed of 30 m/s

of inertia J can be estimated by the use of CAD software like Solidworks, from this program it was found that J_{SG6041} equals 4.9e-5 kg·m^2 and for the NACA rotor, J_{NACA} equals 5.5e-5 kg·m^2. These values include the mass moment of inertia of the generator [47]. It is seen that the torque of the rotor increases till 0.2 sec and then decreases rapidly to almost zero when the rotor is at its free spinning speed. The reason why the torque increases is because of the rotor's increase of rotational speed, resulting in lower AoA which is beneficial for the power production. Lower AoA will lead in this case to higher C_l and C_d. The initial case (when there is no rotational speed) has a high AoA which is above the stall angle. Besides this effect, there is a minor contribution of the increase in Re number which increases the L/D of the airfoil. The mechanical power is defined as

the product of angular speed and torque produced by the rotor. In Figure 8.6 the torque and angular speed are given for each time instance. The power can be determined by multiplying these two signals. This can be seen in the second graph of the figure. The $\lambda - C_P$ curve can be created from the power and Ω signals.

The procedure discussed earlier will be applied for different wind speeds and rotors and the results can be seen in section E.1. The results will be more accurate at lower wind speeds than for higher wind speeds. The reason for this is that when the wind speed is lower the rotor spins slower, which makes it easier to track when the rotor started to turn. This is the reason why the error bars for 15 m/s are smaller than the bars for 30 m/s. A second observation can be made that the error bars are larger for low TSR than for high TSR. There are multiple reasons why this difference is higher for lower TSR. One of these is that it is impossible to determine at what exact time the rotor starts spinning which introduces a larger error at the beginning of the signal when applying a polynomial fit. This results in larger deviations at the beginning of the time signal. The second reason why the error bar for high RPM is easier to monitor is because the angular acceleration is lower resulting in lower angular speed increments and lower uncertainty in the measurements. The procedure as explained above was done for all the rotors for the wind speeds: 10, 15, 20 and 30 m/s. The last reason why there is a larger deviation for low TSR is that the RPM is low and thus the wake has not enough time to develop so small errors are introduced here. This problem is not present for higher tip speed ratios. For high tip speed ratios, the RPM is higher than for low tip speed ratios, which means that the wake will develop faster (around 3 revs/s).

The results from the measurement campaign can be seen in Figure 8.7. There are two rotors tested: SG6041 and NACA4418 and both have two different test conditions. The first is the clean condition of which the results can be seen in Figure 8.7a and Figure 8.7c. The second case is when the shroud is mounted on the wind turbine and these results can be seen in Figure 8.7b and Figure 8.7d.

In Figure 8.7a the results can be seen for the SG6041 clean rotor case. It can be observed that the rotors produce power from a TSR of 0 till 4 and have a maximum C_P value of 0.3378 for a wind speed of 30 m/s with a corresponding TSR is 2.4. It can be seen that the wind speed affects the $C_{P_{max}}$ in a limited way. The results of the $C_{P_{max}}$ and TSR_{max} can be seen in Table 8.2. For 10 m/s the maximum power coefficient is 0.319 and for 30 m/s it is 0.3378, which is a difference of 2% in C_P. The reason for this is that the chosen airfoil is designed for small wind turbines and has good performance for low Re numbers. The TSR is changing from 2.4 (30 m/s) to 2.6 for 10 m/s. There are three possible reasons for this shifting. The first one is due to the limited amount of data points obtained during the measurements, which increases the RMS error during interpolation. The second reason is due to the performance of the airfoil at low Re numbers. If the Re number is low, there is a chance to create earlier laminar separation which could influence the optimum TSR. The last reason is due to the quality of the measurements. The method used to calculate the power is not ideal and it could be that the wake was not yet fully developed for the low speed (low RPM). Besides this, the method is sensitive to the order of polynomial chosen. The slightest difference can result in a large shift in TSR.

In Figure 8.7c the experimental results can be seen for the NACA4418 rotor without a shroud. From a first view, it is observed that the C_P curve looks different than the SG6041 rotor results. For lower wind speeds the curve is significantly lower than for high wind speeds. The reason for this is because of the poor performance of the NACA4418 airfoil for low Re numbers. The NACA airfoil is more vulnerable for separation than the SG6041 airfoil because of its thicker profile. For the NACA rotor, the maximum C_P is 0.2727 for a TSR of 2.153 for 30 m/s, which means that the maximum mechanical power is 79.7 Watt. The performance of the blades is degrading quickly when the wind speed decreases. The C_P of the rotor for a wind speed of 10 m/s is 0.206, this is a performance drop of 30% compared to the 30 m/s wind speed. The shift in optimum TSR between wind speeds is 3% which is lower compared to the SG6041 rotor. The main reason why the power decreases is because of the poor performance of the NACA at low Re numbers. The NACA4418 is a thick airfoil which performs poor for low Re numbers, compared to thin airfoils (e.g. SG6041). The reason why the NACA4418 was chosen was for the root thickness of 4 mm which was used as an input for the optimiser. The first interesting conclusion that can be drawn is that it is important to use appropriate airfoil. As can be seen the thin airfoil has no significant airfoil performance changes (except at 10 m/s) while the thick one does have this problem resulting in a lower efficient rotor for low wind speed in case of the clean case.

The next data set is the one for the SG6041 while the protection shroud is mounted. This data can be seen

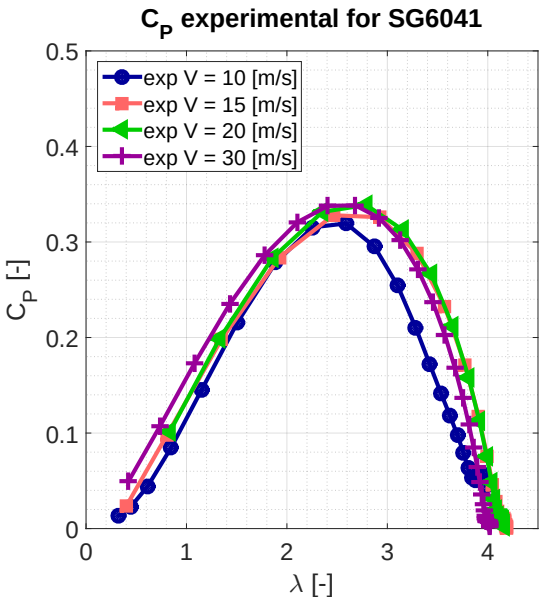

(a) $\lambda - C_P$ curve for SG6041 for different wind speeds

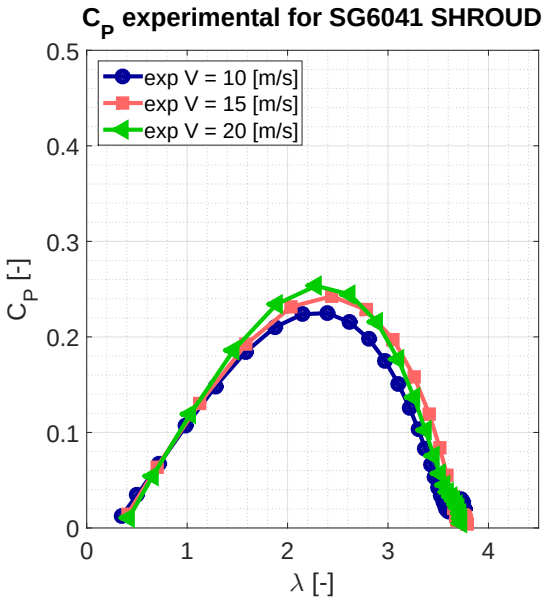

(b) $\lambda - C_P$ curve for SG6041 with shroud for different wind speeds

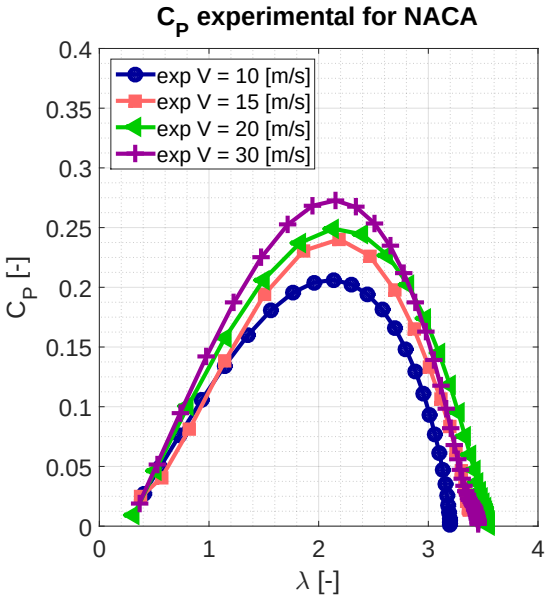

(c) $\lambda - C_P$ curve for NACA4418 for different wind speeds

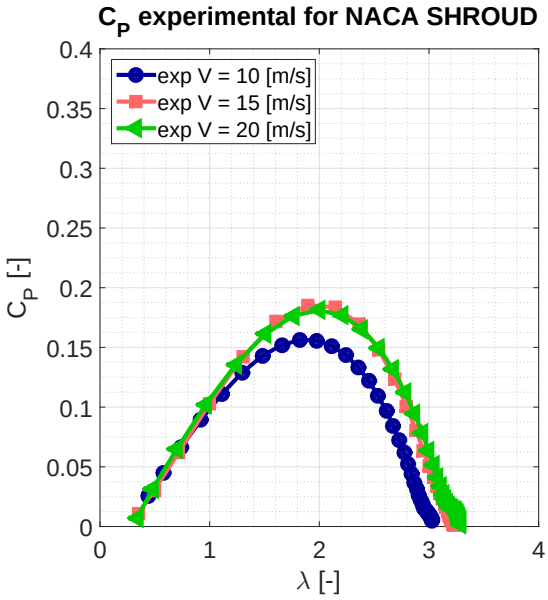

(d) $\lambda - C_P$ curve for NACA4418 with shroud for different wind speeds

Figure 8.7: C_P curves experimental data

in Figure 8.7b. For the shroud, the experiment was not performed for wind speeds of 30 m/s due to the vibration of the shroud when ramping up the wind speed. Comparing the results from the clean with the shrouded case the performance drops at least 30% for all the wind speeds. This is more than anticipated. The maximum C_P for the shrouded case at a wind speed of 20 m/s is 0.2535 at a TSR of 2.28. If the same C_P as 20 m/s can be used for 30 m/s the shrouded rotor will produce 89.6 Watt. There are multiple reasons why the shrouds decrease the power efficiency by such high percentage. The first reason, are the imperfections in the shroud due to the manufacturing by hand, together with difficulty of aligning the shroud completely perfect with the rotor and nacelle. The second reason is that the inflow will be decelerated due to the imperfect cylindrical shroud. The imperfection will increase the turbulence resulting in a more turbulent flow reaching the outer parts of the blade which will decrease the efficiency. The last and most prominent reason for the decrease in

power is because of the interaction of the tip vortices with the inner side of the shroud. The gap between the tip and shroud is around 3-5 mm which can be considered large. The tip vortices will develop and increase the turbulence in the flow. This effect is studied in turbomachinery and propellers and is called tip leakage. It was found that for low advance ratios for propellers (high TSR for wind turbines) the efficiency decreases significantly with increasing gap size [64]. The reason for this is because of a shedding vortex between the tip and inner side of the shroud which lowers the performance of the outer part of the blades. This effect is called tip clearance and more can be found at the end of section 8.2.1. Besides a power drop, a shift in optimum TSR is observed. The optimum TSR shifts from 2.789 for the clean case to 2.28 for the shrouded case. This means that the RPM decreases with 18% which is peculiar. This shift has highly likely to do with the tip clearance effect. For low RPM, the effect of tip clearance is less prominent since the vortex strength at the tip will be lower while for large RPM the performance will decrease faster [64]. This means that the shift of RPM is a direct cause of the tip clearance effect.

In Figure 8.7d the TSR C_P curve can be seen for the NACA rotor with a shroud. This set-up has at 20 m/s a maximum C_P of 0.1811 which is 37% lower than the clean case. Similar behaviour can be observed between the shrouded and clean case. Again, the performance drops significantly for the lower wind speeds. This is because of the poor performance of the NACA4418 airfoil which is more common to use in higher Re flows. It was noted that the C_P decreases when the shroud is mounted. This is mainly because of the same reason as the SG6041 rotor. Due to the imperfect shroud, some extra turbulence is introduced into the flow which decreases the power. Besides the imperfection, the main reason why the performance drops this significantly is due to the tip clearance. This effect is discussed in the section tip clearance. The operational TSR range is lower compared to the clean case. This problem is created with the increase in turbulence due to the shedding vortex between the gap. This shedding vortex will decrease the performance of the blades at the tip which is generating the highest amount of energy.

Table 8.2: Maximum power coefficient values for the different rotors

		10 m/s	15 m/s	20 m/s	30 m/s
SG6041	TSR_{max}	2.483	2.625	2.581	2.408
	$C_{P_{max}}$	0.322	0.332	0.340	0.3378
SG6041 shroud	TSR_{max}	2.318	2.441	2.28	-
	$C_{P_{max}}$	0.226	0.2425	0.2535	-
NACA4418	TSR_{max}	2.136	2.189	2.132	2.153
	$C_{P_{max}}$	0.206	0.2403	0.2491	0.2727
NACA4418 shroud	TSR_{max}	1.8944	2.107	2	-
	$C_{P_{max}}$	0.1562	0.1854	0.1811	-

The Effect of Tip Clearance

The performance of both rotors dropped significantly when mounting a shroud. The reason for this is due to the large gap between the tips and the inner side of the shroud. This space is called the tip clearance. Not much research is done on tip clearance for wind turbine so a look is taken towards propellers. Yongle et al. [64] investigated the effect of increasing the gap size on the performance for propellers. They also investigated the effect of the advance ratio which is the inverse of TSR. The research was done by using different CFD models and they found that for low advance ratios (TSR above 1.25). The efficiency decreases linearly when gap size is increased. If the TSR is lower than 1.25 the efficiency should not decrease but rather increase, this depends on rotor and shroud lay-out. The reason why the efficiency decreases is because of tip leakage. The tip vortex is shaped by three components: tip-separation vortex, the tip-leakage vortex, and the induced vortex [64]. The tip-leakage vortex is formed due to the pressure difference between the suction and pressure side. Separation vortex is because of the separation on the blade. And the last vortex is an effect of the tip-leakage vortex. It was found when increasing the gap size that the core vortex will change from a shedding vortex to a big separating vortex. The large separating vortex will result that the blade will experience different wind speeds resulting in lower performance. It was also found that for bigger gap sizes the turbulence kinetic energy increases due to this separating vortex which contains much more turbulence [64].

8.2.2 Drag

The goal of the wind turbine is to have a drag as minimal as possible so that the complete AWE system is efficient. In this section, the drag results are discussed, again a distinction is made between the rotors and if a shroud is mounted or not. The experimental drag results of the blades can be seen in Figure 8.8. These are measured by the OJF six component balance. Limited data is available for the TSR. The reason for this is that the internal resistance of all other components (e.g. generator, rectifier, and wires) is much higher than the variable load. The variable load's effect is minimised on the rotor and the TSR is constant, resulting in only data for high TSR is available. Drag measurements are only performed for 10, 15 and 20 m/s. 30 m/s wind speed is not possible to be tested since there is a heating problem with the encasing of the generator. This heating problem damaged the generator during testing so no electrical power could be measured. This problem will be solved by creating a full aluminium casing which will dissipate the heat much better than the PVC pipe. The measurements of the individual component such as shroud and nacelle can be found in Figure 8.2.

In Figure 8.8a the result of the drag measurements can be seen for the SG6041 rotor in clean case condition. The data is close to each other and this must be because of the poor performance of the airfoil for low Re numbers. Next, for high TSR the drag decreases this means that the rotor is not operation in heavy loaded conditions. This is important for the whole system that it is known that the drag will decrease if the rotor has higher RPM. The reason why the drag will decrease is because the AoA is decreasing resulting in lower C_l and C_d and lower normal and tangential forces. The maximum C_T is 0.55 for a wind speed of 10 m/s at a TSR of 2.28. It was not expected that the C_T for lower wind speeds would be higher than for the higher wind speeds. More explanation about this is given in the validation of the codes. As expected the rotor's C_T values decrease with increasing tip speed ratio. This means that the rotor is not heavily loaded which is a good characteristic for the AWE system.

The drag of the NACA rotor can be seen in Figure 8.8c. Similar trends are observed as with the SG6041 rotor, the drag decreases for higher TSRs which means that this rotor is not in the high loaded case. The C_T values for different wind speeds do not variate much compared to each other. This was surprising since the C_P curve varies more when looking at the different wind speeds. The reason why this deviation is less compared to the power is because of the reason the power is measured under unsteady condition and it is assumed that the wake is developed almost instantly. While the drag measurements are taken in steady conditions which would give a more representable measurement. This will result that the drag is less sensitive to high wind speeds and less variation will be visible on the C_T values. For the NACA rotor, a drag of 1.81 N was measured for a wind speed of 20 m/s at the TSR for which maximum power is produced.

In Figure 8.8b the drag for the shrouded SG6041 rotor is visible. This is only the drag of the blades so the shroud is not included. The drag values of the individual shroud can be seen in Figure 8.2. The drag is lower compared to the normal clean case. This is because of the tip clearance effect which decreases the blade performance at the tip resulting in a lower power production and drag. The difference in drag of the blades between clean and shrouded case is 20%. From this, it can be argued that the shrouded case is better for the kitepower case. However as stated earlier these measurements are without the shroud drag considered. For the final design, the shroud needs to be taken into account which increases the drag of the complete airborne wind turbine system. The drag curve behaves like the clean case with decreasing drag for higher TSR only the slope is less steep. From Table 8.3 it can be seen that the TSR where maximum C_T is measured is lower than the clean case. This has to do with the tip clearance effect which introduces more turbulence resulting in lower performance for high TSR values. The performance of the blade can only be increased by decreasing the gap size, or increase the gap size such that the blades do not interact anymore with the shroud

In Figure 8.8d the drag can be seen for the blades for the NACA4418 with the shroud mounted. Similar results were obtained compared to the SG6041 rotor. The drag of the blade decreases compared to the clean case. The maximum drag coefficient is 0.29. What is unexpected in this graph is that the C_T values for a wind speed of 15 m/s are higher than for 20 m/s. A physical reason why this happens cannot be given so it is highly likely that there is a deviation in the measurements which needs to be investigated. The behaviour is similar to the clean case with decreasing drag for higher TSR. Again, a similar trend is observed that the TSR at which maximum drag is observed shifts to the lower region due to the tip leakage.

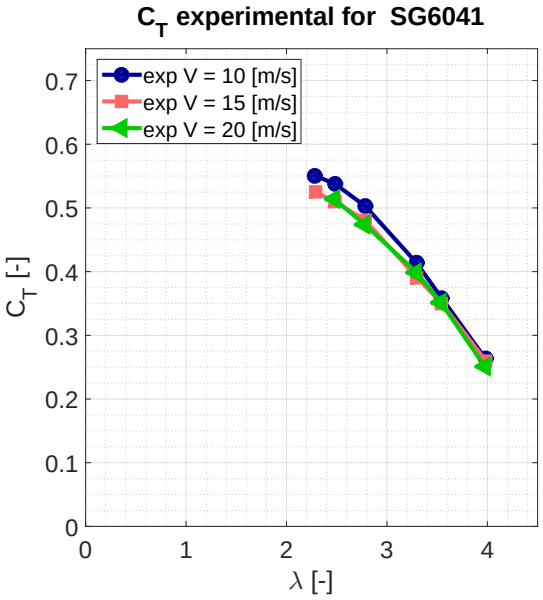

(a) $\lambda - C_T$ curve for SG6041 for different wind speeds

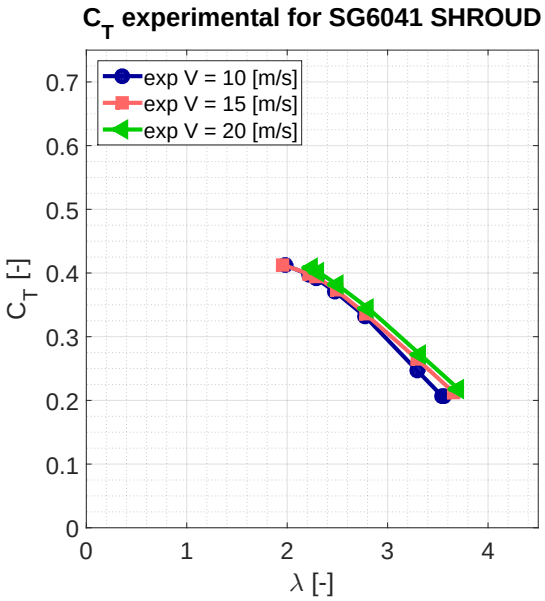

(b) $\lambda - C_T$ curve for SG6041 with shroud for different wind speeds

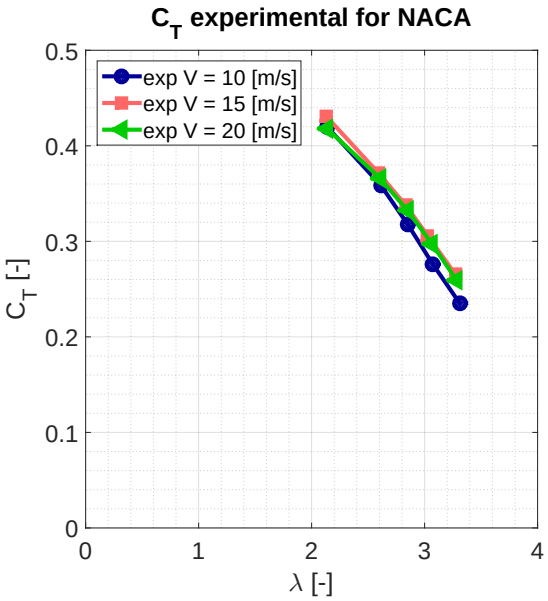

(c) $\lambda - C_T$ curve for NACA4418 for different wind speeds

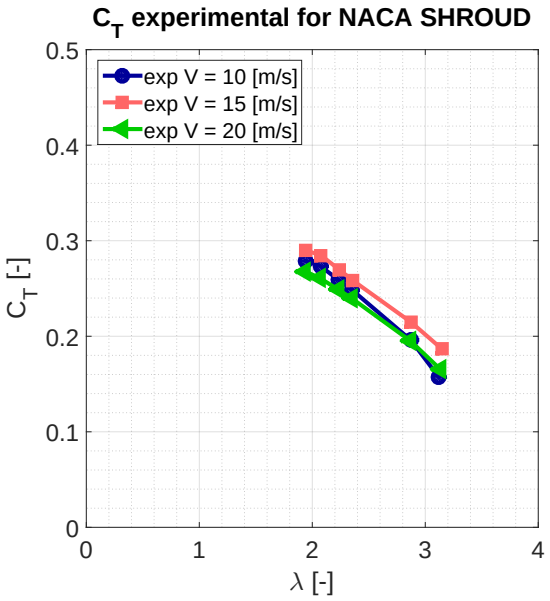

(d) $\lambda - C_T$ curve for NACA4418 with shroud for different wind speeds

Figure 8.8: C_T curves experimental data

8.2.3 Tonal Noise

Besides an investigation on the performance, a measurement was done to see what the effect is on the tonal noise when a shroud is mounted. The first experiments focus on the tonal peaks of the wind turbines and what the effect of the shroud would be. The data presented here is only useful to track the rotational frequency and see trends. The reason for this is due to the low quality of the measurements because of the wind tunnel. The wind tunnel used was not ideal to do noise measurements since no acoustic isolation was used and measurements are performed in the open section of the wind tunnel. Because of this, it is difficult to

Table 8.3: Maximum drag coefficient values for the different rotors

		10 m/s	15 m/s	20 m/s	30 m/s
SG6041	TSR_{max}	2.28	2.29	2.48	-
	$C_{T_{max}}$	0.551	0.525	0.5137	-
SG6041 shroud	TSR_{max}	1.98	1.95	2.242	-
	$C_{T_{max}}$	0.412	0.413	0.4086	-
NACA4418	TSR_{max}	2.137	2.131	2.134	-
	$C_{T_{max}}$	0.420	0. 4308	0.4183	-
NACA4418 shroud	TSR_{max}	1.938	1.942	1.936	-
	$C_{T_{max}}$	0.278	0.290	0.268	-

filter out all the background noise which can be seen in Figure 8.11. The results for all rotors can be seen in Figure 8.9, for a wind speed of 20 m/s and close to the optimum TSR. Here the frequency is normalised to the rotational frequency which was measured with an oscilloscope and RPM sensor. In all figures, there is a tonal present around 311 Hz (between the third and fourth harmonic), this tonal is a frequency produced by the wind tunnel. The other results for different wind speeds can be found in section E.3.

The plots are shown in Figure 8.9 shows is the SPL of the wind turbine 1 meter behind the rotor aligned with the nacelle. It was expected that a peak would arise at 1 (rotational frequency) and 2, which is the most dominant harmonic. Around 4 a peak should be visible due to blade passing frequency. However, there can be seen that there is only one graph that shows a tonal component at the blade passing frequency and that is Figure 8.9b. This was not expected and there are two reasons why the blade passing tonal is not visible. The first one is that there is not enough pressure fluctuation at this frequency, which could be picked up by the microphone. And combining this with the large background noise it can be that the tonal noise for the blade passing frequency is suppressed. The second reason is that the flow blockage due to the tower is less than expected which results in lower unsteady blade loading, resulting in lower tonal peaks at the blade passing frequency. This effect occurs because the rotor is mounted much further forward in comparison to conventional wind turbines. If the rotor is mounted this much forward the influence of the tower blockage will be reduced. Similar behaviour was observed for different wind speeds. Also, due to this forward position, the unsteady loading is less due to the large chord length. Large wind turbine blades are more slender resulting in a more sudden change when passing this blocked region. If the wind turbine blade is thick, it will be longer in this region, so the sudden change will be less strong resulting in lower tonal peaks.

It was already mentioned that the noise experiment was not performed in an ideal conditions. But the measurements can still be used for finding the RPM however it is advised to redo the measurements in an anechoic wind tunnel where the environmental noise is minimised. It can be observed that the tonal noise at the first multiple is higher for the clean cases compared to the shrouded cases. This is also observed in the result from section E.3, meaning that the shroud is suppressing the tonal noise. More research is necessary to support this conclusion. A reason why this can be true is because the wake expands in the shroud. However, since the shroud is long the wake would be destroyed resulting in lower tonal peaks, next, it can also be that the wake is destroyed due to the two struts that support the shroud. However, more research is necessary to say this with 100 % certainty. It can be concluded that only the clean cases have a peak at the rotation frequency.

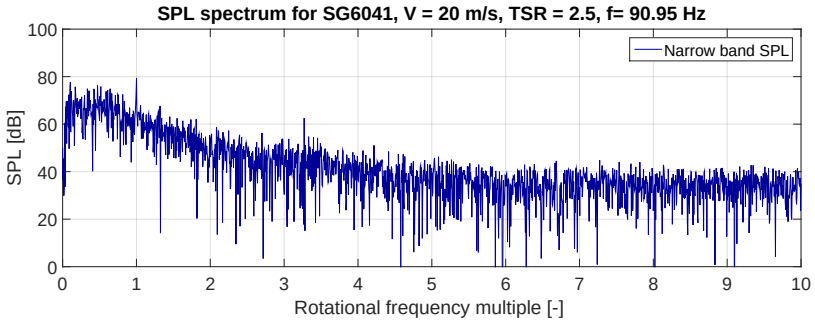

(a) SPL for SG6041, V = 20 m/s TSR=2.5

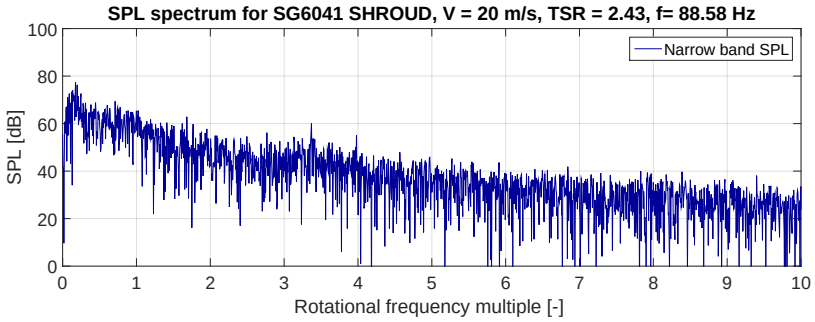

(b) SPL for SG6041 with shroud, V = 20 m/s TSR=2.43

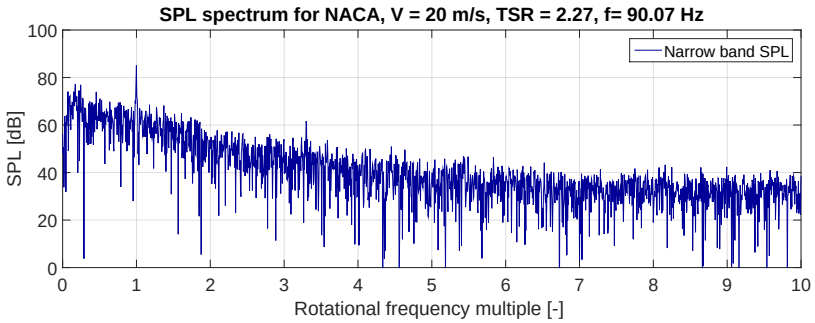

(c) SPL for NACA, V = 20 m/s TSR=2.27

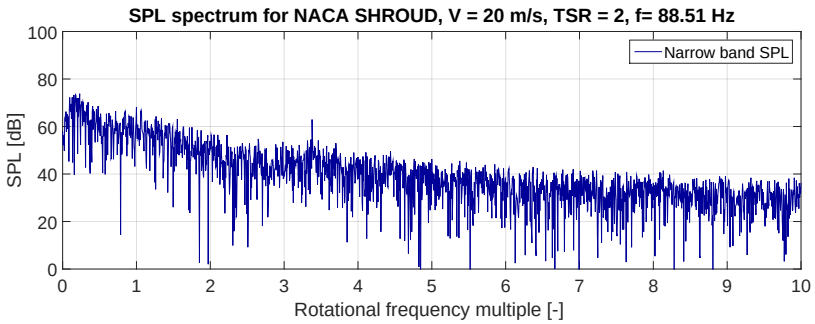

(d) SPL for NACA with shroud, V = 20 m/s TSR=2

Figure 8.9: SPL data for the different rotor configurations in a constant Δf band

8.3 Validation of Software

The experimental result is discussed and in this section, the experimental results are compared with the numerical results. From the comparison, there will be concluded if the codes are valid. The cases tested validated are for 20 m/s wind speeds. And for the BPM model validation, the noise is investigated on the optimum TSR. The validation is also only performed on the clean cases without the shroud. This is because the codes are not able or adapted to take a protection ring into account. The quantities of importance for the valida-

tion are $C_{P_{max}}$ for different wind speeds, the optimum TSR and corresponding C_T. Next, there is looked at the shape of the different TSR curves. Finally, the noise model is validated where the experimental and numerical data are compared based more on similarities.

8.3.1 Validation Performance Codes

Validating the software is the next step, first is the BEMT and next the BPM model. First, the power curves are compared to the predicted values of power and the TSR-C_P curve. In this section, the 20 m/s case will be considered. The cases for 10, 15 and 30 m/s can be found in section E.1. The first $\lambda - C_P$ curve can be seen in Figure 8.10a and Figure 8.10b. A summary of the maximum values can be found in Table 8.4 together with the correlation and root mean square error (RMS) of the graphs. The reason why 20 m/s is chosen is because of the reason that full experimental and numerical data is available and it is the closest wind speed to 30 m/s.

In Figure 8.10a the results for the SG6041 rotor can be seen. The graph shows that the BEMT and experimental result are similar. The $C_{P_{max}}$ is comparable to the calculated BEMT and this is also observed for the other wind speeds. The total maximum errors between the BEMT and experimental data for $C_{P_{max}}$ is 5.18% for the 30 m/s case. Looking at the optimum TSR the errors are considerably larger in the order of 10%. The reason for this could be a combination of the BEMT and the used method to convert an RPM signal to a power signal. The shape of the C_P curve is largely dependent on the quality of the torque and RPM signal and the method on how the torque is calculated from the experimental data. As mentioned the torque is the first derivative of the angular speed signal. The angular speed signal is determined by doing a polynomial fit on scalar data measured which introduces small errors. Besides the small errors that are introduced in converting the RPM signal to power the BEMT has its own simplifications which introduce small deviation compared to experimental data. It is shown that the maximum power coefficients are in an acceptable range while the TSR shows larger deviations. A third reason why the errors are large for the TSR is due to the small prediction errors in Rfoil which results that the BEMT will predict with an offset. It is known that Rfoil under predicts the drag however it is not possible to verify this since there is no data available for the airfoil for high TI values and the same Re numbers. It is seen in Figure 4.18c that the lift is overpredicted by Rfoil which results in a higher L/D at a higher angle of attack. As a result, the optimum TSR is shifted to the lower TSR values according to BEMT. Looking at the general shape of the graphs it is useful to look at the correlation error which describes how Good two data sets are similar in shape. The second error that is of interest to describe the total behaviour of the graph is the RMS error which describes the average difference between the points. Looking at the correlation in Table 8.4 it can be seen that for the wind speeds below 30 m/s the correlation is above 0.95 which is considered high. Looking at the 30 m/s the correlation is 0.8779 which is low compared to the other cases. This is because of the TSR values after the optimum TSR, it is observed in Figure E.1d that the higher TSR values are much higher compared to measured values. This is likely due to the difference between the airfoil performance predicted by Rfoil and experimental performance. Looking at the RMS error the values are all below 0.45, the lower the RMS values the better. The increase in error is mainly due to the larger difference for the TSR lower than optimum TSR. Here it can be seen that the experimental results are for all the graphs lower than what is predicted. The reason for this can only be because of the difference in airfoil polar. In BEMT it is assumed that there is a stall delay, which is an empirical model which increases the lift and decreases the drag due to the rotational component. For the 30 m/s case, it is also observed it predicts much higher C_P for higher TSR which increases the average distance between the two curves increasing the RMS results.

The drag values (C_T) of the SG6041 rotor for experimental results are comparable to the numerical results. The error is in the range of -1.5% for higher wind speeds. It is noted that the error for 10 m/s is 5% which is high compared to the other values. The results for the low wind speeds (low force) predicted by BEMT are lower comparable to experimental results as can be seen in Figure E.3a. A reason why the deviation is so high is maybe due to the resolution of the measuring equipment. The force measured at 10 m/s is in the range of 1.28 Newton which is low compared to the higher wind speeds. This could result in deviation of the C_T value but more research is necessary to come to this conclusion. It would explain why the C_T is higher for lower wind speeds if there is an error in the measurement. The second possible reason is that the drag or lift is under-predicted by Rfoil which also explains the large deviation in TSR. The last reason could be a laminar bubble but this is highly unlikely since there is no deviation observed in the $\lambda - C_P$ curve.

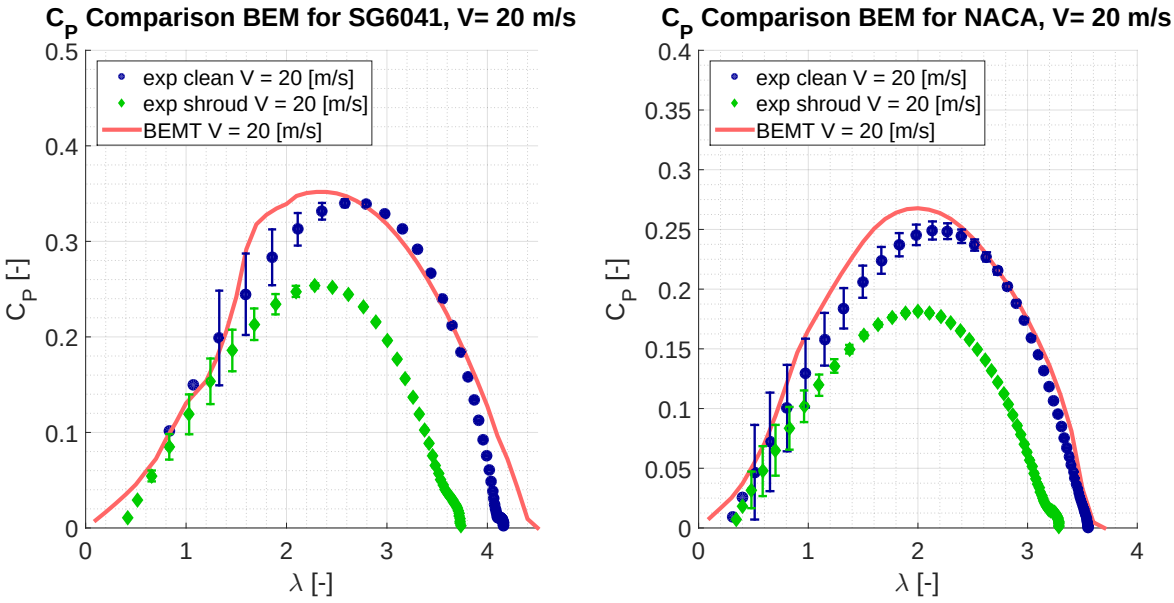

(a) $\lambda - C_P$ curve for SG6041 with a speed of 20 m/s

(b) $\lambda - C_P$ curve for NACA4418 with a speed of 20 m/s

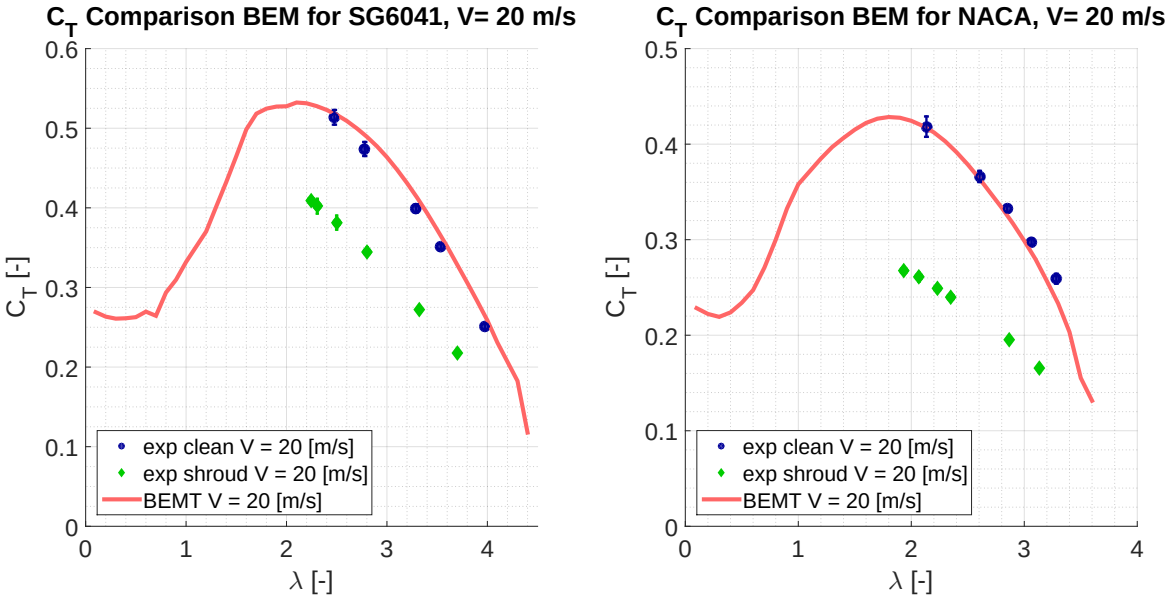

(c) $\lambda - C_T$ curve for SG6041 with a speed of 20 m/s

(d) $\lambda - C_T$ curve for NACA4418 with a speed of 20 m/s

Figure 8.10: Rotational frequency for NACA 4 bladed rotor

For the NACA4418 rotor the tabulated results can be seen in Table 8.4, in Figure 8.10b the $\lambda - C_P$ curve can be found and in Figure 8.10d the results for the drag coefficient of the blade can be found. The C_P errors are larger compared to the other rotor, the maximum C_P difference is -7.5% for a wind speed of 20 m/s. Comparable behaviour is noticed between the NACA and SG6041 rotors. Both under predict the optimum TSR. The BEMT under predicts the optimum TSR with a difference of around 7%. This is possible due to the method used to determine the power and the small errors introduced by BEMT assumptions and the lack of qualitative airfoil data predicted by Rfoil. Looking at the $C_{P_{max}}$ for 20 m/s the error is around 7.5 % which is acceptable for such a thick airfoil. Looking at the shape of the power coefficient graph there is a similarity between the BEMT and experimental values. The experimental values have a slightly higher operational TSR range. For high TSR there is a slight offset between experimental and BEMT results, which is mostly visible for the 30 m/s case in Figure E.2d. Looking at the shape of the data sets there is again looked at the correlation and RMS values. The correlation of the NACA rotor is higher than the SG6041 rotor. All values are above 0.98

which means that the shape of the graphs is similar. The main reason why this value is so high is due to the higher TSR regions which agree well with the experimental values. The main difference is for the low TSR regions where the BEMT result increases faster compared to experimental. The difference is probably due to the cut-off in the Kirke extrapolation which will increase the lift coefficient. This effect is noted in all four comparisons. Next, the RMS values are for all the cases lower than the SG6041 rotor. This means that the experimental and numerical data are comparable to each other on the graph and this is also observed in the figures. The largest deviation comes from the lower TSR region, where the numerical values are higher due to Kirke correlation and stall delay. In general, it can be concluded that the prediction and experimental results are comparable and BEMT calculates reliable results for the power. For the drag measurements, it can be seen that the C_T is under predicted for the 10 and 15 m/s case. The main reason for this is probably since the airfoil is relatively thick for these Re numbers. This will result in a drag prediction from Rfoil that is too low which explains the increase in C_T measured. The general shape of the graphs is similar to the BEMT results but for the higher C_P values the graph is shifted to the higher TSR region. The operating range of TSR is predicted accurately. The $\lambda - C_T$ curve has a similar shape but is under-predicted by BEMT and for the higher TSR, this effect seems to be bigger. For the 20 m/s case, the result agrees well.

Table 8.4: Maximum values of BEMT and experimental plus error in percentage compared to BEMT

			10 [m/s]	15 [m/s]	20 [m/s]	30 [m/s]
SG6041	$C_{P_{max}}$	BEMT	0.3291	0.3438	0.3518	0.3553
		EXP	0.3217(-2.3%)	0.3321 (-3.5%)	03399 (-3.5%)	0.3378 (-5.18%)
	TSR_{opt}	BEMT	2.3	2.3	2.3	2.4
		EXP	2.483(+7.37%)	2.625(+12.38%)	2.581(+10.9%)	2.408 (+3.3%)
	$C_{T_{TSRopt}}$	BEMT	0.5105	0.5211	0.5278	0.5339
		EXP	0.5378(+5.08%)	0.5098(-2.2%)	0.5137(-1%)	/
	R_{C_P}	Correlation	0.9842	0.9699	0.9527	0.8779
	RMS_{C_P}	RMS error	0.4034	0.4087	0.4374	0.4406
NACA4418	$C_{P_{max}}$	BEMT	0.2157	0.249	0.2678	0.248
		EXP	0.2062(-4.6%)	0.2403(-3.6%)	0.2491(-7.5%)	0.2727 (-4.1%)
	TSR_{opt}	BEMT	2	2	2	2
		EXP	2.136 (+6.4%)	2.189(+8.6%)	2.132(+6.2%)	2.153 (+7.1%)
	$C_{T_{TSRopt}}$	BEMT	0.3767	0.4033	0.4198	0.4372
		EXP	0.4198 (+10.27%)	0.4308 (+6.38%)	0.418 (+0.4%)	/
	R_{C_P}	Correlation	0.9817	0.9868	0.9886	0.9683
	RMS_{C_P}	RMS error	0.3910	0.4004	0.4114	0.4346

From these experimental results, it was found that the BEMT has accurate power predictions and that the C_P are in an acceptable range if the right airfoils are used. The right airfoils are airfoils which are designed for low Reynolds number that has high L/D and high $C_{l_{max}}$. It was found that the optimum TSR predicted by BEMT is around 10% lower than what was found by experimental. Two possible reasons were identified for this error. The first one is due to the conversion from the rotational frequency signal to the power. Secondly, Rfoil under predicts the drag and over predicts lift. This effect is more notable at lower velocities. It was observed that for thick airfoils and low wind speed the $\lambda - C_T$ curve measured is higher than what is predicted by BEMT. This is due to Rfoil drag under prediction this is especially visible for thick airfoils. The main conclusion is that BEMT performs better than expected since the $C_{P_{max}}$ error for appropriate airfoils are in a small range and the shape of the graph is similar. Looking at the correlation it confirms that BEMT is able to predict same trends. The difference between two data sets is small since the RMS error is low. From this, the conclusion is that BEMT performs accurate enough but caution is advised when using Rfoil and analysing results due to the difference in wind turbine drag.

8.3.2 Validation Airfoil Self-noise

The noise model developed is based on Lowson turbulence inflow model [16] and the airfoil self-noise model developed by Brook, Pope and Marcoline [10]. This model is coupled to BEMT to predict the aeroacoustic noise generated by small wind turbines. The next step is to validate the results. The BPM model does not take a shroud into account so the rotor in the clean case is only used for validation. The rotors are validated on

the data set that was closest to the optimum TSR which was obtained by measuring. The results from BPM discussed here are only the total SPL. To see each individual noise component one can consult section E.5. The SPL data validated here is based on a 1/3th-octave band and has an A-weighting which represents a correction for the frequencies where the human ear is most sensitive too.

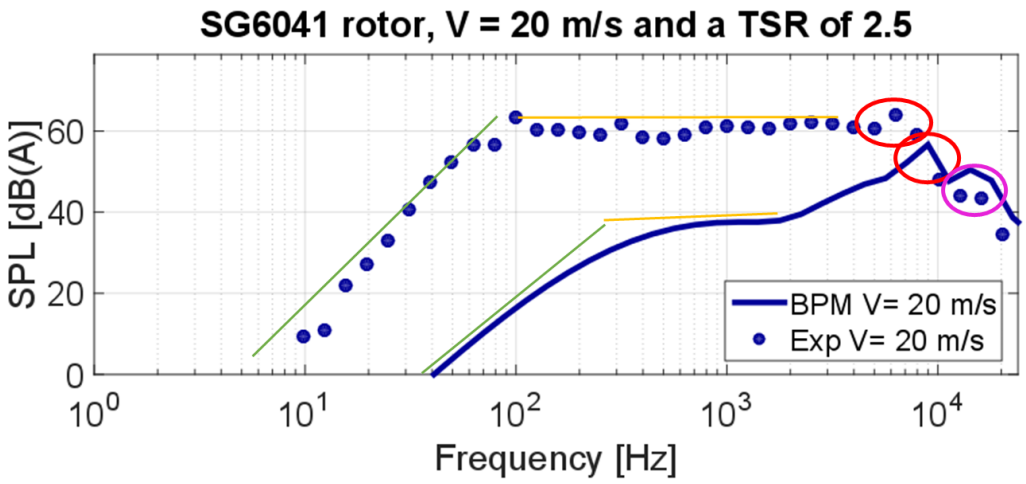

Figure 8.11: BPM calculation and experimental results for a wind speed of 20 m/s at 1 m behind the SG6041 rotor

In Figure 8.11 the results for the SG6041 rotor can be seen at a wind speed of 20 m/s and a TSR of 2.5. The first observation that can be made from the graph is that the experimental data has around 20 dB(A) more SPL than what the noise model predicts for the low frequency range. The reason for this is due to the quality of the measurements. The wind tunnel used is not suited for acoustic measurements due to numerous reasons. As already mentioned it is difficult to filter out the environmental broadband noise of the wind tunnel, as well as the background noise from neighbouring wind tunnels. Besides the wind tunnel background noise, there is a possibility that there is a lot of reflection of the noise. However, the graph shows some similar trends between the two signals. These trends are marked with lines and circles with each a different colour. For both data sets, a peak can be observed for the bluntness noise (red circle). This is the main noise source and is predicted with the BPM model, there is a frequency offset visible between the two peaks. This is because of the different airfoils used in the rotor and the airfoil used in developing the model. The purple circle represents the LBL-VS noise which in BPM is a bit more dominant and has a tonal characteristic, while for the experiments there is a small flat plateau. It can also be seen that for the lower frequency there is a similar slope for the experimental data and BPM (Green line). It must be noted the slope starts earlier for the experimental data. The last small similarity that can be seen is the yellow line which represents a small horizontal plateau. It seems that the BPM model is predicting similar trends as measured and it predicts most of the dominant noise sources correct but with a frequency offset. As can be seen, the bluntness peak occurs at a lower frequency. Last, there are two small peaks on the experimental data in the lower frequency range which are not visible in the BPM data. These two peaks are tonal of which one is from the rotational frequency and the other is a wind tunnel tonal which could not be filtered out. The BPM model seems to perform well for this first rotor and the main reason why the data does not resemble the experimental data is due to background noise during the measurements.

For the second rotor (Figure 8.12) the same analysis was performed. It is seen that there is around 20 dB(A) and more difference in the lower frequency ranges (lower than 1500 Hz). However, there are again similarities between the two signals. In the lower frequency ranges, there is a similar slope. The yellow horizontal line in Figure 8.12 represents the small horizontal part which in experimental data is longer compared to the BPM results. In the horizontal part of the experimental data, two small peaks are revealed. These are tonal peaks. The first one is of the rotors rotational frequency, and the second is the tonal peak of the wind tunnel. Next, the orange line represents a small hill which according to the BPM is mainly due to TBL-Separation noise, which is due to the acts that the NACA4418 will separate easier than the SG6041 airfoil. The red circle represents the noise contribution of the bluntness of the wing. Last, the slope for the higher frequency ranges is predicted well comparing to the experimental results.

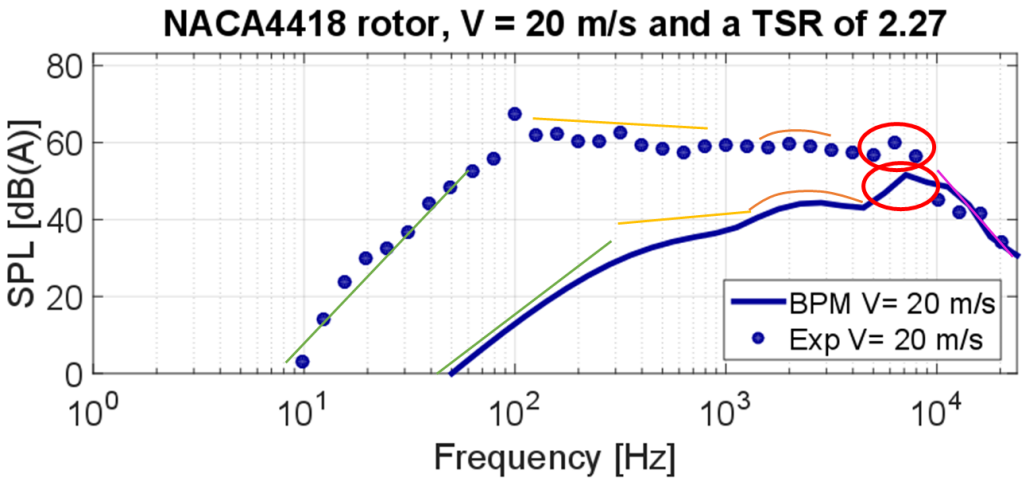

Figure 8.12: BPM calculation and experimental results for a wind speed of 20 m/s at 1 m behind the NACA4418 rotor

It is shown that there is a discrepancy between the experimental and numerical results for the lower frequency ranges. This offset has at least a difference of 20 dB, and is highly likely due to the noise of the wind tunnel reflecting against walls and amplifying the noise. Then it is observed for two cases that the higher frequency bands are similar to what is measured. This is also observed in the results in section E.4. What is observed in experimental data that besides the offset there is some similarity between the two signals. It was seen for all the signals that the dominant noise source is the bluntness noise. This is due to the 0.7 mm thickness at the TE due to the 3D printing process. It was also seen in the NACA4418 case that the S-S noise is visible. Because of the big offset between numerical and experimental data, it can be advised that the experiments should be redone to be sure that the BPM method performed as expected. The problem with current experiments is that there is too much broadband noise from the environment which is not possible to filter out. There are some similarities between BPM and experiments, and BPM developed here shows similar results as other validated software such as NAFNoise. From this, the early conclusion can be made that the BPM works and results calculated are representable. However, it is advised that the measurements are redone in more appropriate conditions. If this is done it can be concluded with more certainty if the model is reliable or not.

8.4 Final Redesign

It was concluded that the BEMT calculations are comparable to the experimental data. From experiments, it was found that the optimal TSR is higher than what the BEMT predicted. This is due to the method used to calculate the power and the airfoil data used to calculate the BEMT result. The experimental noise data showed large deviations with the BPM data but there were some trends observed that where similar. The BPM showed good results with NAFNoise and from this, it was concluded that the BPM works as expected but more testing is needed in the appropriate facilities. The last step in this project is to create a final rotor that Kitepower B.V. will be able to use for their system.

Before the real designing starts the optimiser is revised. The optimiser for the first two designs showed large deviations as soon as the initial design was verified with a full BEMT. The reason for this is because, for each airfoil, one airfoil polar is used which is determined by a fictitious Re numbers. This is a large limitation and this is solved by taking the airfoil polar calculation from the outer loop into the inner loop which will result in a larger computational time but a more accurate prediction with more certainty to have a low drag design. The airfoil polar will now be calculated for each different design instead of calculating the airfoil polar once, this can be observed in Figure A.4 when following the green path. For each design, still one airfoil polar is calculated since calculating all the polar for each section would be computational to expensive. The airfoil polar calculated uses as input the average Re number and Mach number over the blade. The optimiser developed now had to run significantly longer, and used 18 airfoils, 20 different RPM, and diameters.

The old designs have a 5-cm hub so that it would be easy to insert the different blades. The last design will be a full solid rotor meaning that the hub size can be reduced significantly. The new hub diameter will be 2 cm which will just give enough space for a center hole for mounting the rotor to the shaft of the generator. It was observed by experimental data that the shroud decreases the performance, this was mainly due to the gap between the tip of the blade and the inner side of the shroud. In the final design, most of the parts will be machined and made stiffer which will make it possible to decrease the gap significantly, resulting in smaller shedding vortices. It can now be assumed that the performance between clean and shrouded will not drop more than 10 %. It is assumed that the total electrical efficiency of the system will be 70 % which is 10% higher than the first assumed efficiency. It was noted when comparing the electrical data with the mechanical data that the electrical system performed better than expected and the efficiency is around 73 %, this was done before the heating problem arises and was done for 30 m/s at high TSR values, so that low loading was placed on the generator. This will result in a mechanical power necessary of 69.84 Watt (44/(0.7*0.9)). The other inputs are kept the same as in the earlier optimiser and they can be found in Table 7.1. It was noted that during simulation Rfoil has sometimes problems with convergence resulting in an error in the program. This was solved by calculating the whole polar instead of only a specific set of angles.

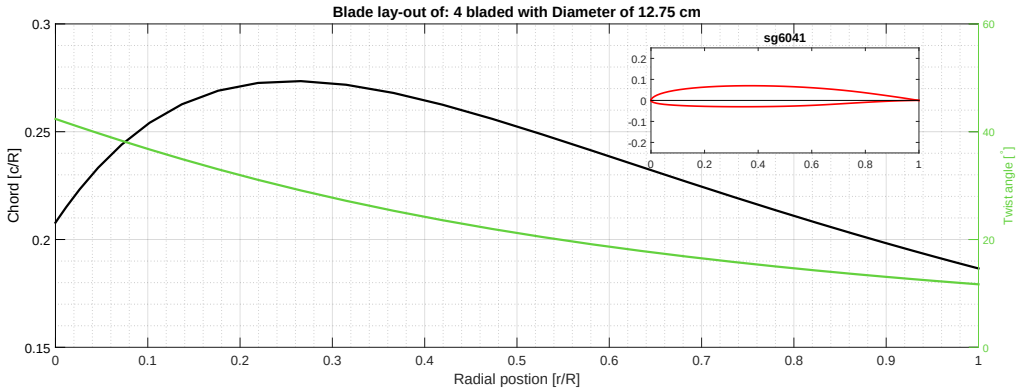

Figure 8.13: Blade lay-out for final design

The best rotor according to the optimiser is a 4-bladed rotor with a diameter of 12.75 cm. The blades will consist of an SG6041 airfoil which has a high L/D ratio. The rotor lay-out can be seen in Figure 8.13 and the tabulated values of the design can be seen in Table B.5. The root chord is 1.117 cm with a root twist of 42.373° which means that the blade is much thinner and has a higher twist compared to previous designs. From this optimiser, it followed that the TSR optimum is around 2.5 with a power of 70.5012 Watt which corresponds to a C_P 0.334 and a drag force of 3.49 N.

The next step is to verify the optimisers calculations with the results of the BEMT code. The results can be found in Figure 8.14. It is noticeable that the optimum TSR is 2.6 per BEMT which is close to 2.5 and that the maximum C_P is also in a good range. According to BEMT, the maximum power at 30 m/s will be 72.8 Watt which is 2 Watt more than the mechanical power requirement. This shows that the optimiser works better as initially, but this came at a cost of longer computational time and an unstable code. The code became unstable when Rfoil did not converge which resulted in an error. This was solved by changing the angles such that Rfoil can use older results to base its new calculations on. It can be seen in Figure 8.14a that the power coefficient will decrease and the maximum C_T varies from 0.49 to 0.46 for the different wind speeds. The optimum TSR is 4% lower according to the optimiser. The reason why this error is present is because of the reason that the optimum TSR is calculated based on the optimum TSR of the initial blade. However, when looking at the new blades with a smaller chord this optimum TSR might shift a bit more than assumed with the constant TSR. To reduce this error, it might be better to not assume that the optimum TSR is constant and there is actively searched for the optimum TSR this can be done by using the same polar but calculate the BEMT over a set of different TSR and picking the optimum TSR. This, in the end, will give a more representable TSR and more reliable result which will be closer to what the BEMT predicts (almost no significant error).

For Kitepower it is interesting to know what the forces will be at the optimum TSR for different wind

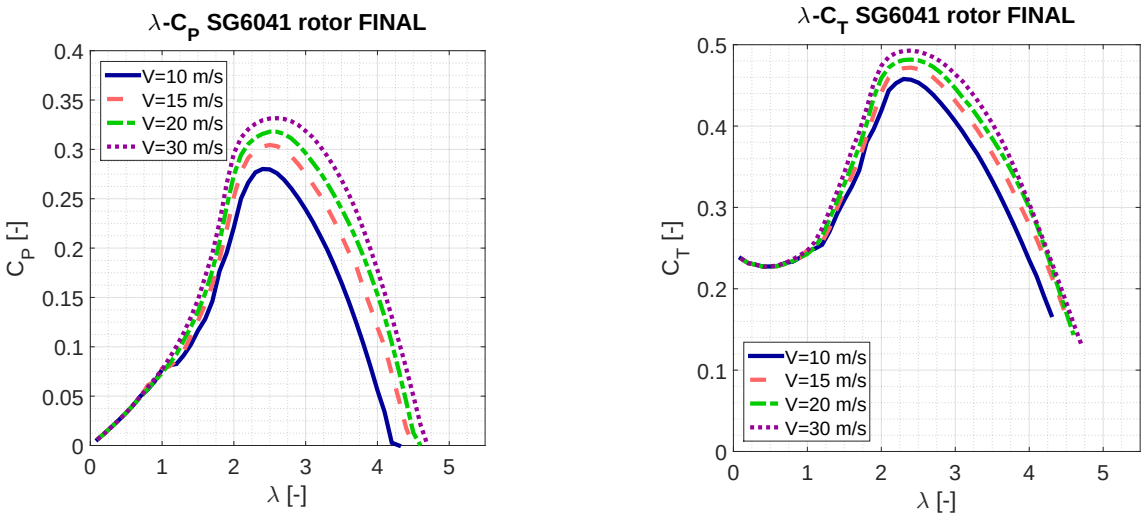

(a) C_P curve for final rotor

(b) C_T curve for final rotor

Figure 8.14: Power coefficient and thrust coefficient BEMT calculations for SG6041, D= 12.75 cm (blade length)

speeds. In Figure 8.15 the power curve can be seen as well as the drag curve. These are made by calculating the maximum power coefficient for each wind speed and using this to calculate the power with Equation 2.1. The red line represents the electrical power that will be obtained which is 63% of the mechanical power. The main requirement is that the electrical power is higher than 44 Watt for 30 m/s and the new design has just enough electrical power which means that the key requirement is satisfied. The drag of the blades will be 3.5 N at a speed of 30 m/s. When flying the wind turbine, the drag will be higher. This is because of the whole set-up which contains the mounting struts, the nacelle and the shroud.

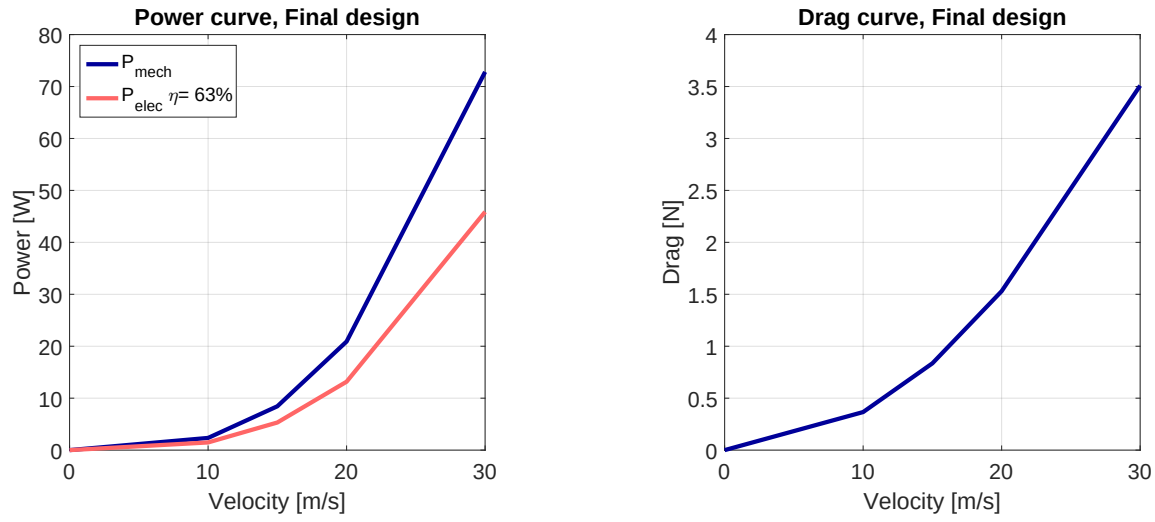

(a) Power curve for final rotor

(b) Drag curve for final rotor

Figure 8.15: Power curve and drag curve for SG6041, D= 12.75cm

8.4.1 Noise of the Final Wind Turbine

The design created has enough power but it would still need to comply to the certification which has as requirement that the SPL_{den} is below 47 dB at sensitive locations. First the SPL is calculated using BPM at a wind speed of 30 m/s at the optimum TSR. This result can be seen in Figure 8.16. It is still assumed that the

TE thickness is 0.7 mm (3D printing limit). But this should be adjusted when other manufacturing methods are used which is advised for this thin blade.

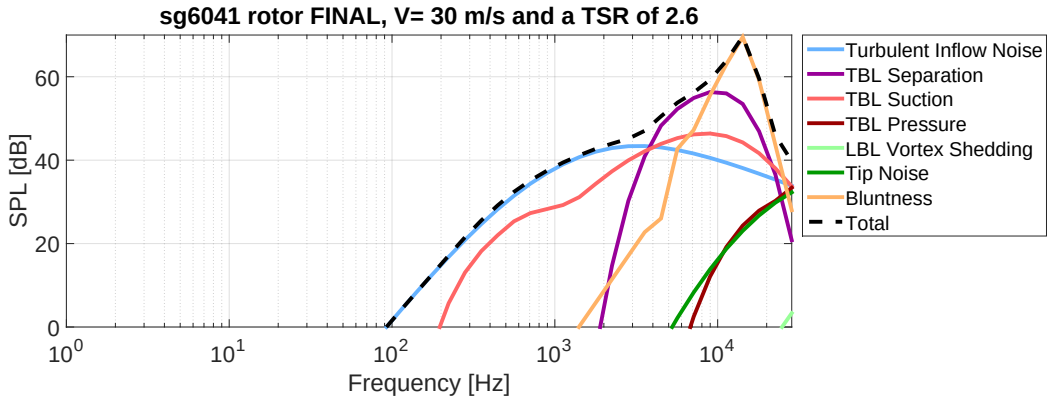

Figure 8.16: BPM calculation for the final rotor

The most dominant noise sources are the TE bluntness and the separation. The reason for the large TE bluntness noise is because of the thick TE compared to the boundary layer. The separation is another dominant noise source because of the low Re number the flow will separate earlier which will result in the generation of this noise source. The total noise is mainly focused in the higher frequency ranges and the TIN noise has a lower frequency component.

The sound at the source is of minor importance. The SPL at the noise sensitive locations is of much more importance for regulations. In this area, there will be looked more at noise-sensitive locations such as a residential area. Three locations of interest were chosen which are discussed in chapter 6. In the atmospheric attenuation model three losses are taken into account: spherical spreading (not frequency dependent), atmospheric absorption and reflection (both frequencies depended). The atmospheric absorption depends on humidity and temperature and these are calculated according to ISA conditions. The reflection is influenced by the wind which for this case will be 7 m/s at ground level. It is also assumed that there is a homogenous material at the ground which is grass. This will mean that the surface roughness scale is 0.03 m (z_0) and the representative flow resistivity is 80 $kNsm^{-4}$.

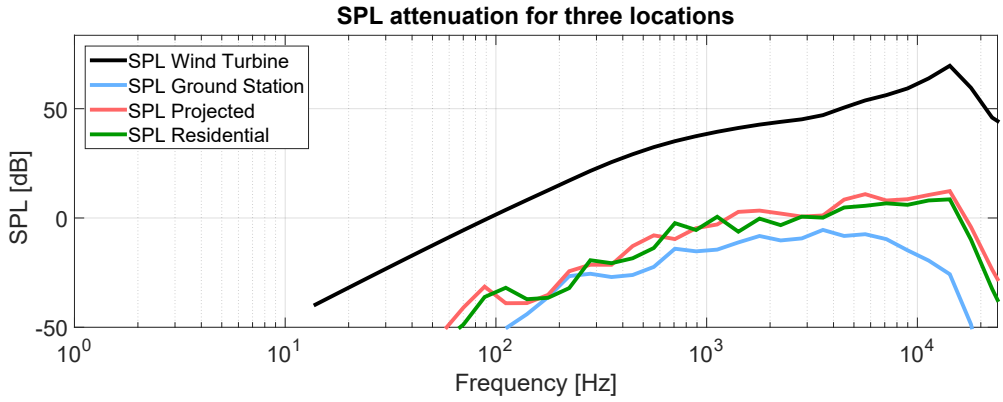

Figure 8.17: Atmospheric attenuation for three location

The noise levels drop significantly for all the different locations. The main noise loss is spherical spreading and atmospheric absorption for the high-frequency ranges. The noise at the ground station is for all frequencies below 0 dB(A), which means that one tone will not be hearable by humans. The noise level at the projected location of the kite is the highest. The most interesting location is the one at the residential area which will be the critical decisive criterion for certification. It was observed that the noise levels decrease

more than expected over the distance and this is normal. The reason for this is that the SPL at the wind turbine is mainly high-frequency noise which is especially sensitive for atmospheric absorption this can be seen in Figure 6.4b. This resulted that the bluntness noise decreases more compared to the lower frequencies. The reflection and wind influence is rather arbitrary and for one frequency it increases the SPL while for other it decreases it. This has mainly to do with the time shift of the reflected ray.

The last step is to see if the noise level does not exceed the 47 dB. The first step is to calculate the frequency signals to overall sound pressure level (OSPL). The results of this can be seen in Table 8.5. Where the OSPL of the wind turbine is 71.57 dB. Due to the atmospheric attenuation, the OSPL drops significantly to 15.4 dB for the residential area. The next step is to recalculate is to SPL_{den} which adds different weighting factors to the noise (+5 dB and +10 dB for evening and night). The equation can be found in Equation 6.6. The results for all the locations can be found in the third column of Table 8.5. From here it is clear that the small wind turbine is below the 47 dB that is prescribed by the Dutch government for all the cases. Which means that the wind turbine complies with governmental restrictions. It can even be stated that the noise levels of the wind turbine will never be a problem if the kite is above 100 meters since the SPL_{den} at the projected (kite) location is 24.9 dB, which is well below the certification restrictions.

It can be concluded that the final wind turbine complies with all the requirements set by Kitepower and government. There will be sufficient electrical power and the wind turbine will have a low drag. Next, it is investigated if the wind turbine will comply with the appropriate certification test. For this, the SPL_{den} should be lower than 47 dB at a noise sensitive location. It can be concluded that the noise will not be any problem if one looks at SPL_{den} which is 21.8 dB in a residential area which is 100 meters away from the kite (projected distance).

Table 8.5: OSPL and SPL_{den} at WT, GS, Projected and Residential

	OSPL [dB]	SPL_{den} [dB]
Wind turbine	71.576	77.97
Ground Station	1.2316	7.62
Projected to the ground	18.5	24.9
Residential area	15.4	21.8

8.4.2 Tripping

It was explained that with low Re number flows the danger exists that laminar separation or laminar separation bubbles can arise. If the blade is 3D printed there is no big problem due to the surface roughness which creates some turbulence. However, Kitepower might mill the rotor out of aluminium which has much better manufacturing accuracy, which is desired for this thin blade. Besides, the better accuracy and durability the rotor will have a much better surface finishing compared to 3D printing. This increases the chance of having laminar separation bubbles which need to be avoided at all time. This can be done by tripping the flow by placing a trip wire on top of the airfoil. This will make the laminar boundary layer turbulent resulting in a lower lift and higher drag, but will still have better overall performance compared to a blade where a bubble is present. A small study was done to see where this wire would need to be placed and what the effect would be on the total produced power at optimal TSR.

The tripping location would depend on the angle of attack since the bubble location depends on the pressure gradient which moves when the angle is changed. The angle of attack of the blade varies in span wise position meaning that for each section the location would change. This is not ideal so the tripping location will be determined by one angle of attack, which is the average of all angles across the blade span. This angle is 6.9° at optimum TSR for an apparent wind speed of 30 m/s. Besides the angle, Rfoil needs the Re number which in this case is again the average of all the Re numbers of each station. From the BEMT it follows that the Re number is 42000. It was noticed that there is a minor bubble which starts around 0.15(x/c) this can be seen in Figure 8.18. It is advised that the tripping takes place bit before the separation bubble start so tripping is done at 13 % of the chord length.

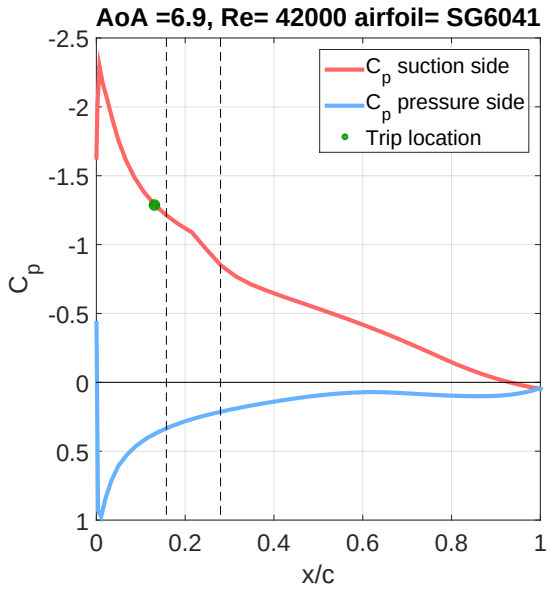

Figure 8.18: Pressure distribution over the SG6041 airfoil. Dashed line shows separation bubble region

If tripping is applied over the span of the blade at 13% of the chord length the loads will change. If the blade forces change the power produced of the blade will change. It will likely decrease since slightly more drag is introduced. The BEMT code developed has as an option to include tripping locations and this resulted in the graph that can be seen in Figure 8.19. For lower TSR regions (where the bubble is more dominant) more power will be produced and when going to higher TSR regions the power decreases since there is a decrease in airfoil performance. The C_P difference at TSR = 2.6 between the two data sets is less than 1% which is acceptable. What is seen in Figure 8.19a is that the TSR optimum shifts from 2.6 to 2.35 for the tripped case.

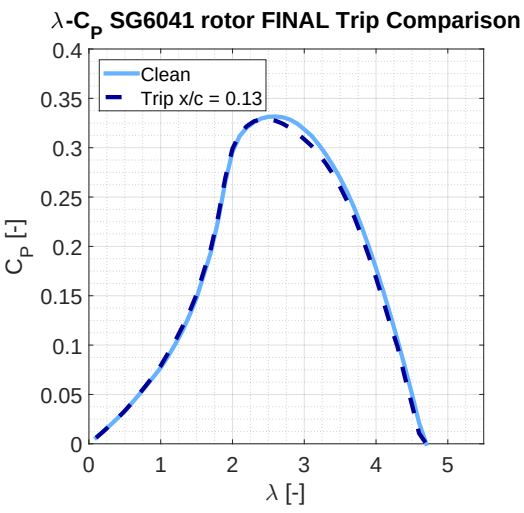

(a) C_P curve for final rotor

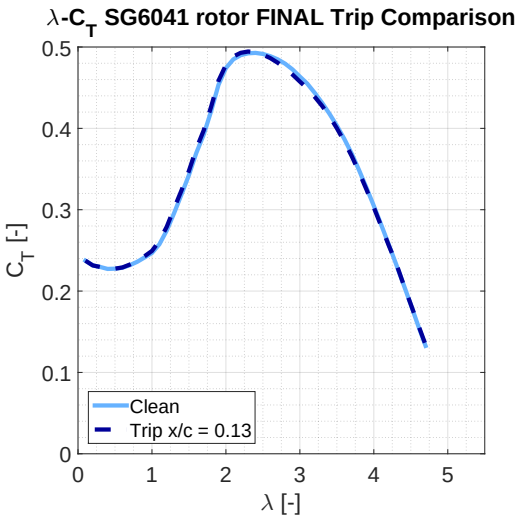

(b) C_T curve for final rotor

Figure 8.19: Power coefficient and thrust coefficient BEMT calculations for SG6041, D= 12.75 cm (blade length)

It is advised to place this trip so that there are no unexpected separation bubbles. If this trip is placed the rotor can be milled and a more durable rotor can be manufactured.

Chapter 9

Kite Power

Going back to the real objective of the thesis which is to design a wind turbine that can charge/ power the batteries from the KCU to keep control over the kite. It is chosen to design low drag wind turbine to keep the efficiency of the complete system as high as possible. This will be obtained by designing the wind turbine so that it will have a minimum drag. In previous chapters, it was described what the procedure is to design a low drag wind turbine.

It is investigated what the effect of the wind turbine will be on power and annual energy production of the kitepower system. Kitepower B.V. has an in-house quasi-steady model that can calculate the power curve of a kite power system. The physics of this model are out of the scope of this thesis and it is only used to compare what the extra energy produced will be, by being able to stay in the air for longer times without the need to land the kite to replace the battery. As a comparing case, it is assumed that the kite has an availability of 80%. It is assumed that the kite can produce 2 hours of energy and then it needs to land to replace the battery. When the kite lands it will take up to 30 minutes to replace the battery manually. This cycle is done over and over and can be seen in Figure 9.1. It is not feasible in real life to have a standard team replacing batteries but this is just a theoretical comparison.

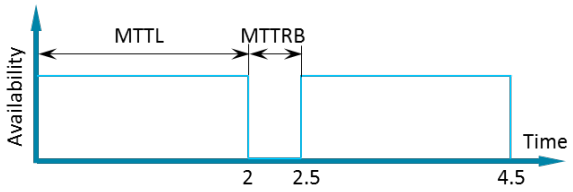

Figure 9.1: Availability of the kite system without the wind turbine with Mean Time To Land (MTTL) and Mean Time To Replace Battery (MTTRB)

9.1 Power Profit

It is assumed that the C_T is around 1.3299 which considers the shroud, blades and total mount set-up for the final rotor and a weight of 500 grams. The drag coefficient was normalised to the kite area. The performance was analysed for three cases with different kite surface area. The kite surface area can be seen in Table 9.1. The power curve for all the different kite surface areas can be seen in Figure 9.2a. For all the cases, it was found that the difference between power curves is negligibly small, the difference is only visible for the 25 m^2 kite. The difference for the wind turbine case is that it is on average 1% lower for all wind speeds. The energy per year was calculated by assuming a Weibull distribution with a shape factor of 2.12 and a scale parameter 10.06, this can be observed in Figure 9.2b. To calculate the annual energy production, the Weibull curve is multiplied with the power curve and then multiplied with 8760 hours. The 8760 hours is the total number of

hours that are available in a year. From this, the energy produced per year can be determined by summing all the energy for each wind speed bin.

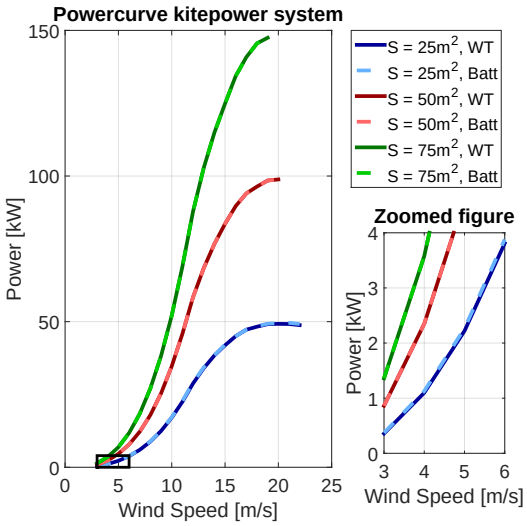

(a) Power curve of kite system with different surface areas

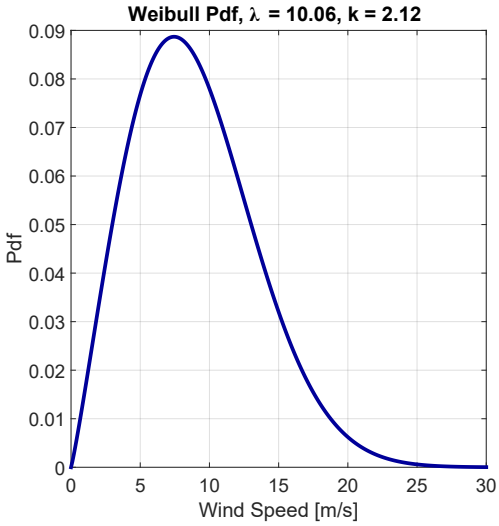

(b) Weibull probability density function for kite power system

The total annual energy produced by the kite with and without wind turbine can be seen in Table 9.1. There is almost no difference between the two cases. The difference is always in the order of 1MWh/year. When assuming an availability of 80% due to the replacing of the battery the difference between the wind turbine and battery becomes much higher. This will result in a power profit for the kite system of 24% when applying a wind turbine.

Table 9.1: The result of mounting a wind turbine on top of KCU compared to landing kite

	Power [MWh/year]			
Kite Area $[m^2]$	WT	Battery	Battery (80% operation)	profit for mounting WT
25	133.181	134.192	107.354	24%
50	268.175	268.866	215.092	24%
75	402.889	403.865	323.092	24%

Chapter 10

Conclusions & Recommendations

This final chapter will give a summary of the research performed and what the main findings are. The main conclusion will be discussed while answering the research question in section 10.1, and in section 10.2 the recommendations will be formulated for further research on this topic. The recommendations are split into two parts, one is research related which contains everything to improve the project or some interesting topics for the future. The second part is engineering recommendations which will contain recommendations related to the design and what can be improved on the total set-up so that continuous flight can be assured.

10.1 Conclusions

The objective of this research is to design a small wind turbine that will be mounted on top of the KCU of Kitepower. For this system, it is important that the drag of the wind turbine is as low as possible so that annual energy produced by the AWE system is high. The second objective is to perform an analysis to investigate what the noise levels are of the wind turbine and if it not exceeds the noise levels defined by regulations. The following objectives will go over the success of the thesis. The first is the investigation on the procedure to design low drag wind turbines by using numerical as well as experimental methods. Second, the noise sources need to be investigated and predicted by numerical and experimental methods to see if the noise would not exceed governmental limits for sensitive areas. At the end of the thesis, a final design was developed for Kitepower that will produce the required power and have a minimum drag.

From chapter 3 the research questions can be found that were created to solve the problem. In the following sections, the answers to these questions will be given. The questions are answered based on the two wind turbines designed and tested.

How can a combination of blade element momentum theory and lifting line method be used to develop a low drag wind turbine?

- *Is the BEMT or LL method accurate enough to predict the performance of a fast spinning small wind turbine?* It was found that BEMT showed good comparison with Bladed and experimental data. When Comparing BEMT predictions with experimental data it was found that the $C_{P_{max}}$ is around 1-6 % difference for appropriate airfoils. The optimum TSR was noted to be shifted to higher TSR than anticipated. The lifting line method showed only good agreement for the large NREL 5MW rotor. When comparing the smaller and mini rotors large discrepancies were observed between lifting line and Bladed. This must do with the Kutta-Joukowski theorem which relates the circulation to lift. The problem with low Re number flow is that the flow separates easier resulting in lift loss which is not considered by the Kutta condition. Because of this analysis, it can be concluded that lifting line will currently not work for small wind turbines. Small rotors have high RPM and compressible effects should be considered for large TSR. This is done by a built-in function in Rfoil which is the Karmen-Tsien rule.
- *What is the difference in accuracy between the two methods compared to Bladed?* In general, the BEMT and Bladed agree well with each other. It was seen in most cases that the root and tip give different values which are probably due to the different engineering models used. The lifting line agrees well for the NREL 5MW wind turbine except at the root section some deviation can be seen. This is because

of the high angles of attack at the root section which will result in wrong circulation prediction by the Kutta-Joukowski theorem. The error for the lifting line model became much higher for the small wind turbines. The small wind turbines operate at much lower Reynolds numbers which will introduce a larger viscous effect which is not considered by the Kutta-Joukowski theorem. This resulted in unrealistic high C_l values due to the high angles. It was noticed that the AoA is in the deep stall region according to lifting line. It can be concluded that the BEMT agrees with minor differences compared with Bladed while lifting line does not agree for small wind turbines.

- *What is the best method for determining the airfoil polar data?* It was decided early in the thesis to limit the use of measured data sets. It was chosen to either use Xfoil or Rfoil. These are panel codes that can determine the lift and drag polar for different airfoils. The next step is to determine which one gave the best result for low Re numbers flow. This was done by comparing measured data from Selig with the results from Xfoil and Rfoil. The input used in both programs is to use N=11 because of the low-turbulence tunnel used for the measurements. It was found that Xfoil predicted for one case the stall angle correctly and for the other, it was completely off. The $C_{l_{max}}$ was determined better by Xfoil for both cases. Next, there is looked at the drag-lift curve which is predicted better by Rfoil for all the cases. Last besides looking at the critical point the shape of the polar was investigated. Here it was found that in all cases Rfoil predictions were better. Since L/D and the shape of the curve is an important factor it was chosen to use Rfoil over Xfoil. The wind turbine was tested in the W-tunnel which has much higher TI values than the experiments performed by Selig. For this reason, during the simulation, the critical amplification ratio was kept fixed at 3. This seemed to be a good choice since the errors are low when comparing the performance of the wind turbine.

- *Is a Brute force optimiser efficient enough to create an initial low drag blade design?* The optimiser chosen was a brute force optimiser due to its simplicity. It was chosen to optimize for low drag. The first version of the optimiser assumed that the Re number stayed constant which resulted in large deviations of the power and drag. For this reason, the optimiser was updated for the final design and it is now assumed that the Re changed, which gave better results. The main assumption of the optimiser is that the twist stays constant which was the main cause of the shift in optimum TSR. The weakness in this optimiser is the simplifications made. To solve this and make better predictions it would be advised to make a higher order optimiser.

- *What is the effect of the airborne wind turbine on the performance of the AWE system?* The effect of the wind turbine on the kite will be that extra drag and mass will be introduced which will decrease the performance. The performance drop is negligibly small in the order of 1% for the power curve. The wind turbine is necessary for Kitepower BV to succeed. However, the question arises what will be the difference in energy production over a year if the kite has to land every 2 hours. This will result that the wind turbine set up will generate up to 24 % more energy a year. This is only from a theoretical standpoint and is practical, not feasible.

What is the effect measured when mounting a shroud on the wind turbine?

- *What happens with the mechanical power?* It was observed that the power decreased significantly when mounting the shroud. Normally the power was assumed to go down with less than 20% but from the measurements, it was found that the performance decreased up to 30%. The reason why the efficiency went down is because of the imperfect manufacturing of the shroud. The main reason is that the efficiency will go down because of the gap between the shroud and blades. This effect is called tip leakage. Tip leakage will create a large shedding vortex decreasing the efficiency of the blades. This vortex will change the performance of the outer side of the blade resulting in a significant power drop. The final design will experience less trouble from this effect because the gap can be made smaller.

- *What happens with the drag of the blades?* Similar effect was noticed for the drag as for the power. The drag decreased significantly compared to the initial case. This has to do with the tip leakage resulting in lower blade loading and lower rotor drag. From the measurements, it was seen that for the clean case the drag was significantly higher than anticipated so an exact value in the decrease in drag cannot be measured but the trends were visible when mounting on the shroud.

- *What happens with the noise?* The quality of noise measurements is not good due to the environmental noise. No real meaningful conclusion could be drawn between the noise differences between the

shrouded and clean case on the 1/3 octave spectrum. From the measurements, it seems that the rotational frequency will be suppressed by the shroud but this cannot be concluded with 100 % certainty.

What is the difference between measured noise and predicted? And do small spinning wind turbine make more than 47 dB(A) noise at sensitive locations?

- *Can the tonal peaks be observed in an experimental set up?* Due to the large background noise, it was difficult to filter out the environmental noise. However, for the clean case tonal components are visible at the rotational frequency. It was expected that a tonal peak would be visible at the blade passing frequency but this was not the case. This could be due to the background noise but more likely is that the tower does not have a big blockage effect resulting in lower unsteady loading when a blade passes.
- *Can BPM be used to determine the general noise levels of small wind turbines?* 5 out of 7 noise sources were verified against NAFNoise and showed good similarities. From these 5 all of them are dominant noise sources for small wind turbines. Tip vortex shedding was not verified since NAFNoise cannot predict this. However, this noise source will be for the small wind turbine in the non-hearing range for humans. The turbulent inflow noise is not verified and is the main noise source for low-frequency noise. It was observed that similar results were obtained as Dijkstra [33]. Next, the predicted results are validated against the experimental measurements. This showed that the values from experimental are much higher than what was predicted. This is to blame on the quality of the measurements. However, most of the data showed similar trends and dominant noise sources were predicted correctly. From this, it was concluded that the BPM model works but more research is necessary.
- *What is the effect of the shroud on the sound pressure levels?* No real conclusion could be drawn regarding this question due to the bad measurement quality. What can be said is that the TSR optimum is lower for the shrouded data which will result that the tonal noise and harmonics will be at a lower frequency. The small differences could not be observed due to the background noise.
- *What are the main noise losses in the atmosphere and what is the effect?* It is assumed that four main attenuation losses are present. The main loss is from spherical spreading and for the high frequencies, the atmospheric absorption will have a significant effect. Besides these two, reflection with the ground and the wind are considered. This will lead that for some frequencies the SPL is increased while for others it is decreased. It was found that when the kite has a reeled out tether of 400 meters with an elevation angle of 20° the regulated SPL_{den} of 47 dB would never be surpassed.

Over the course of this thesis, several research questions have been answered. At the end of the thesis, a final redesign was developed by using the revised optimiser and BEMT. It was shown that the noise would never be a problem if the kite stays higher than 136 meters above the ground since the SPL_{den} is lower than 24.9 dB(A). The software coded is developed in such a way that only a power requirement is necessary together with generator manual and an estimate of the efficiency of the complete electrical system. From the findings, it was shown that the BEMT has a sufficient accuracy and there is an under-prediction of the optimum TSR. The BPM model seems to perform well and similar trends were observed with the experimental data. It can be concluded that the BPM works but more validation and verification is necessary.

10.2 Recommendations

Many phenomena have been investigated but still, many more things can be done. This section elaborates more on what still can be done. Since there are two main groups the recommendations will be divided in research related recommendations and engineering recommendations.

10.2.1 Research Recommendations

The BEMT was used and it was tried to use the lifting line free wake method to investigate the performance of the wind turbine. The initial goal was to investigate the yawed inflow with the lifting line. Since the lifting line does not work for small wind turbines it is advised to develop a dynamic BEMT to simulate the inflow from different directions. This dynamic model can maybe be tuned such that it can simulate simple flying patterns. When flying different patterns unsteady effects will play an important role. However, probably current models are not yet able to simulate such complicated flying patterns.

It would be an interesting research project to investigate the behaviour of an airborne wind turbine when flying different patterns. It would be nice to see the unsteady effect of the different inflows and would be valuable since now it is assumed that the wind speed is always 30 m/s and the flow is aligned. It is expected that there will be some delay with the power when the inflow angle is suddenly changed.

One of the most important recommendations is to redo the experimental campaign to acquire new noise data to validate the BPM model. This will need to be performed in an appropriate wind tunnel with low background noise so it is easier to filter out the signals of the wind turbine. Based on this, a better conclusion could be drawn on what the effect is on the shroud.

The current model assumes 20% efficiency decrease due to adding the shroud. It would be beneficial to update the BEMT such that it takes the effect of the shroud into account. This can be done by placing circulation on the shroud and see what the induced speed is. If this model works the wind turbine shroud could be optimised to increase the wind turbine performance. The diffuser can be investigated with simple methods and more advanced methods like CFD.

It would be valuable to redo the power measurements with a torque transducer, so the accuracy of current methods can be defined. It is expected if the torque transducer is used the wake could be further developed and more representable data can be obtained.

It is of importance to mount the wind turbine on the kite demonstrator. So that it can be seen how the wind turbine performance and more insight is obtained. This project can only be succesfull if reliable sensor are used to measure the electrical power, apparant wind speed and inflow angles.

Last the optimiser used now is not efficient and it is easy to make mistakes. It could be interesting to investigate a more complex optimiser. Different blade optimisers could be considered such as a generic optimiser.

10.3 Engineering Recommendations

The next part is to make the wind turbine more efficient and reliable. For this, there are some recommendations which are more valuable for Kitepower. The first recommendation is to investigate and take an appropriate generator where all the data is available from. Meaning not using a motor as an alternator. Next, there were also lots of heating problems during testing. This can be resolved by using a custom designed metal encasing with heating paste to conduct the heat in a much more efficient way.

Next, a proper analysis needs to be performed of the power consumption of the KCU. The required 44 Watt was now determined with engineering guesses and this could be much more accurate if the consumption would be measured on a test panel.

Before flight it is advised to test the whole system with the maximum power point tracker(MPPT), to see if the MPPT can track if large power drops are present.

A study needs to be performed on which material should be used for the final design. 3D printing is a good method for prototyping but is not feasible for long and reliable power generation. For the final design, it might be good to look at a more durable material such as aluminium. Like already mentioned trough the report if this material is chosen a trip need to be placed. It is important to design the trip so that it is not too high.

Next, the manufacturing of the shroud should be performed by the right tools. If this is done the shroud can be made smaller and the gap between the blades and shroud can decrease to 1 mm. This will reduce the tip leakage and minimise the efficiency drop of the power. Currently, Maxon motors will manufacture a 5 cm shroud it would be interesting to make the shroud just thin enough so that less mass is introduced in the system.

Because of delays, it was not possible to test the whole system on the kite system. This would be the next big step to mount it on the KCU and fly and see how the wind turbine performs. According to the calculations

and wind tunnel measurements, there should be enough power. Next, a data link should provide information on how much power the wind turbine is producing.

Bibliography

[1] S. Wagner, G. Guidati, and R. Bareib, *Wind Turbine Noise*, 1st ed. (1996) p. 216.

[2] D. Russel, *Acoustics and Vibrations,* (2001).

[3] S. Oerlemans, *Validation Against Experiment,* **8**, 555 (2009).

[4] M. O. L. Hansen, J. N. Sorensen, S. Voutsinas, N. Sorensen, and H. A. Madsen, *State of the art in wind turbine aerodynamics and aeroelasticity,* Progress in Aerospace Sciences **42**, 285 (2006).

[5] T. Burton, D. Sharpe, N. Jenkins, and E. Bossanyi, *Wind Energy Handbook*, 1st ed., edited by John Wiley & Sons (John Wiley & Sons, West Sussex, 2001) pp. 1–596.

[6] D. Wood, *Snall Wind Turbines: Analysis, Design, and Application* (Springer, 2012).

[7] a. V. Garrel, *Development of a wind turbine aerodynamics simulation module*, Tech. Rep. (2003).

[8] Katz, *Low speed aerodynamics,* .

[9] J. Anderson, *Fundamentals of Aerodynamics*, 2nd ed. (Mcgraw-Hill, 1991) p. 771.

[10] T. F. Brooks, S. Pope, and M. A. Marcolini, *Airfoil Self-Noise and Prediction,* NASA Reference Publication 1218 , 1 (1989).

[11] B. Plovsing and J. Kragh, *Nord2000. Comprehensive Outdoor Sound Propagation Model. Part 1: Propagation in an Atmosphere without Significant Refraction*, Tech. Rep. (DELTA, 2001).

[12] Plovsing, *Nord2000. Comprehensive Outdoor Sound Propagation Model. Part 2: Propagation in an Atmosphere with Refraction*, Tech. Rep. (DELTA, 2006).

[13] U. Fechner, *A Methodology for the Design of Kite-Power Control Systems*, Ph.D. thesis, Delft University of Technology (2016).

[14] K. Boorsma, *Power and loads for wind turbines in yawed conditions*, Tech. Rep. November (2012).

[15] M. Loyd, *Crosswind kite power (for large-scale wind power production),* Journal of Energy **4**, 106 (1980).

[16] M. Lowson, *new Prediction model for wind noise,* Response , 177 (1993).

[17] R. Schmehl, *Airborne Wind Energy* (Springer, 2013) p. 609.

[18] A. Cherubini, A. Papini, R. Vertechy, and M. Fontana, *Airborne Wind Energy Systems : A review of the technologies,* Renewable and Sustainable Energy Reviews **51**, 1461 (2015).

[19] M. O. L. Hansen and H. A. Madsen, *Review Paper on Wind Turbine Aerodynamics,* Journal of Fluids Engineering **133**, 114001 (2011).

[20] M. Clifton-Smith, *Wind Turbine Blade Optimisation with Tip Loss Corrections,* Wind Engineering **3**, 477 (2009).

[21] O. de Vries, *Fluid Dynamics Aspects of Wind Energy Conversion,* Advisory Group for Aerospace Research and Development (2013).

[22] Z. Du and M. Selig, *A 3-D Stall-Delay Model for Horizontal Axis Wind Turbine Performance Prediction,* AIAA **21** (1997), 10.2514/6.1998-21.

[23] M. Vicente, J. Carlos, and R. G. Annes, *a Vortex Lattice Program for Steady State Aerodynamic Analysis of Wind Turbine Blade Loads,* **2** (2011).

[24] M. Døssing, *Vortex Lattice Modelling of Winglets on Wind Turbine Blades,* **1621** (2007).

[25] a. V. Garrel, *Development of a Wind Turbine Rotor Flow Panel Method,* (2011).

[26] N. Ramos-García, J. Sørensen, and W. Shen, *Three-dimensional viscous-inviscid coupling methodfor wind turbine computations,* Wind Energy **17**, 657 (2014), arXiv:arXiv:1006.4405v1 .

[27] D. Hartwanger and A. Horvat, *3D Modelling of a Wind Turbine Using Cfd,* Control **2**, 1 (2008).

[28] M. S. Selig, *Low Reynolds Number Airfoil Design Lecture Notes VKI Lecture Series Various Approaches to Airfoil Design,* (2003) pp. 24–28.

[29] M. Selig, J. J. Guglielmo, A. P. Broeren, and P. Giguere, *Summary of Low-Speed Airfoil*, Vol. 1 (SoarTech Publications, Virginia, 1995) p. 315.

[30] M. S. Selig and B. D. McGranahan, *Journal of Solar Energy Engineering*, Vol. 126 (2004) p. 986.

[31] M. S. Selig, C. A. Lyon, P. Giguere, C. P. Ninham, and J. J. Guglielmo, *Summary of Low-Speed Airfoil Data*, Vol. 2 (1996).

[32] O. F. Gasch, *Assessment , Development and Validation of Wind Turbine Rotor Noise Prediction Codes,* (2014).

[33] P. Dijkstra, *Rotor noise and aero- acoustic optimization of wind turbine airfoils*, Ph.D. thesis (2015).

[34] G. Müller and M. Möser, *Handbook of Engineering Acoustics*, edited by G. Müller and M. Möser (Springer, 2013) p. 702.

[35] P. Breysse and P. Lees, *Noise Lecture 6,* (2006).

[36] M. Friman, *Directivity of sound from wind turbines*, Ph.D. thesis, KTH Vetenskap och konst (2011).

[37] M. . J. . Lighthill, *On Sound Generated Aerodynamically . II . Turbulence as a Source of Sound,* Royal Society of London **222**, 1 (1953).

[38] M. Lighthill, *On sound generated aerodynamically I. General theory,* **358**, 467 (1951).

[39] N. Curle, *The Influence of Solid Boundaries upon Aerodynamic Sound,* The royal society of London **231**, 50 (1955).

[40] J. E. Ffowcs Williams and L. H. Hall, *Aerodynamic sound generation by turbulent flow in the vicinity of a scattering half plane,* Journal of Fluid Mechanics **40**, 657 (1970), arXiv:arXiv:1011.1669v3 .

[41] R. K. Amiet, *Acoustic Radiation from an airfoil in a turbulent stream,* **41**, 407 (1975).

[42] S. Vanhaeverbeke, *Simulation of Aeroacoustic Emission For Small Wind Turbines,* , 1 (2007).

[43] P. Moriarty, *NAFNoise,* (2005).

[44] C. Tam, *Computational aeroacoustics-Issues and methods,* AIAA journal **33**, 1788 (1995).

[45] *Acoustic-Attenuation of sound during propagation outdoors-Part2: General method of calculation (ISO9613-2)*, Tech. Rep. (1996).

[46] J. Steenis, H. Geleijns, and M. Dijkstra, *Literatuuronderzoek laagfrequent geluid windturbines*, Tech. Rep. September (Agentschap NL: Ministerie van Economische Zaken, Utrecht, 2013).

[47] M. Motors, *maxon EC motor M 1 : 2,* (2011).

[48] W. Shen, *Tip Loss Corrections for Wind Turbine Computations,* Wind Energy **8**, 457 (2005).

[49] Z. Du and M. Selig, *A 3-D stall-delay model for horizontal axis wind turbine performance prediction,* AIAA , 11 (1998).

[50] A. Bianchini, . Balduzzi, J. M. Rainbird, J. M. R. Graham, G. Ferrara, and L. Ferrari, *An Experimental and Numerical Assessment of Airfoil Polars for Use in Darrieus Wind Turbines — Part II : Post-stall Data Extrapolation Methods,* **138**, 1 (2016).

[51] T. Sebastian, *Wake Induced Dynamics Simulator —WInDS—*, Tech. Rep. (2011).

[52] T. Cebeci, *Analysis of Turbulent Flows with Computer Programs* (2013).

[53] M. Drela, *XFOIL:An Analysis and Design System for Low Reynolds Number Airfoils*, Tech. Rep. (MIT Dept. of aeronautics and Astronaitics, Massachusetts, 1989).

[54] R. P. J. O. M. V. Rooij and W. Timmer, *Roughness Sensitivity Considerations for Thick Rotor Blade Airfoils,* ASME **125**, 468 (2003).

[55] G. A. Williamson, B. D. Mcgranahan, B. A. Broughton, R. W. Deters, J. B. Brandt, and M. S. Selig, *Summary of Low-Speed Airfoil*, Vol. 5 (2012).

[56] C. A. Lyon, A. P. Broeren, P. Gigu, A. Gopalarathnam, and M. S. Selig, *Summary of Low-Speed Airfoil Data*, Vol. 3 (1997).

[57] J. Jonkman, S. Butterfield, W. Musial, G. Scott, J. Jonkman, S. Butterfield, W. Musial, and G. Scott, *Definition of a 5-MW Reference Wind Turbine for Offshore System Development Definition of a 5-MW Reference Wind Turbine for Offshore System Development*, Tech. Rep. February (NREL, 2009).

[58] J. A. Karlsen, *Performance Calculations for a Model Turbine,* (2009).

[59] ISO, *Acoustics-Attenuation of sound during propagation outdoors,* (1996).

[60] G. Kenway, *Aerostructural Shape Optimization of Wind Turbine Blades Considering Site-Specific Winds,* , 1 (2008).

[61] B. V. D. Kieboom, *Stage verslag Kitepower,* (2013).

[62] T. Delft, *w-tunnel-hsl,* (2017).

[63] R. Kishore, *Small-scale Wind Energy Portable Turbine (SWEPT)*, Ph.D. thesis (2013).

[64] D. Yongle, S. Baowei, and W. Peng, *Numerical investigation of tip clearance effects on the performance of ducted propeller,* International Journal of Naval Architecture and Ocean Engineering **7**, 795 (2015).

IV

Appendix

Appendix A

Code Flow Charts

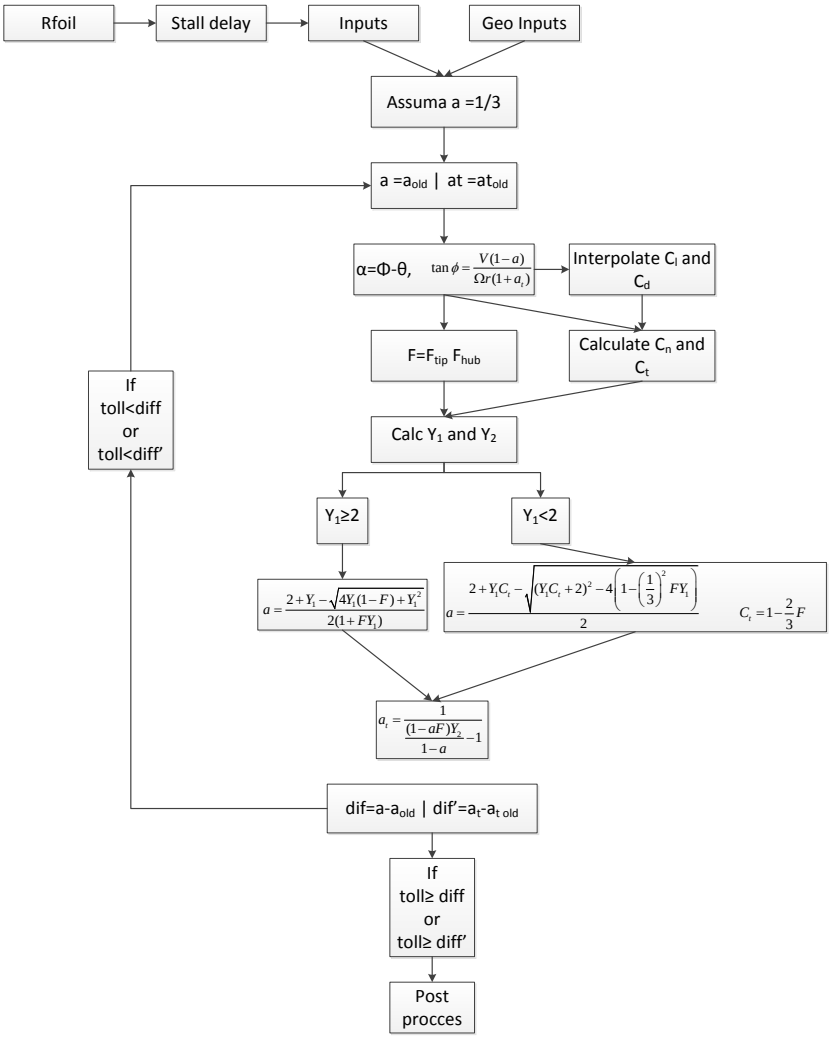

Figure A.1: Flow chart BEMT

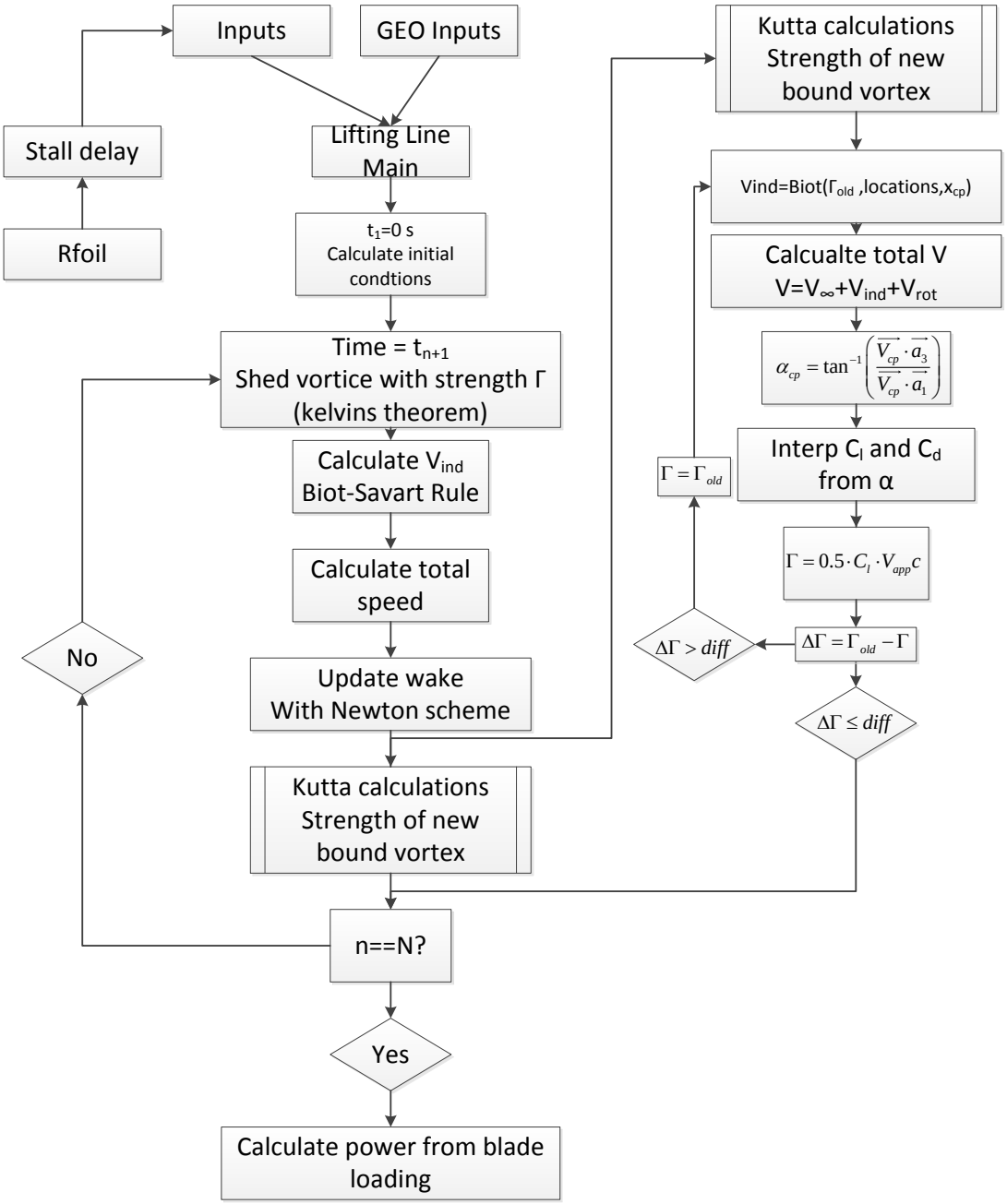

Figure A.2: Flow chart lifting line

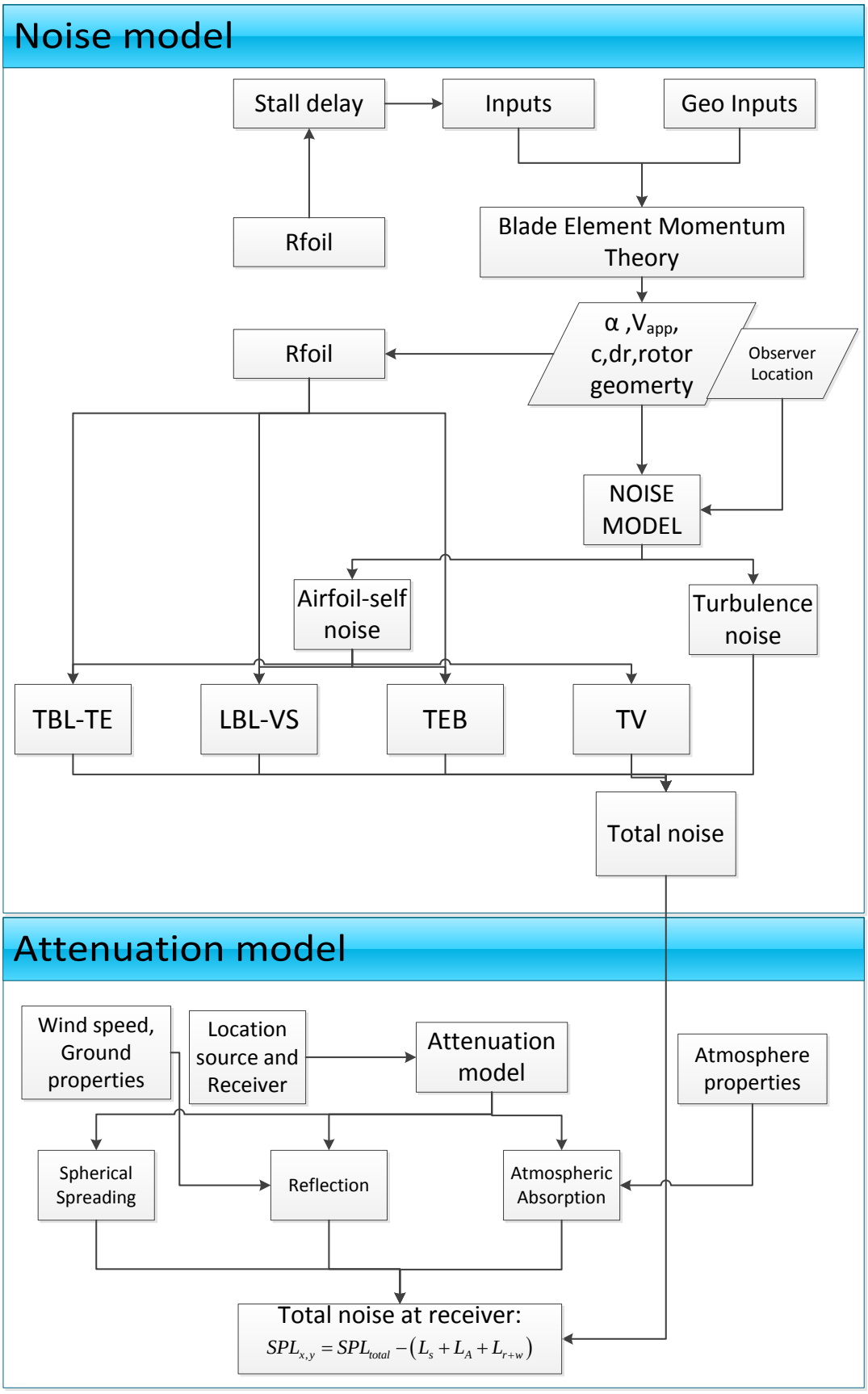

Figure A.3: Noise model flow chart

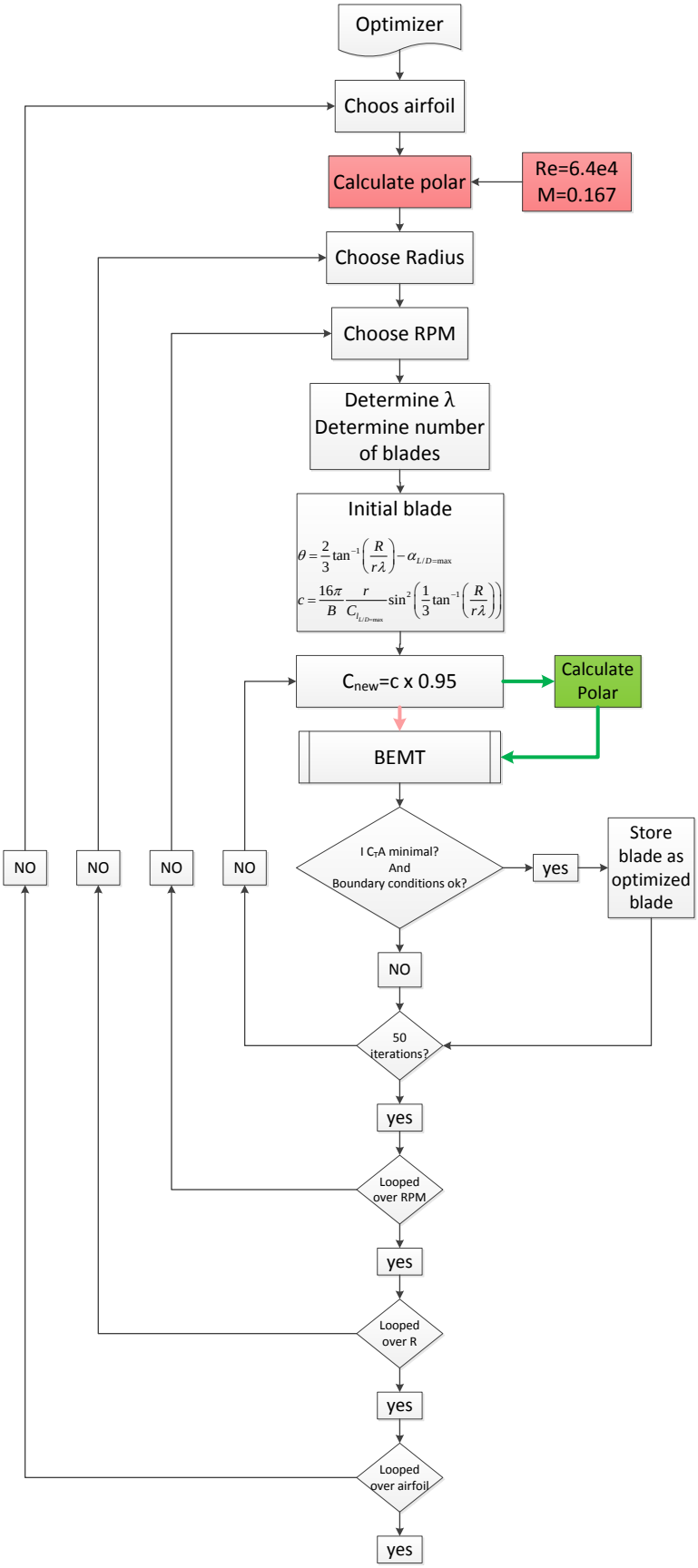

Figure A.4: Optimizer, red blocks are old optimizer from chapter 7 and green blocks are new one

Appendix B

Rotor Designs

B.1 Verified Rotors

Table B.1: Geometrical distribution of the NREL 5 M Watt wind turbine [57]

Radial [m]	Chord[m]	Twist [°]	Airfoil
0	3.542	13.308	Cylinder1
2.87	3.542	13.308	Cylinder1
5.6	3.854	13.308	Cylinder1
8.33	4.167	13.308	Cylinder2
11.75	4.557	13.308	DU40_A17
15.85	4.652	11.48	DU35_A17
19.95	4.458	10.162	DU35_A17
24.05	4.249	9.01	DU30_A17
28.15	4.007	7.795	DU25_A17
32.25	3.748	6.544	DU25_A17
36.35	3.502	5.361	DU21_A17
40.45	3.256	4.188	DU21_A17
44.55	3.01	3.125	NACA64_A17
48.65	2.764	2.319	NACA64_A17
52.75	2.518	1.526	NACA64_A17
56.1667	2.313	0.863	NACA64_A17
58.9	2.086	0.37	NACA64_A17
61.633	1.419	0.106	NACA64_A17

Table B.2: 0.9 m verification rotor blade lay-out[58]

Radial position [cm]	Chord [cm]	Twist angle [∘]	Airfoil
4.5	4.95	38	S826
5.5	4.95	38	S826
11.25	7.3125	25.26	S826
15.75	6.110231	18.03	S826
20.25	5.120424	13.067	S826
27.75	3.96	7.9877	S826
30.75	3.62007	6.564977	S826
36.75	3.081913	4.1316	S826
39.75	2.866371	2.943336	S826
44.25	2.592566	-0.7167	S826
45	2.592566	-0.7167	S826

B.2 Optimised Rotors

Table B.3: NACA rotor blade layout

Radial position [cm]	Chord [cm]	Twist angle [◦]	Airfoil
2.5	2.375285	36.57567	NACA4418
2.514655	2.379123	36.48377	NACA4418
2.558449	2.390158	36.21054	NACA4418
2.630867	2.407011	35.76327	NACA4418
2.731061	2.427589	35.15385	NACA4418
2.857857	2.449361	34.3983	NACA4418
3.009767	2.469667	33.51609	NACA4418
3.185011	2.486038	32.52937	NACA4418
3.381534	2.496454	31.4619	NACA4418
3.597032	2.499517	30.33804	NACA4418
3.828979	2.494525	29.18167	NACA4418
4.074655	2.481451	28.01518	NACA4418
4.331179	2.460844	26.8588	NACA4418
4.595545	2.433686	25.73002	NACA4418
4.864653	2.401237	24.64335	NACA4418
5.135347	2.364887	23.61033	NACA4418
5.404455	2.326035	22.63965	NACA4418
5.668821	2.286001	21.7375	NACA4418
5.925345	2.245972	20.90793	NACA4418
6.171021	2.206971	20.15325	NACA4418
6.402968	2.169853	19.47442	NACA4418
6.618466	2.135312	18.87145	NACA4418
6.814989	2.103896	18.34364	NACA4418
6.990233	2.076029	17.88991	NACA4418
7.142143	2.052031	17.50895	NACA4418
7.268939	2.032137	17.19944	NACA4418
7.369133	2.016516	16.96015	NACA4418
7.441551	2.005284	16.79003	NACA4418
7.485345	1.998518	16.68828	NACA4418
7.5	1.996258	16.65442	NACA4418

Table B.4: SG6041 rotor blade layout

Radial position [cm]	Chord [cm]	Twist angle [◦]	Airfoil
2.5	3.092598	34.05379	SG6041
2.516853	3.095948	33.93945	SG6041
2.567216	3.105211	33.60026	SG6041
2.650497	3.11817	33.04756	SG6041
2.765721	3.131569	32.29963	SG6041
2.911536	3.141675	31.38073	SG6041
3.086232	3.144893	30.31982	SG6041
3.287763	3.138306	29.14885	SG6041
3.513764	3.120041	27.90097	SG6041
3.761587	3.089423	26.60865	SG6041
4.028326	3.046917	25.3021	SG6041
4.310853	2.993906	24.00797	SG6041
4.605856	2.932399	22.74856	SG6041
4.909877	2.864716	21.5416	SG6041
5.219351	2.793227	20.40028	SG6041
5.530649	2.720151	19.33374	SG6041
5.840123	2.647443	18.34763	SG6041
6.144144	2.576731	17.4448	SG6041
6.439147	2.509316	16.62599	SG6041
6.721674	2.446189	15.89036	SG6041
6.988413	2.388079	15.23607	SG6041
7.236236	2.335495	14.66063	SG6041
7.462237	2.288779	14.16128	SG6041
7.663768	2.248141	13.73521	SG6041
7.838464	2.213701	13.37973	SG6041
7.984279	2.185516	13.09241	SG6041
8.099503	2.163606	12.87118	SG6041
8.182784	2.147968	12.71438	SG6041
8.233147	2.138591	12.62079	SG6041
8.25	2.135467	12.58967	SG6041

B.3 Final Rotor Design

Table B.5: Final rotor design

Radial position [cm]	Chord [cm]	Twist angle [o]	Airfoil
1.000	1.117	42.373	SG6041
1.016	1.127	42.201	SG6041
1.063	1.156	41.691	SG6041
1.141	1.200	40.856	SG6041
1.248	1.254	39.723	SG6041
1.385	1.311	38.327	SG6041
1.548	1.366	36.710	SG6041
1.736	1.412	34.925	SG6041
1.948	1.446	33.026	SG6041
2.179	1.465	31.068	SG6041
2.429	1.470	29.105	SG6041
2.693	1.461	27.180	SG6041
2.969	1.440	25.332	SG6041
3.253	1.411	23.587	SG6041
3.542	1.376	21.963	SG6041
3.833	1.337	20.472	SG6041
4.122	1.297	19.116	SG6041
4.406	1.257	17.895	SG6041
4.682	1.218	16.806	SG6041
4.946	1.181	15.842	SG6041
5.196	1.148	14.996	SG6041
5.427	1.117	14.261	SG6041
5.639	1.090	13.630	SG6041
5.827	1.067	13.098	SG6041
5.990	1.047	12.657	SG6041
6.127	1.031	12.303	SG6041
6.234	1.019	12.032	SG6041
6.312	1.010	11.841	SG6041
6.359	1.005	11.727	SG6041
6.375	1.003	11.689	SG6041

B.4 Verification of the Optimiser

Large deviations arise between the optimiser and BEMT when comparing the optimum TSR, power, and drag. This means that there is a chance that the result of the optimiser might not give the reel lowest drag design. To see if this is not the case and that the optimiser gives the lowest drag the optimiser is started and all the optimised blades are saved during convergence. When the final design is ready after N optimised designs the last three design are compared with BEMT. From BEMT the optimum TSR, drag, and power are calculated. It can be assumed that the optimiser works if the drag is decreasing when going from N-2 design to the Nth design. The rotors were optimised for a wind speed of 30 m/s a hub diameter of 5 cm and a minimum mechanical power of 63. The rotors designed here are for a proof of concept that the optimiser work ad gives the right rotor for minimum drag, for this reason, there is only chosen for 1 airfoil in the optimiser and that is the SG6041 airfoil. The three last design according to the optimiser can be seen in Table B.6, all three blades have 4 blades and a hub diameter of 5 cm. The rotor consists of 4 blades. Their performance that the optimiser calculated can be seen in Table B.7.

From the three different blades, it can be seen that two out of three rotors have a diameter of 13.64 cm and the last design has a diameter of 13.28 cm.

The next step was to calculate the performance of the rotors with BEMT and compare what the drag is of the individual rotors at optimum TSR. In Table B.7 the result of BEMT and optimiser can be seen. It is clear that the final design has the lowest drag. The drag of this wind turbine is 3.191 N according to BEMT. This is still 9% higher than what the optimiser calculated. It can also be seen that the optimum TSR is shifted 5 % to the right. This means that the assumption of keeping twist constant can have as an effect that the power

Table B.6: Blade design from optimiser all blades have an SG6041 airfoil with a hub radius of 5 cm and 4 blades

Design N-2			Design N-1			Design N		
r [cm]	c [cm]	twist[°]	r [cm]	c [cm]	twist[°]	r [cm]	c [cm]	twist[°]
2.50	1.03	24.78	2.50	1.28	28.57	2.50	1.08	24.78
2.55	1.02	24.37	2.55	1.28	28.17	2.55	1.07	24.39
2.71	1.01	23.21	2.71	1.27	27.03	2.71	1.06	23.28
2.97	0.98	21.49	2.97	1.25	25.31	2.95	1.03	21.61
3.31	0.94	19.44	3.31	1.22	23.23	3.28	0.99	19.63
3.72	0.89	17.31	3.72	1.18	21.02	3.67	0.94	17.56
4.18	0.83	15.28	4.18	1.12	18.86	4.11	0.88	15.57
4.66	0.78	13.46	4.66	1.06	16.89	4.57	0.83	13.78
5.14	0.73	11.91	5.14	1.01	15.17	5.03	0.77	12.24
5.60	0.68	10.63	5.60	0.95	13.75	5.47	0.73	10.97
6.01	0.65	9.62	6.01	0.91	12.61	5.86	0.69	9.97
6.35	0.62	8.87	6.35	0.88	11.75	6.19	0.66	9.21
6.61	0.60	8.34	6.61	0.85	11.15	6.44	0.64	8.68
6.77	0.59	8.03	6.77	0.84	10.79	6.59	0.63	8.37
6.82	0.58	7.93	6.82	0.83	10.68	6.64	0.63	8.27

is higher when comparing it to BEMT. The second reason why this variation is present is due to the assumption in the optimiser to use only one airfoil polar with the average Re number. Since this only airfoil polar is used during optimization the optimum TSR will differ and the power and drag will vary. However, this still proofs that the optimiser creates the lowest drag design and as mentioned the verification should always be performed by BEMT.

Table B.7: Numerical values of optimised and Verified values

		design N-2	**design N-1**	**design N**
Optimum TSR	optimiser	3.2 (-8.5 %)	2.3 (-13 %)	3.34 (-5 %)
	BEMT	3.5	2.6	3.5
Thrust	optimiser	2.955(-11 %)	2.925 (-10 %)	2.898 (-9 %)
	BEMT	3.294	3.214	3.191
$C_T \cdot A$	optimiser	0.5311 (-11 %)	0.5306 (-10 %)	0.5256 (-9 %)
	BEMT	0.5976	0.583	0.5788
Power	optimiser	64.57 (-7 %)	64.27 (-5 %)	64.03 (-3,8 %)
	BEMT	69.21	67.9	66.5

In Figure B.1a the convergence of the optimiser can be seen, as mentioned the optimiser start with an over design and then rapidly decreases the drag. In this figure for the BEMT, only the last three design are verified because the trend was visible and it would take much time to calculate all the older steps. It can be seen that the $A \cdot C_T$ for BEMT is much higher than for the optimiser, this is because of the low values and because the drag is divided by the Velocity^2. In figure b and c from Figure B.1 the power and drag calculations can be seen according to BEMT with each their optimum TSR clearly visible.

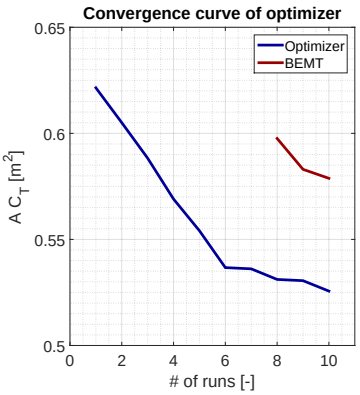

(a) Convergence of the optimzer

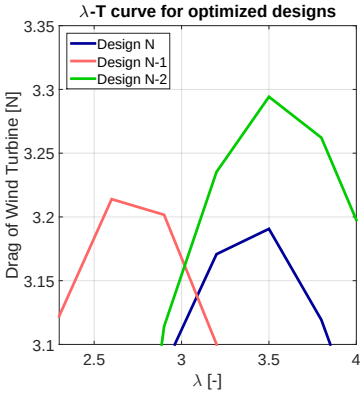

(b) Drag of last three design according to BEMT

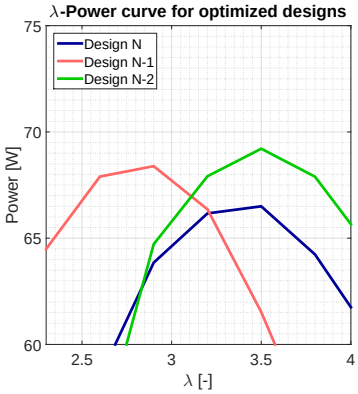

(c) Power of last three design according to BEMT

Figure B.1: $\lambda - C_P$ experimetnal data for SG6041 and shroud

Appendix C

BPM Equations

C.1 Shape Functions

The BPM model is an empirical model with different noise sources. All these sources are predicted using shape function based on the Strouhal number. The shape function can depend on different variables depending on the noise source. In general, the most used variable are 1/3 octave band frequencies and boundary layer parameters. An example of a shape function can be seen in Figure C.1 which is defined by Brooks et al. [10]

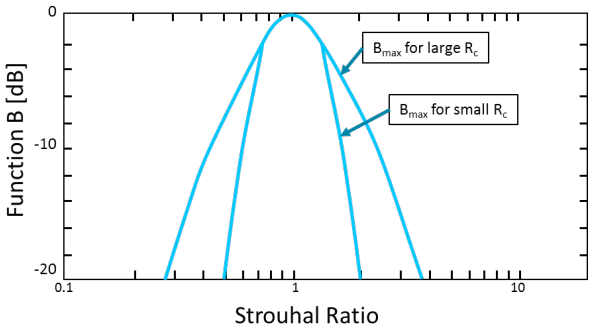

Figure C.1: Shapefunction adapted from Brooks et al. [10]

C.2 TBL-TE

The Strouhal equations for TBL-TE noise are defined according to Equation C.1-C.5

$$St_p = \frac{f\delta_p^*}{U} \tag{C.1}$$

$$St_p = \frac{f\delta_s^*}{U} \tag{C.2}$$

$$St_1 = 0.02M^{-0.6} \tag{C.3}$$

$$\bar{St_1} = \frac{St_1 + St_2}{2} \tag{C.4}$$

$$St_2 = St_1 \times \begin{cases} 1 & (\alpha < 1.33^\circ) \\ 10^{0.0054(\alpha-1.33)^2} & (1.33^\circ \leq \alpha \leq 12.5^\circ) \\ 4.72 & (12.5^\circ < \alpha) \end{cases} \tag{C.5}$$

Next step is to determine the spectral shape function A which depends on a. a depends on St which is depending on the pressure or suctions side St_p or St_s, St_{peak} is defined as the product of St_1 and $\bar{St_1}$.

$$A_{min}(a) = \begin{cases} \sqrt{67.552 - 886.788a^2} - 8.219 & (a < 0.204) \\ -32.665a + 3.981 & (.204 \leq a \leq 0.244) \\ -142.795a^3 + 103.656a^2 - 57.757a + 6.006 & (0.244 < a) \end{cases} \tag{C.6}$$

$$A_{max}(a) = \begin{cases} \sqrt{67.552 - 886.788a^2} - 8.219 & (a < 0.13) \\ -15.901a + 1.098 & (0.13 \leq a \leq 0.321) \\ -4.669a^3 + 3.491a^2 - 16.699a + 1.149 & (0.321 < a) \end{cases} \tag{C.7}$$

$$a = \left| \log_{10}\left(\frac{St}{St_{peak}}\right) \right| \tag{C.8}$$

Equation C.9 is a value that depends solely on the chord based Reynolds number.

$$a_0(R_c) = \begin{cases} 0.57 & \left(R_c < 9.52 \times 10^4\right) \\ \left(-9.57 \times 10^{-13}\right)\left(R_c - 8.57 \times 10^5\right) + 1.13 & \left(9.52 \times 10^4 \leq R_c \leq 8.57 \times 10^5\right) \\ 1.13 & \left(8.57 \times 10^5 < R_c\right) \end{cases} \tag{C.9}$$

$$A_R(a_0) = \frac{-20 - A_{min}(a_0)}{A_{max}(a_0) - A_{min}(a_0)} \tag{C.10}$$

$$A(a) = A_{min}(a) + A_R(a_0)\left[A_{max}(a) - A_{min}(a)\right] \tag{C.11}$$

A similar function to A is defined for the separation. This function is called the shape function B and is calculated in a similar way as A.

$$B_{min}(b) = \begin{cases} \sqrt{16.88 - 886.788b^2} - 4.109 & (b < 0.13) \\ -83.607b + 8.138 & (0.13 \leq b \leq 0.145) \\ -817.810b^3 + 355.210b^2 - 135.024b + 10.619 & (0.145 < b) \end{cases} \tag{C.12}$$

$$B_{max}(b) = \begin{cases} \sqrt{16.88 - 886.788b^2} - 4.109 & (b < 0.10) \\ -31.330b + 1.854 & (0.10 \leq b \leq 0.187) \\ -80.541b^3 + 44.174b^2 - 39.381b + 2.344 & (0.187 < b) \end{cases} \tag{C.13}$$

$$b = \left| \log_{10}\left(\frac{St_s}{St_2}\right) \right| \tag{C.14}$$

$$b_0(R_c) = \begin{cases} 0.30 & \left(R_c < 9.52 \times 10^4\right) \\ \left(-4.48 \times 10^{-13}\right)\left(R_c - 8.57 \times 10^5\right) + 0.56 & \left(9.52 \times 10^4 \leq R_c \leq 8.57 \times 10^5\right) \\ 0.56 & \left(8.57 \times 10^5 < R_c\right) \end{cases} \tag{C.15}$$

$$B_R(b_0) = \frac{-20 - B_{min}(b_0)}{B_{max}(b_0) - B_{min}(b_0)} \tag{C.16}$$

$$B(b) = B_{min}(b) + B_R(b_0)\left[B_{max}(b) - B_{min}(b)\right] \tag{C.17}$$

The last part is the amplitude function K_1 which is depended on the Reynolds number based on chord and δ^*.

$$K_1 = \begin{cases} -4.31\log_{10}(R_c) + 156.3 & \left(R_c < 2.47 \times 10^5\right) \\ -9.0\log_{10}(R_c) + 181.6 & \left(2.47 \times 10^5 \leq R_c \leq 8. \times 10^5\right) \\ 128.5 & \left(8.0 \times 10^5 < R_c\right) \end{cases} \tag{C.18}$$

$$\Delta K_1 = \begin{cases} \alpha\left[1.43\log_{10}\left(R_{\delta_p^*}\right) - 5.29\right] & \left(R_{\delta_p^*} \leq 5000\right) \\ 0 & \left(5000 < R_{\delta_p^*}\right) \end{cases} \tag{C.19}$$

$$K_2 = K_1 + \begin{cases} -1000 & (\alpha < \gamma_0 - \gamma) \\ \sqrt{\beta^2 - (\beta/\gamma)^2(\alpha - \gamma_0)^2} + \beta_0 & (\gamma_0 - \gamma \leq \alpha \leq \gamma_0 + \gamma) \\ -12 & (\gamma_0 + \gamma < \alpha) \end{cases} \tag{C.20}$$

$$\left.\begin{array}{ll} \gamma = 27.094M + 3.31 & \gamma_0 = 23.43M + 4.651 \\ \beta = 76.65M + 10.74 & \beta_0 = -34.19M - 13.82 \end{array}\right\} \tag{C.21}$$

C.3 LBL-VS

The strouhal number for LBL-VS is defined in Equation C.22-C.24. The strouhal number depends on boundary layer thickness that can be calculated with Green's entrainment method. G_1 is a shape function that relates the laminar boundary layer noise into account.

$$St' = \frac{f\delta_p}{U} \tag{C.22}$$

$$St'_1 = \begin{cases} 0.18 & \left(R_c < 1.3\times10^5\right) \\ 0.001756R_c^{0.3931} & \left(9.521.3\times10^5 \le R_c \le 4\times10^5\right) \\ 0.28 & \left(4\times10^5 < R_c\right) \end{cases} \tag{C.23}$$

$$St'_{peak} = St'_1 \times 10^{-0.04\alpha} \tag{C.24}$$

e is defines as $\frac{St'}{St'_{peak}}$ and d for Equation C.26 is defined as $\frac{R_c}{(R_c)_0}$.

$$G_1(e) = \begin{cases} 39.8\log_{10}(e) - 11.12 & (e \le 0.5974) \\ 98.409\log_{10}(e) + 2 & (0.5974 < e \le 0.8545) \\ -5.076 + \sqrt{2.484 - 506.25\left[\log_{10}(e)\right]^2} & (0.8545 < e \le 1.17) \\ -98.409\log_{10}(e) + 2 & (1.17 < e \le 1.674) \\ -39.8\log_{10}(e) - 11.12 & (1.674 < e) \end{cases} \tag{C.25}$$

$$G_2(d) = \begin{cases} 77.852\log_{10}(d) + 15.328 & (d \le 0.3237) \\ 65.188\log_{10}(d) + 9.125 & (0.3237 < d \le 0.5689) \\ -14.052\left[\log_{10}(d)\right]^2 & (0.5689 < d \le 1.7579) \\ -65.188\log_{10}(d) + 9.125 & (1.7579 < d \le 3.0889) \\ -77.852\log_{10}(d) + 15.328 & (3.0889 < d) \end{cases} \tag{C.26}$$

$$(R_c)_0 = \begin{cases} 10^{0.215\alpha+4.978} & (\alpha \le 3) \\ 10^{0.120\alpha+5.263} & (3 < \alpha) \end{cases} \tag{C.27}$$

$$G_3(\alpha) = 171.04 - 3.03\alpha \tag{C.28}$$

C.4 TEB

For the EB the strouhal number is defined by the height of the TE, which for this thesis is kept constant at 0.7 mm due to the 3D printing. Strouhal numbers can be determined with Equation C.30 and Equation C.31.

$$St''' = \frac{fh}{U} \tag{C.29}$$

$$St'''_{peak} = \begin{cases} \frac{0.212-0.0045\Psi}{1+0.235(h/\delta^*_{avg})^{-1}-0.0132(h/\delta^*_{avg})^{-2}} & \left(0.2 \le (h/\delta^*_{avg})\right) \\ 0.1(h/\delta^*_{avg}) + 0.095 - 0.00243\Psi & \left((h/\delta^*_{avg}) < 0.2\right) \end{cases} \tag{C.30}$$

$$(h/\delta^*_{avg}) = \frac{(h/\delta^*_p) + (h/\delta^*_s)}{2} \tag{C.31}$$

The shape functions are based on the TE slope angle and on the ratio between the height and the average displacement thickness.

$$G_4(h/\delta^*_{avg}, \Psi) = \begin{cases} 17.5\log_{10}\left(h/\delta^*_{avg}\right) + 157.5 - 1.114\Psi & \left(h/\delta^*_{avg} \le 5\right) \\ 16.7 - 1.114\Psi & \left(5 < h/\delta^*_{avg}\right) \end{cases} \tag{C.32}$$

$$G_5\left(\frac{h}{\delta^*_{avg}}, \Psi, \frac{St'''}{St'''_{peak}}\right) = (G_5)_{\Psi=0^\circ} + 0.0714\Psi\left[(G_5)_{\Psi=14^\circ} - (G_5)_{\Psi=0^\circ}\right] \tag{C.33}$$

$$(G_5)_{\Psi=14^\circ} = \begin{cases} m\eta + k & (\eta < \eta_0) \\ 2.5\sqrt{1-(\eta/\mu)^2} - 2.5 & (\eta_0 \leq \eta < 0) \\ \sqrt{1.5625 - 11794.99\eta^2} - 2.5 & (0 \leq \eta < 0.03616) \\ -155.543\eta + 4.375 & (0.0316 \leq \eta) \end{cases} \tag{C.34}$$

$$\eta = \log_{10}\left(\frac{St'''}{St'''_{peak}}\right) \tag{C.35}$$

$$\eta = \begin{cases} 0.1221 & \left(h/\delta^*_{avg} < 0.25\right) \\ -0.2175\left(h/\delta^*_{avg}\right) + 0.1755 & \left(0.25 \leq \left(h/\delta^*_{avg}\right) < 0.62\right) \\ -0.0308\left(h/\delta^*_{avg}\right) + 0.0596 & \left(0.62 \leq \left(h/\delta^*_{avg}\right) < 1.15\right) \\ 0.0242 & \left(1.15 \leq \left(h/\delta^*_{avg}\right)\right) \end{cases} \tag{C.36}$$

$$m = \begin{cases} 0 & \left(h/\delta^*_{avg} \leq 0.02\right) \\ 68.724\left(h/\delta^*_{avg}\right) - 1.35 & \left(0.02 < h/\delta^*_{avg} \leq 0.5\right) \\ 308.475\left(h/\delta^*_{avg}\right) - 121.23 & \left(0.5 < h/\delta^*_{avg} \leq 0.62\right) \\ 224.811\left(h/\delta^*_{avg}\right) - 69.35 & \left(0.62 < h/\delta^*_{avg} \leq 1.15\right) \\ 1583.28\left(h/\delta^*_{avg}\right) - 1631.59 & \left(1.15 < h/\delta^*_{avg} \leq 1.2\right) \\ 268.344 & \left(1.2 < h/\delta^*_{avg}\right) \end{cases} \tag{C.37}$$

$$\eta_0 = -\sqrt{\frac{m^2\mu^4}{6.25 + m^2\mu^2}} \tag{C.38}$$

$$k = 2.5\sqrt{1 - \left(\frac{\eta_0}{\mu}\right)^2} - 2.5 - m\eta_0 \tag{C.39}$$

$$\left(\frac{h}{\delta^*_{avg}}\right)' = 6.724\left(\frac{h}{\delta^*_{avg}}\right)^2 - 4.019\left(\frac{h}{\delta^*_{avg}}\right) + 1.107 \tag{C.40}$$

C.5 TV

The last equations are for tip vortex noise. BPM defines two tip flat and round, for this thesis only the flat tip is used. The Strouhal number is defined on the parameter l which is the span wise extend of the vicious core of the tip vortex. l can be determined with Equation C.42 which is for the round tip. While Equation C.45 is the equation for determining l for the flat case.

$$St'' = \frac{f\,l}{U_{max}} \tag{C.41}$$

$$l/c = 0.008\alpha_{TIP} \tag{C.42}$$

$$M_{MAX}/M \approx (1 + 0.036\alpha_{TIP}) \tag{C.43}$$

$$U_{MAX} = c_0 M_{max} \tag{C.44}$$

$$l/c = \begin{cases} 0.0230 + 0.0169\alpha_{TIP} & (0^\circ \leq \alpha_{TIP} \leq 2^\circ) \\ 0.0378 + 0.0095\alpha_{TIP} & (2^\circ < \alpha_{TIP}) \end{cases} \tag{C.45}$$

Appendix D

Verification Results

D.1 BPM Verification

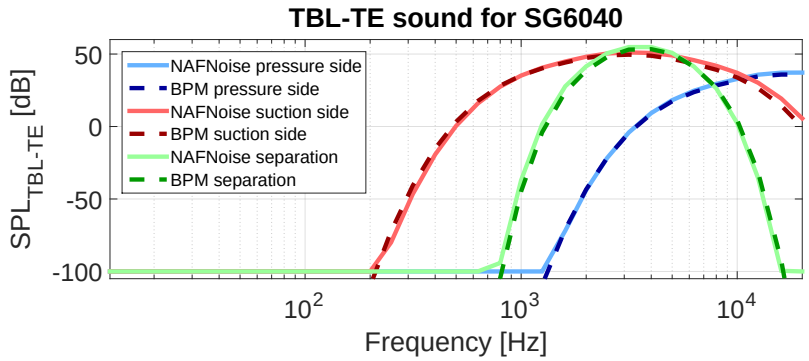

Figure D.1: TBL-TE noise verification between NAFNoise and Code

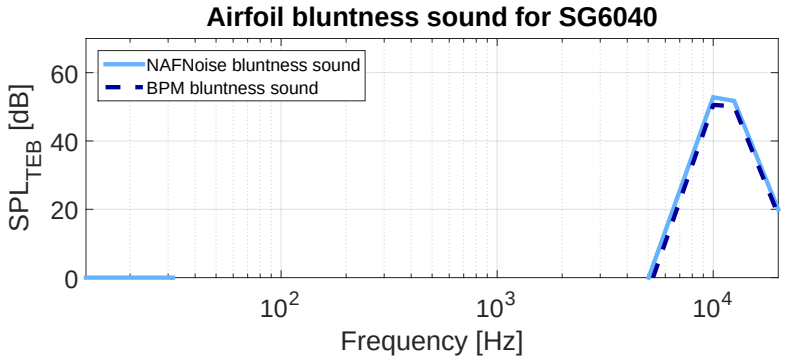

Figure D.2: TEB noise verification between NAFNoise and Code

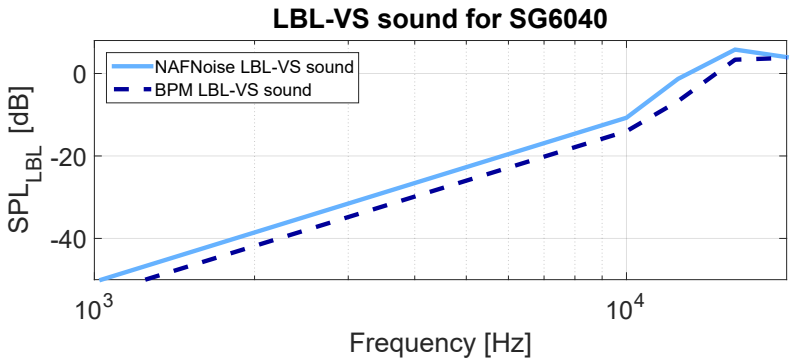

Figure D.3: LBL-VS noise verification between NAFNoise and Code

Appendix E

Validation Results

E.1 $\lambda - C_P$ Curves Experimental Data

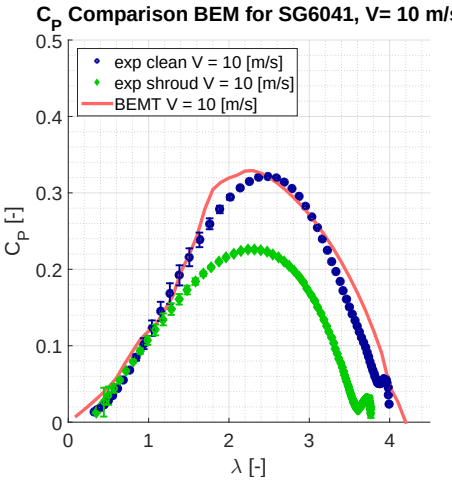

(a) $\lambda - C_P$ curve for SG6041, V = 10 m/s

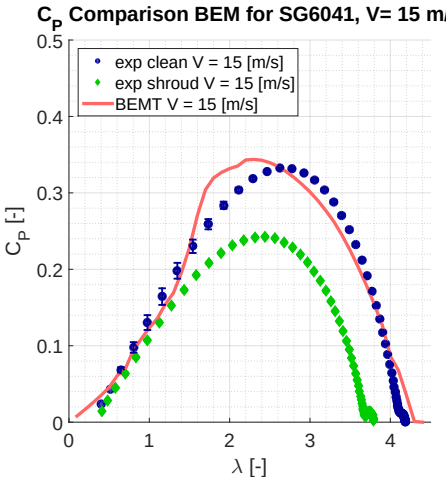

(b) $\lambda - C_P$ curve for SG6041, V = 15 m/s

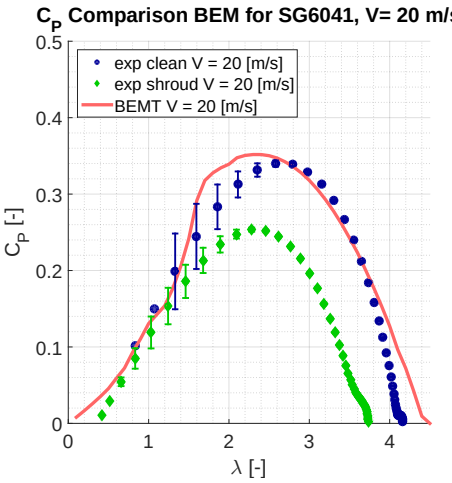

(c) $\lambda - C_P$ curve for SG6041, V = 20 m/s

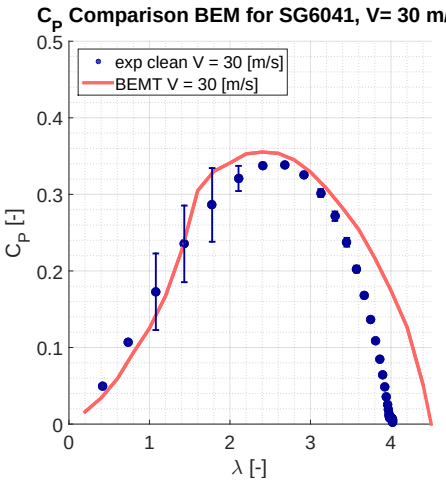

(d) $\lambda - C_P$ curve for SG6041, V = 30 m/s

Figure E.1: $\lambda - C_P$ experimetnal data for SG6041 and shroud

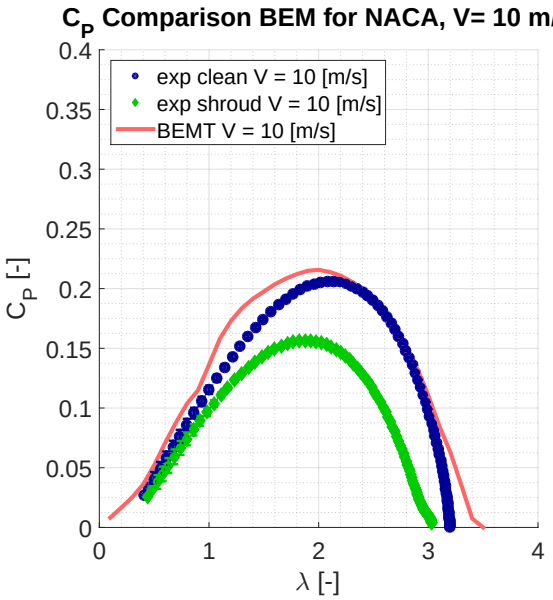

(a) $\lambda - C_P$ curve for NACA4418, V = 10 m/s

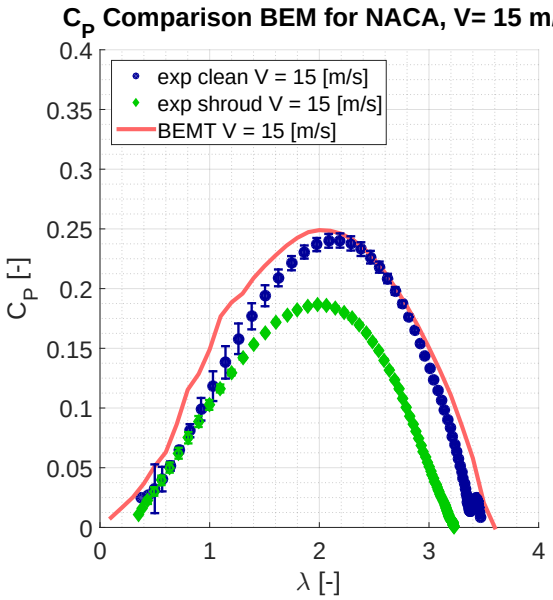

(b) $\lambda - C_P$ curve for NACA4418, V = 15 m/s

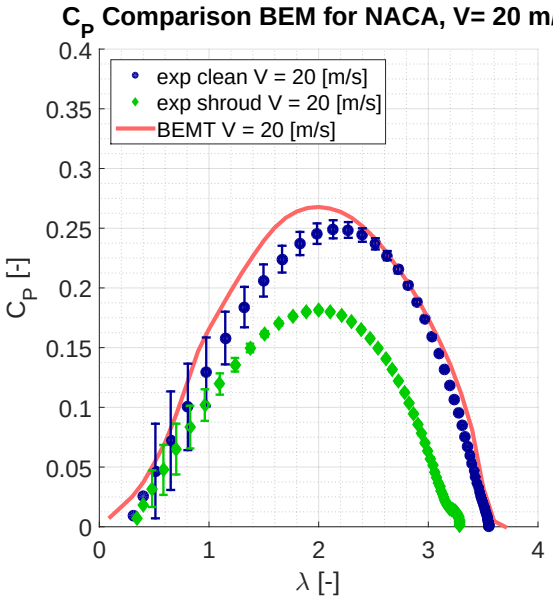

(c) $\lambda - C_P$ curve for NACA4418, V = 20 m/s

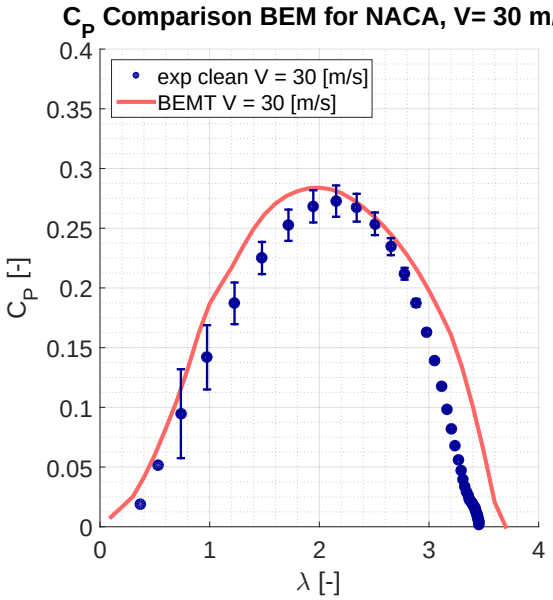

(d) $\lambda - C_P$ curve for NACA4418, V = 30 m/s

Figure E.2: $\lambda - C_P$ experimetnal data for NACA4418 and shroud

E.2 $\lambda - C_T$ Curves Experimental Data

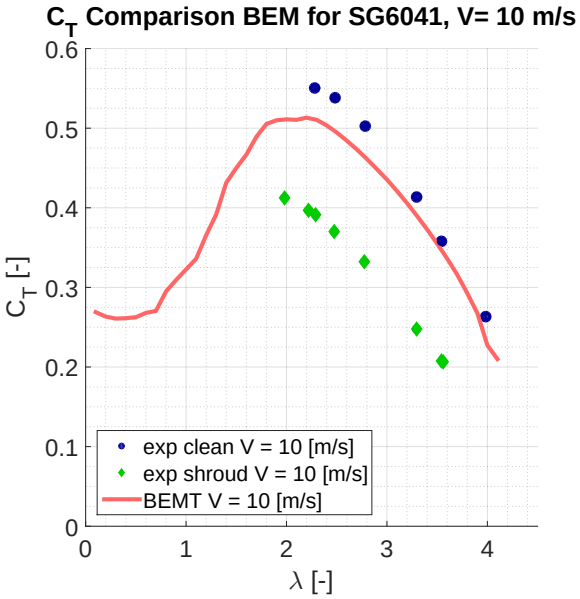

(a) $\lambda - C_P$ curve for SG6041, V = 10 m/s

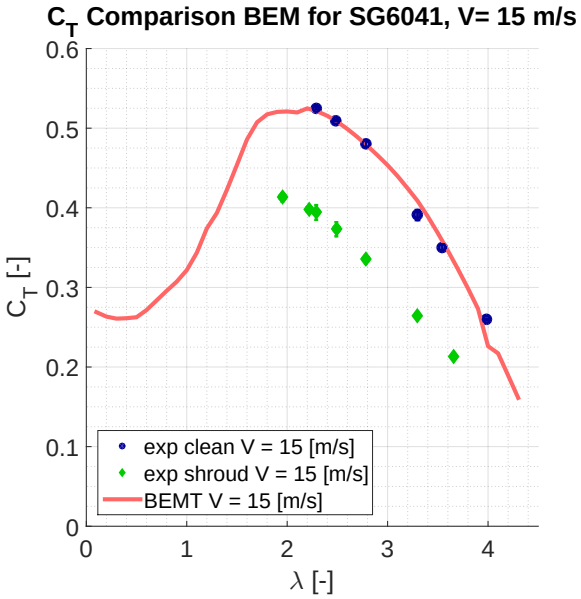

(b) $\lambda - C_T$ curve for SG6041, V = 15 m/s

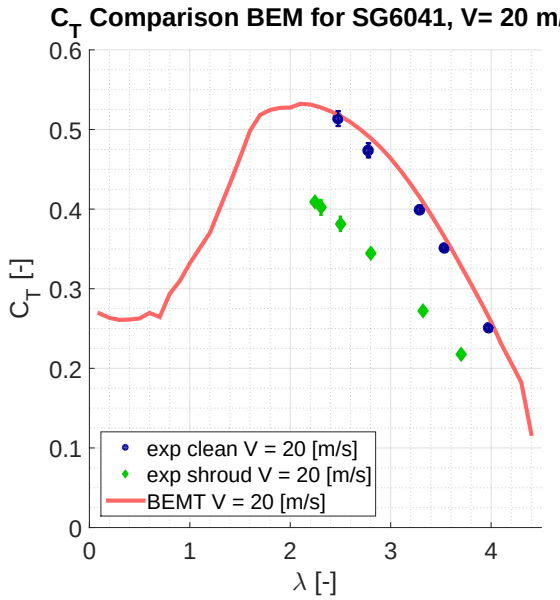

(c) $\lambda - C_T$ curve for SG6041, V = 20 m/s

Figure E.3: $\lambda - C_T$ experimetnal data for SG6041 and shroud

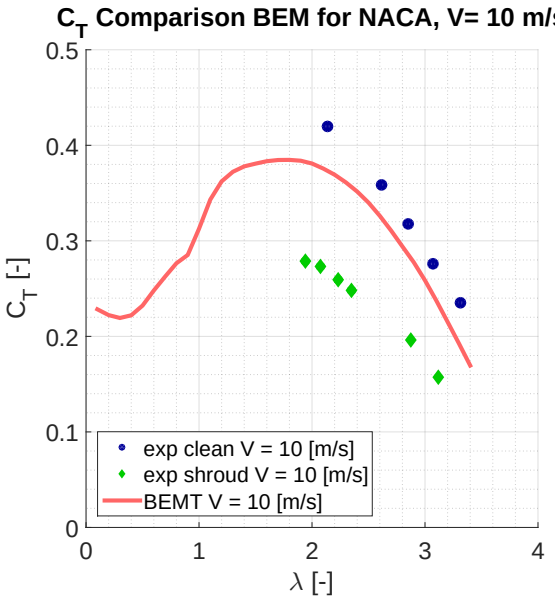

(a) $\lambda - C_T$ curve for NACA4418, V = 10 m/s

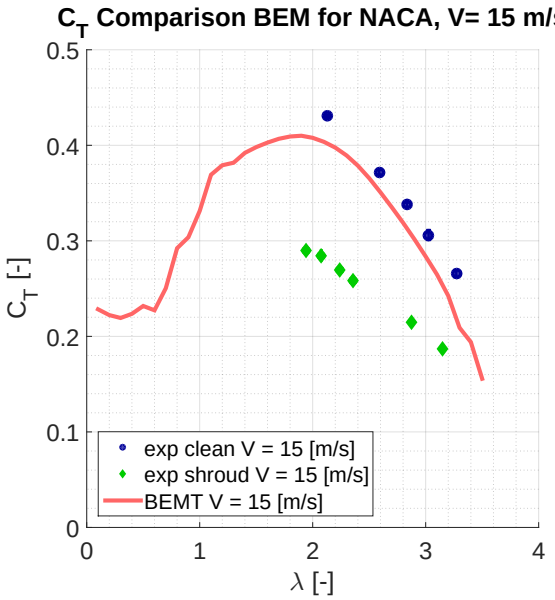

(b) $\lambda - C_T$ curve for NACA4418, V = 15 m/s

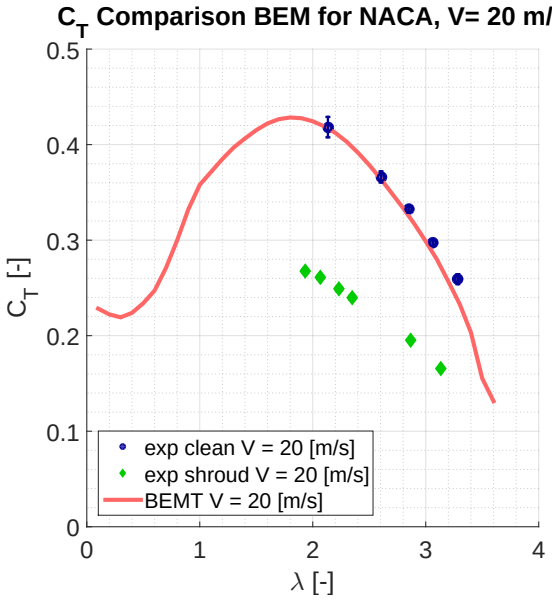

(c) $\lambda - C_T$ curve for NACA4418, V = 20 m/s

Figure E.4: $\lambda - C_T$ experimental data for NACA4418 and shroud

E.3 Tonal Noise Experimental Data

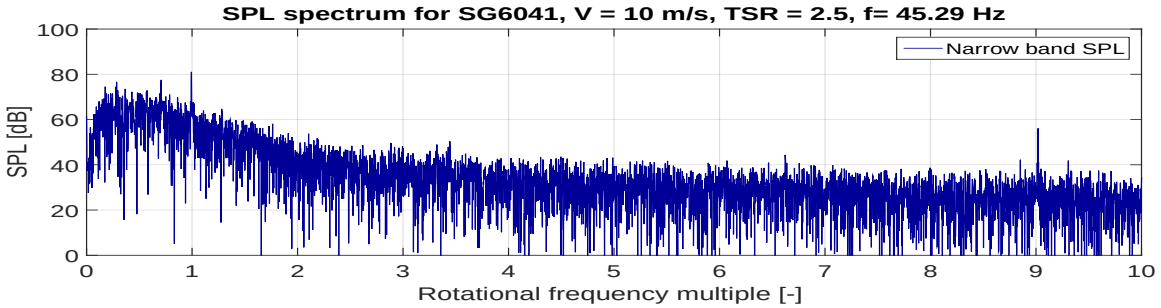

(a) SPL for SG6041, V = 10 m/s TSR=2.5

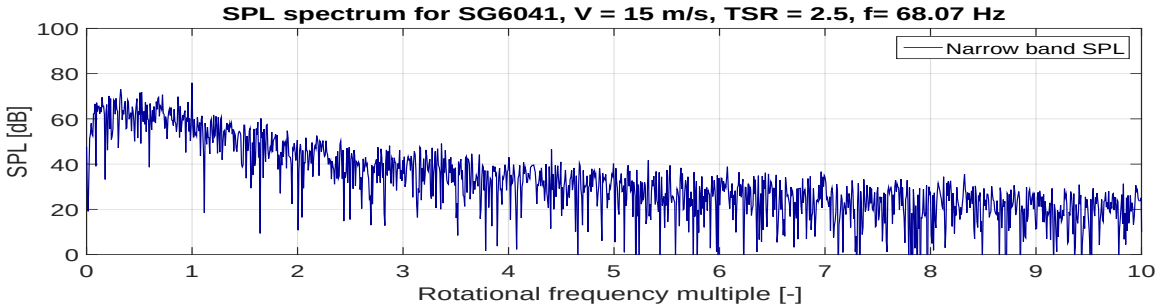

(b) SPL for SG6041, V = 15 m/s TSR=2.5

Figure E.5: SPL data for SG6041 rotor, blue line is narrowed band normalized to rotational frequency

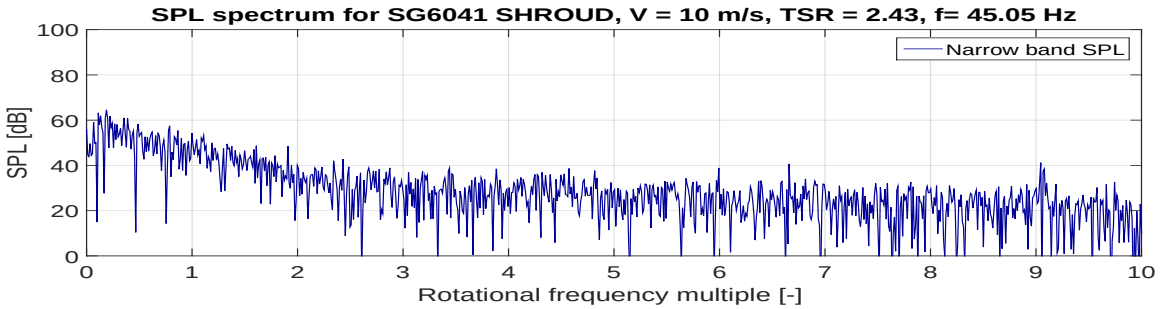

(a) SPL for SG6041 with shroud, V = 10 m/s TSR=2.43

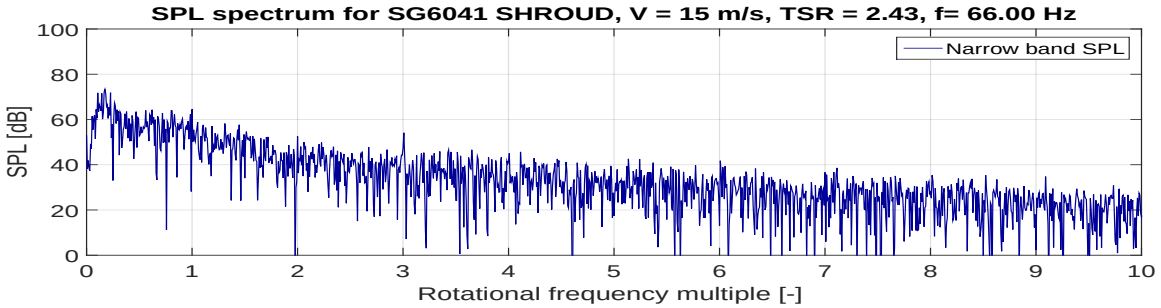

(b) SPL for SG6041 with shroud, V = 15 m/s TSR=2.43

Figure E.6: SPL data for SG6041 with shroud, blue line is narrowed band normalized to rotational frequency

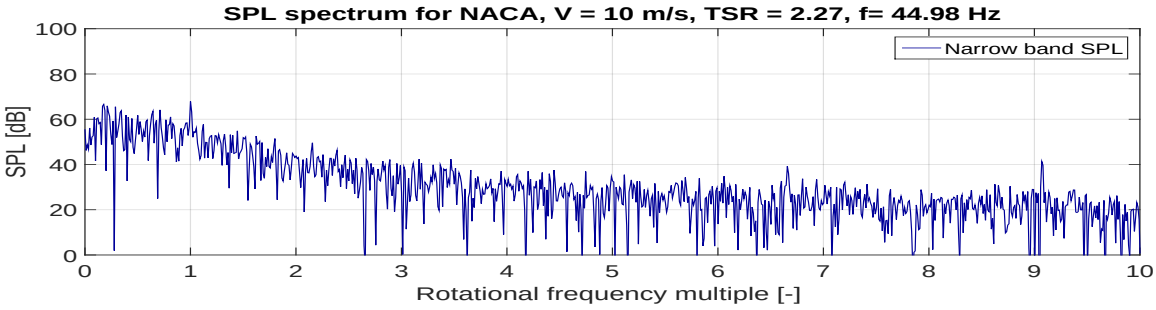

(a) SPL for NACA4418, V = 10 m/s TSR=2.27

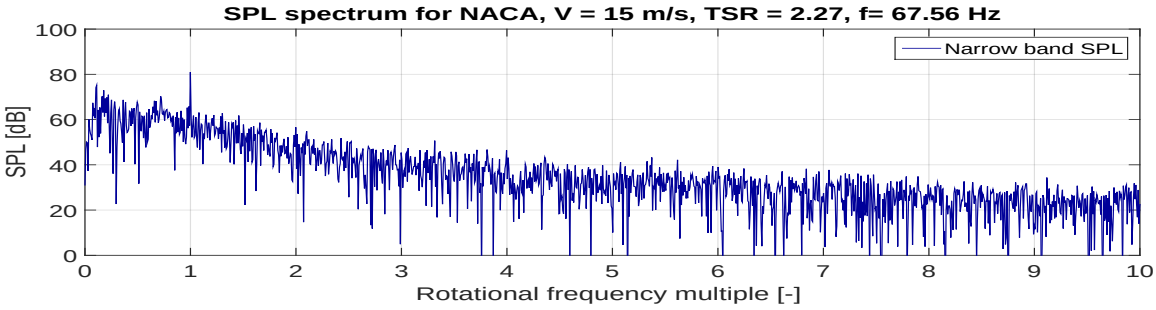

(b) SPL for NACA4418, V = 15 m/s TSR=2.27

Figure E.7: SPL data of NACA4418, blue line is narrowed band normalized to rotational frequency

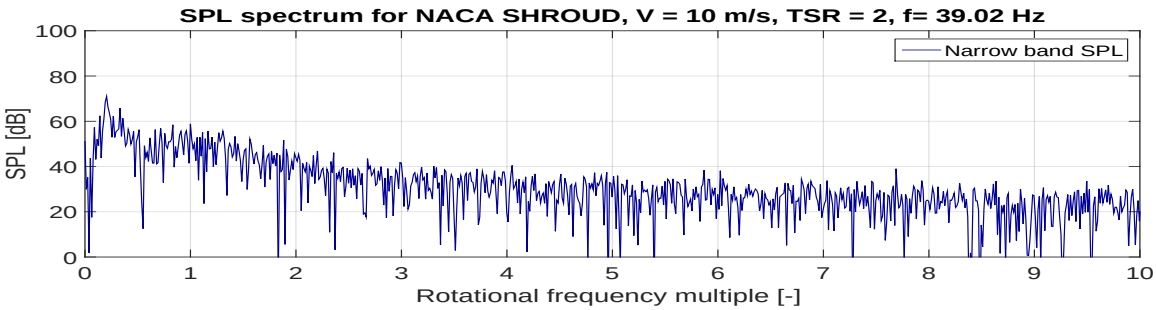

(a) SPL for NACA4418 with shroud, V = 10 m/s TSR=2

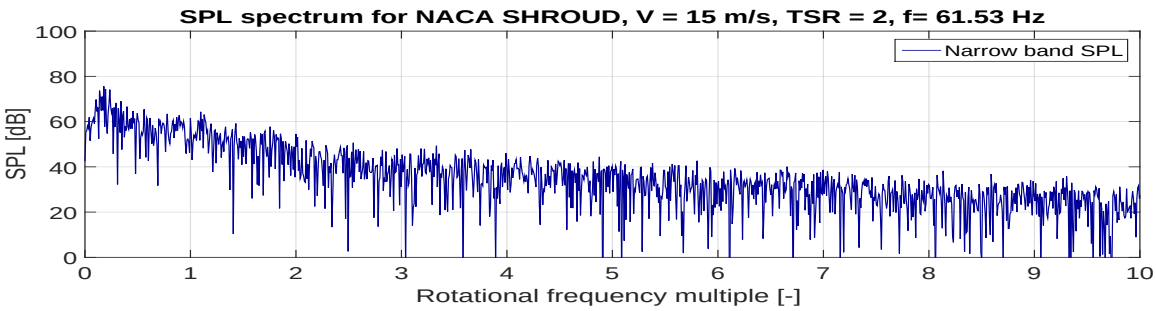

(b) SPL for NACA4418 with shroud, V = 15 m/s TSR=2

Figure E.8: SPL data of NACA4418 with shroud, blue line is narrowed band normalized to rotational frequency

E.4 BPM & Experimental Comparison

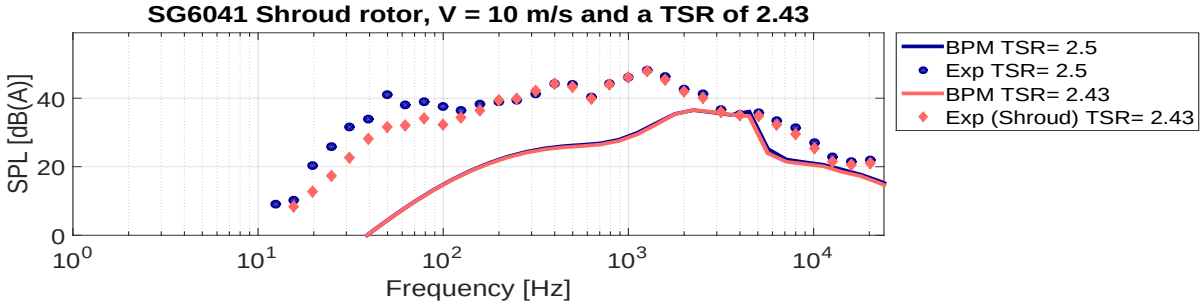

(a) SPL for NACA4418 with shroud, V = 10 m/s TSR=2

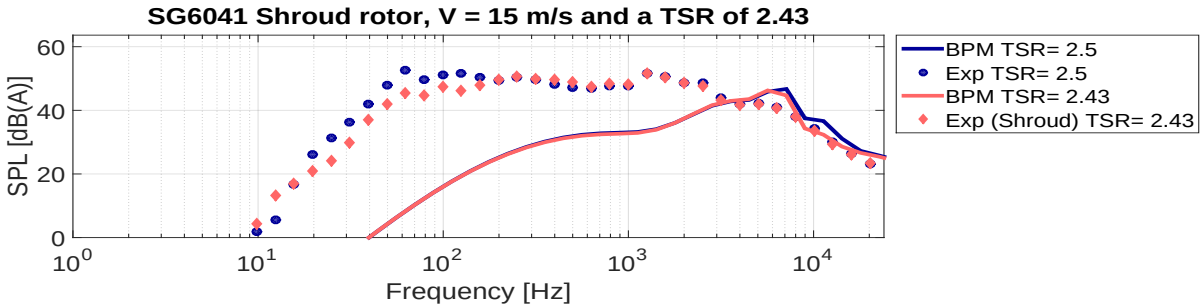

(b) SPL for NACA4418 with shroud, V = 15 m/s TSR=2

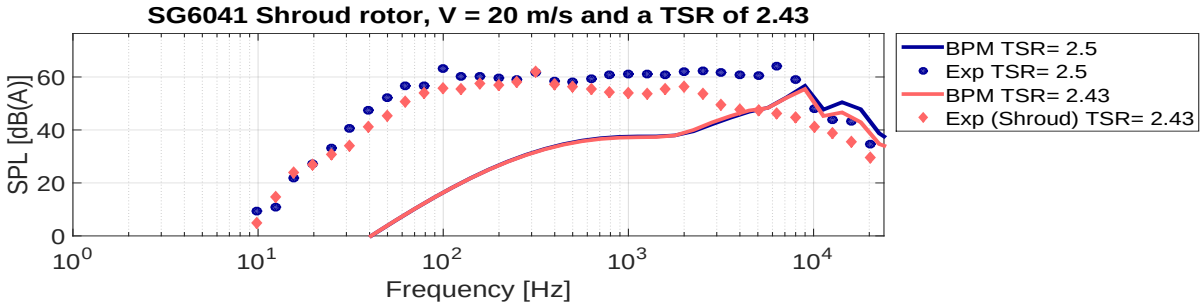

(c) SPL for NACA4418 with shroud, V = 15 m/s TSR=2

Figure E.9: SPL data blue line is non shrouded rotor and red line is shrouded rotor

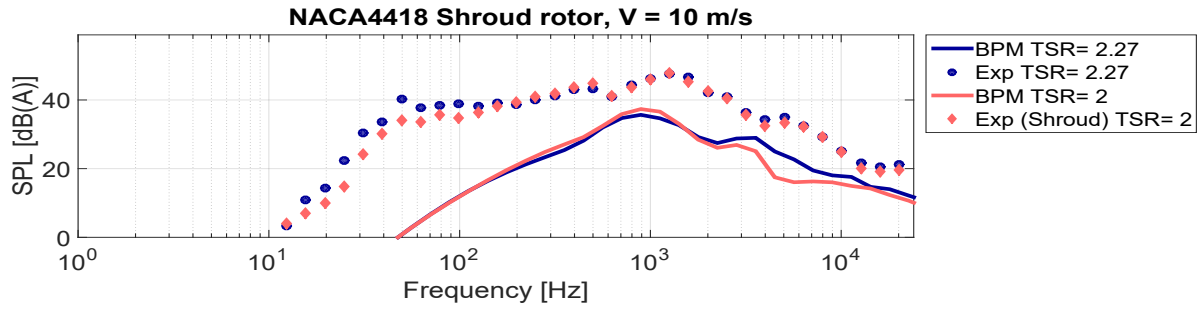

(a) SPL for NACA4418 with shroud, V = 10 m/s TSR=2

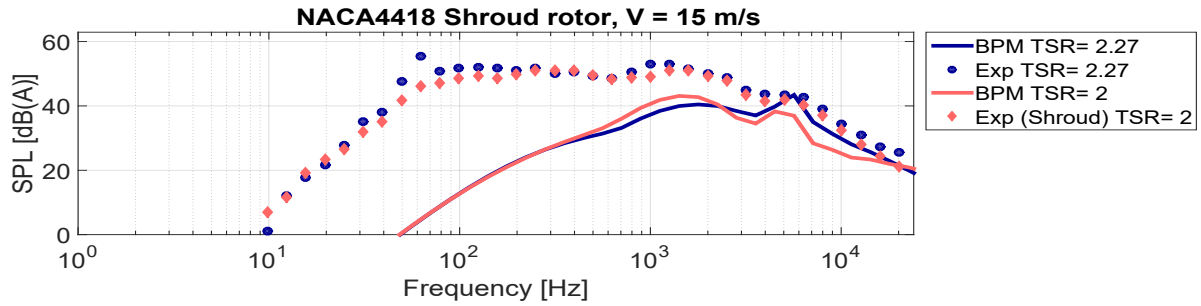

(b) SPL for NACA4418 with shroud, V = 15 m/s TSR=2

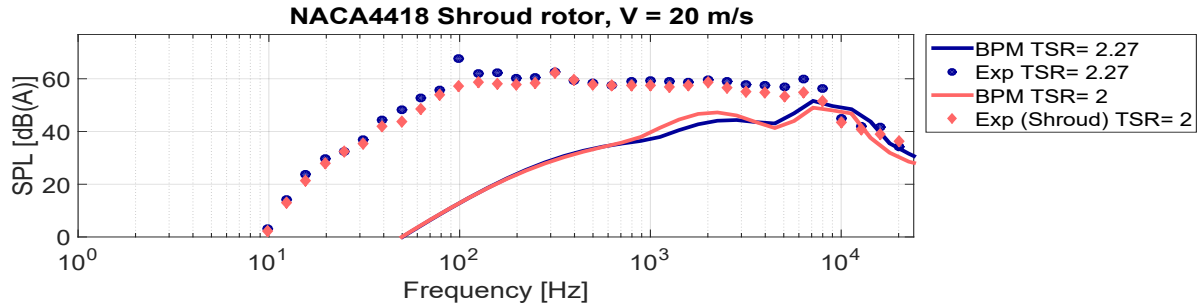

(c) SPL for NACA4418 with shroud, V = 15 m/s TSR=2

Figure E.10: SPL data blue line is non shrouded rotor and red line is shrouded rotor 1/3 octave band

E.5 BPM Calculations

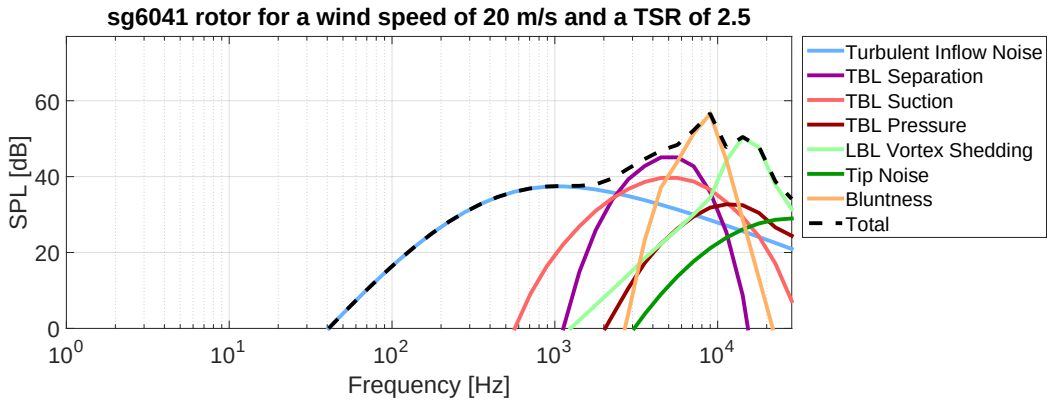

Figure E.11: SG6041 rotor airfoil self-noise for a wind speed of 20 m/s

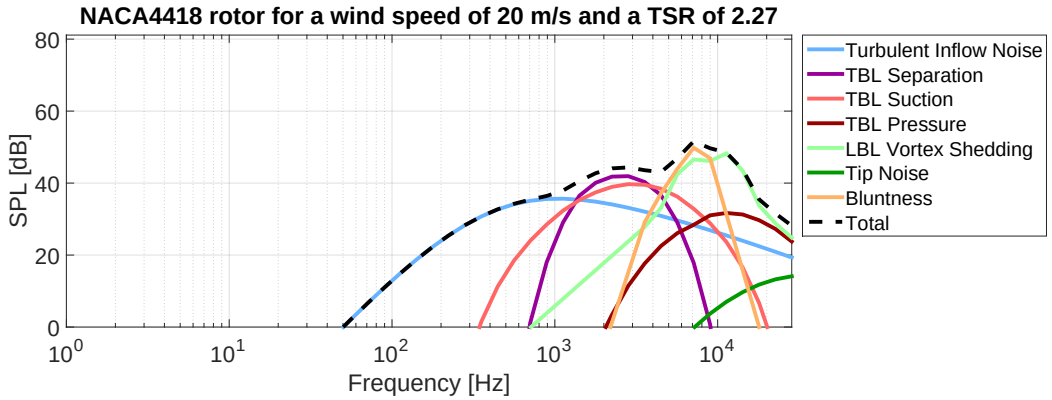

Figure E.12: NACA4418 rotor airfoil self noise for a wind speed of 20 m/s